ALMA Mater Studiorum
Universita` degli Studi di Bologna

SCUOLA DI SCIENZE

Corso di Laurea Magistrale in Astrofisica e Cosmologia

Dipartimento di Fisica e Astronomia

Searching for outflows signatures in SDSS spectra of X-ray selected, obscured AGN in the COSMOS field

Elaborato Finale

Candidato:

Giustina Vietri

Relatore:
Chiar.mo Prof.:

Andrea Cimatti

Co-relatore:

Dott.ssa Marcella Brusa

Sessione II
Anno Accademico 2013-2014

SOMMARIO

Contesto scientifico e scopi É ormai ritenuto molto probabile che al centro della maggior parte delle galassie si trovi un buco nero supermassiccio. La stretta correlazione tra la massa del buco nero e la dispersione delle velocità nel bulge galattico, nota come relazione M-σ, suggerisce che la formazione della galassia e del buco nero al suo centro siano tra loro collegate. La presenza di un buco nero (BN) supermassiccio infatti ha un'importante conseguenza sulla storia evolutiva della galassia stessa, in quanto attraverso una fase di accrescimento può dar vita ad un Nucleo Galattico Attivo (AGN), che rilascia una grande quantità d'energia sotto forma di radiazione e può produrre venti, spinti dalla pressione della radiazione, che influenzano la vita della galassia e del BN stesso. Questi venti interagiscono con l'ambiente della galassia ospite, portando alla formazione di flussi di gas su larga scala, che possono influenzare la massa finale della galassia. Infatti questi flussi di materia, che possono essere sotto forma molecolare, neutra e ionizzata, possono essere condotti al di fuori del bulge, bloccando la crescita del BN e la formazione di stelle nella galassia. Senza il gas necessario alla formazione di nuove stelle, la galassia ospite diventa un insieme di stelle vecchie che fanno apparire la galassia più arrossata, giungendo così alla cosiddetta fase red and dead. Esaminando la riga d'emissione proibita dell'ossigeno, [OIII]λ5007, che viene prodotta in un ambiente a bassa densità, chiamato Narrow Line Region (NLR), è possibile tracciare la cinematica del gas ionizzato in questa regione dell'AGN. La FWHM di questa riga è in genere pari a $\sim$400-500 km s^{-1}, quindi un eventuale allargamento o asimmetria del profilo di riga è il risultato di un forte gradiente di velocità o di cinematica disturbata.
Nel nostro lavoro di tesi abbiamo deciso di esaminare AGN selezionati in X, con lo scopo di identificare i flussi di gas ionizzato attraverso la riga proibita dell'ossigeno, [OIII]λ5007.

Metodi e campione utilizzato Partendo dal campione di AGN presente nella survey di XMM-COSMOS, abbiamo cercato la sua controparte ottica nel database DR10 della Sloan Digital Sky Survey (SDSS), ed il match ha portato ad una selezione di 200 oggetti, tra cui stelle, galassie e quasar. A partire da questo campione, abbiamo selezionato tutti gli oggetti con un redshift $z<0.86$ per limitare l'analisi agli AGN di tipo 2, quindi siamo giunti alla selezione finale di un campione di 30 sorgenti.
L'analisi spettrale è stata fatta tramite il task SPECFIT, presente in IRAF. Abbiamo creato due tipi di modelli: nel primo abbiamo considerato un'unica componente per ogni riga di emissione, nel secondo invece è stata introdotta un'ulteriore componente limitando la FWHM della prima ad un valore inferiore a 500 km s^{-1}. Le righe di emissione di cui abbiamo creato un modello sono le seguenti: Hβ, [NII]$\lambda\lambda$ 6548,6581, Hα, [SII]$\lambda\lambda$ 6716,6731 e [OIII]$\lambda\lambda$ 4959,5007. Nei modelli costruiti abbiamo tenuto conto della fisica atomica per quel che riguarda i rapporti dei flussi teorici dei doppietti dell'azoto e dell'ossigeno, fissandoli a 1:3 per entrambi; nel caso

del modello ad una componente abbiamo fissato le FWHM delle righe di emissione; mentre nel caso a due componenti abbiamo fissato le FWHM delle componenti strette e larghe, separatamente. Tenendo conto del chi-quadro ottenuto da ogni fit e dei residui, è stato possibile scegliere tra i due modelli per ogni sorgente. Considerato che la nostra attenzione è focalizzata sulla cinematica dell'ossigeno, abbiamo preso in considerazione solo le sorgenti i cui spettri mostravano la riga suddetta, cioè 25 oggetti. Su questa riga è stata fatta un'analisi non parametrica in modo da utilizzare il metodo proposto da Harrison et al. (2014) per caratterizzare il profilo di riga. Sono state determinate quantità utili come il 2° e il 98° percentili, corrispondenti alle velocità massime proiettate del flusso di materia, e l'ampiezza di riga contenente l'80% dell'emissione.

Risultati L'analisi spettrale restituisce il flusso, le FWHM e i centroidi di ogni riga d'emissione inserita nel modello. Abbiamo utilizzato i flussi dell' [OIII]λ5007, [NII]λ6731, Hα e di Hβ per costruire il diagramma diagnostico di Baldwin, Phillips e Terlevich (BPT), utile per classificare gli oggetti in base alla ionizzazione delle righe. E' stato possibile costruirlo per 12 sorgenti. Per cercare correlazioni tra i flussi di gas uscenti e l'AGN, abbiamo confrontato le FWHM delle componenti larghe dell'[OIII] con la luminosità totale della riga dell'ossigeno e con la luminosità bolometrica dell'AGN. Abbiamo confrontato i nostri risultati con quelli in letteratura, ottenendo un intervallo di valori per la FWHM consistente con quelli dei campioni utilizzati nel confronto. Per indagare sull'eventuale ruolo che ha l'AGN nel guidare questi flussi di materia verso l'esterno, abbiamo calcolato la massa del gas ionizzato presente nel flusso e il tasso di energia cinetica, tenendo conto solo delle componenti larghe della riga di [OIII] λ5007. Per la caratterizzazione energetica abbiamo considerato l'approccio di Cano-Diaz et al (2012) e di Heckman (1990) in modo da poter ottenere un limite inferiore e superiore della potenza cinetica, adottando una media geometrica tra questi due come valore indicativo dell'energetica coinvolta. Confrontando la potenza del flusso di gas con la luminosità bolometrica dell'AGN, si è trovato che l'energia cinetica del flusso di gas è circa lo 0.3-30% della luminosità dell'AGN, consistente con i modelli che considerano l'AGN come principale responsabile nel guidare questi flussi di gas.

Applicazioni future La nostra analisi si basa su spettri non spazialmente risolti, questo non ci permette di avere delle informazioni spaziali riguardo all'estensione dei flussi di gas. Quindi l'uso di spettroscopia risolta è necessaria per effettuare un'analisi decisamente migliore e più utile, ai fini di caratterizzare in modo più veritiero la cinematica del gas preso in esame. In più è possibile considerare un numero maggiore di oggetti in modo da dare una valenza statistica ai risultati ottenuti o utilizzare una banda di osservazione diversa come l'infrarosso (IR), per lo studio di AGN a più alto redshift, in quanto in questo caso la riga dell'[OIII] risulta essere spostata nella banda del vicino infrarosso (NIR).

Contents

List of Figures

List of Tables

Chapter 1

Introduction

One of the most active research areas in astrophysics is the study of the formation and evolution of galaxies. Even if some ideas are now widely accepted, many questions on the formation and evolution of galaxies remain unanswered. The current paradigm of galaxy formation assumes that galaxies grew out of primordial Gaussian density fluctuations, generated during inflation and amplified by gravitational instability acting on Cold Dark Matter (CDM), the dominant mass component of the Universe. In this scenario structures form beginning with small objects which then merge to form ever larger structures: it is called bottom-up formation. Its competitor is top-down scenario, where hot dark matter is the main character. In this scenario large scale objects form first, which fragment into smaller objects. [1]

Before the CDM cosmology became the favored cosmological model, many others appeared. Press and Schecther (1974) used a spherical model (Gunn & Gott 1972) to describe the evolution of a uniform, spherically symmetric overdensity in an otherwise unperturbed universe and to predict the number of objects as a function of their mass M, basing on the idea that primordial density perturbations were Gaussian fluctuations and evolved into bound objects with mass M, after they reached an amplitude greater than some critical value, δ_c. In this model the sequence of structure formation is hierarchical: the universe fragments into low-mass clumps at high redshift, following which a number of clumps merges into larger units at later times. But Press and Schecther involved a gas of self-gravitating mass in this scenario, there is as yet no dark matter.

White and Rees (1978), which may be considered the progenitors

---

[1] The observations favor the bottom-up scenario, thus only CDM will be discussed in the text.

of nearly all current theoretical models of galaxy formation, adopted a model based on the hierarchical clustering scenario proposed by Press and Schechter (1974) but with two new ingredients: dark matter and the cooling of baryons, in order to reproduce the structures we observe as galaxies. They proposed a two stage theory of galaxy formation with dark haloes forming in a dissipationless, gravitational collapse and galaxies forming inside these haloes, following the radiative cooling of baryons.

The first semy-analitical model of galaxy formation was produced by White & Frenk (1991), which included elements such as cold dark matter, gas cooling, star formation, feedback and stellar populations, at the root of today's models.

The current standard model is based on a cold dark matter with a cosmological constant Λ, that accounts for the presence of dark energy, a hypothetical force that appears to be accelerating the expansion of the Universe. According to the ΛCDM theory, the Universe was hot, smooth and homogeneous immediately after the Big Bang. However small fluctuations in density began to appear and grow, which were characterized by the following density contrast:

$$\delta = \frac{\delta\rho}{\langle\rho\rangle} = \frac{\rho - \langle\rho\rangle}{\langle\rho\rangle} \tag{1.1}$$

where $\langle\rho\rangle$ is the average density of the Universe and ρ is the perturbation density.

The medium was composed of cold dark matter, baryonic matter and radiation, which initially were coupled. The dark matter was the first component to decouple with radiation, since experiences only the weak and gravitational forces. After the decoupling, the dark matter began to collapse and the first potential wells were formed. The density fluctuations of baryon-radiation plasma oscillated until the baryonic matter decoupled from the radiation. Thereafter the matter fell into the potential wells created by DM, collapsed and condensed to form stars, i.e. Population III[2] and galaxies. Part of this gas was probably used to form a massive black hole (MBH). There are three possible scenario about its formation:

---

[2]. Population III (Pop III) stars are composed entirely of primordial gas, i.e. hydrogen, helium and very small amounts of lithium and beryllium. This means that the gas from which Pop III stars formed had not been 'recycled' (incorporated into, and then expelled) from previous generations of stars, but was pristine material left over from the Big Bang. As such, these stars would have a [Z/H] $\sim$ -10 and would constitute the very first generation of stars formed within a galaxy. These Pop III stars would then produce the metals observed in Pop II stars and initiate the gradual increase in metallicity across subsequent generations of stars.

- One star per galaxy more massive than 250 $M_\odot$ forms then collapses and gives rise to a MBH of 100 $M_\odot$
- If a globally unstable disk is formed then the unstable gas infalls towards the galaxy center and forms a supermassive star. The stellar core collapses and forms a BH of a few tens of $M_\odot$, which is embedded in what is left of the star thus it can grow by eating its surrounding and reach a mass of million solar masses.
- If a locally unstable disk is formed then the gas flows towards the galaxy center and stars start to form in this central region, giving rise to a dense stellar cluster. The collision between stars can produce a very massive star that collapses into a massive black hole.

These BH seeds, in place when the Universe was only few hundreds of Myr old, then will grow their mass through accretion of material and will begin the Supermassive Black Holes (SMBH) we observe today at the centre of the galaxies (with masses of $10^6 - 10^9$ M⊙). When SMBHs grow through accretion of nearby matter, the gravitational potential of the accreted mass is converted into radiation making the central object luminous. In this case the SMBH is called **active galactic nucleus (AGN)** (Salpeter 1964, Lynden-Bell 1969, Shakura & Sunyaev 1973).

1.1 The emission of AGN

The AGN phase occurs when the BH is accreting matter. The gravitational field of the AGN draws the matter orbiting it inward, forming an accretion disk and leading to viscous heating and to an observational signature in the emitted radiation. The rate at which energy is emitted by the nucleus, i.e. its luminosity, gives us the rate at which energy must be supplied to the nuclear source by accretion:

$$L = \eta \dot{M} c^2 \tag{1.2}$$

where $\dot{M} = dM/dt$ is the mass accretion rate and η is the mass-to-energy conversion efficiency, which determines the viability of accretion as a source of energy, and c is the speed of light.

The potential energy of a mass m at a distance r from the central source of mass M is

$$U = \frac{GMm}{r} \tag{1.3}$$

the rate at which the potential energy of infalling material can be converted to radiation is given by

$$L \approx \frac{dU}{dt} = \frac{GM}{r}\frac{dm}{dt} = \frac{GM\dot{M}}{r} \tag{1.4}$$

Combining equations 1.2 e 1.4 follows that $\eta \propto$ M/r, which is a measure of the compactness of a system. Considering a characteristic scale of the BH, i.e. Schwarzschild radius $R_S = 2GM/c^2$, the energy available from a particle of mass m falling to within this scale is:

$$U = \frac{GMm}{5R_S} = \frac{GMm}{10GM/c^2} = 0.1mc^2 \tag{1.5}$$

and this leads to a mass-to-energy conversion efficiency of 0.1.

The accretion onto a BH is limited by the effects of the radiation pressure experienced by the infalling matter. As first pointed out by Arthur Eddington in the 1920s, this limit depends on the mass of the central source and the opacity of the infalling material. The so called Eddington luminosity is the observable quantity corresponding to the critical mass accretion rate and, supposing that the gas around the BH is fully ionized hydrogen and assuming spherical symmetry, is obtained by equating the outward radiation force

$$F_{rad} = \frac{L\sigma_T}{4\pi r^2 c} \tag{1.6}$$

to the inward force due to the gravity:

$$F_{grav} = \frac{GMm_p}{r^2} \tag{1.7}$$

where in equation 1.6 σ_T is the Thomson cross-section and in equation 1.7 M is the central object mass and m_p is the proton mass. The Eddington luminosity is therefore:

$$L_{Edd} = \frac{4\pi GMm_p c}{\sigma_T} \simeq 1.3\ 10^{38}\frac{M}{M_\odot} erg\ s^{-1} \tag{1.8}$$

Thus the Eddington accretion rate is:

$$\dot{M}_{Edd} = L_{Edd}/\eta c^2 \tag{1.9}$$

Angular momentum considerations must take into account, since the orbiting material must lose angular momentum: the total angular momentum of the system must be conserved, thus the angular momentum lost due to matter falling onto the center has to be offset by angular momentum gain of matter far from the center.

The physics underlying this angular momentum transport remains an active field of study, even if the problem seems to be now qualitatively understood. Balbus and Hawley (1992) involves a magnetic field with a component in the axial direction of the disk, which leads to a dynamically unstable situation so that angular momentum transport occurs. But an approximate solution to the problem was proposed by Shakura and Sunyaev (1973), applicable to geometrically thin optically thick accretion disks. The assumption is that the energy from accreted material is dissipated within a small region at its radius r and since the disk is optically thick, the spectrum is that of a black body with a temperature T(r). Gravitational potential energy is released at the rate GM$\dot{M}/r$ and from the virial theorem, half of this goes into heating the gas and the other half is radiated away at the rate L:

$$L = \frac{GM\dot{M}}{2r} = 2\pi r^2 \sigma T^4 \tag{1.10}$$

where σT^4 is the black body radiation formula for the energy per unit area and 2 πr^2 is the disk area. This leads to a temperature at r:

$$T \propto (M\dot{M})^{1/4} r^{-3/4} \tag{1.11}$$

Taking into account how the energy is dissipated in the disk through viscosity and rewriting the relation in terms of Eddington accretion rate (eq. 1.9), the eq. 1.11 can be also written as follows:

$$T(r) = 6.3\ 10^5 (\dot{M}/\dot{M}_{Edd})^{1/4}\ M_8^{-1/4} (\frac{r}{R_S})^{-3/4}\ K \tag{1.12}$$

where R_S is the Schwarzschild radius. From eq 1.12 one would expect that the peak temperature of the accretion disk is lower for more massive BHs. The thermal emission from an AGN accretion disk is expected to be prominent in the UV spectrum with a temperature peak T$\sim 10^5$ K.

1.2 Observational picture of AGN

A key observational aspect of AGN is the continuum spectral distribution, that ranges from radio to hard X-ray. The AGN spectral energy distribution (SED) shows the following features:

- Big blue bump (BBB): it covers the wavelength range from 4000Å to 1000Å. This bump is attributed to the thermal emission from the accretion disk surrounding the SMBH.
- The infrared bump: it is a broad feature with a peak at 10μm. This bump is thought to arise from reprocessing of BBB emission by dust with temperature in the range of 10-1800 K and at a range of distances from the central source (Phinney 1989).
- The near-infrared inflection: it appears as a dip between the two bumps.
- The submillimeter break: it marks a sharp drop in emission. The exact location of this feature and the size of the drop varies within the AGN population. In radio-loud objects the drop in power output is only ~ 2 decades, while for the more common radio-quiet objects it may be ~ 5 or 6 decades (Elvis et et al. 1994). This part is associated to synchrotron radiation from powerful jets in radio-loud AGN.
- X-ray region: it can be divided in soft and hard X-ray band.
  In the soft region there is the soft X-ray excess that may be the high energy continuation of the BBB. In the hard X-ray band the shape of the SED, a power law spectrum, is due to Compton upscattering of optical/UV photons by hot or nonthermal electrons of the corona above the disk. Superimposed on this power law are Fe Kα emission line at 6.4 keV and a Compton reflection hump above 10 keV. These two features are thought to be due to fluorescence and reflection from the accretion disk.

In figure 1.1 it is shown a schematic representation of the broad-band continuum spectral energy distribution seen in different types of AGNs.

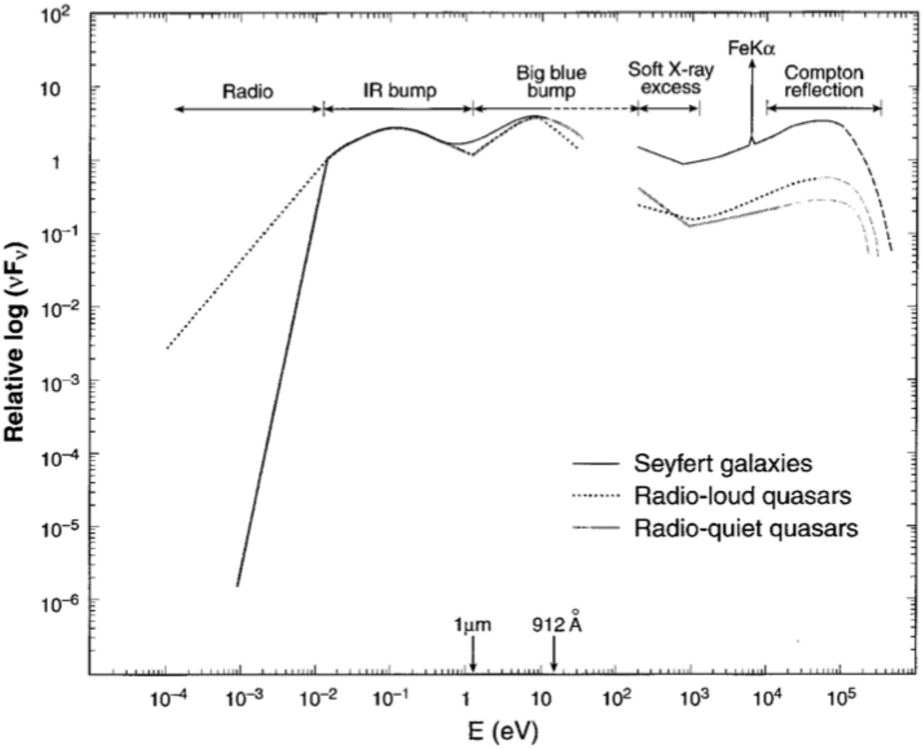

Figure 1.1: Scheme of an AGN continuum spectrum in different types of AGN.

One of the first distinguishing observational properties of AGN is the presence of redshifted, time variable intensity emission lines with Doppler widths of order of 10^3 to a few of 10^4 km s^{-1}.

These broad lines, such as hydrogen Balmer series lines H$\alpha\lambda$6563, H$\beta\lambda$4861, H$\gamma\lambda$4340 and hydrogen Ly$\alpha\lambda$1216, come from to the so called Broad Line Region (BLR). This region is assumed to be in photoionization equilibrium: the rate of photoionization is balanced by the rate of recombination. Thus it is possible to infer physical parameters such as the different number density of ions stage and the gas temperature. In general temperatures of 10^4 K and densities of $n_e \sim 10^9$ cm^{-3} are found. Since this value of temperature corresponds to line widths of order of 10 km s^{-1}, this means that line broadening is due to supersonic bulk motion of BLR, interpreted as an orbital motion about the central compact object. BLR provides therefore important insight into the BH.

There are also narrower forbidden and permitted lines but their widths and lack of variability suggest that they are originated from a region that is much larger and kinematically separated from BLR: the Narrow Line Region

(NLR). Photoionized by the UV/X-ray continuum radiation emitted by the central source, this region shows lines, such as [O III] $\lambda\lambda$4959, 5007, [N II]$\lambda\lambda$6548, 6583, [O I] $\lambda\lambda$6300, 6364, [S II] $\lambda\lambda$6716, 6731, that have FWHM of ~400-500 km s^{-1}, and the presence of forbidden lines is indicative of gas densities of ~10^3-10^5 cm^{-3}, much lower than those of BLR.

1.2.1 AGN classification and Unified Model

The AGN phenomenon was first defined by means of optical spectra and two groups were identified: broad-line emission galaxies (or Type-1) and narrow-line emission galaxies (or Type-2).

The former are characterized by broad permitted lines such as Balmer lines, mainly Hα, Hβ, Hγ and Lyα, CIV, MgII, with line widths that indicate velocities of 10^3-10^4 km s^{-1} and by narrow forbidden lines such as oxigen [OII] and [OIII], and the nitrogen and neon [NII], [NeII] and [Ne IV], with typical velocities of a few hundred km s^{-1}. The latter class is characterized by forbidden and permitted lines, which show the same narrow width.

A further classification can be made according to the radio emission. AGN can be divided in radio loud, objects that produce large scale radio jets and lobes, and radio quiet, objects with radio ejecta energetically insignificant.

Recently various unification schemes have been developed to explain AGN as different appearances of the same underlying phenomenon. Antonucci 1993 and Urry & Padovani 1995 proposed that there are basically radio quiet and radio loud AGN. For each type, different luminosities lead to different classes but all other differences are explained by different orientations to the observer.

In this scenario the basic idea is that the SMBH is surrounded by an optically thick torus, consisting of gas and dust. If the observer looks at the AGN through the torus then the broad-line region, nearby the central engine, is hidden by the toroidal material. As a consequence, the narrow-line region, far from the nucleus (from 10 pc up to 100 pc from the center) is visible. At any other angles both the broad and narrow regions are visible. Analyzing radio quiet Seyfert, in the first case we have the Seyfert 2, in the second the Seyfert 1. According to unified model there is no real distinction between the two cases: Seyfert 2 are Seyfert 1 with hidden broad line region and occur in spiral galaxies.

A distinction between Seyfert 1 and Seyfert 2 can be also made in X-rays. It is based on the intrinsic absorption measurement in the soft X-ray band; the differences result from the amount of absorbing material close to the central engine. The absorption is measured as a column density of hydrogen N_H in the line of sight in atoms per cm^2, taking into account the absorption in our Galaxy.

The hydrogen column density of $N_H=10^{22}$ cm^{-2} was chosen as dividing line from Seyfert 1, which, but not all, have lower absorption than this value, and Seyfert 2 which reside above of this value, but again not all (Panessa & Bassani 2002)

Another distinction can be made if we consider radio galaxies: broad line radio galaxies (BLRG) and narrow line radio galaxies (NLRG). These look like radio loud Seyfert but they seem to occur in ellipticals rather than spirals. In case of radio loud AGN, if the source is seen face-on, the spectrum is dominated by the jet and no lines are visible: we have the so called Blazar.

In the following three panels there are represented an AGN portion of a galaxy (upper panel), the emitted particles from different locations (medium panel) and what we see based on the orientation (bottom panel).

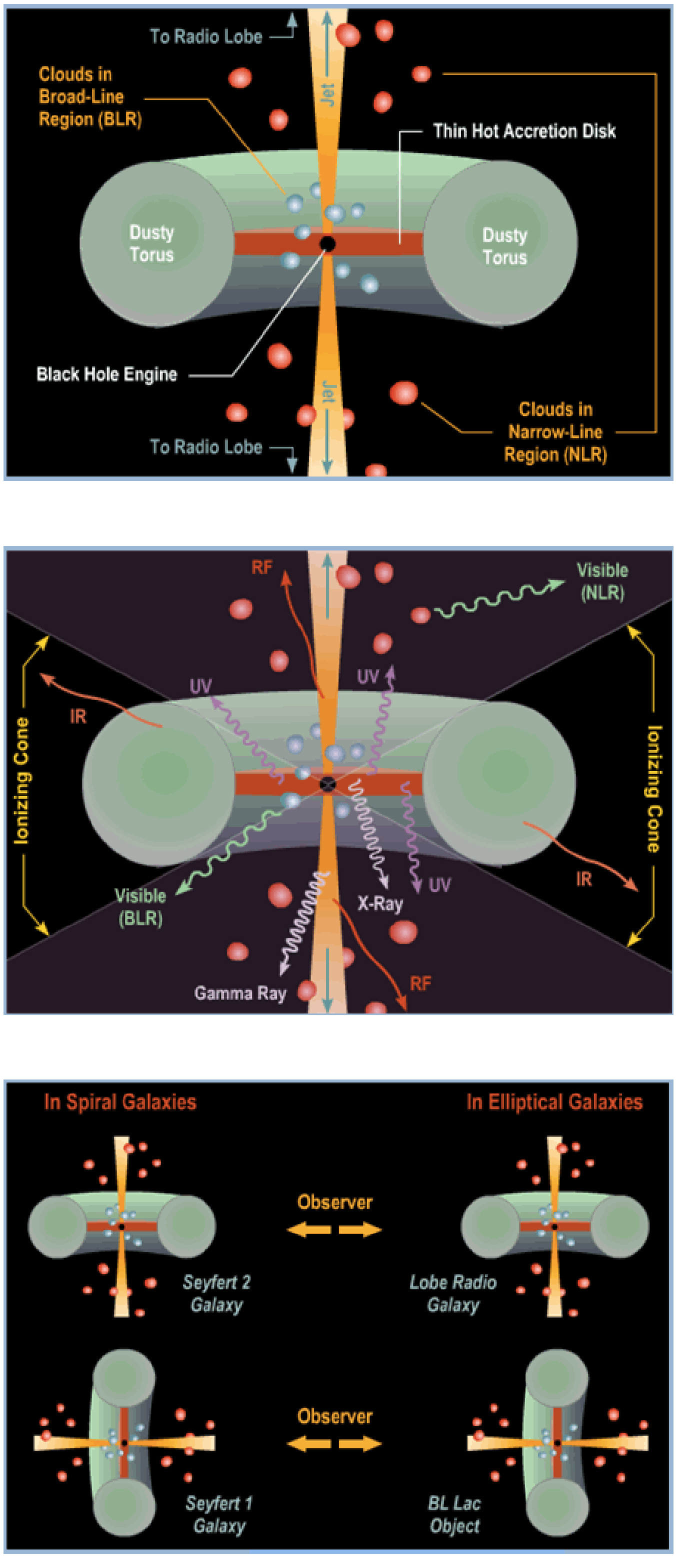

Figure 1.2: (***Top panel***) It is illustrated a model of AGN. (***Medium panel***) The AGN emission from different locations and a schematic description of the Unified Model (***Bottom panel***) (credit: Brooks/Cole Thomson Learning)

1.2.2 Diagnostics based on emission lines

As it was described previously, there is no single signature of an AGN, but the most commonly distinguishing characteristics are found in optical band. Indeed still in the modern era of astronomy the most extensive studies of AGN activity in the local Universe have utilised optical spectroscopy (Heckman et al 2004, Ho 2008). Since the NLR extends beyond the obscured central region, optical spectroscopy is able to identify even heavily obscured AGN. The optical classification is not so efficient in presence of significant host-galaxy dust and star formation, but in this case mid-IR spectroscopy, radio and X-ray observations can provide the identification of AGN.

Some galaxies show emission line spectra similar to those of Seyfert 2 galaxies, thus it is necessary to examine these emission lines in order to correctly classify an AGN spectroscopically. These Seyfert 2-like emission lines are often produced by massive gas clouds of ionized hydrogen, HII regions. Through the study of ionization level of various emission lines it is possible to discriminate between type 2 objects and HII/starburst galaxies. Baldwin, Phillips & Terlevic (Baldwin et. al 1981) presented a classification diagram, based on measured line ratios, to distinguish different object classes: the BPT diagram. This tool compares the following flux ratio pairs: [OIII]5007/Hβ vs [NII] 6584/Hα. There are two commonly used BPT diagnostics: [SII]6717,6731/Hα vs [OIII]5007/Hβ and [OI]6300/Hα vs [OIII]5007/Hβ (Veilleux & Osterbrock 1987, Kewley et al 2006, Kauffmann et al 2003).

The [OIII]/Hβ line ratio is sensitive to the ionisation parameter and temperature of the line emitting gas, and is enhanced both in the presence of low metallicity stars, where a lack of metals prevents the nebula from cooling efficiently, and in the presence of an AGN due to the hard radiation field. But this degeneracy between pure star formation and AGN activity can be broken comparing this emission line ratio with another one. For example it is possibile to use the [NII]6584/Hα ratio which is sensitive to metallicity in star forming galaxies but the contribution from AGN radiation field causes this ratio to become enhanced.

As we previously mentioned, [SII]6717,6731/Hα and [OI]6300/Hα ratios can be used, since are also enhanced in the presence of hard ionising radiation field like the one of AGN in the BPT diagram with [NII]6584/Hα.

The same diagram can be used for type 1 AGN providing that only the narrow components of Balmer lines are considered (Stern & laor 2012a).

Below are listed the two demarcations found by Kauffmann et al. 2003a and Kewley et al. 2001 used to distinguish among starforming galaxies, composite galaxies and AGNs in the BPT diagram with [OIII]/Hβ vs [NII]/Hα:

- (Kauffmann et al. 2003a)

$$log([OIII]/H\beta) = 0.61/(log([NII]/H\alpha) - 0.05) + 1.3 \qquad (1.13)$$

- (Kewley et al. 2001)

$$log([OIII]/H\beta) = 0.61/(log([NII]/H\alpha) - 0.47) + 1.19 \qquad (1.14)$$

In the figure 1.3 it is represented an example of a BPT diagram from Chen et al. 2009. The dotted curve is the demarcation found by Kauffmann et al. (2003a) and the dashed curve that found by Kewley et al. (2001). The solid line defined by Shuder et al. (1981) shows the separation between LINERs and Seyfert 2s.

Low-ionization nuclear emission galaxies (LINERs) show faint core luminosities and strong emission lines originating from low ionized gas. LINERs are assumed to represent the link between HII regions and Seyfert galaxies: different from Seyfert, LINERs can show [OIII] λ5007/Hβ <3 and in comparison to HII regions, LINERs have stronger [NII] lines when compared to the Hα line flux.

LINERs have low luminosity and accretion rates, this leads to the idea that are not emitting through the same processes as the more active Seyfert and Quasar cores. The infalling matter will be optically thin at such low luminosity, thus they may be accreting with low radiative efficiency. Energy will be transported outward through flow of matter, thus these types of AGN are better described by models like Advection Dominated Accretion Flow (ADAF), where accreting gas is heated viscously and cooled radiatively but any excess heat is stored in the gas and transported in the flow (Ho 2008). ADAFs may be associated with jets.

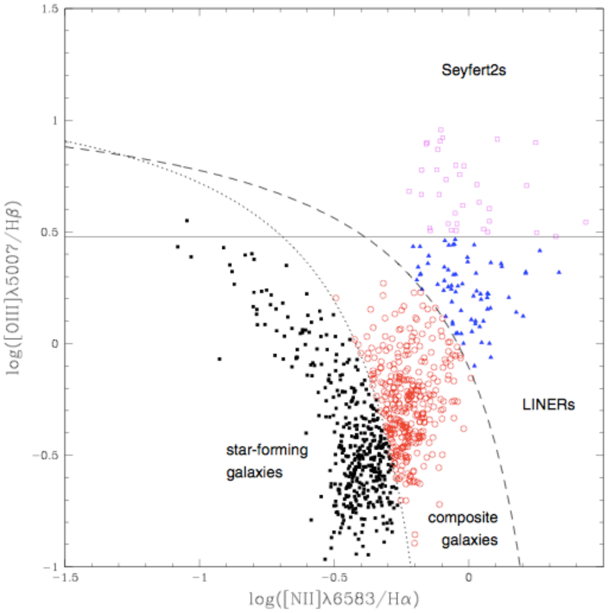

Figure 1.3: BPT diagram from Chen et al 2009. The dotted curve defined by Kauffmann et al. (2003a) and the dashed curve defined by Kewley et al. (2001) show the separation among starforming galaxies, composite galaxies, and AGNs. The solid line defined by Shuder et al. (1981) shows the separation between LINERs and Seyfert 2s.

Optical spectroscopy is also effective at identifying distant obscured AGN (Alexander et al 2008, Yan et al 2011), however the AGN emission-line diagnostics move into near IR band at z>0.4, so it can be limited in identifying large numbers of AGN. The most efficient identification of distant AGN is made with X-ray observations, since X-ray emission from star formation is typically weak. In presence of high absorbing column density, so high that not even X-ray photons can escape, IR and radio observations can help AGN identification (Hickox et al 2007, Bauer et al 2010).

1.3 AGN Galaxy co-evolution

In the present-day universe a bimodality sequence in the galaxy population is observed (Kauffmann et al 2003b):

- blue galaxies (Hubble late type), with on going star formation, low stellar surface density and characterized by a tigh relation between SFR and stellar masses: star forming main sequence (Brinchmann et al. 2004)
- red galaxies (Hubble early type), with little or absent star formation, large stellar masses and high stellar surface density

In figure 1.4 it is represented the relation between the stellar masses and the specific SFR of a sample of blue and red galaxies, at low redshift.

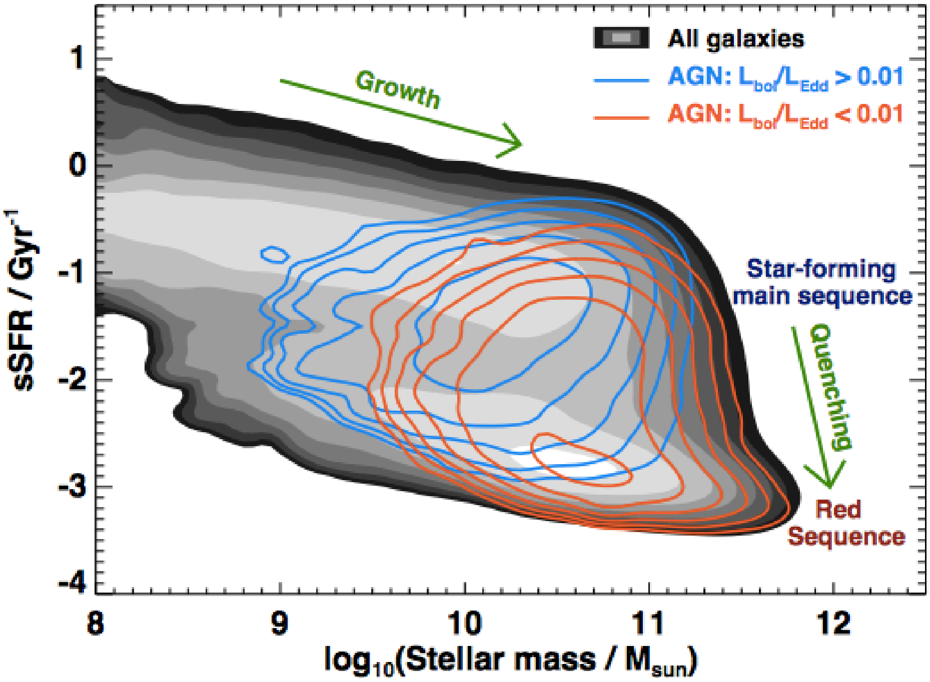

Figure 1.4: The distribution of galaxies (SDSS sample) in the present-day universe. In grey there are represented all the galaxies, with the existence of two regions: main sequence of star forming galaxies and a red sequence of red and dead galaxies. The blue and red contours represent the distributions of high and low Eddington-fraction AGN) (Heckman et al. 2014)

Since this bimodality is a characteristic of the galaxy population out to at least z∼2 (Whitaker et al. 2013), it is possible to put this distribution in a evolutionary context where the principal responsible for the move from blue to red seems to be the AGN, as many numerical simulations suggest. Moreover, we can put the different AGN population in the same scenario and not just in a geometrical one.

1.3.1 The need for AGN feedback

The idea that there is a connection between the growth of the SMBH and its host galaxy has been put forward (Silk & Rees 1998, Granato et al. 2004, Di Matteo et al. 2005, Menci et al. 2008).

To understand what kind of role the AGN can have on the host galaxy, it is useful to compare the energy released by the growth of the BH and the binding energy of the galaxy. An important result turns out.

The binding energy can be expressed as follows:

$$E_{gal} = M_{gal}\sigma^2 \tag{1.15}$$

where M_{gal} is the galaxy mass and σ is the velocity dispersion of the galaxy. The energy released by the growth of the BH is:

$$E_{BH} = \epsilon M_{BH} c^2 \tag{1.16}$$

where ϵ is the radiative efficiency for the accretion process and it is $\sim$ 10%. Considering that the mass of the BH is observed to be $M_{BH} = 1.4\ 10^{-3} M_{gal}$ (Kormendy & Gebhardt 2001, Merritt & Ferrarese 2001, Häring & Rix 2004) and that most galaxies have $\sigma < 400\ km\ s^{-1}$, the ratio E_{BH}/E_{gal} is greater than 80. This means that the AGN can have an important effect on the formation and evolution of the host galaxy.

As we already mentioned, the mass of a SMBH is only a small fraction of that of the host galaxy but we know that the two masses correlate. A tighter relation is found with the inner part of the galaxy, i.e. bulge, which suggests that galaxies hosting classical spheroids grew in concert with their BHs. A connection between the growth of the BH (via accretion) and the galaxy spheroid (via star formation) may be expected since both processes are driven by the availability of cold gas on nuclear scales, which is provided by the host galaxy or the larger-scale extragalactic environment. The majority of the mass accretion onto BHs occured at high redshift, at z>0.1(Marconi et al 2004, Hopkins et al. 2007, Merloni & Heinz 2008), in particular there is a steep rise from z=0 to z=1 until it is reached a maximum at z$\sim$ 2-3 followed by a steep decline. A similar trend is found for star formation (Hopkins & Beacom 2006). The evolution at low redshift is probably due to a decrease in the cold gas used as fuel for both processes in the central regions of galaxies, but the amount of cold gas required to fuel these processes is different. While the star formation process requires a large amount of cold gas, only a small fraction of it is needed for BH activity. This leads to a time delay between the shut down of star formation and AGN activity ($\sim$ 0.1 Gyr (Hopkins 2012)) and between the peak of SF and the accretion onto the BH ($\sim$ 0.5 Gyr (Schawinski et al 2009)).

Anyway, because of the difference in physical size scale of the BH and the host galaxy, a causal connection between the two systems is not obvious.

The gas has to lose nearly all its angular momentum to flow into the vicinity of the BH and accrete it, rather than to collapse and form stars. On large scale the gravitational torques, produced by galaxy bars, galaxy interactions and galaxy major mergers, can remove the angular momentum and allow the gas to flow inward (Barnes & Hernquist, 1992, 1996, Bournaud & Combes 2002, Garcia-Burillo et al 2005) and on the sub-kpc scales, processes such as nested bars and nuclear spirals act (Englmaier & Shlosman 2004).

The idea that AGN are fed by merger events had been very popular but the scenario that involved major mergers has yet to be verified.

In figure 1.5, taken from Hopkins et al. 2008a it is represented a scheme of a galaxy evolution, which goes through a gas-rich major merger. As we see in the figure, the galaxy evolution can be divided into three phases:

- Strong interactions between galaxies
- Coalescence of galaxies and nuclear activity
- Passive evolution toward a red spheroid

In the first phase gas-rich mergers are expected to drive nuclear inflows of gas, fuel a rapid starburst and lead to a phase of obscured BH growth: this phase is associated to heavily obscured quasar.

The second phase corresponds to the coalescence of galaxies that triggers starbursts but the mass in stars formed in this phase is small compared to that formed during the merger. The rapid growth of BHs, obscured at optical wavelengths by dust and gas, ends when the nuclear gas is consumed by the starburst and the residual gas is dispersed by strong winds originated by SN explosions and by the black holes energy released into the ISM.

This phase is followed by an unobscured phase of quasar, when the dust is removed and the BH becomes visible. After that, when no more fuel is available, star formation and quasar activity decline, leaving to an evolving passively, quiescent galaxy, that satisfies observed correlations between black hole and its spheroid.

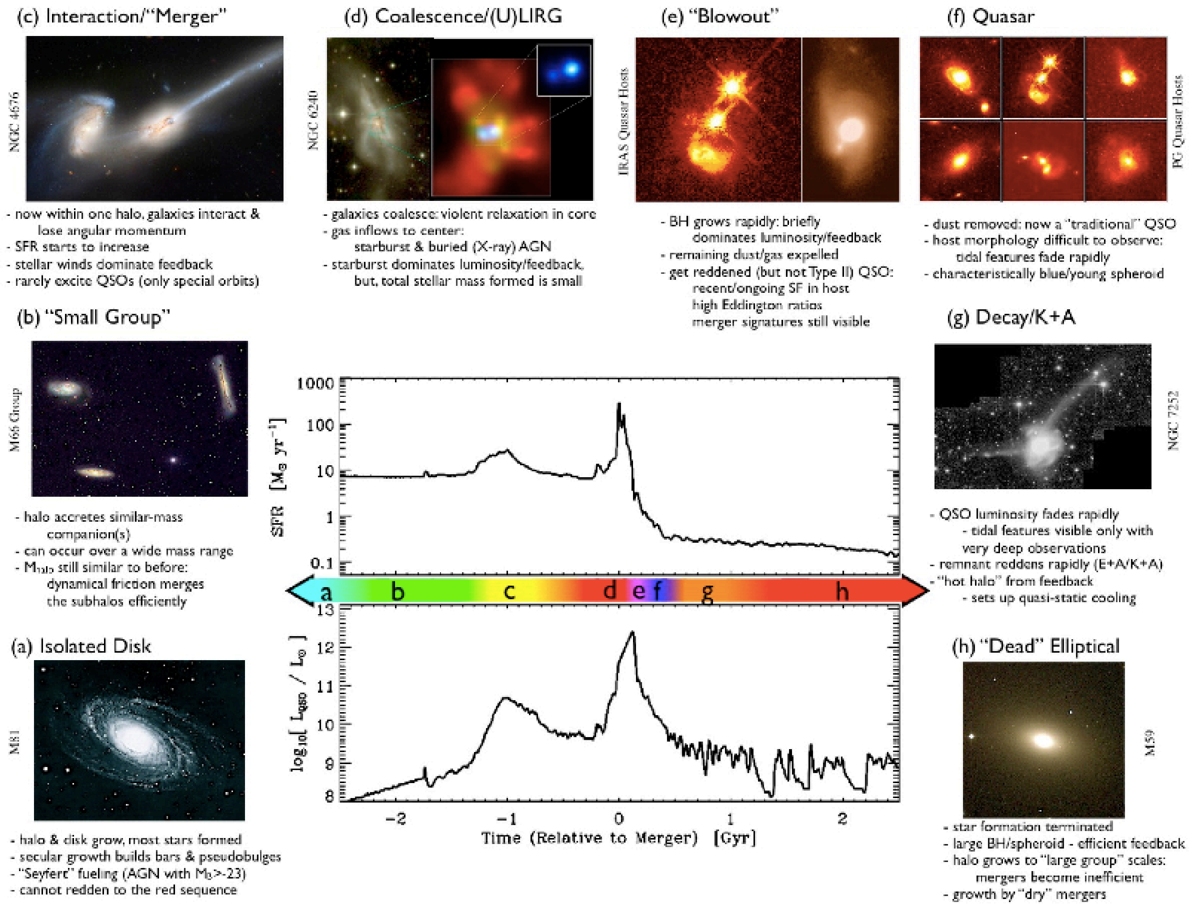

Figure 1.5: A scheme of the galaxy formation mechanism (Hopkins et al. 2008a)

1.4 Fundamentals of AGN feedback

As discussed previously, what we know is that the quenching of star formation led to a gas-poor elliptical galaxy, but the mechanism responsible for the quenching remains unclear. In order to reproduce this bimodality of the color distribution of local galaxies and the observed break in the present day luminosity, some "feedback" processes are invoked. The most common feedback is the Supernova driven wind that can eject the cold gas from the galactic disk (Larson 1974). This feedback was invoked since it was necessary the reduction of efficiency of star formation in low mass haloes in order to reproduce the slope of faint end of galaxy luminosity function. With a combination of SN feedback and its gas cooling suppression, and the observational evidence of supernova driven wind in dwarf galaxies (Ott, Walter & Brinks 2005) an agreement between model predictions and observations is reached (Croton et al 2006).

A similar problem concerns the bright end of the galaxy luminosity function (and mass function). It was suggested a superwind model, as in the case of faint end, but in massive haloes the supernova driven wind has a little effect, thus a different mechanism is required (Benson et al. 2003). It was suggested that these winds were driven by the energy released by the accretion of material onto the BH at the centre of the galaxy. Many semi analytical models shows how the central engine can be the responsible of the suppression of the cooling flow in massive galaxies. As an example of this, Croton et al (2006) simulated the growth of galaxies and their central SMBH by implementing semi-analytic model on the output of the Millennium Run, a N-body computer simulation used to investigate the evolution of structure in the concordance ΛCDM cosmogony (Springel et al 2005b). This model required quasar mode, i.e. the SMBHs grow during galaxy mergers both by merging with each other and by accretion of cold disc gas and radio mode, i.e. hot gas accretion onto the SMBHs occurs. The former mode is responsible for the growth of the central engine, the latter feedback injects sufficient energy into the surrounding medium to reduce or stop the cooling flow in more massive haloes. The AGN heating allows to reproduce the high luminosity cut-off in the galaxy luminosity functions in the K and b_J bands (See figure 1.6)

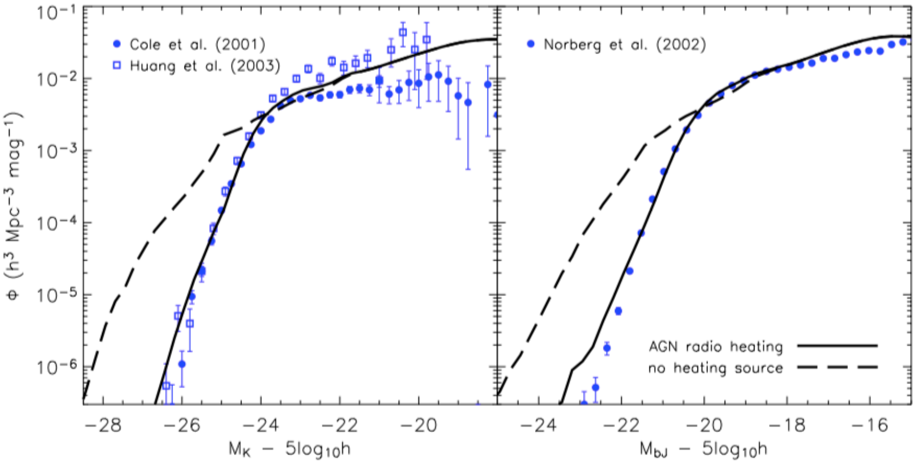

Figure 1.6: Galaxy luminosity function in the K (*left*) and b_J (*right*) photometric bands. The solid line represents the galaxy luminosity function with radio mode feedback; the long dashed line represents the galaxy luminosity function without feedback.

The AGN feedback has also a significant effect on bright galaxy colours. The feedback model of Croton et al. shows how the colour distribution changes with or without the feedback. In particular the radio mode feedback modifies the luminosities, colours and morphologies of high-mass galaxies. If no feedback acts, there are more massive, much bluer elliptical galaxies than to what is observed. Instead AGN heating cuts off the gas supply allowing the massive galaxies to redden (See figure 1.7)

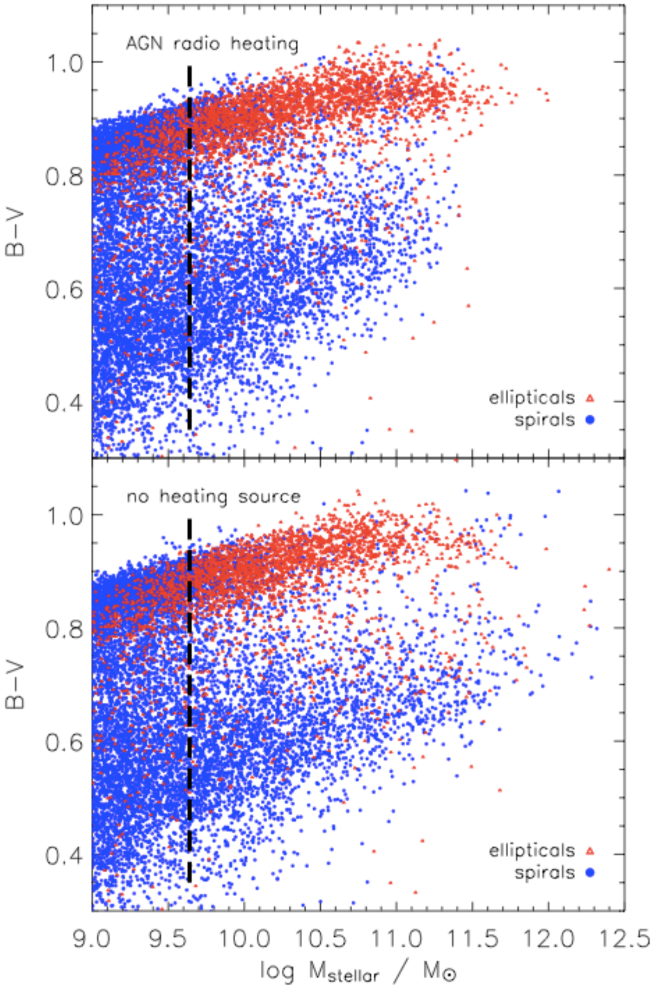

Figure 1.7: The B-V colours of model galaxies vs stellar masses with (*top*) and without (*bottom*) radio mode feedback. Red triangles and blues circles corrispond to early and late morphological type respectively. The thick dashed lines mark the resolution limit to which morphology can be determined in the Millennium Run and it corrispond to the stellar mass of 4 x 10^9 $M_\odot$

In conclusion, it seems to be necessary a feedback from AGN, in order to reproduce the observed properties of massive galaxies, thus it is invoked in both semi-analytic models and numerical simulations (Di Matteo et al. 2005, Croton et al. 2006, Bower et al. 2006, Hopkins et al 2006, Ciotti et al 2010).

1.4.1 Quasar mode and Kinetic mode

As mentioned briefly in the previous section, feedback from AGN is invoked in two flavors, which are related to the two fundamental modes of AGN activity:

1. radiative/quasar mode
2. kinetic/maintenance/radio mode

The first is associated with actively growing BHs that produce radiant energy powered by accretion of cold gas at rate close to the Eddington limit. This mode seems to be the responsible of the termination of the SF and the transition from the blue sequence to the red one. It is also the most likely explanation for relation between the black hole mass and the stellar velocity dispersion (Fabian 2010).

In the second mode, the bulk of energetic output is in form of jets and it seems to prevent further gas cooling, thus can keep the galaxies as red and dead.

1.4.2 Kinetic feedback

When cold gas is not available, the hot corona can play an important role. The SMBH may accrete the hot gas via Bondi accretion (Allen et al. 2006); the accretion is radiatively inefficient and almost the accretion energy is channeled into relativistic jets. This mode of AGN is called radio mode and the BH is coupled to the hot gas (Kormendy et al 2009) adjusting its residual accretion rate to provide energy that is needed to maintain it at constant temperature (Rafferty et al 2006, Cattaneo et al. 2007), through a continuous series of minor events (Fabian et al. 2006) or through episodic quasar activity (Binney et al 1995, Ciotti et al. 2007). In massive system, with hot ionized atmospheres, such as central dominant elliptical of a cluster, jets extend outward in a bipolar flow, inflating lobes of radio-emitting plasma. These lobes push aside the X-ray emitting gas of the cluster atmosphere, lead to the formation of bubbles or cavities in the X-ray images. In the Perseus cluster, that is the best-studied case, bubbles are spherical and surrounded by a thick high-pressure region fronted by weak shock. It is found that these bubbles can transfer energy to the cluster gas, $\sim$ 4PV, which is the internal energy of a cavity dominated by relativistic plasma. In the case of Perseus cluster, the energy is dissipated through sound waves, indeed Chadra imaging shows concentric ripples which are just interpreted as sound waves, generated by repetitive blowing bubbles (See figure 1.8). In general the energy transferred to the cluster gas through bubbles can diminish the cooling, this is expected in massive galaxies in the center of clusters, since the radiative cooling time of the hot surrounding gas is short enough that a cooling flow should be taking place but spectra show no evidence for strong mass cooling rates of gas below 1-2 keV (Fabian 1994).

Maybe the general scenario includes a cycle in which the cooling of hot gas onto the nucleus of the galaxy fuels intermittent AGN outbursts, which in turn provide sufficient heating to slow down or stop the accretion flow (Pope 2011).

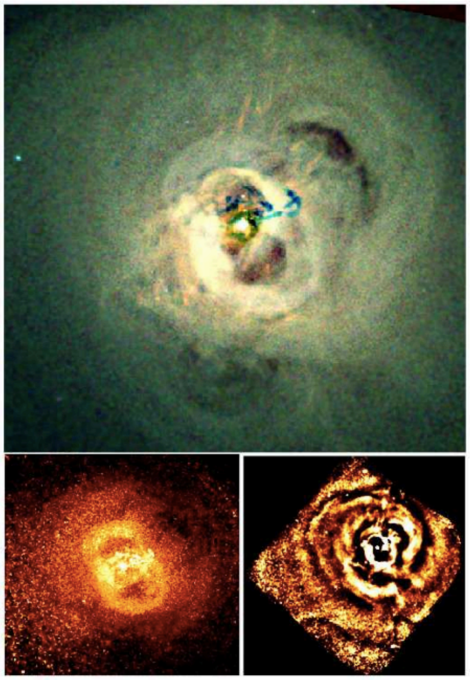

Figure 1.8: *(Top panel)* Chandra X-ray image of the Perseus cluster. Red-green-blue indicates soft to hard X-rays. The dark blue filaments in the center are likely due to a galaxy that is falling into NGC 1275, the giant galaxy that lies at the center of the cluster. *(Lower Left)* Pressure map derived from Chandra imaging X-ray spectroscopy of the Perseus cluster. Note the thick high pressure regions containing almost 4PV of energy surrounding each inner bubble, where V is the volume of the radio-plasma filled interior (Fabian et al 2006). *(Lower Right)*: unsharp-masked image showing the pressure ripples or sound waves.

Besides heating hot atmospheres surrounding elliptical galaxies and brightest cluster galaxies (BCGs), the radio mechanical feedback is able to sweep higher density molecular gas away from their centers. Warm molecular hydrogen gas at high velocities was found in the Seyfert galaxy IC5063 by Tadhunter et al. (2014), that used near-infrared long-slit spectroscopic observations to find a link between the molecular outflows and relativistic jets. What they found is consistent with the following model: dense molecular clouds embedded in a lower density medium (Mellema et al 2002, Wagner et al 2012), shocked by relativistic jets, which are expanding through the clumpy ISM in the disk of the galaxy, are accelerated and heated to high temperatures: the gas is ionized and the molecules are dissociated. The post-shock gas cools, leads to the formation of warm ionized gas and to molecular hydrogen and other molecules, when it cools below 10^4 K.

In this scenario the high velocity molecular gas formed through cooling in the compressed, post-shock gas that can lead to the formation of stars (see section 1.4.5)

1.4.3 Radiative feedback

Local scaling relations are an evidence of the connection between the central source and its spheroid. A tight relation exists between the velocity dispersion of stars σ in the bulge of a galaxy and the mass of the black hole: the M-σ relation (Gebhardt et al. 2000a ; Ferrarese & Merritt 2000)

Silk and Rees (1998) proposed a model based on the energy transfer (energy-driven flow) that led to a slope for the M- σ relation of α=5, which is higher than what is observed. Instead a model based on a momentum driven flow (Fabian 1999, King 2003, 2005) led to a slope of α=4 and to a correct normalization, a factor $c/\sigma \sim 10^3$ times larger than in Silk & Rees's relation.

These two different models realize under different conditions in galaxies. The momentum-driven flow occurs if the shocked wind gas can cool on a timescale short compared with the motion of the shock pattern. The loss of thermal energy results in a drop of pressure support and the shocked wind gas is compressed to high density and radiated away almost all of the wind kinetic energy. Only the ram pressure is conserved. Momentum-driven flows occur when shocks happen within $\sim$ 1 kpc of the AGN.

The energy-driven flow occurs if the wind gas is not efficiently cooled, thus the energy injected by the wind is fully conserved throughout the outflow, thus the flow expands adiabatically. This occurs when the supermassive black hole mass attains the critical M-σ value.

A diagram of these two different outcome is represented in figure 1.9.

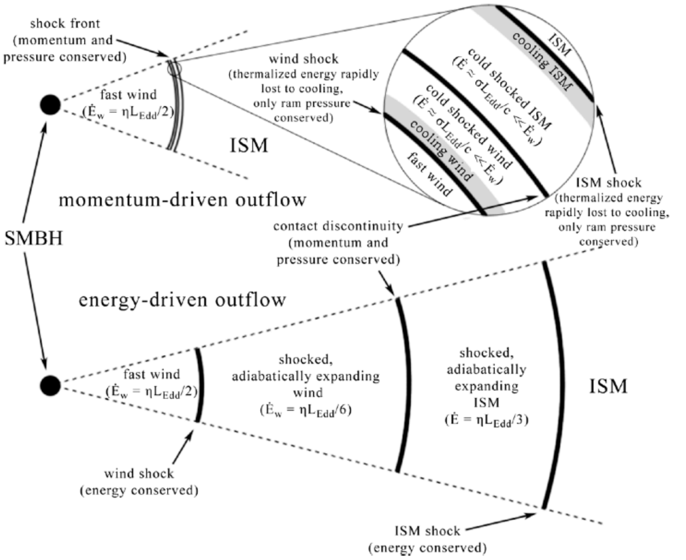

Figure 1.9: Schematic representation of momentum-driven (*top*) and energy-driven (*bottom*) outflows. In both cases a fast wind impacts the interstellar gas of the host galaxy, producing an inner reverse shock slowing the wind, and an outer forward shock accelerating the swept-up gas. In the momentum-driven case, the shocks cool to become isothermal. Only the ram pressure is communicated to the outflow, leading to very low kinetic energy. In an energy-driven outflow, the shocked regions do not cool. They expand adiabatically, communicating most of the kinetic energy of the wind to the outflow (Zubovas & King 2012)

In Fabian 2012 it is shown how the M-σ relation can be understood when the quasar is at the Eddington limit.

Assuming that the galaxy bulge is an isothermal sphere with radius R, its mass is

$$M_{bulge}(< R) = \frac{2\sigma^2 R}{G} \tag{1.17}$$

The radiation pressure will drive out a fraction f of the M_{bulge} to the edge of the galaxy bulge, at radius R, and this outward force is balanced by the inward gravitational one:

$$\frac{L_{Edd}}{c} = G M_{bulge} f \frac{M_{bulge}}{R^2} \tag{1.18}$$

where

$$L_{Edd} = \frac{4\pi G M_{BH} m_p c}{\sigma_T} \tag{1.19}$$

L_{Edd} is the Eddington luminosity computed for pure hydrogen composition, σ_T is the Thomson scattering cross-section and m_p is the proton mass. The combination of (1.17), (1.18) and (1.19) equations leads to the relation between M_{BH} and velocity dispersion:

$$M_{BH} = \frac{f\sigma^4 \sigma_T}{\pi G^2 m_p} \tag{1.20}$$

f∼0.1 gives a good representation of the observed M-σ relation (G*ü*ltekin et al 2009). A recent calibration of the relation by G*ü*ltekin et al 2009 leads to a slope of α=4.24 (See figure 1.10).

If the gas is coupled with dust grains (Raimundo et al. 2010) then the effective cross-section can be defined as follow:

$$\sigma_d = A\sigma_T \tag{1.21}$$

where A is a boost factor (Fabian et al. 2006, 2009).
We can redefine equation 1.19:

$$L_{Edd_{dust}} = \frac{4\pi G M_{BH} m_p c}{\sigma_d} \tag{1.22}$$

The effective Eddington limit (for dusty gas) can be redefined as a function of classical Eddington limit:

$$L_{Edd_{dust}} = \frac{\sigma_T}{\sigma_d} L_{Edd} = \frac{L_{Edd}}{A} \tag{1.23}$$

The limit at which the radiation pressure can expel the dusty gas is reduced by a factor of 1/A.

Starting by considering the effective Eddington luminosity, it is possible to derive the bulge mass, considering the gas concentrated in a shell at the edge of the galaxy of radius R, after being swept out by a quasar at its effective Eddington limit (Fabian 2009, Raimundo et al. 2010). The result is the following:

$$M_{bulge} \sim \frac{f\sigma^4 \sigma_d}{\pi m_p G^2} \tag{1.24}$$

Using Eq.1.20 and 1.24 the BH mass and the bulge mass can be related: $M_{BH}/M_{bulge} \propto \frac{\sigma_T}{\sigma_d}$

Considering that the maximum boost factor is 500 (Fabian et al. 2008), if the M_{BH}/M_{bulge} >1/500 this means that the black hole is above the effective Eddington limit. The gas can be pushed out to a radius that contain a mass lower or greater than 500 times the BH mass then the gas moves outward in the first case, inward in the second. This process repeats until the gas can no longer be retained and therefore it is pushed out of the bulge.

Thus the basic structure of galaxy bulges is shaped by the effects of radiation pressure on dust.

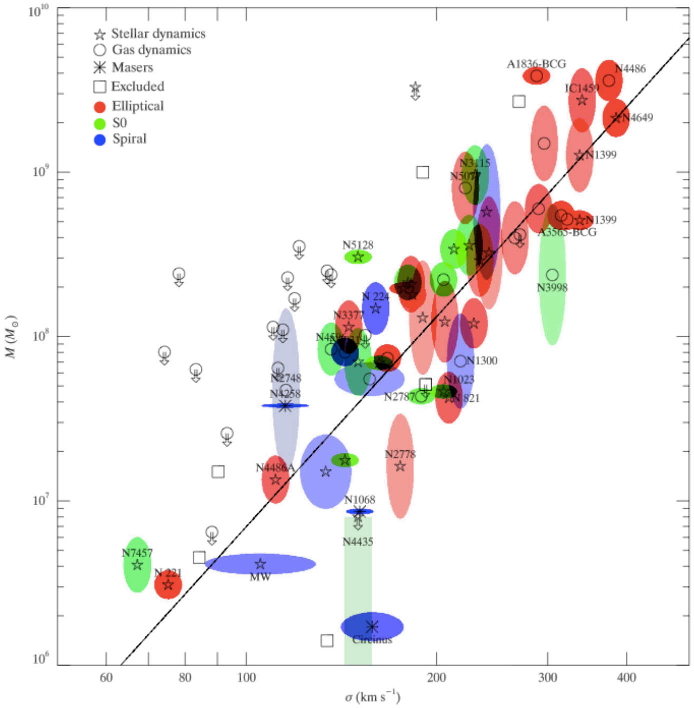

Figure 1.10: Recent calibration of M-σ relation from G*ültekin* et al 2009. Different galaxy types are indicated with different colors and the symbols indicate the method of BH mass measurement: stellar dynamical with pentagrams, pas dynamical with circles and masers with asterisks

1.4.4 Radiative-driven outflows

AGNs in radiative mode can drive powerful winds that are postulated to occur in galaxies with actively growing BHs and they may be the responsible for the termination of star formation and BH accretion. In opposition to more common powerful kpc-scale outflows, sustained by relativistic jets in radio galaxies (Nesvadba et al. 2008, 2010), galaxy-wide (i.e $>$ 0.1-10 Kpc) energetic outflows predicted by many models (Silk & Rees 1998; Fabian 1999; Benson et al. 2003; Granato et al 2004; Di Matteo et al. 2005; Hopkins et al 2006, 2008) are less commonly observed.

Over the past few years efforts have been made to search for AGN winds evidence, not so easy to find because they arise during a short-lived phase ($< 100\ Myr$). Best place to search for these types of outflows is in high-redshift far-infrared luminous galaxies, ULIRGs, systems that could be in transition from starformation dominated to an AGN dominated phase, maybe facilitated by kpc-scale outflows. Since their emission lines are shifted in NIR band, only recently it has been possible to study these systems by means of high resolution NIR spectrograph.

Also luminous X-ray selected obscured AGNs with red colors are an optimal place to search outflows, since these occur when BH is accreting at its maximum (see Brusa et al. 2010 for selection method).

These galactic-scale outflows driven by AGN are expected to propagate into the ISM with velocity greater than 500-1000 km/s; instead lower velocity components are probably driven by stellar processes (Lagos et al. 2013).

Therefore, one possible way to search for outflows is to isolate objects with kinematics components witnessing the presence of high velocities ($>$500-1000 km/s) in their emission lines.

Evidences of radiatively-driven winds (in terms of disturbed kinematics) are observed in both low redshift (Rupke & Veilleux 2011, Cicone et al. 2014) and high redshift (Harrison et al 2012, Cano-Diaz et al 2012, Förster-Schreiber et al 2014, Cimatti et al. 2013).

For example Cicone et al. 2014 studied the properties of massive, galactic-scale outflows of molecular gas in galaxies, spanning a wide range of starburst and AGN activities, using CO(1-0) kinematics. The detected CO broad wings trace molecular outflows on Kpc scales, indicating that these outflows are affecting their host galaxies on large scales. The starburst dominated galaxy are found to power the massive molecular outflows but a powerful AGN can have an important role boosting the outflows rate, when the AGN dominates the energetic output of the galaxy. In the starburst-dominated galaxies, where AGN is present but its contribution to bolometric luminosity is low, the outflows rate are not much larger than their SFRs but the outflows energetic follows the same relation as AGN-dominated galaxies, suggesting that even in these cases AGN can be the main driving source of the ouflows. This leads to the conclusion that AGN can be more effective to drive outflows respect to starburst or that the past activity of AGN may be the responsible for driving most of the outflow. Furthermore they found that AGN-driven massive molecular outflows are capable of exhausting the cold gas reservoir of the host galaxy and thus quenching star formation with a depletion time-scale that anti-correlates with the AGN power.

High-velocity outflows driven by high-accretion rate AGNs were found on sub-parsec scale, close to their accretion disk (Tombesi et al.2010, Gofford et al. 2011), but to have a global effect on the galaxy they must be also found on galactic scale (1-10 Kpc). An extreme example of molecular outflow was observed in the nearby quasar Mrk 231, where CO line observations shown broad wings corresponding to high-velocity wind ($\sim$ 750 Km/s), resolved in Kpc scales and with mass of $\sim$700 $M_\odot$ yr $^{-1}$ (Feruglio et al. 2010).

A diagnostic that is used to search for kpc-scale outflows is the broad, asymmetric and high-velocity [OIII]λ5007 emission line profile. This forbidden line is produced in the NLR, thus it is a good tracer of the NLR kinematics (Wampler et al. 1975, Wilson &Heckman 1985, Osterbrock 1989). Early studies were made on small samples of nearby AGN (Heckman 1984, Whittle 1985b) but with the availability of large spectroscopic data, such as SDSS, the study of NLR kinematics of thousand of AGN (Mullaney et al.2013) has been enabled so that the ubiquity of outflows can be constrained.

An example of what we can find analyzing the [OIII] emission line profile is represented in figure 1.11, taken from Harrison et al. 2012. They used spatially resolved spectroscopy to search for outflows, analyzing IR spectra of high-redshift ultra-luminous infrared galaxies (ULIRGs), including submillimetre luminous galaxies (SMGs). As we can see in the figure, the spectra show narrow (FWHM$\sim$ few hundred km s^{-1}) and broad (FWHM $\sim$ 900-1500 km s^{-1}) components, which can be blueshifted or redshifted with respect to the narrow emission.

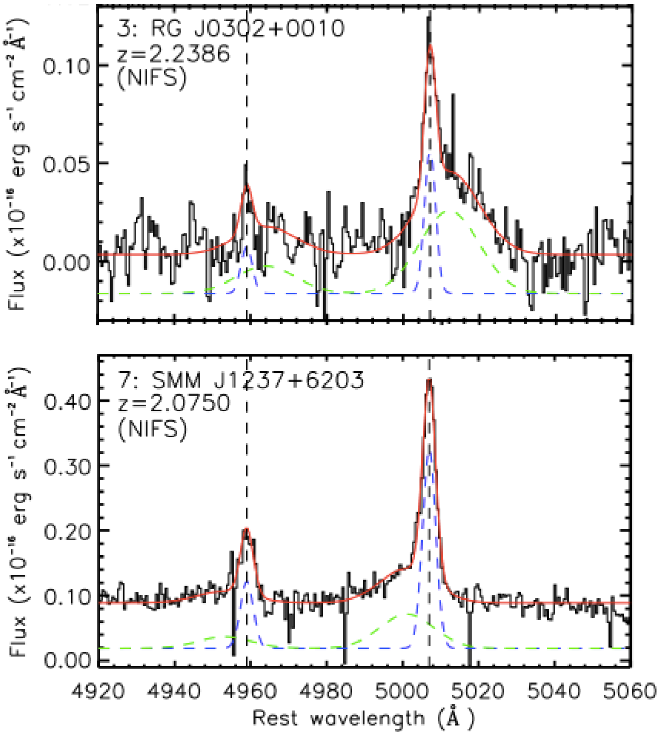

Figure 1.11: Galaxy-integrated spectra from Harrison et al. 2012. The spectra are shifted to the rest-frame, around the [OIII]$\lambda\lambda$4959,5007 emission line doublet. (*Top panel*) RG J0302+0010 exhibits a redshifted component with respect to the narrow component. (*Bottom panel*) SMM J1237+6203 exhibits a blueshifted component with respect to the narrow component. In both panels the red lines represent the best-fit, blue dashed lines represent the narrow component and green dashed lines represent the broad component.

The narrow [OIII] components are likely to be tracing the host galaxy dynamics and merger remnants, while the broad components are most likely due to energetic outflows. A possible interpretation of the observations of the broad emission line is shown in the following figure.

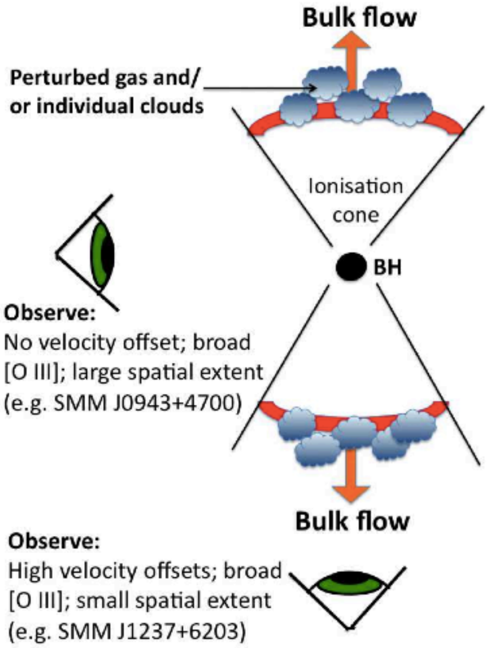

Figure 1.12: Scheme of a possible interpretation of the observations of the broad [OIII] emission lines. (For more details see the current subsection)

Harrison et al. define the velocity offset of the broad emission lines from the systemic as the velocity differences between the broad and narrow [OIII] emission lines. The velocity offset and the spatial extent observed can be explained by the presence of an AGN driven bi-polar outflow with the addition of obscuring material in the host galaxy. The galactic outflows are associated to expanding bubbles, which shape is influenced by the denser material in the centre of the host galaxy (Zubovas & King 2012). As illustrated in figure 1.12 the orientation with respect to the line of sight will determine the velocity offsets and spatial extent observed: high velocity offset and small spatial extent are observed if the outflow is oriented along the line of sight, instead if the outflow is in the plane of the sky then small velocities offset and large spatial extend are observed; in both cases broad emission lines are always observed.

Blueshifted emission line are commonly associated with outflow (Heckman et al 1981) but according to this scheme, it is possible to find broad redshifted [OIII] emission lines that can be also associated to outflows in the far-side and explained by the orientations of the AGN and obscuring material in the host galaxy (Crenshaw et al 2010).

The integrated spectra provide no information regarding the extent of the gas but with survey such as SDSS, which provides these spectra, it is possible to analyze large samples of objects, thus to have statistics needed to establish the prevalence of outflows among different AGN population.

1.4.5 Positive feedback

Until now we argued about negative feedback that causes the suppression of formation of stars and thus prevents the over-production of very massive systems. In addition to such feedback some studies found positive feedback from AGN, which triggers SF episodes through induced pressure of the cold gas.

Pressure inside an accretion disc around the SMBH gives rise to a wind, accelerated by AGN radiation pressure (King 2003, 2010). This wind shocks against the surrounding material and drives in outflow in the host galaxy. The quasar outflows lead to two shocks: one inner, the primary shocked outflow, one outer, shocked host galaxy gas. These two shocks are separeted by a contact discontinuity (Zubovas & King 2012).

Nayakshin and Zubovas (2012) showed in numerical simulations that quasar outflows affect the gas in the host galaxy, it dipends on whether the outer shock rapidly cools radiatively or not. If the cooling time is short, then the gas rapidly cools and the shocked outer layer becomes very dense and unstable (Mac Low et al. 1989) and leads to the break of the shell into thin dense filaments. These filaments cannot be driven outward easily, it is more likely that quasar outflows affect these regions by compressing them and triggering (or accelerating) star formation there. This scenario can explain the observed large-scale outflows that contain molecular gas (Cicone et al 2012), infact their high velocities imply temperatures far above those necessary for molecule dissociation.

Silk (2013) argued that AGN radio-jets can trigger star formation via pressure-regulation. The jet causes shocks and induce turbulence (Ishibashi & Fabian 2012) leading to a much more efficient clumping of molecular hydrogen and thus accelerated star formation. Zinn et al 2013 have shown that the star formation rate is correlated with radio jet power, in particular low jet power are associated to low star formation rate and high jet power to high SFR.

While jet-triggered star formation is associated with radio-loud objects, Ishibashi et al 2013 suggest a radiation pressure-driven feedback that may be applied to a wider range of sources. In this scenario stars are formed in the feedback-driven outflow at larger radii and build up the outer regions of the host-galaxy.

In general this positive feedback is expected to be most effective at high redshift, close to the peak epoch of AGN activity ($z\sim2$) and rare at low z. Anyway the interplay between AGN activity and star formation is complex and both negative and positive feedback mechanism seem to be important.

Aim of the thesis project

In the above sections we discussed why it is necessary to introduce a co-evolutionary model, since geometrical arguments are not enough to characterize different AGN populations. These objects are powered by an accreting SMBH and the local scaling relations suggest that there is a connection between BH and host galaxy. The existence of a feedback between these two objects is fundamental in the galaxy formation and evolution, as invoked by most successful models. This activity can affect the final mass of host galaxy; in fact, it can sweep the gas in it, quench star formation and terminate its own activity, when no fuel is then more available. Thus it is important to understand this critical phase of the life of nucleus and host galaxy and their close relationship, therefore observational evidences are needed to prove what models suggest. As we already mentioned, large-scale outflows have been detected using the [OIII]λ5007 emission line, produced in the NLR and visible in the rest-frame optical spectra of AGN.

Using this approch, we searched for outflows signatures in obscured X-ray selected AGN in the COSMOS field, looking at their optical spectra. For this reason we made a cross-correlation with the SDSS latest database, therefore we worked on high quality spectra.

We analysed targets with [OIII] emission line detected, finding broad components for some sources. In the hypothesis that the broadest components are associated to the outflowing wind, we found interesting results about the outflow kinetic power compared with the bolometric AGN luminosity.

This thesis work is structured as it follows:

- Chapter 2. The sample selection resulting from the match between XMM-Newton sample in COSMOS field and SDSS DR10 database is given, with a complete description of COSMOS field, XMM-COSMOS and SDSS survey.

- Chapter 3. The spectral analysis by means of IRAF task SPECFIT is presented, with a description of the two models we used and of the non parametric analysis made on the [OIII] emission line profiles.

- Chapter 4. It is described how we used the results of emission line fitting. We built the BPT diagram for 12 sources, found the extinction for 7 targets and we compared the FWHM of the broadest component of [OIII]λ5007 with total observed [OIII] luminosity and with bolometric AGN luminosity, in order to find some trends between outflows and AGN properties.
- Chapter 5. The energetic of outflows is derived. In particular the comparison between the kinetic power associated to the ionized outflowing gas and the bolometric AGN luminosity is discussed, with an additional comparison with the predicted kinetic output from SF, in order to understand what is the driving mechanism of the observed outlows.
- Chapter 6. The conclusion and the perspectives are discussed.

Chapter 2

Sample selection

Most AGNs are obscured, in other words the nucleus is hidden behind a screen of absorbing material. The largest surface density of AGNs is obtained by means of X-ray surveys. X-rays can penetrate the obscuring dust and are not sensitive to dilution by starlight in the host galaxy: the X-ray selection of AGNs is not affected by some of the biases of the optical selection. Thus because of the efficiency of the X-ray observations in localizing and identifying AGNs and distant clusters of galaxies, an important step forward in the past decade has been made with large area and deep X-rays surveys performed with the XMM-Netwon and Chandra Satellites (Brandt & Hasinger 2005, Alexander & Hickox 2012))

The advantage of having the nucleus obscured is to make easier the observations of those emission components which originate in circumnuclear matter outside the absorbing regions, because in this case they are not outshined by the nuclear emission. These emission components, resulting from accretion disk photons ionizing the surrounding gas, are produced in gas hundreds of parsecs away from the accresion disk, in the so called Narrow line region and they are visible in the optical spectra of AGN. Thus the combination of an X-ray selection (able to pick up the largest majority of AGN) and the optical spectroscopy sampling the NLR represents the best tool to study the circumnuclear region of AGNs.

We analysed a sample of obscured X-ray selected AGN in the Cosmic Evolution Survey (COSMOS) field (Brusa et al. 2010 (hereafter B10)) and studied their optical counterparts, resulting from the match between the XMM-Newton sample in (COSMOS) field and Sloan Digital Sky Survey (SDSS) DR10 database. Before we move on the sample selection, a brief description of these two fields is needed.

2.1 COSMOS field

The Cosmic Evolution Survey (COSMOS) is a Hubble Space Telescope Treasury Project, using Advanced Camera for Survey (ACS) and realized with a large number of state-of-the-art telescopes. It is the largest HST survey, with a 2 square degree equatiorial area, large enough to avoid cosmic variance and centered on R.A (J2000.0)=$10^h 00^m 28.6^s$ and DEC (J2000.0)=+02°12'21.0".The field is devoid of bright X-ray, UV, and radio sources and, compared to other equatorial fields, has a low and uniform Galactic extinction, i.e. $E_{(B-V)}$ ~0.02 mag. It detected over 2 million objects with I_{AB} <27, out to a redshift of z=6 and its goal is to perform a detailed study of galaxy and super massive black hole evolution through cosmic time (Ilbert et al. 2011), with emphasis on the influence of environment(Scoville et al. 2013) and large scale structure. The COSMOS field is equatorial for easy access to telescopes in both hemispheres; it has been studied in all of the accessible parts of the electromagnetic spectrum, from radio using VLA , to infrared with Spitzer (Sanders et al. 2007) and Herschel, optical with Hubble, Subaru and other ground-based telescopes, near and far ultraviolet with the Galaxy Evolution Explorer (GALEX) (Zamojski et al. 2007) and X-rays with XMM-Newton (Hasinger et al. 2007) and Chandra (Elvis et al. 2009). The extensive spectroscopic coverage with VIMOS/VLT (Lilly et al. 2007,2010) and IMACS/Magellan (Trump et al. 2007, 2009) and a multiband photometry, that allows to estimate the photometric redshift of those faint sources for which spectroscopic information is not available (Ilbert et al 2011, Salvato et al 2011) enable a comprehensive and complete redshift information.

In figure 2.1 it is shown the 2 square degree COSMOS field captured through X-rays by XMM and Chandra (upper panels), in Infrared by Herschel and in radio with VLA (bottom panels). For more details see Scoville et al. 2007.

Figure 2.1: (*upper left panel*)The image combines data collected by the EPIC instrument on board XMM-Newton at energies [0.5-2] keV (red), [2-4.5] keV (green) and [4.5-10] keV (blue) (Cappelluti et al. 2009). (*upper right panel*) The image shows the 0.9 square degree COSMOS field captured though in X-ray by Chandra (Elvis et al. 2009) at energies [0.5-2] keV (red), [2-4.5] keV (green) and [4.5-7] keV (blue) (*bottom left panel*) The image shows a composite, three-colour view of the COSMOS field, observed with Spitzer/MIPS at 24μm (blue) and with Herschel/PACS at 100 μm (green) and 160 μm (red) (credit: ESA / NASA / JPL-Caltech / PEP Key Programme consortium / Dieter Lutz). (*bottom right panel*) The VLA-COSMOS field is represented (Schinnerer et al. 2007)

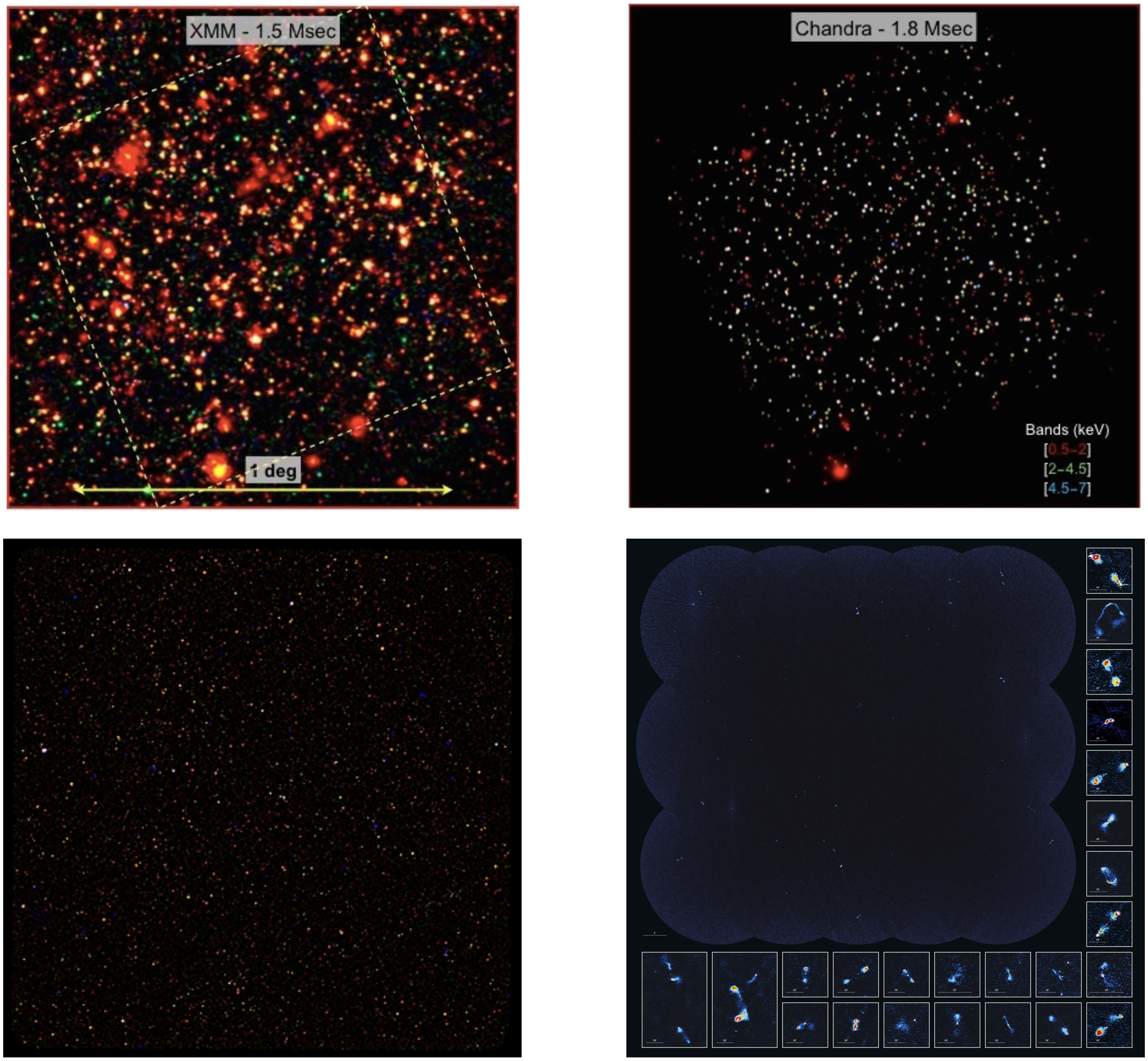

2.2 XMM-COSMOS

XMM-Newton has devoted 1.5 Ms to a complete X-ray survey of the COSMOS field in the 0.5-10 keV, split over 55 EPIC pointings (Hasinger et al. 2007, Cappelluti et al. 2009). The central 0.9 deg^2, of the 2.13 deg^2 surveyed by XMM-Newton, has also been observed in X-rays with Chandra, for a total of 1.8 Ms by Elvis et al. 2009.

The understanding of the coevolution of galaxies and their central black holes, out to high redshifts represents one of the primary goals of XMM-COSMOS survey.

XMM-COSMOS survey includes 1800 X-ray sources, detected down to limiting fluxes of $\sim 5\ 10^{-16}$, $3\ 10^{-15}$ and $7\ 10^{-15}$ erg/cm^2/s in the 0.5-2 keV, 2-10 keV and 5-10 keV bands, respectively. The classification of these sources was made by the match between the I band and K band, IRAC catalogs and X-ray positions (B10). The sources were splitted into three classes: reliable ID ($\sim$ 1465), ambigous ($\sim$ 175) and not identified ($\sim$ 11). In this sample we have galactic ($\sim$ 99 stars) and extragalactic sources: our attention is focused on the latter.

The spectroscopic redshifts are available for $\sim$ 890 sources of the sample; they were compiled in B10 from Magellan/IMACS and MMT observation campaigns (Trump et al. 2007, 2009), from zCOSMOS bright project (Lilly et al. 2009), from zCOSMOS faint project (Lilly et al. 2007), from SDSS survey catalog (Adelman-McCarthy et al. 2006; Kauffmann et al. 2003), literature(Prescott et al. 2006) and from DEIMOS observations (P.I P. Capak, M. Salvato, N.Scoville).

When including also photometric redshift calculated with templates for SED fitting including AGN component, the completeness of the X-ray sample in terms of redshifts information is >98%. The redshift distribution splitted in objects with spectroscopic redshifts and with photometric redshift is shown in Figure 3.3 (left) taken from B10.

By means of optical spectra, the sources were divided into three classes: Broad-line AGN ($\sim$ 421), Narrow-line AGN ($\sim$ 370) and Normal galaxies ($\sim$ 53). In the BL AGN class there are all the sources with at least one broad emission line in the optical spectrum (with FWHM > 2000 Km/s); in the second class those presenting high ionization emission lines or line ratios tipically of type 2 AGN (e.g. from BPT diagram); and in the latter those with typical galaxy spectrum, showing only absorption lines or having emission lines consistent with star-forming galaxies. Since the standard diagnostic diagram, used to distinguish between star forming galaxies and the type 2 AGNs, i.e. BPT diagram, do not work at high redshift, a further method of discrimination was used for the last two classes described above: a luminosity threshold of 2 x 10^{42} erg s^{-1} in the hard band. All the sources with L_X larger than this threshold and without a broad line in their spectra are classified as NL AGN, despite their optical classification. This is justified by the fact that the most powerful local, starburst galaxy, NGC 3256 has a [2-10] keV luminosity lower than this value ($5 \cdot 10^{41}$ erg s^{-1}) and because, following Ranalli et al. (2003), this luminosity level can be ascribed to stellar processes only in objects with star formation rate (SFR) larger than ~ 400 $M_{\odot}$ yr^{-1}.

The multiwavelength properties of all the XMM-COSMOS sources have been presented in B10 (see `http://www2011.mpe.mpg.de/XMMCosmos/xmm53_release/` for the table in its entirely). Here in figure 2.2 we report as a guidance a portion of the same Table, to have an idea of the information available for all the sources. The most important values from this Table we will use in the following are the redshifts and spectral classification, and the X-ray fluxes and HR (from which we compute the X-ray luminosity).

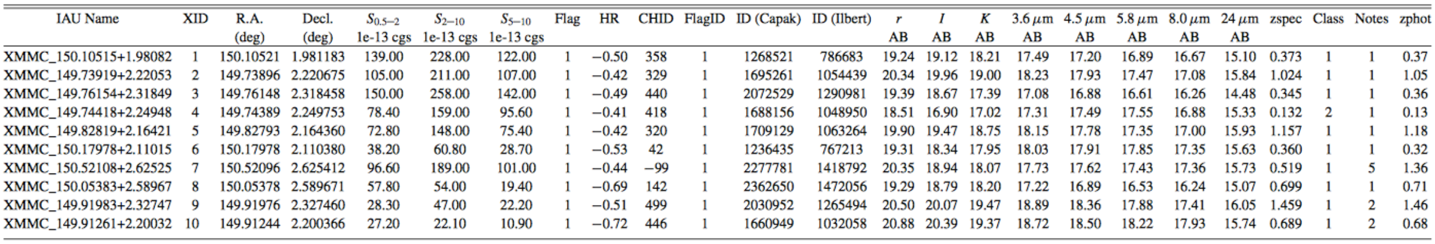

IAU Name	XID	R.A.	Decl.	$S_{0.5-2}$	S_{2-10}	S_{5-10}	Flag	HR	CHID	FlagID	ID (Capak)	ID (Ilbert)	r	I	K	3.6 μm	4.5 μm	5.8 μm	8.0 μm	24 μm	zspec	Class	Notes	zphot
		(deg)	(deg)	1e-13 cgs	1e-13 cgs	1e-13 cgs							AB	AB	AB	AB	AB	AB	AB	AB				
XMMC_150.10515+1.98082	1	150.10521	1.981183	139.00	228.00	122.00	1	−0.50	358	1	1268521	786683	19.24	19.12	18.21	17.49	17.20	16.89	16.67	15.10	0.373	1	1	0.37
XMMC_149.73919+2.22053	2	149.73896	2.220675	105.00	211.00	107.00	1	−0.42	329	1	1695261	1054439	20.34	19.96	19.00	18.23	17.93	17.47	17.08	15.84	1.024	1	1	1.05
XMMC_149.76154+2.31849	3	149.76148	2.318458	150.00	258.00	142.00	1	−0.49	440	1	2072529	1290981	19.39	18.67	17.39	17.08	16.88	16.61	16.26	14.48	0.345	1	1	0.36
XMMC_149.74418+2.24948	4	149.74389	2.249753	78.40	159.00	95.60	1	−0.41	418	1	1688156	1048950	18.51	16.90	17.02	17.31	17.49	17.55	16.88	15.33	0.132	2	1	0.13
XMMC_149.82819+2.16421	5	149.82793	2.164360	72.80	148.00	75.40	1	−0.42	320	1	1709129	1063264	19.90	19.47	18.75	18.15	17.78	17.35	17.00	15.93	1.157	1	1	1.18
XMMC_150.17978+2.11015	6	150.17978	2.110380	38.20	60.80	28.70	1	−0.53	42	1	1236435	767213	19.31	18.34	17.95	18.03	17.91	17.85	17.35	15.63	0.360	1	1	0.32
XMMC_150.52108+2.62525	7	150.52096	2.625412	96.60	189.00	101.00	1	−0.44	−99	1	2277781	1418792	20.35	18.94	18.07	17.73	17.62	17.43	17.36	15.73	0.519	1	5	1.36
XMMC_150.05383+2.58967	8	150.05378	2.589671	57.80	54.00	19.40	1	−0.69	142	1	2362650	1472056	19.29	18.79	18.20	17.22	16.89	16.53	16.24	15.07	0.699	1	1	0.71
XMMC_149.91983+2.32747	9	149.91976	2.327460	28.30	47.00	22.20	1	−0.51	499	1	2030952	1265494	20.50	20.07	19.47	18.89	18.36	17.88	17.41	16.05	1.459	1	2	1.46
XMMC_149.91261+2.20032	10	149.91244	2.200366	27.20	22.10	10.90	1	−0.72	446	1	1660949	1032058	20.88	20.39	19.37	18.72	18.50	18.22	17.93	15.74	0.689	1	2	0.68

Figure 2.2: Column 1: XMM-COSMOS IAU designation; Column 2: XMM-COSMOS identifier number (from Cappelluti et al. 2009); Columns 3-4: coordinates of the optical/IR counterpart; Columns 5-7: X-ray fluxes in the soft, hard, and ultra-hard bands (from Cappelluti et al 2009); Column 8: flag identifying the sources included in the flux-limited sample (1) or not (0); Column 9: X-ray hardness ratio, HR; Column 10: Chandra-COSMOS identifier number (from Elvis et al.2009); Column 11: flag for the optical identification, according to the classes described in the text: sources flagged with 1 are the reliable counterparts; sources flagged with 2 are the ambiguous counterparts; sources flagged with 0 are statistically not identified. Column 12: identifier number from Capak et al. 2007 catalog; Column 13: identifier number from the Ilbert et al. 2009 catalog; Columns 14-15: the r-band and I-band magnitudes (AB system, from Capak et al. 2007); Column 16: K-band magnitude (AB system, from McCracken et al. 2010); Column 17-20: magnitudes in the four IRAC channels (AB; from Ilbert et al. 2009); Column 21: MIPS 24 μm magnitude (AB, from Le Floch et al. 2009); Column 22: spectroscopic redshift; Column 23: spectroscopic classification: 1= BL AGN; 2= NL AGN; 3= normal/star-forming galaxy; Column 24: origin of the spectroscopic redshifts. The code for the source of the spectroscopic redshift is the following: 1: SDSS; 2: MMT (Prescott et al. 2006); 3, 4: IMACS runs (Trump et al.2007, 2009); 5: zCOSMOS 20k catalog (Lilly et al. 2007); 6: zCOSMOS faint 4.5k catalog; 7; Keck runs; Column 25: photometric redshift (from Salvato et al. 2009).

The spectroscopic breakdown of the sample, for BL AGNs, NL AGNs and normal galaxies, is shown in figure 2.3 (right). In particular BL AGNs compose $\geq$50% in the soft and hard subsamples, and more than 60% in the ultra-hard sample. This higher fraction is due to the limits of detection in ultra-hard band, because of the shallower sensitivity of XMM and thus a minor fraction of obscured AGN is revealed spectroscopically. In this figure it is also represented the redshift distribution of the sources for which only photometric redshifts are available.

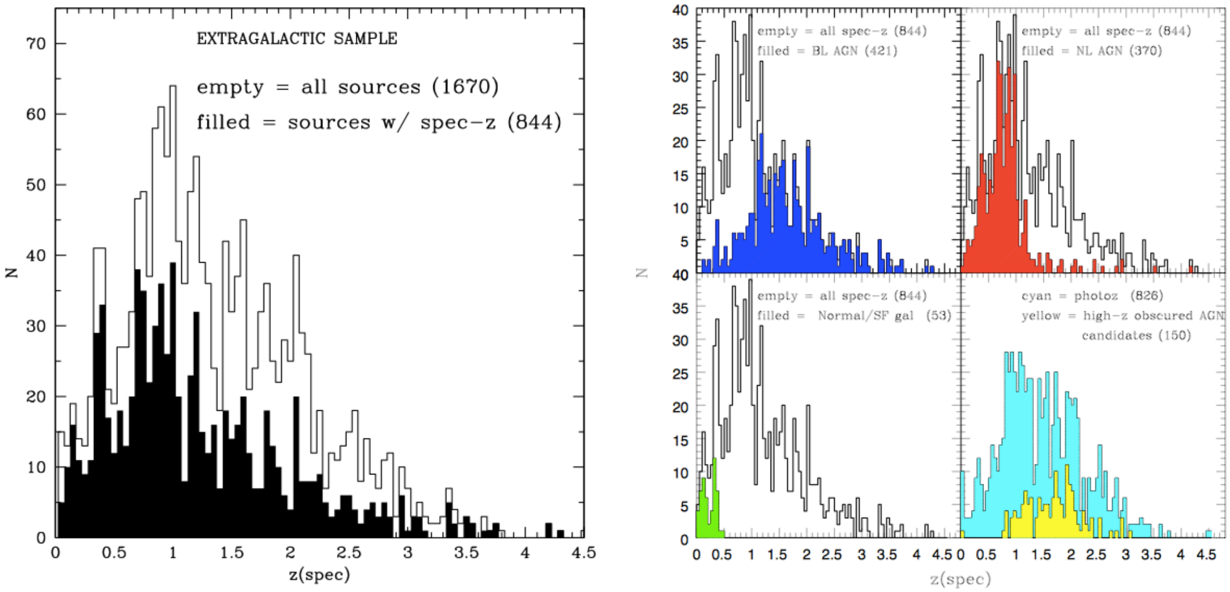

Figure 2.3: (*left panel*)Redshift distribution of the extragalactic XMM-COSMOS counterparts in Δz=0.05. Open histogram contains all sources with spectroscopic or photometric redshift available; filled histogram contains all sources with spectroscopic redshift. *(right panel)* Spectroscopic breakdown of the sample (open histogram) in the three classes discussed in the text: BL AGN (blue filled histogram), NL AGN (red upper histogram) and normal/SF galaxies (green filled histogram). In the bottom right panel it is represented the distribution of the sources with photometric redshift only (cyan). The yellow filled histogram represent the redshift distribution for the high-z obscured AGN candidates.(From B10)

In figure 2.4 it is shown the luminosity-redshift plane for the three classes of sources discussed above, with spectroscopic redshift, detected in the soft and hard band. Significantly, at z>2, in the hard band, only 12 objects are classified as NL AGN in opposition to 124 BL AGN, due to the fact that, at high redshift, obscured AGNs are optically faint and have not been targeted yet with dedicated spectroscopic campaigns.

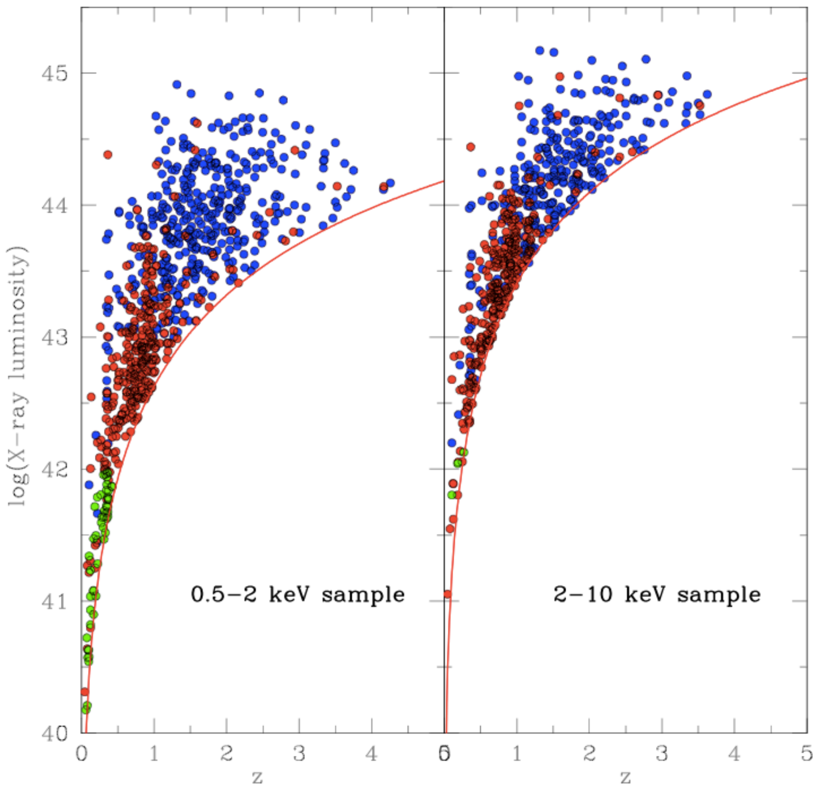

Figure 2.4: Luminosity-redshift plane for the sources with spectroscopic redshift detected in the soft band *(left panel)* and hard band *(right panel)*. In both panels blue circles are AGN 1, red circles are AGN 2 and green circles are normal/SF galaxies.From B10

2.3 Sloan Digital Sky Survey

The Sloan Digital Sky Survey (SDSS) is a multi-filter imaging and spectroscopic redshift survey, aiming to make a map of one quarter of the sky (10000 square degrees), centered on the North Galactic Pole. The sky coverage of Data Release 10 (DR10) of SDSS and BOSS is shown in figure 2.5.

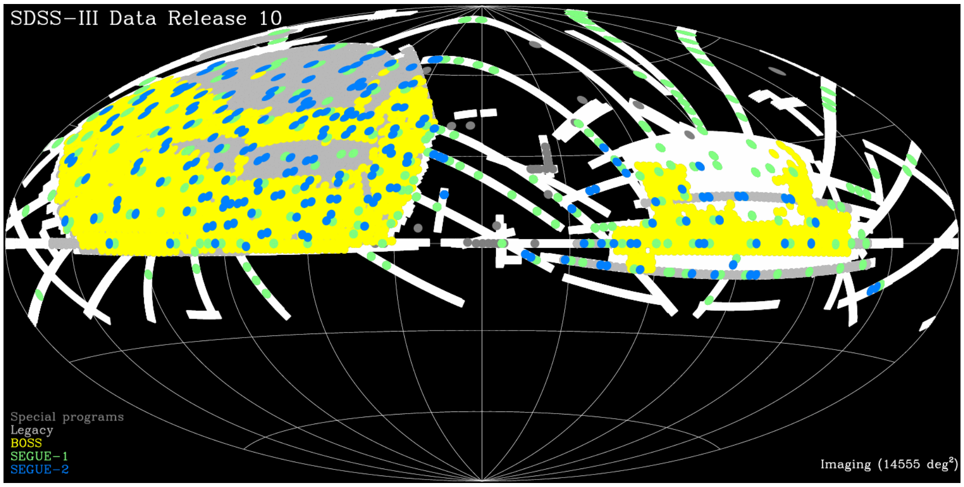

Figure 2.5: DR10 SDSS/BOSS sky coverage (taken from `www.sdss3.org/dr10/`)

Until now the project consists of three phases, SDSS-I (2000-2005), SDSS-II (2005-2008), SDSS-III (2008-2014). The SDSS-III data release 10 (DR10), that we are going to examinate, offers the latest data from the SDSS, in particular contains the full imaging survey from the SDSS imaging camera, all of the spectra from the original SDSS 640-fiber spectrograph, and an additional 684.000 new spectra from the Baryon Oscillation Spectroscopic Survey (BOSS) 1000-fiber spectrograph. DR10 also includes the first release of spectra from Apache Point Observatory Galactic Evolution Experiment (APOGEE), that uses infrared spectroscopy to study tens of thousands of stars in the Milky Way.

BOSS will measure the large-scale distribution of 1.5 million galaxies to $z \sim 0.7$, and the Lyman-alpha forests of 160.000 quasars, to measure the signature of baryon acoustic oscillations. Its two identical spectrographs are rebuilt from the original SDSS spectrographs. There are two cameras for each spectrograph, one red and one blue. The red cameras cover at least 5650-10000 Angstroms, blue cameras cover at least 3600-6350 Angstroms.

BOSS has a broad range of spectroscopic resolution, by means of it could achieve its main scientific goals. In the blue channel the resolution runs from R=1560 at 3700 Angstroms to R=2270 at 6000 Angstroms; in the red channel it runs from R = 1850 at 6000 Angstroms to R = 2650 at 9000 Angstroms.

The optical imaging and spectroscopic information are listed in the following tables 2.1-2.2.

Table 2.1: Optical imaging information

Total unique are covered	14,555 square degrees				
Number of catalog objects	1,231,051,050				
	u	g	r	i	z
Effective wavelengths and magnitude limits	3551	4686	6165	7481	8931
	22.0	22.2	22.2	21.3	20.5

Table 2.2: Optical spectroscopic information:SDSS vs BOSS

	SDSS spectrograph		BOSS spectrograph	
Area covered	Full unique coverage	9274 square degrees	Full unique coverage	6,373 square degrees
	SEGUE-1 coverage	1438 square degrees		
	SEGUE-2 coverage	1317 square degrees		
	Legacy coverage	7966 square degrees		
Plate area	1.49 deg radius, 6.97 deg^2		1.49 deg radius, 6.97 deg^2	
Fibers per plate	640		1000	
Wavelength coverage	3800 to 9200 Å		3600 to 10,400 Å	
Resolution	1800 to 2000		1400 to 2600	
Approximate magnitude limits	Main sample galaxies	Petrosian $r < 17.77$	Luminous Galaxies	$i< 19.9$
(Corrected for Galactic dust extinction)	Luminous Red Galaxies	Petrosian $r < 19.2$	Quasars	$g < 22; i< 22$
	$z < 3$ quasars	PSF $i< 19.1$		
	$z >3$ quasars	PSF $i < 20.2$		
	SEGUE-1 Faint	PSF $17.8< r< 20.1$		
	SEGUE-1 Bright	PSF $r < 17.8$		
	SEGUE-2	PSF $r< 20.2$		

SDSS spectra measured with both SDSS and BOSS spectrographs have resolution of 194 km/s at 3800 Å and 120 km/s at 9000 Å. This spectral resolution allows spectra with narrow features to be resolved.

As an example of the kind of sources that we can find at low, medium and high redshifts in a random area of SDSS, in figure 2.6 the spectra of three objects are represented, in particular the spectrum of a starburst galaxy at $z \sim 0.24$, a QSO at $z \sim 0.8$ and a QSO at $z > 2$. In each figure the emission lines detected are indicated.
The COSMOS field described in section 2.1 lies in the region of the sky observed in the SDSS survey. In figure 2.7 there are shown the first 50.000 sources from SDSS in the XMM-COSMOS field (filled green circles), with available spectra in the SDSS DR10.

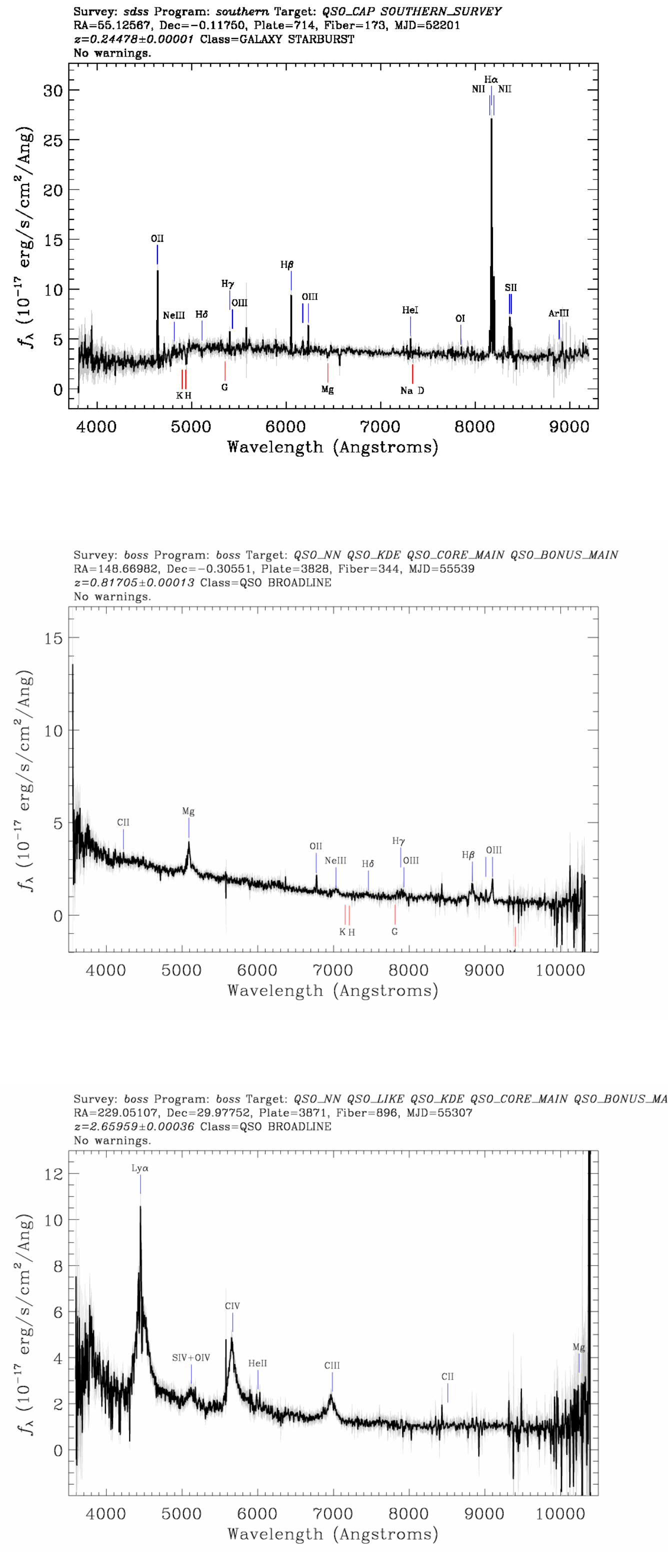

Figure 2.6: Three examples of spectra at low, medium and high redshifts: a starburst galaxy with z∼0.24 (*top panel*), a QSO broadline with z∼0.81 (*medium panel*) and QSO broadline with z∼2.7 (*bottom panel*)

2.4 The XMM-SDSS match

We cross-correlated the sources in the XMM-COSMOS sample with those presented in the SDSS database (DR10) around the COSMOS area. We used a 1" radius to match the sources. This yields 200 matches, that in the SDSS are classified as stars (6), galaxies (67) and QSO (127). For our analysis we considered only the last two types of sources (194 targets). The XMM-COSMOS sample (filled black circles), SDSS sample in COSMOS field (filled green circles) and the cross-correlated sample (filled red circles) are represented in figure 2.4 .

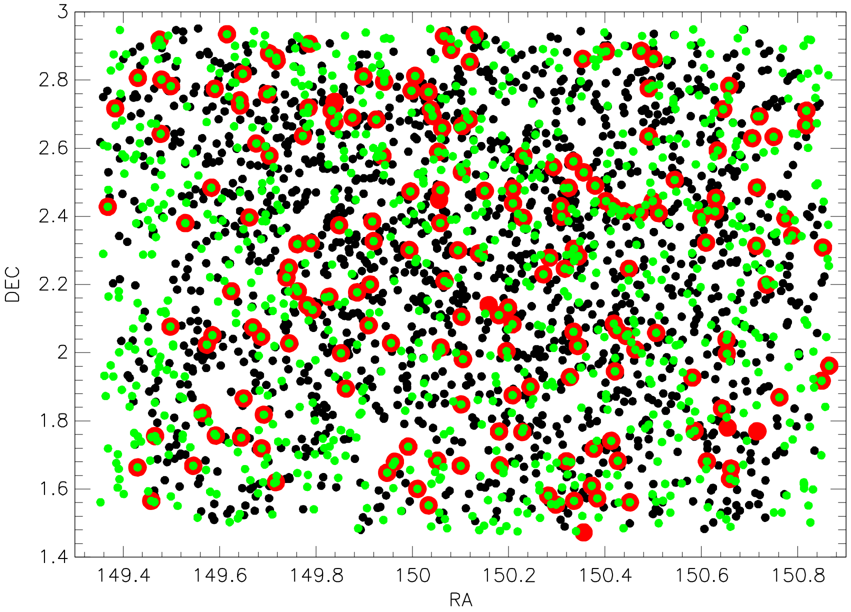

Figure 2.7: The two-square-degree COSMOS field as seen by XMM-Newton (*filled black circles*) and SDSS (*filled green circles*). The sample of 194 sources, resulting from the cross-correlation between XMM-COSMOS and SDSS, is represented as filled red circles. North is up, East is right.

194 extragalactic objects common to the XMM-COSMOS and SDSS DR10 catalogs have redshift between 0.03<z<3.5, and contains type-1 AGNs, type-2 AGNs and normal galaxies.
For 183/194 sources the spectroscopic redshift was already tabulated in B10. In addition we were able to retrieve 11 new spectroscopic redshifts, thanks

to the latest release of SDSS. In total all 194 spectra were retrieved from the SDSS archive in fits format. The spectroscopic redshift distribution of this sample of 194 objects is shown in Figure 2.8. The luminosity-redshift plane in the hard band [2-10] keV is shown in figure 2.9. Different colours refer to the three classes discussed above, green circles are associated with BL AGN, red circles with NL AGN and blue with Normal/SF galaxies
The full atlas of XMM-SDSS spectra with the redshift, L_X and XID information is reported in the appendix. Along each spectrum, we also show the cutout extracted from the SDSS database, combining the u-g-r-i-z bands.

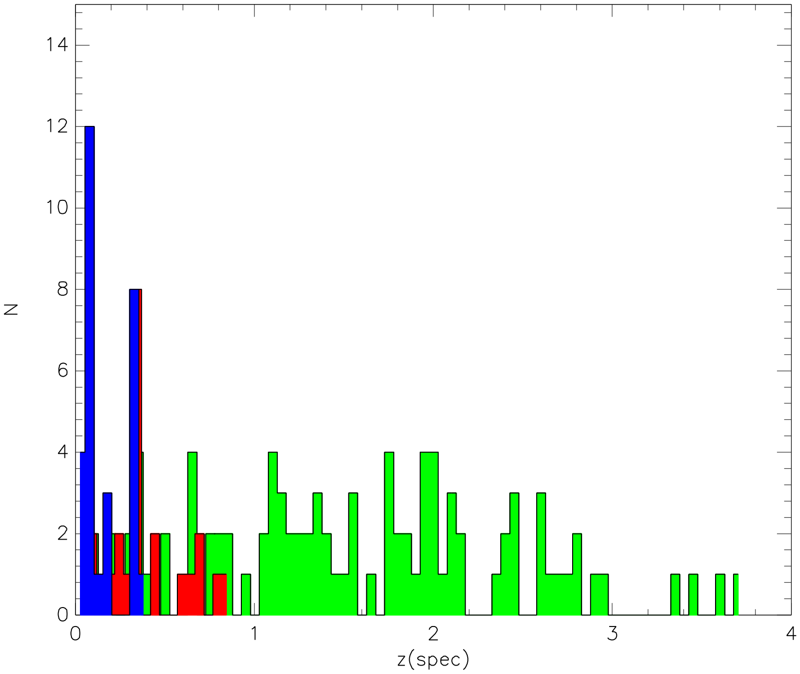

Figure 2.8: Redshift distribution of the XMM-COSMOS sample cross-correlated with SDSS DR10 database, in Δz=0.05. Based on combined optical and X-ray classification there are three classes: Normal/SF galaxies (filled blue), Narrow Line AGN (filled red) and Broad Line AGN (filled green)

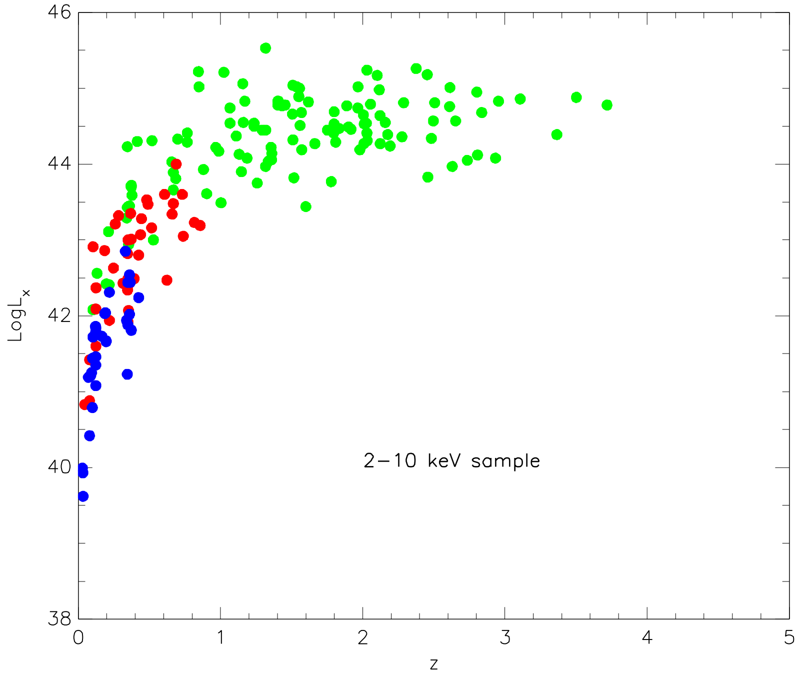

Figure 2.9: Luminosity-redshift plane for all sources of the new sample, in the hard band. Blue circles are Normal/SF galaxies, red circles are NL AGN and green circles are BL AGN

2.5 Host galaxies properties

We have collected all the multiwavelength information available in COSMOS. We have the SFR, stellar mass and L_x for 138 sources and, with reference to the three classes discussed above, 100 of them are BL AGN, 36 are NL AGN and 2 are Normal/SF galaxies.

The AGN and host galaxy properties were measured by Bongiorno et al 2012 (hereafter Bo12), fitting the spectral energy distribution (SED) of the sources by means of a two component model, AGN+galaxy.

The typical SED of a pure QSO is characterized by two bumps in the UV and IR regions, creating a dip at around 1μm. The UV bump is associated to the thermal emission from the accretion disk, while the IR bump is probably associated to dusty clouds in the AGN torus, that absorb intrinsic AGN UV, X-ray and optical radiation and re-radiate this energy at IR frequencies.

Taking into account galaxy, the SED is usually modeled as due to the integrated light of the stellar populations of the galaxy, which are generated by different starformation histories. Galaxy SEDs peak typically at around 1μm for a very wide range of SFR histories. Some examples of the SED fitting for unobscured (upper panels) and obscured (bottom panels) AGN are shown in figure 2.10. Black circles are rest-frame fluxes corresponding to the observed bands used to constrain the SED. Purple and blue lines correspond to the galaxy and the AGN template found as best-fit solution through the χ^2 minimization, while the black line shows their sum.

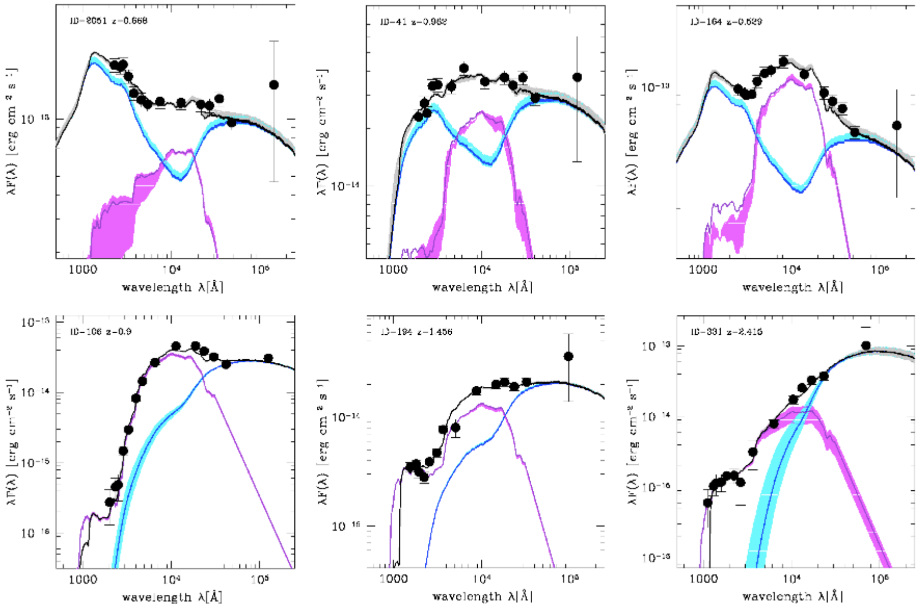

Figure 2.10: *(Left panel)* Examples of SED decompositions for unobscured AGN (upper panels) and obscured ones (bottom panels). Black circles are rest-frame fluxes corresponding to the observed bands used to constrain the SED. Purple and blue lines correspond to the galaxy and the AGN template found as best-fit solution through the χ^2 minimization, while the black line shows their sum. Pink and cyan shaded areas show the range of the SED template library within 1σ of the best-fit template, and light gray their sum.

As already mentioned, a two component model was used in Bo12, since in most of AGN both the central source and the host galaxy contribute to the SED.

By means of the SED decomposition, Bo12 estimated the SFR from the UV emission measurements, scaled up by the dust correction factor. In type-1 AGN there is a degeneracy for the UV emission, due to the combined contribution of star formation and central AGN, while in type-2 AGN, the UV emission, belonging to the accretion disk, is suppressed by obscuration, thus avoiding the contamination from the central source. More plausible values of SFR are determinated in this last case.

SFR versus stellar mass for the 138 sources is shown in figure 2.11. There are three different colors for the three classes of sources, in particular green circles are associated with BL AGN, red circles with NL AGN and blue with Normal/SF galaxies. The net separation of the three classes is probably due

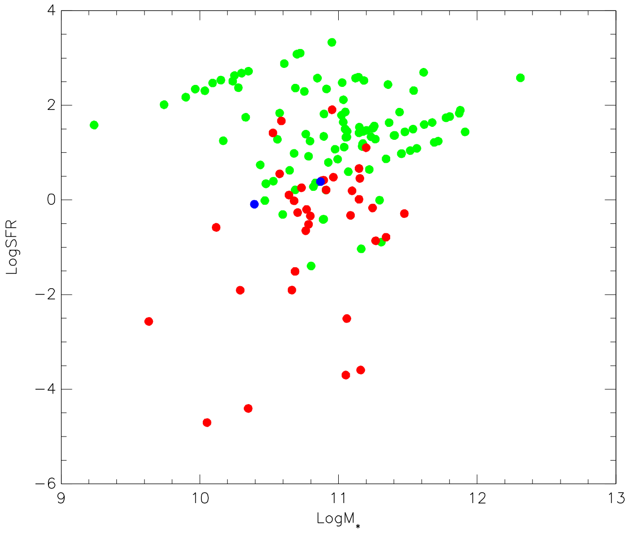

Figure 2.11: SFR versus stellar mass. The green circles represent BL AGN, the red NL AGN and blue normal/SF galaxies

to selection effect, since at z>0.8 only BL AGNs are detected. Given that the SFR is known to increase with redshift (e.g. Madau et al. 1998, Karim et al. 2011) this can explain the higher SFR of BL AGN than NL AGN.

2.6 Bolometric luminosities

Another key parameter that is needed to estimate the energetic associated to the AGN is the bolometric luminosity.
In general bolometric luminosity can be espressed as:

$$L_{bol} = Log_{10} \int_{Log\nu_i}^{Log\nu_j} \nu L_\nu dLog\nu \tag{2.1}$$

where νL_ν is the broad band rest-frame SED.
Lusso et al. 2012 (hereafter L12) derived bolometric luminosity for the entire XMM-COSMOS sample. In particular for type-2 AGN, representing the sources that we will examine in the next sections, it is computed as follow:

$$L_{bol} = L_{IR} + L_X \tag{2.2}$$

where L_{IR} and L_X are the total infrared and X-ray luminosities, respectively. By means of a SED fitting, L12 separated the contribution from AGN and host-galaxy emission, and consequently, only the nuclear component was integrated, in order to calculate the bolometric AGN luminosity. The total IR luminosity was obtained integrating the nuclear template between 1 and 1000 μm and the X-ray luminosity was estimated by integrating the X-ray SED in the 0.5-100 keV range.
In L12 it was also derived the bolometric correction. It was used the standard following definition:

$$k_{bol} = \frac{L_{bol}}{L_{band}} \tag{2.3}$$

where L_{bol} is the bolometric luminosity and L_{band} is the luminosity in a certain band.
We derived the bolometric luminosities from the X-ray luminosities in the hard band and assuming the bolometric corrections of Lusso et al. 2012 obtained for the spectroscopic and photometric samples. In particular we used the following equation:

$$y = a_1 x + a_2 x^2 + a_3 x^3 + b \tag{2.4}$$

where

$$x = LogL - 12$$

and

$$y = Log[L/L_{Band}]$$

L is the bolometric luminosity in units of $L_\odot$. In figure 2.12 it is represented the bolometric correction of our sources, as a function of the bolometric luminosity and it is shown a comparison with Marconi et al. 2004 (hereafter M04), where there are higher k_{bol} values, because in M04 luminous optically selected quasars were analyzed. For different coefficients of the best-fit relation see Table 2.3

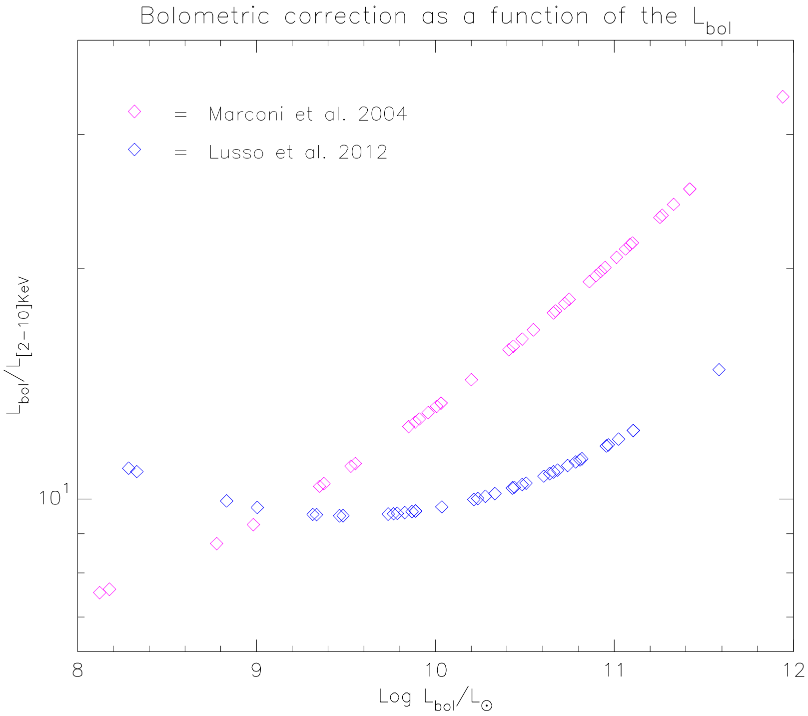

Figure 2.12: Bolometric correction as a function of the bolometric luminosity in the [2-10]keV band for type-2 AGN sample. Blue diamonds refer to values determinated by means of the best-fit relation described in Lusso et al. 2012. Magenta diamonds refer to those described in Marconi et al 2004

Table 2.3: Bolometric correction relations for X-ray selected Type-2 AGN sample in [2-10]keV band

	a_1	a_2	a_3	b
Lusso et. al	0.230	0.050	0.001	1.256
Marconi et. al	0.24	0.012	-0.0015	1.54

2.7 The sample for the outflows study: [OIII] lines

Up to z=0.8 we had all the three classes, making a total of 98 sources; at higher redshift only BL AGNs are detected: this is due to selection effects, since at these redshifts NL AGNs are on average optically fainter than BL AGNs and are expected to be below the optical magnitude limit of SDSS. We were only interested in 38 of the 98 sources, such as obscured AGN, but it was possible to obtain a best-fit spectrum only for 30 sources.
In order to search for outflows in type-2 AGN, another subsample of 25 sources was created, i.d. those with [OIII]λ5007 emission line detected. For more details about the entire final sample see Tables 2.4-2.5.

Table 2.4

Sample	*Match*	*BLAGNs*	*NLAGNs*	*Galaxies*	*Stars*	*Hα*	*[OIII]*
Total	200	122	38	34	6		
z<0.8	98	26	38	34		20	25
SFR	138	100	36	2			
BPT			12			12	12

Table 2.5: Final sample coordinates, redshifts, SFRs, stellar masses, $LogL_x$ and $LogL_{bol}$

XID	RA	DEC	z	$LogM_*$	$LogSFR$	$LogL_{bol}$	$LogL_x$
140	150.23 006	2.39552	0.045	9.63	-2.57	41.87	40.83
5435	149.70277	2.87868	0.079	10.05	-4.7	42.42	41.42
5284	149.77295	2.63615	0.079	10.29	-1.91	41.92	40.88
2021	150.37260	1.60938	0.104	10.77	-0.2	43.92	42.91
54517	149.93826	2.57758	0.124	10.35	-4.41	42.59	41.6
2608	150.42494	2.06622	0.125	10.66	-1.9	43.35	42.37
157	150.13800	2.29167	0.185	-99.0	-99.0	43.86	42.86
5075	150.04227	2.69489	0.218	11.06	-2.51	42.92	41.94
2218	150.61147	1.68108	0.248	10.64	0.1	43.62	42.63
5112	149.83873	2.6751	0.26	11.15	0.67	44.25	43.21
5443	149.94786	1.64789	0.283	10.7	-0.27	44.37	43.32
5537	149.67624	2.61425	0.315	10.12	-0.58	43.41	42.43
191	150.49063	2.63474	0.346	10.96	0.48	43.82	42.82
385	150.22832	1.76731	0.35	10.73	0.26	44.01	43.0
2570	150.65216	2.0382	0.368	11.1	0.19	44.4	43.35
5318	149.64258	2.7257	0.393	10.76	-0.65	43.47	42.49
2195	150.4183	2.08515	0.424	10.53	1.42	43.8	42.8
293	149.86203	1.89485	0.444	11.15	0.46	44.32	43.28
5002	150.81723	2.66745	0.481	10.88	0.4	44.61	43.53
5626	149.61542	2.93486	0.49	10.91	0.21	44.54	43.47
2681	150.0106	1.60022	0.516	10.89	0.42	44.19	43.16
5484	150.7142	2.31388	0.607	11.34	-0.79	44.69	43.6
217	149.88544	2.1772	0.66	10.95	1.91	44.39	43.34
70	150.15024	2.4752	0.688	10.59	1.67	45.17	44.0
5196	150.63022	2.45457	0.817	10.78	-0.52	44.27	43.23

Chapter 3

Spectral analysis

We are interested in the presence of ionized gas outflows in Type-2 AGN and the forbidden [OIII] emission lines are an ideal tracer of them, since a broad [OIII] profile is the result of a disturbed kinematics in the NLR of AGN, which can be ascribed to winds in the system. In order to search for [OIII] broad components we modelled the emission line profiles of the spectra of our sample, using IRAF task SPECFIT in STSDAS package. What follows are a brief description of this tool, a detailed description of the analysis of individual emission line fits and of stacked spectra.

3.1 The fitting program: SPECFIT

This interactive tool can fit complex physical models to data, spanning a wide range in wavelength. Data can be input as ASCII files with two header lines, one with a descriptive name, the other with the number of data points, the integration time and the Julian date of the observations. The data are organized in three columns containing wavelength, flux and error for each data point.

We extracted the wavelength and flux columns from the FITS files of SDSS DR10; we used the square root of the flux as error, for each data point. Prior to the modeling of the emission line profiles, the spectra were shifted to the galaxy rest frame:

$$\lambda_{\mathrm{emit}} = \frac{\lambda_{\mathrm{obs}}}{1+z} \tag{3.1}$$

where λ_{emit} is the emitted wavelength, λ_{obs} is the observed wavelength and z is the redshift. We also multiplied the flux by (1+z) in order to conserve the observed integrated flux in the rest-frame fit.

Since SPECFIT is an IRAF task, general parameter input is controlled by the usual IRAF parameter file system; using **eparam** task it is possible to modify general parameters like the input file name, names of log files and plot files and the names of the database files used for the parameters in the model. The database is a directory of simple text files, which contains the initial guesses for the parameters, provided by the users. An example of this file is shown in figure 3.1. The database text file begins with a line starting with the keyword "begin". The rest of the line is the name of database file. Here lines following the keyword "components" describe the model: functional ingredients of the model are listed.

After listing the components, the parameters for each component appear following keywords consisting of the component name with the component number appended. Indeed each component has a specific number of associated parameters. In our case we used two types of components:

- Power law, with associated parameters such as flux and power law index
- Gaussian, with associated parameters such as flux, or area under the gaussian, centroid of the line, FWHM of the line in km/sec and Skewness (1=symmetric emission line)

In each line, thus for each components, there are six parameters: the parameter value, the minimum allowable value and the maximum allowable value within the parameters are permitted to vary, the step size for the minimization search, the tolerance for judging convergence of the fit and a flag indicating whether the parameter is free to vary (0), fixed at the given value (-1) or linked to an another parameter (a positive integer). Link one parameter with another led to reduce the number of free parameters in a fit and allows to test for realistic physical constraints on a spectrum. When a parameter is linked to the corresponding parameter of another component, the step size is used as a scale factor. In fig 4.1 the intensity of the [NII]λ6581 is fixed at 3.0 times the values of [NII]λ6548, this is also the case of [OIII]$\lambda\lambda$5007,4959. The wavelengths of the lines were constrained to be equal to the laboratory differences, indeed the wavelength of the first emission line modelled is free to vary and the others are linked to this wavelength.

Fitting was done via Chi-square minimization using three different algorithms: Simplex algorithm, Marquardt algorithm and Numrecipe, an optimal Marquardt algorithm, that seems to be usually the most effective and the fastest. For more details about SPECFIT see Kriss 1994.

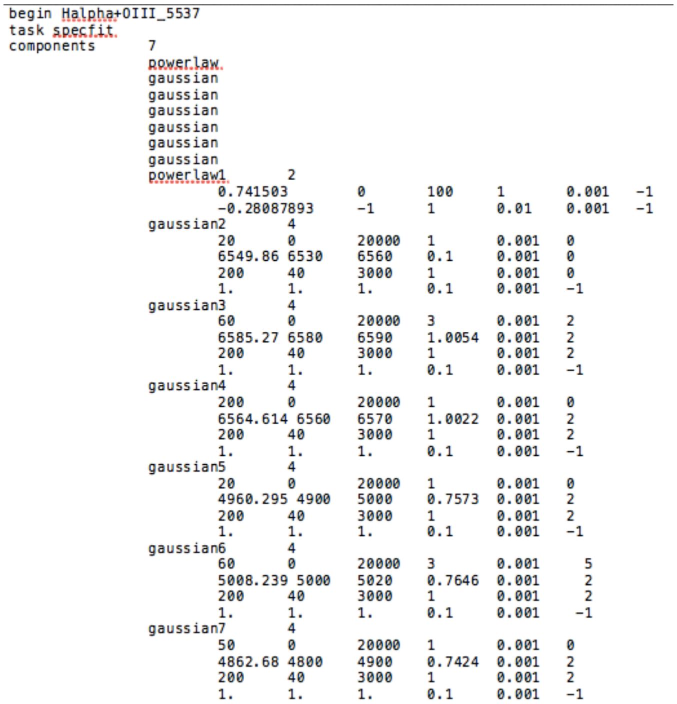

```
begin Halpha+OIII_5537
task specfit
components      7
                powerlaw
                gaussian
                gaussian
                gaussian
                gaussian
                gaussian
                gaussian
                powerlaw1       2
                        0.741503        0       100     1       0.001   -1
                        -0.28087893     -1      1       0.01    0.001   -1
                gaussian2       4
                        20      0       20000   1       0.001   0
                        6549.86 6530    6560    0.1     0.001   0
                        200     40      3000    1       0.001   0
                        1.      1.      1.      0.1     0.001   -1
                gaussian3       4
                        60      0       20000   3       0.001   2
                        6585.27 6580    6590    1.0054  0.001   2
                        200     40      3000    1       0.001   2
                        1.      1.      1.      0.1     0.001   -1
                gaussian4       4
                        200     0       20000   1       0.001   0
                        6564.614 6560   6570    1.0022  0.001   2
                        200     40      3000    1       0.001   2
                        1.      1.      1.      0.1     0.001   -1
                gaussian5       4
                        20      0       20000   1       0.001   0
                        4960.295 4900   5000    0.7573  0.001   2
                        200     40      3000    1       0.001   2
                        1.      1.      1.      0.1     0.001   -1
                gaussian6       4
                        60      0       20000   3       0.001     5
                        5008.239 5000   5020    0.7646  0.001     2
                        200     40      3000    1       0.001     2
                        1.      1.      1.      0.1     0.001    -1
                gaussian7       4
                        50      0       20000   1       0.001   0
                        4862.68 4800    4900    0.7424  0.001   2
                        200     40      3000    1       0.001   2
                        1.      1.      1.      0.1     0.001   -1
```

Figure 3.1: Example of database file containing the initial guesses for parameters.

3.2 The models

Two models were made and are discussed in the following sections. We will refer to the first model as ”one component model” and to the second as ”two components model”.

3.2.1 One component model

We tried to fit all 38 type-2 AGNs of our sample, using SPECFIT tool. For each source we created a model with the following lines: Hβ, [NII]$\lambda\lambda$6548,6581, Hα, [SII]$\lambda\lambda$ 6716,6731 and obviously, [OIII]$\lambda\lambda$ 4959,5007. SPECFIT allows users to choose the wavelength intervals to be used in fitting the spectrum, thus we decided to fit simultaneously all the emission lines.

The SDSS data describing spectral line wavelengths use vacuum wavelenghts. In the following Table (3.1) there are specified the vacuum wavelength of the transitions we used in the fit.

Table 3.1: Vacuum wavelength of some atomic transitions

Line	*Vacuum*
Hβ	4862.721
[O III]	4960.295
[O III]	5008.239
[N II]	6549.86
Hα	6564.614
[N II]	6585.27
[S II]	6718.29
[S II]	6732.68

First of all we estimated the continuum for each source by fitting a power-law to the spectra on the side of doublets [OIII], [NII] and [SII], using those wavelength ranges not affected by prominent features. The best-fit of continuum was put in the database file of each source, in order to fix the power law parameters.

Each line was fitted by means of one gaussian component, with no limit for the value of FWHM

We used two constraints, taking into account atomic physics: theoretical flux ratio for [NII]$\lambda\lambda$ 6548,6581 and for [OIII]$\lambda\lambda$ 4959, 5007 set to 1:3 for both.

For [SII]$\lambda\lambda$6716,6731 the flux ratio was required to be within the range 0.44<[SII](6716/6731)<1.42, the ratios corresponding to the high and low density limits respectively.

The wavelengths of the lines was constrained to be equal to the laboratory differences: the wavelength of the first emission line modelled is free to vary and the others are linked to this wavelength.

We obtained the best fit for 30/38 sources, since SPECFIT was no able to fit the spectra of 8 targets due to low signal-to-noise. Furthermore five of these 30 sources for which we had a best-fit were not considered in the next steps of analyses since we focused on the [OIII]λ5007 emission line.

In figure 3.2 two examples of best-fit to the data obtained by means of the one component model are shown. Fluxes and FHWM obtained from the one component model fitting are listed in Table 3.2

Figure 3.2: (*Upper panel*) Zoom in the regions of [OIII] of the source XID5626. The black solid curve represent the original spectrum and the red solid one is the best-fit to the data obtained from one component model fitting. (*Bottom panel*) Zoom in the regions of [OIII] of the source XID54517. The black solid curve and the red solid one have the same meaning as above. Under each spectrum the residuals with respect to the best fit are shown.

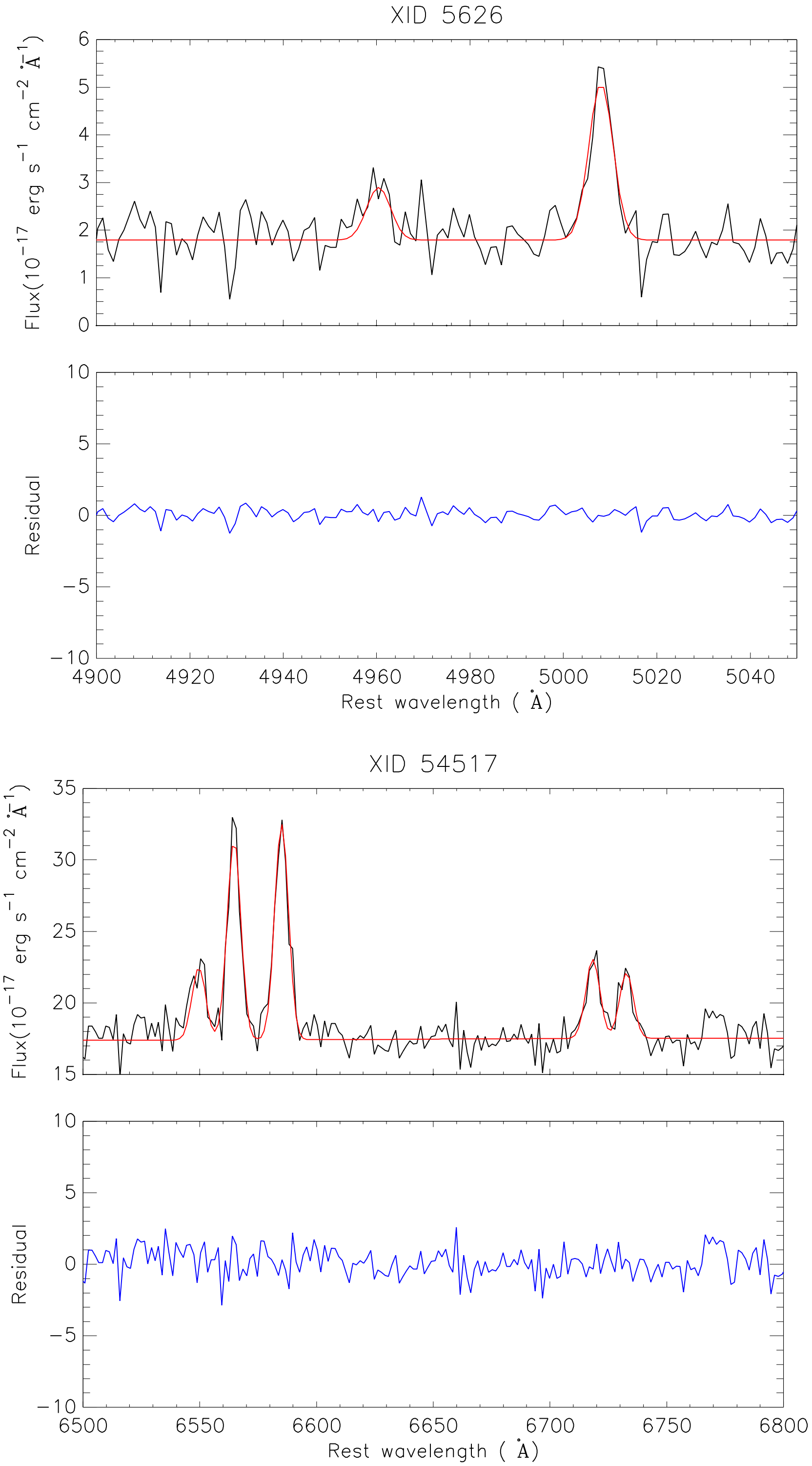

Table 3.2: Fit to the Hα, Hβ,[OIII]λ5007,[OIII]λ4959,[NII]λ6548,[NII]λ6581 with χ^2

XID	FWHM km s^{-1}	[OIII]λ4959 (10^{-17})	[OIII]λ5007 (10^{-17})	Hβ (10^{-17})	Hα (10^{-17})	[NII]λ6548 (10^{-17})	[NII]λ6581 (10^{-17})	χ^2
140	282 ±13	41 ± 6	123 ± 6	-	79 ± 7	36 ± 3	108 ± 3	26
5435	1318 ± 151	23± 11	69± 11	75± 13	412± 47	71± 9	213± 9	55
2021	343 ± 9	51 ± 6	152 ± 6	17 ± 5	191± 8	54± 2	162± 2	36
5112	752 ± 39	22± 5	66 ± 5	54 ± 5	263± 10	55± 3	164 ± 3	40
30744	224 ± 61	-	2± 1	-	6± 4	4± 1	12 ± 1	39
5484	584± 155	4± 1	12 ± 1	-	-	-	-	17
70	401 ± 71	2 ± 1	6 ± 1	6 ± 2	-	-	-	30
157	569 ± 32	4 ± 0.8	13 ± 1	13 ± 2	76 ± 4	21 ± 1	62 ± 1	28
5075	708 ± 39	3 ± 2	7 ± 2	-	42 ± 4	27 ± 1	82 ± 1	13
2218	338 ± 9	7± 1	21± 1	18 ± 2	118 ± 4	24 ± 1	73 ± 1	25
5443	325 ± 23	4 ± 1	11± 1	-	34 ± 3	5 ± 1	16 ± 1	26
5537	336 ± 51	3 ± 1	8 ± 1	3 ± 2	16 ± 4	8 ± 1	23 ± 1	75
191	323 ± 22	6 ± 1	18 ± 1	-	22 ± 1	6 ± 1	19 ± 1	15
385	421 ± 29	4 ± 1	11 ± 1	-	35± 3	13 ± 1	38 ± 1	28
392	1928 ± 97	-	-	-	240 ± 23	61 ± 5	182 ± 5	14
2570	504 ± 21	5 ± 1	15 ± 1	2 ± 1	61 ± 3	10 ± 1	30 ± 1	23
5318	614 ± 45	8 ± 1	24 ± 1	-	21 ± 3	10 ± 1	30 ± 1	16
2195	495 ± 46	16 ± 3	48± 3	32± 8	191 ± 20	38 ± 5	113 ± 5	509
293	985 ± 31	63 ± 2	188 ± 2	15 ± 3	114 ± 7	60 ± 3	60 ± 3	38
5626	287 ± 35	6± 1	19 ± 1	-	-	-	-	27
2681	417 ± 25	5 ± 1	16 ± 1	4± 2	39 ± 4	6 ± 1	19 ± 1	39
217	622 ± 127	17 ± 3	51± 3	-	-	-	-	265
5196	332 ± 60	5 ± 1	14 ± 1	-	-	-	-	3
5284	448 ± 14	12 ± 2	37 ± 2.	-	266 ± 11	77± 3	232 ± 3	23
54517	315 ± 15	6 ± 1	19 ± 1	6 ± 3	102 ± 6.	37± 2	111 ± 2	24
2608	466 ± 23	20 ± 1	59 ± 1	-	42 ± 5	34 ± 6	103 ± 6	12
5002	640 ± 23	68± 3	204± 3	35± 5	155± 10	30± 3	90 ± 3	99

Notes: Fluxes are in units of 10^{-17} erg cm^{-2} s^{-1}

3.2.2 Two components model

In the second model we added a second gaussian component for each emission line and some more constraints. We put the FWHM $<$ 500 km/s for one component and no constrains were put on the FWHM of the other one. Furthermore we fixed to the same value of FWHM for narrow and broad components, separately, for each line fitted and, as in the case of one component model, the wavelength of the narrow and broad components were linked to the first wavelength modelled as narrow and broad, respectively.

From a physical point of view the first narrow component is likely to be tracing the host galaxy dynamics, thus what is expected is a FWHM$\sim$400-500 km s^{-1} for this reason we constrained the FWHM; while the other broad one, i.e. exceeding that expected from galaxy dynamics, is most likely due to the outflowing gas.

The two components model was applied to all 30 sources. Similar to the case of one component model, we focused on 25 sources, those with [OIII] emission line detected.

In figures 3.3-3.4 two examples of how the one component model can not always reproduce the observed emission are shown.

Figure 3.3: In all panels is represented a zoom in the region of [OIII]. In the left panels are represented the best-fit to the data (violet solid curve) of one component model of XID5112 (upper left panel), XID5435 (bottom left panel). In the right panels the best-fit to the data (blue solid curve) of the two components model of the same sources are shown. The red dot-dashed curve represents the narrow component with FWHM<500 km/s in each panel; the green dashed curve represents the broad component in each panel. Under each fit the residuals with respect to the best fit are shown.

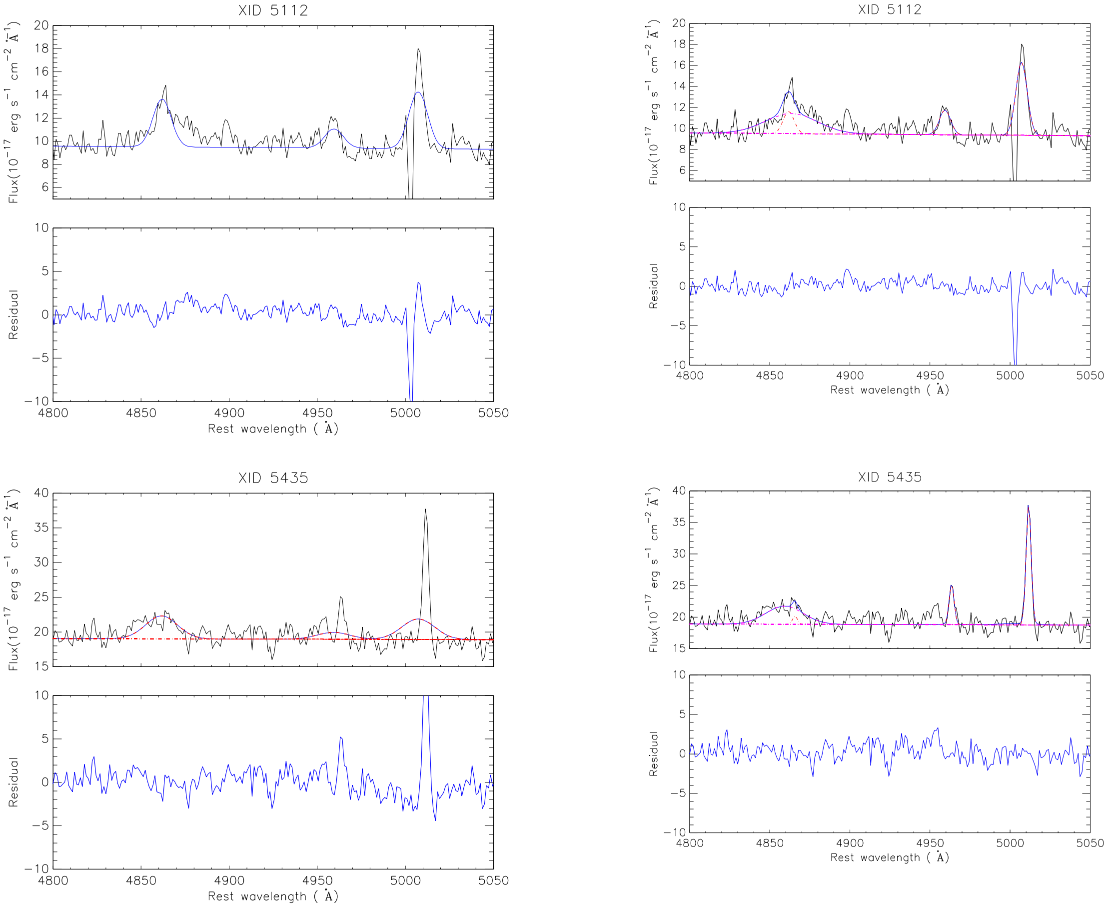

Figure 3.4: In all panels is represented a zoom in the region of Hα. In the left panels are represented the best-fit to the data (blue solid line) using the one component model of XID5112 (upper left panel), XID5435 (bottom left panel), The red dot-dashed curve represents the narrow component . In the right panels best-fit to the data (blue solid line) using two components model of same sources are shown. The red dot-dashed curve represents the narrow component with FWHM<500 km/s in each panel; the green dashed curve represents the broad component in each panel. Under each fit the residuals with respect to the best fit are shown.

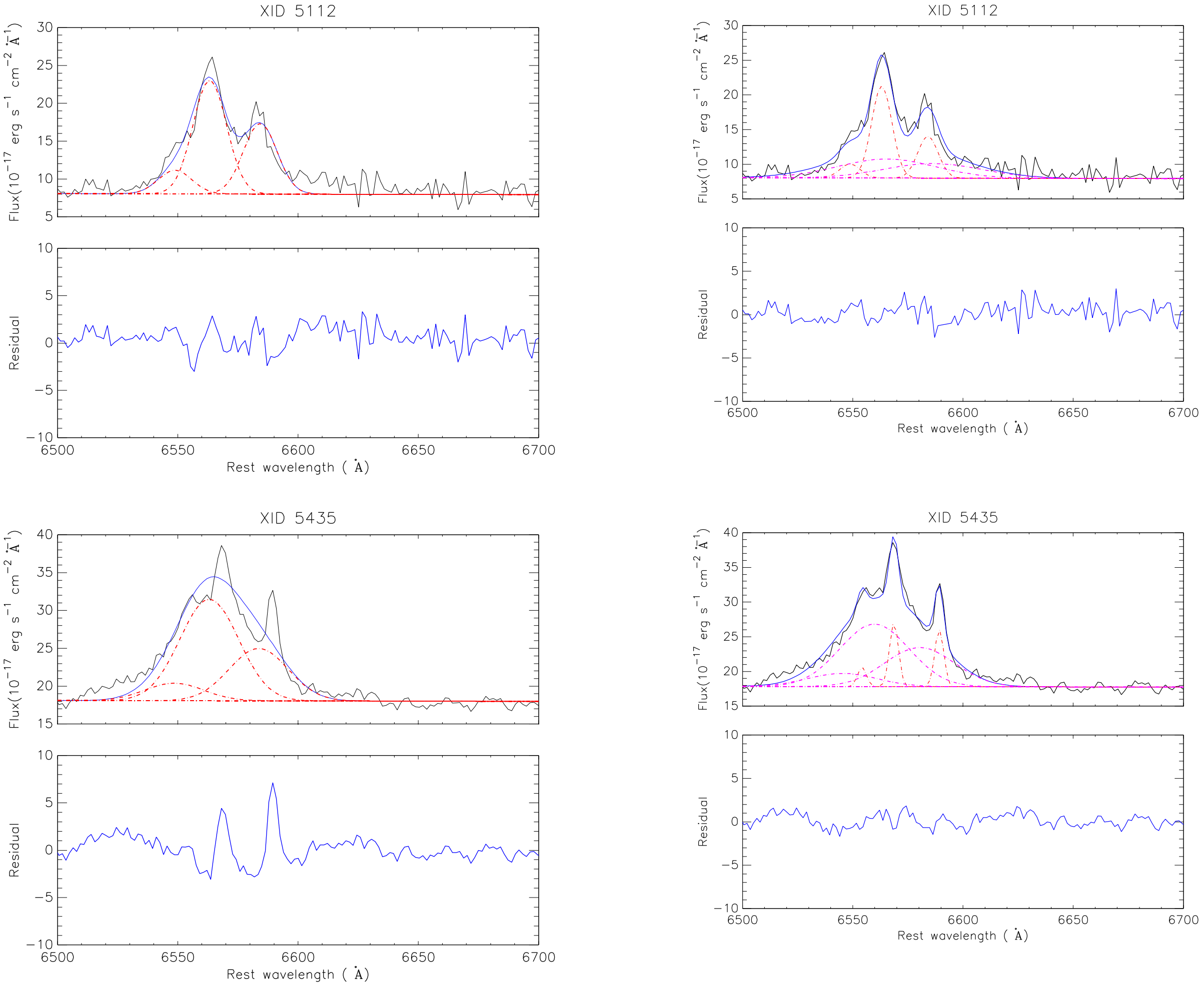

3.3 Choice of the best fit model

As we can see in figures 3.3-3.4, the residuals show how the second model better reproduces the emission line profiles in these cases.

Another check can be made comparing the chi-square of the best-fit to the data, of the two models. What we found is a lower or comparable chi-square in the two components model than in the one component model.

In order to choose between the two models, we used the χ^2 difference test, for which the difference of the χ^2 values of the two models is taken as well as the difference of the degrees of freedom, thus the difference of free parameters.

This test can be applied if the models in question are nested models, i.e. one of the models could be obtained simply eliminating or fixing parameters in the other model, as in our case.

The results is that 16 sources are well fitted with one component model and 11 with two components model. Fluxes and FWHM of those sources well modelled by means of the two components model are listed in Table 3.3.

Table 3.3: Fit to the Hα, Hβ,[OIII]λ5007,[OIII]λ4959,[NII]λ6548,[NII]λ6581 with χ^2 and the velocity shift of broad component with respect to the narrow component.

XID	Component	FWHM km s^{-1}	[OIII]λ4959 (10^{-17})	[OIII]λ5007 (10^{-17})	Hβ (10^{-17})	Hα (10^{-17})	[NII]λ6548 (10^{-17})	[NII]λ6581 (10^{-17})	χ^2	Δv km s^{-1}
5435	N	218± 10	25± 4	74 ± 4	5± 3	45± 3	14 ± 2	42± 2	23	
	B	1691± 136	-	-	84± 8	355± 76	74± 19	223± 19		403
2021	N	182± 32	-	40± 27	21± 4	64± 30	15± 9	46± 9	32	
	B	338± 43	38± 29	113± 29	-	131± 31	38± 10	115± 10		151
5112	N	496± 38	20± 3	61± 3	18± 4	153± 21	23± 4	70± 4	29	
	B	2370± 260	-	-	78± 9	151± 38	39± 6	116± 6		-103
157	N	344± 38	4± 1	12± 1	9±1	39 ± 5	8±2	24 ± 2	24	
	B	2372±272	-	-	-	-	33±3	99±3		83
5075	N	500	3±2	7±2		12±8	-	-	10	
	B	804±64	-	-	-	26±11	29±2	87±2		92
2218	N	296±9	5±1	15±1	17±2	100±4	19±1	56±1	23	
	B	1752±344	6±1	17±1	-	34±6	8±3	25±3		125
392	N	500	-	-	-	25±7	15±2	44±2	11	
	B	2585±79	-	-	-	409±15	-	-		35
2195	N	312±93	12±3	35±3	13±9	107±24	18±7	55±7	494	
	B	1397±338	5±4	15±4	36±15	136±57	-	40±20		-19
293	N	500	15±3	45±3	5±3	59±12	-	-	32	
	B	1204±55	49±4	148±4	10±5	19±18	73±3	219±3		-23
2681	N	175±7	3±1	10±1	2±1	12±10	3±1	10±1	33	
	B	380±202	3±1	9±1	3±1	32±8	3±1	10±1		251
5002	N	338±49	36±13	107±13	16±8	70±33	11±7	34±7	92	
	B	487±130	33±13	98±13	17±9	83±33	19±7	57±7		355

3.4 Non parametric velocity distribution

This thesis work is concentrated mostly on [OIII]λ5007 emission line, since from this line we can derive important quantities in order to achieve our purpose. For this reason we are interested in kinematics of the [OIII]λ5007 and thus in those sources with this emission line detected (25 targets).

Following Harrison et al. 2014, we used non parametric definitions in order to characterize the velocities and widths of the [OIII] emission line profile.

First of all we converted spectra from wavelength space into velocity space by means of:

$$v = \frac{\Delta\lambda}{\lambda} \cdot c \tag{3.2}$$

where c is the speed of light and lambda is the wavelength corresponding to the emission line peak, so that it has zero velocity in the velocity space.

Then we calculated the velocity at 2nd, 5th, 10th, 90th, 95th and 98th percentiles.

The definitions that we used for describing the [OIII]λ5007 emission line profile are the following:

- The peak velocity is the velocity of the peak flux density of the emission line profile.

- W_{80} is the velocity width of the line that contains 80% of the emission-line flux and it is defined as $W_{80}=v_{90}-v_{10}$ where v_{90} and v_{10} are the velocities at the 90th and 10th percentiles, respectively.

- v_2 and v_{98}, which are the 2nd and 98th percentiles of the flux contained in the emission line profiles and can be considered the maximum projected velocity of the gas.

An example of the [OIII] emission line with the different non-parametric velocity definitions indicated is shown in figure 3.5

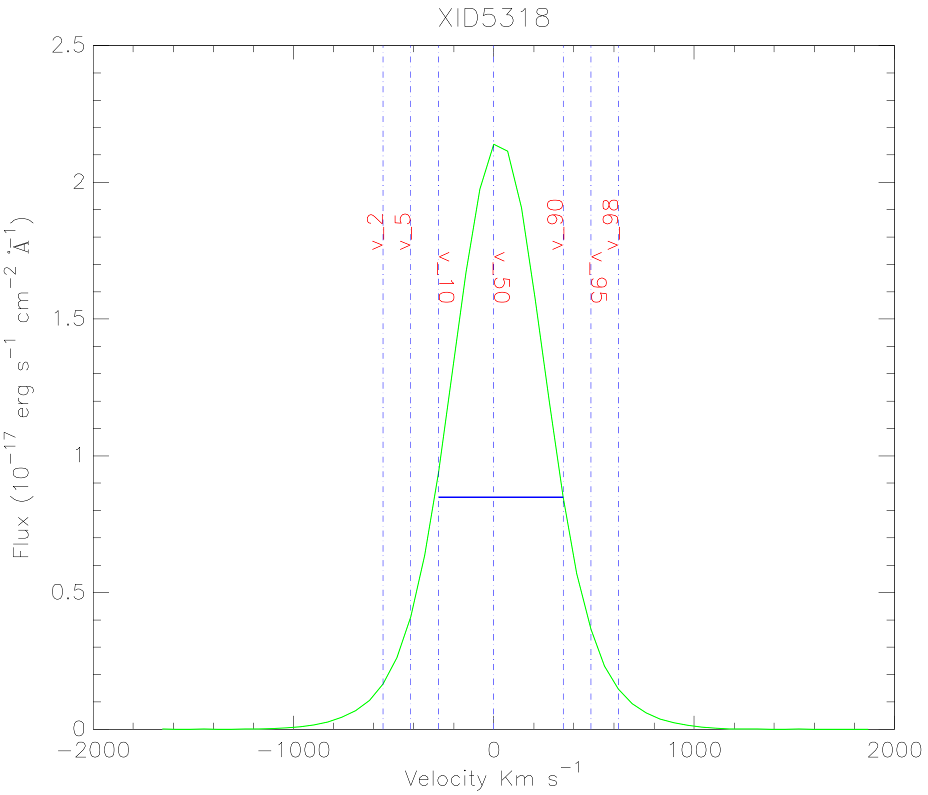

Figure 3.5: Illustration of non parametric velocity definitions in [OIII]λ5007 emission line profile of XID5318. The vertical dot-dashed lines show different percentiles to the flux contained in the emission line profile (from the left to the right: 2th, 5th, 10th, 50th, 90th, 95th and 98th). The horizontal line represents W_{80}, the line width that contains 80% of the flux.

In order to calculate the kinetic power associated to the outflows we will use the 2nd or the 98th percentiles of the flux contained in the emission line profiles, according to the velocity shift of broad component with respect to the narrow component, and the velocity width of the line that contains 80% of the emission-line flux. For those souces with a broad component of [OIII]λ5007 the 2nd or 98th percentiles are listed in Table 3.4

Table 3.4: Non parametric velocities: v_2 or v_{98} and W80

XID	$v_2/v_{98}(km\ s^{-1})$	W80 $(km\ s^{-1})$
2021	-414	414
2218	-1309	1312
2195	968	691
293	1038	1174
2681	-552	483
5002	-690	691

3.5 Stacked spectra

In addition to our fits of individual spectra we also focused on spectral stacking to derive average [OIII]λ5007 profile of our sample. The benefit of spectral stacking is to obtain an improved signal-to-noise ratio, that has an impact on the ability to detect broadened components.

We used IRAF task SCOMBINE to derive the stacked spectra. We built three types of models, considering different sources in each model:

- those sources with a single component of [OIII]λ5007 emission line, derived from individual emission line fits
- those sources with a narrow and broad component of [OIII]λ5007 emission line, derived from individual emission line fits
- all the sources with [OIII]λ5007 emission line detected.

In figure 3.6 it is shown the average [OIII]λ5007 profile derived from stacking those sources with only a single component of [OIII]λ5007 emission line. The source XID 2608 was excluded in this analysis because of contamination in its spectrum by sky emission at [OIII]λ4960.

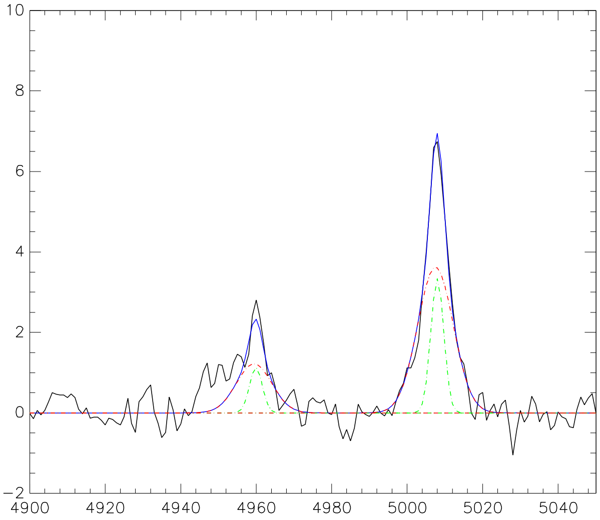

Figure 3.6: Average [OIII] profile of sources with one single component resulting in individual fitting. This profile shows a blue asymmetric wing well modelled by a broad component (red dot-dashed curve). The narrow component is represented with green dot dashed curve. The fit produced by combining these two components is shown with blue solid curve.

As we can see in the figure, the profile is well modelled by a narrow component with a FWHM=243± 55 km s^{-1} and a broad, asymmetric component with a FWHM=662±76 km s^{-1}. The stacked spectrum shows a broad component missing in individual fit of these sources.

In figure 3.7 it is represented the average profile derived from stacking those sources with broad component of [OIII]λ5007. The profile is well modelled by a narrow component with a FWHM=262± 20 km s^{-1} and a broad component with a FWHM= 722±24 km s^{-1}, consistent with the average FWHM of broad components FWHM=744 km s^{-1}.

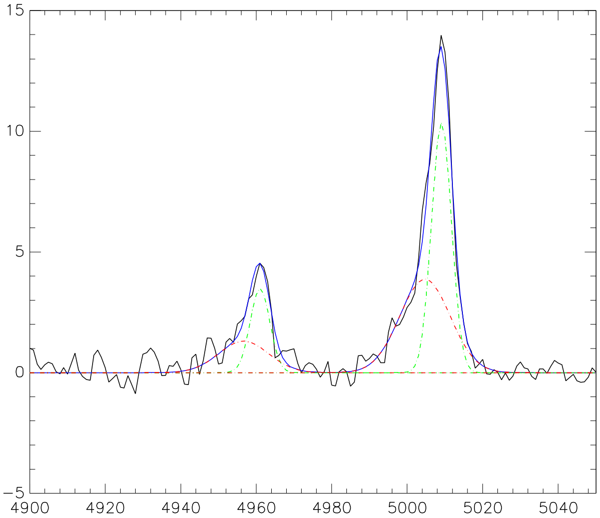

Figure 3.7: Average [OIII] profile of sources with a broad component resulting in individual fitting. This profile shows a blue asymmetric wing well modelled by a broad component (red dot-dashed curve). The narrow component is represented with green dot dashed curve. The fit produced by combining these two components is shown with blue solid curve.

The third stacked spectrum is represented in figure 3.8. Here sources of all our sample (25 targets) are included in the fit. As in the previous cases, the profile is modelled by a narrow component with a FWHM of 384±24 km s^{-1} and a broad, asymmetric component with a FWHM of 847±66 km s^{-1}. The FWHM of the three stacked spectra, labelled as narrow, broad and total models, are listed in Table 3.5.

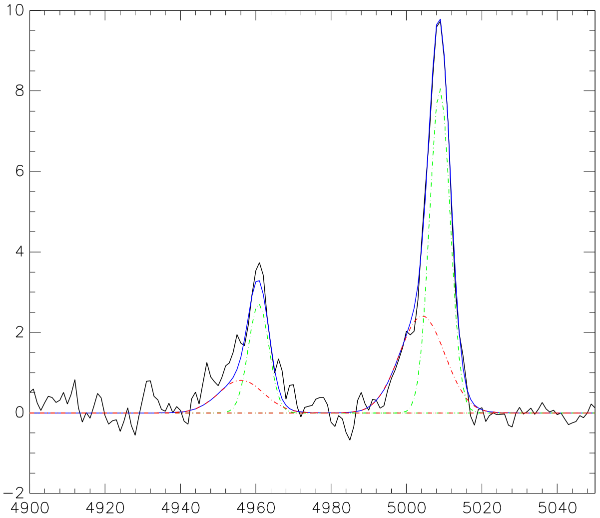

Figure 3.8: Average [OIII] profile of all sources with [OIII] emission line detected. This profile shows a blue asymmetric wing well modelled by a broad component (red dot-dashed curve). The narrow component is represented with green dot dashed curve. The fit produced by combining these two components is shown with blue solid curve.

Table 3.5: FWHM and fluxes of [OIII]λ5007 in stacked spectra

Model	FWHM (N) (km s^{-1})	Flux(N) 10^{-17}	FWHM (B) (km s^{-1})	Flux(B) 10^{-17}
Narrow	243± 55	14± 6	662±76	43± 6
Broad	261± 20	45±5	722±24	115±6
Total	384±24	55±7	847±66	36±7

Notes: Fluxes are in units of 10^{-17} erg cm^{-2} s^{-1}, FWHM(N) and Flux(N) denote the best-fit parameteres and errors for the narrow component; FWHM(B) and Flux(B) refer to the broad component.

Chapter 4

Results

In this chapter we will first describe how we used the results of emission line fitting in order to build optical BPT diagnostic line ratio diagram, discussed in subsection 1.2.2. Then we will discuss the reddening of [OIII]λ5007 emission lines in order to find some clues to the nature of broad components. In the last two sections we will discuss the comparison between the FWHM (broad component) of [OIII]λ5007, the [OIII] emission line luminosity and AGN bolometric luminosity, in order to search for trends between outflows and AGN properties.

4.1 BPT diagram

In order to investigate the location of sources in the BPT diagram all of four lines, [OIII]λ5007, Hα6563, Hβ4861 and [NII]λ6584, need to be present in the SDSS spectra. Therefore we were able to construct the BPT for only 12 sources at $z<0.5$. At $z>0.5$ Hα+[NII]λ6584 are shifted out of the wavelength coverage of the SDSS spectra. (λ >9000 Å)

The BPT diagram for our sources is shown in figure 4.1.

As we can see in the figure three sources, well fitted by one component model, lie in the NL AGN region (blue filled triangle). Nine sources, well fitted by the two components model and for which we used the total observed flux of emission lines in the BPT diagram, are in two different regions: four of them lie in the composite AGN/SF region and five in the NL AGN region. Two of these sources (red diamonds) have both the narrow and broad components of [OIII]5007, Hβ, [NII]λ6584 and Hα, thus there are also represented the emission line ratios of the narrow and broad components separately (green squares).

As we can see for one source the narrow component lies in the composite region and the broad component lies in NL AGN region. Since we have no spatial information, we can not derive some physical constraint but an emphasis can be placed on different behaviour of narrow and broad components.

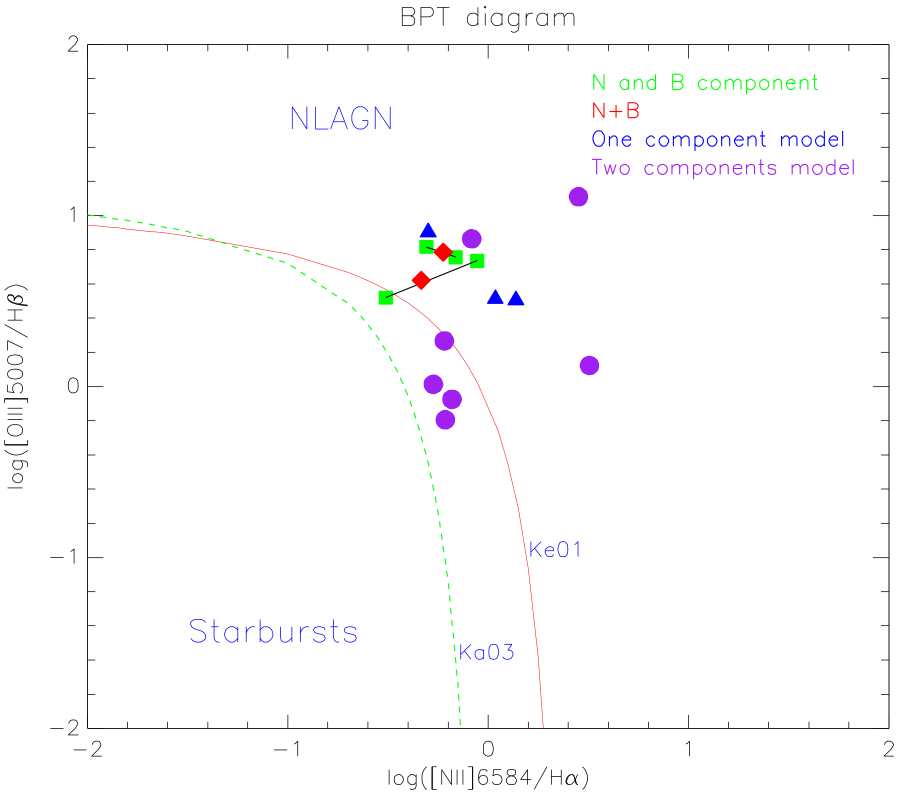

Figure 4.1: BPT diagram. [OIII]λ5007/ Hβ vs [NII]λ6584/Hα of 12 sources of our sample. Red solid line represents the criteria used to discriminate between NLAGN and HII galaxies from Kewley et al 2001. Green dashed line indicates that used by Kauffman et al 2003. Blue triangles represent the sources fitted with one component model; red diamonds represent sources fitted with two components model, with both narrow and broad components; green squares represent the narrow and broad components of sources fitted by two components model. Violet circles represent sources fitted with a narrow or a broad component for each line.

As Rodriguez-Zaurin et al 2013 emphasise in their study, a trend with emission line kinematics can exist: the line ratios for the broad components in most cases fall in Seyfert part of the BPT diagram and the narrow components fall in the transition zone between HII region and Seyfert classification. These behaviours probably suggest a different dominant mechanism of ionization: AGN photonization for broad components and combination of AGN and stellar population for narrow components.

4.2 Extinction

An important quantity that can be useful to understand if there are large amounts of gas and dust is the reddening of the optical spectrum. The reddening or color excess in B and V filter bands is defined as follows:

$$E(B-V) = A(B) - A(V) \tag{4.1}$$

where A(B) and A(V) are the total extinction, i.e. the difference of the observed magnitude and the magnitude in the absence of the dust, in B and V bands respectively.

The effect of the extinction on the observed flux of a source can be described by the following equation:

$$F_{(\lambda,obs)} = F_{(\lambda,intr)} \cdot 10^{-0.4A_{\lambda}} \tag{4.2}$$

where $F_{(\lambda,obs)}$ and $F_{(\lambda,intr)}$ are the observed flux and the intrinsic flux of the source at a given λ, respectively, and A_{λ} is the extinction at a given λ:

$$A_{\lambda} = k(\lambda)E_{(B-V)} \tag{4.3}$$

where $E_{(B-V)}$ is the color excess defined above and k(λ) is the extinction or reddening curve, which depends on the dust grains nature and on their geometrical distribution.

Hydrogen Balmer decrements, i.e. the ratio of Balmer line intensities, are often used to determine the amount of dust extinction attenuating the observed emission lines, since the intrinsic decrements of Balmer recombination lines are quite insensitive to the gas temperature and density in low density, dilute radiation field conditions (Osterbrock 1989). By means of the Balmer decrement it is possible to derive the color excess as follows:

$$E_{(B-V)} = -\frac{2.5log\frac{R_{int}}{R_{obs}}}{k(\lambda1) - k(\lambda2)} \tag{4.4}$$

where R_{int} and R_{obs} are the intrinsic and observed Balmer decrements, k(λ1) and k(λ2) are the value of the extinction curve at the wavelengths of emission lines used in the ratio of Balmer line intensities.

The Flux(Hα)/Flux(Hβ) is the Balmer decrement most frequently used. For HII region photoionized by a hot star, an intrinsic Hα/Hβ value of 2.87 is found, as predicted by Case B recombination[1] (at a typical electron density of $< 10^4$ cm^3 and temperature of 10^4 K). A value of 3.1 is generally adopted for the NLR of AGN, where Hα emission is slightly enhanced by collisional excitation due to the presence of gas of higher densities and the presence of partly ionized transition region resulting from much harder ionizing continuum (Gaskell & Ferland 1984, Halpern & Steiner 1983).

In order to derive extinction in our sources using eq 4.3, first we used the IDL routine GET_EBV in order to derive the color excess. The routine allows user to choose between the following Balmer decrement: Flux(Hα)/Flux(Hβ), Flux(Hβ)/Flux(Hγ) and Flux(Hα)/Flux(Hγ). Their theoretical values and the extinction curve can be also chosen; in particular the keyword "extra" calls the IDL routine K_LAMBDA, which returns a variety of extinction curves.

We chose Flux(Hα)/Flux(Hβ) as Balmer decrement and 3.1 as its theoretical value, and the extinction curve of Cardelli, Clayton, and Mathis (1989), commonly used in reddening estimates in AGN .

The Balmer decrement, the color excess $E_{\text{B-V}}$ and the extinction at λ5007 of sources for which we have both narrow and broad components of H_α and H_β are listed in Table 4.1. It must be underlined that the fluxes of Hα and Hβ are not corrected for the stellar absorption, thus they, in particular Hβ, may be underestimated and the Balmer decrement overestimated.

---

[1] Case B assumes that all transitions more energetic than Lyα are absorbed and reradiated via Lyα and longer wavelengths. This is an upper limit of Balmer decrement. Case A assumes the optically thin limit where hydrogen emission from all energy levels can escape the HII region unabsorbed.

Table 4.1: Decrement, E(B-V) and A_V of narrow and broad components

	Component	H_α/H_β	$E(B-V)$	$A_\lambda 5007$
XID5435	N	9.65992	1.23070	4.27385
	B	4.25055	0.40063	1.39128
XID5112	N	8.47906	1.10918	3.85186
	B	3.55870	0.22100	0.76748
XID157	N	6.20510	0.78317	2.71969
	B	6.45435	0.82299	2.85798
XID2195	N	8.66389	1.12067	3.89174
	B	3.24941	0.12907	0.44823
XID293	N	10.9282	1.35543	4.70701
	B	1.95506	0	0
XID2681	N	6.50374	0.83069	2.88475
	B	12.3760	1.48123	5.14388
XID5002	N	4.26325	0.40365	1.40176
	B	4.79991	0.52353	1.81807

Taking into account the reddening, some clues to the nature of broad components may be obtained. As we can see in Table 4.1 there is no clear trend between the extinction of narrow and broad components of the [OIII]λ5007 emission lines. In three sources seems to be a trend of increasing reddening with linewidth but for the other there is the opposite trend. So the results in these cases are inconclusive.

4.3 FWHM and luminosity of [OIII] emission line

A method to determine the driving mechanism of outflows is to search for trends between outflow and AGN properties. For this reason we compared the FWHM of the broadest component of [OIII]λ5007 line with the total *observed* [OIII]λ5007 luminosity (i.e. not corrected for extinction), which is often considered to be an indicator of the average AGN power (e.g., Zhang et al. 2010).

In fig 4.2 we plotted the FWHM against the [OIII] luminosity of our targets. In order to calculate the luminosity, we adopted the cosmological parameters H_0=71 km s^{-1} Mpc^{-1}, Ω_m=0.27 and Ω_Λ=0.73, corresponding to ΛCDM universe.

We compared our results with different literature samples of Seyfert 2 and Type 2 QSOs, at both low and high redshift, with observed [OIII] luminosities larger than those of our sources.

In fig 4.2 we plotted as blue filled circles the FWHM of the broad components in our measurements and as magenta filled circles the single component of those sources fitted by one component model and with a FWHM>500 km s^{-1}. We also plotted the stacked spectrum (black filled circle) of all our sample (25 target at z<0.8).

The results from Mullaney et al. 2013 are also shown in fig 4.2 (orange filled squares). They presented the analysis from multicomponent line fit of the [OIII]λ5007 emission line in the entire SDSS population. The orange filled squares represent the average values of the broad FWHM of SDSS population in two luminosities ranges (10^{40} <L[OIII]< 10^{41} erg s^{-1} and $10^{41.5}$ <L[OIII]< $10^{42.5}$ erg s^{-1}). The average FWHM at L[OIII]~ $10^{40.5}$ is FWHM~449 km s^{-1} and at L[OIII]~ 10^{42} is FWHM~716 km s^{-1}. We noted that all but three of our sources have FWHM consistent with the average values in the SDSS population. The FWHM of the stacked spectrum is consistent with the sample analysed by Mullaney et al. 2013.

We also plotted 8 dust-reddened QSOs at z=0.5-1, from Urrutia et al 2012 (red filled squares), selected on the basis of a red J-K color, and radio-quiet Type-2 QSOs at L[OIII]> 10^{43} erg s^{-1} from Liu et al 2013 [2] (green diamonds), for which the existence of large scale (10 kpc) outflows over most of the extent of the gas emitting region was demonstrated by means of IFU spectroscopy. We noted that the range of FWHM of our broadest component is comparable to that of these two samples. Again these sources have larger observed [OIII] luminosities than our targets.

The results for 15 type 2 QSOs from the SDSS studied in Greene et al 2009, 2011 (Violet diamonds) with L[OIII]~ 10^{42} erg s^{-1} are also reported. The observed broad widths are associated with outflows on scales extending from few up to 10 Kpc. On average the FWHM are consistent with those of our sources with a FWHM<1000 km s^{-1}, even if Type-2 sources from Green et al. are more luminous than of those of our sample.

We reported the results from Brusa et al. 2014 (yellow circles) of z~ 1.5 obscured QSOs from XMM COSMOS, expected to be caught in transitioning phase from starburst to AGN dominated systems and with FWHM associated to the broad components in the range of 900-1600 km s^{-1}. The sources presented in Brusa et al. 2014 are also drawn from the XMM-COSMOS sample, but, differently from the sample analysed in this work they are at z~ 1.5 and they have been selected on the basis of a SED with a dominant contribution of the host galaxy in the rest-frame optical bands. Our

---

[2] In this case we plotted the W_{80} non parametric width, which can be used as FWHM of the lines

sources instead have not been preselected a priori in terms of host galaxies properties and the main difference from the SDSS sample is only the X-ray luminosity.

We also plotted the stacked spectrum of ∼110 XMM-COSMOS Type 2 QSOs (Violet-red circle) in the range z=0.5-0.9, for which [OIII] is visible in the zCOSMOS spectra, constructed by Brusa et al 2014. The fit is consistent with a single and symmetric line component with FWHM∼540 km s^{-1}, consistent with the average value of the broadest component observed in the SDSS sample at comparable observed luminosities and with the FWHM of our sources with a single component of [OIII] emission line.

We have not found a clear trend of the broad FWHM with the observed [OIII] luminosity, as already pointed out in Harrison et al 2014 and in Brusa et al. 2014.

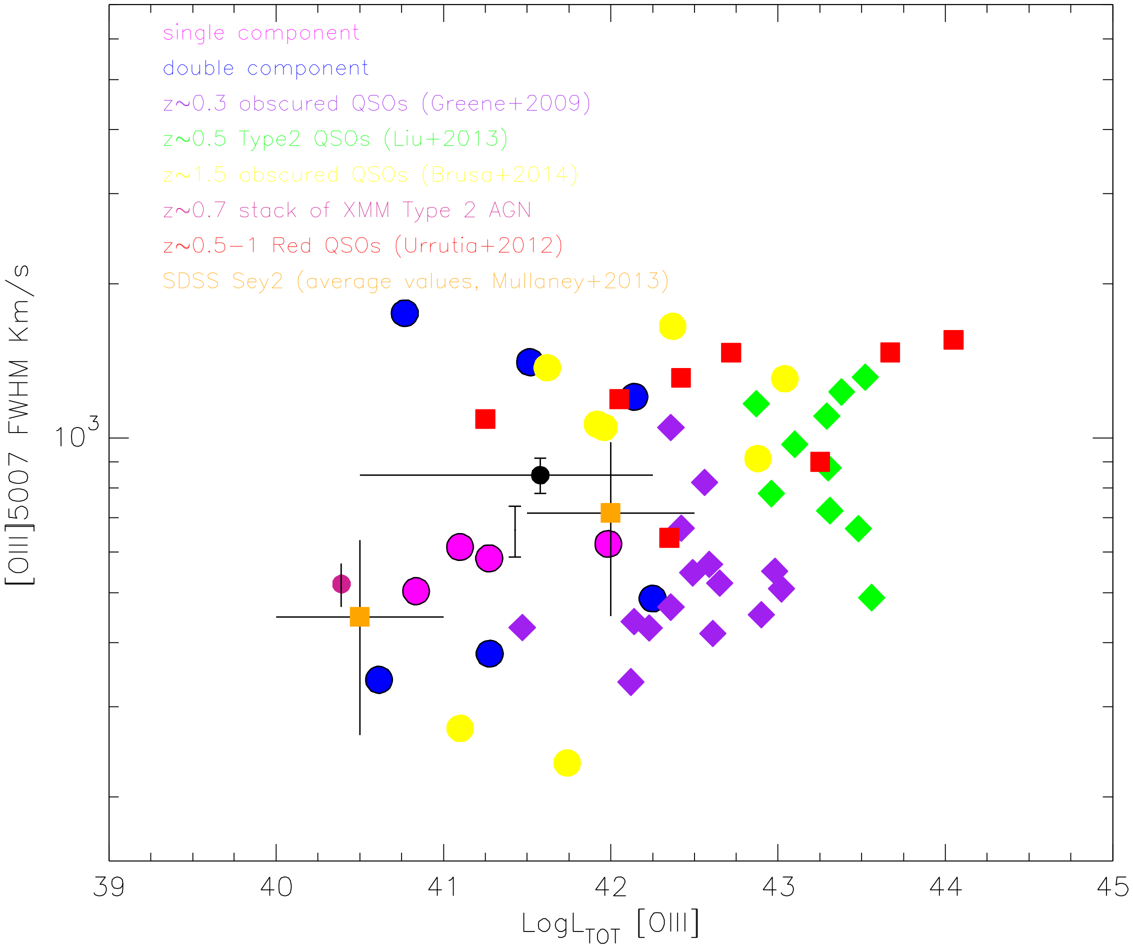

Figure 4.2: FWHM of the broadest component of [OIII]λ5007 line vs total [OIII]λ5007 luminosity. The blue circles marked the broadest components. Single components of [OIII]λ5007 with FWHM$>$ 500 km s^{-1} of those sources well fitted by one component model are also plotted (magenta circles). We reported as yellow circles the results of Brusa et al. 2014 of z$\sim$ 1.5 obscured QSOs from XMM COSMOS. The orange filled squares represent the average values of the broad FWHM of SDSS population studied by Mullaney et al 2013 in two luminosities ranges (10^{40} <L[OIII]$<$ 10^{41} erg s^{-1} and $10^{41.5}$ <L[OIII]$<$ $10^{42.5}$ erg s^{-1}). Violet-red circle represent the stacked spectrum of $\sim$110 XMM-COSMOS Type2 QSOs (in the range z=0.5-0.9). 8 dust-reddened QSOs at z=0.5-1, from Urrutia et al 2012 are plotted as red filled squares. Green diamonds represent radio-quiet Type-2 QSOs at L[OIII]$>$ 10^{43} erg s^{-1} from Liu et al 2013(in this case we plotted the W_{80} non parametric width, which can be used as FWHM of the lines). Violet diamonds represent 15 type 2 QSOs from the SDSS studied in Greene et al 2009,2011 with L[OIII]10^{42} erg s^{-1}.

4.4 FWHM and bolometric AGN luminosity

We also compared the broadest FWHM with intrinsic bolometric AGN luminosity, since in this way we have a direct link between the outflows and the central engine, removing the effect of the reddening on the [OIII] luminosities (See figure 4.3).

Here we plotted the samples of Liu et al 2013, Urrutia et al 2012, Brusa et al 2014, previously discussed and that from Harrison et al 2012, which is composed of 8 SMG/ULIRGs at z$\sim$2 with AGN signatures, with an average FWHM of 1000 km s^{-1}. By means of IFU spectroscopy, the presence of large scale outflows was traced up to scales of 10-20 Kpc in the majority of SMG/ULIRGs systems.

We plotted an estimate of intrinsic AGN luminosity, as derived in Section 2.6. In a similar way, i.e. by means of multiwavelength SED fitting, Harrison et al 2012, Urrutia et al 2012 and Brusa et al 2014 derived the bolometric luminosities for their samples.

As we can see in the figure our sample lies in a region of lower luminosities than the other samples, but with a range of FWHM comparable to that of the reported samples.

Again no clear trend between these two quantities is found, instead a positive correlation between the mid-infrared luminosity and [OIII] widths but in SDSS luminous type 2 quasar is found by Zakamska & Greene (2014), suggesting that outflows are ultimately driven by the radiative output of the quasar (Murray et al. 1995; Proga et al. 2000).

Thanks to accurated estimates of bolometric luminosities by means of a SED fitting, our results can be seen as a reliable extension at low luminosity in the bolometric luminosity-FWHM plane of the updated results at larger luminosities.

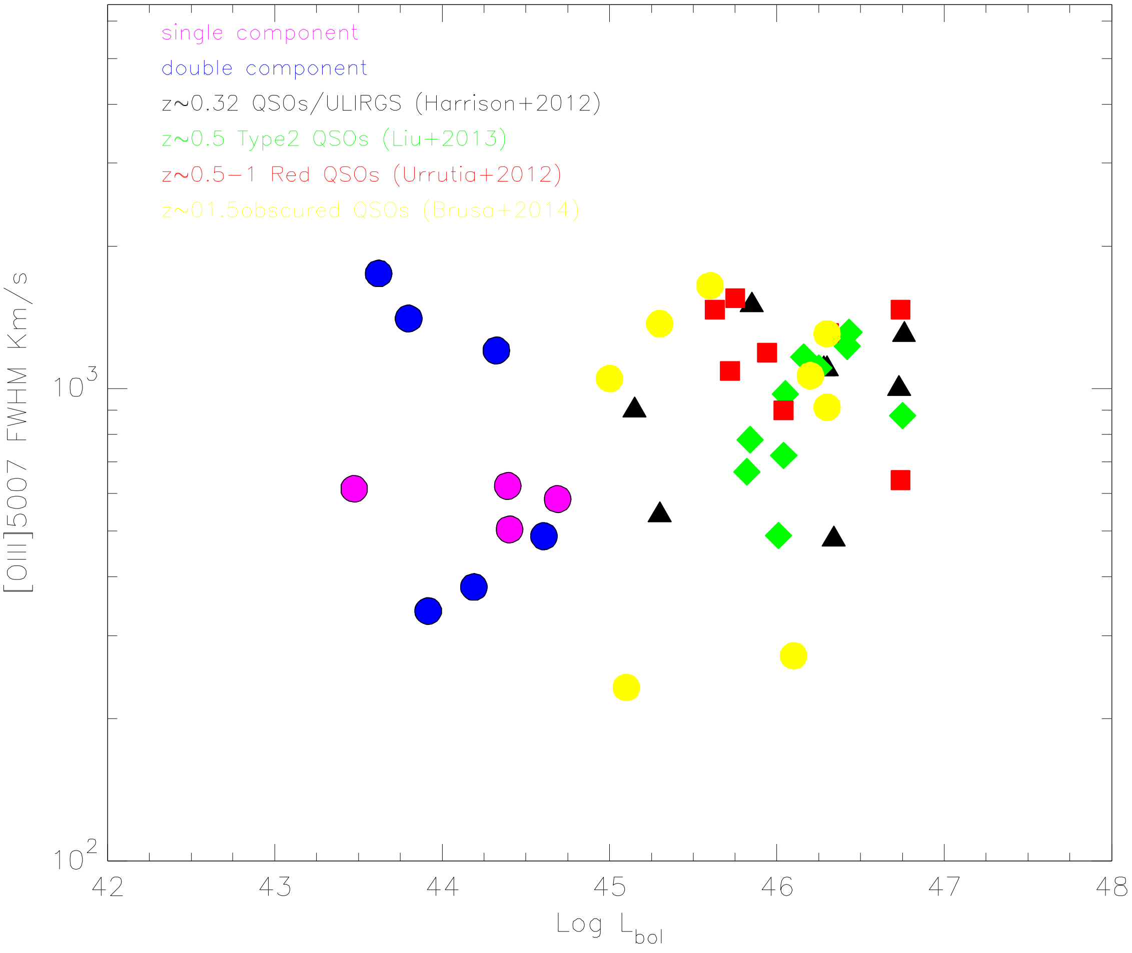

Figure 4.3: FWHM of the broadest component of [OIII]λ5007 line vs the AGN bolometric luminosity. The blue circles marked the broadest components. The single component of [OIII]λ5007 with FWHM>500 km s^{-1} of those sources well modelled by the one component model are also plotted (magenta circles).As in the previous plot we reported the samples of Liu et al 2013 (green diamonds), Urrutia et al 2012 (red squares), Brusa et al 2014 (yellow circles). Black triangles represent the sample from Harrison et al 2012, which is composed of 8 SMG/ULIRGs at z∼2.

4.5 Mass outflows rates and energetic

In the hypothesis that the broadest components are associated to the outflowing wind[3], in the previous chapter we discussed about searching for trends between outflow and AGN properties, in order to understand the link between them. First we compared the FWHM of the [OIII]λ5007 broad components with the total observed [OIII] luminosity and no trend were found, as already pointed out by Harrison et al 2014 and Brusa et al 2014 (to be submitted); and FWHM of the [OIII]λ5007 broad components with bolometric AGN luminosity, again no trends is found, as in the case of Brusa et al 2014, but at odds with the results recently presented by Zakamska & Greene (2014), where a positive correlation between the mid-infrared luminosity and [OIII] widths but in SDSS luminous type 2 quasar was found, suggesting that outflows are ultimately driven by the radiative output of the quasar.

In this chapter, in order to understand if the central engine is the physical mechanism that is driving outflows, we constrained some quantities such as mass and energy being carried by galaxy-wide outflows.

4.5.1 Mass and mass rates of the ionized outflowing gas

Outflows are likely to be entraining gas in multiple phases, i.e ionised, molecular and neutral, thus multiple gas observations are required to fully characterize the outflows properties (Rupke & Veilleux 2013). We analyzed ionised gas, by means of [OIII] emission line, which provides initial information on the total outflows. An important quantity for measuring ionised gas masses is the density of the gas.

We measure this quantity from the emission line ratio [SII]λ6716/λ6731 which is sensitive to electron density (Osterbrock & Ferland 2006). The intensity ratio of these collisionally excited lines is the following:

$$\frac{F_{31}}{F_{21}} = \frac{A_{31} g_3}{A_{21} g_2} \frac{A_{21} + Zx}{A_{31} + Zx} \tag{4.5}$$

where

$$Z = 8.629x10^{-4} \left\{ \frac{\Upsilon_{21}}{g_2} + \frac{\Upsilon_{32}}{g_2} + \frac{\Upsilon_{32}}{g_3} \right\} \tag{4.6}$$

---

[3] We should remember that [OIII]λ5007 is produced through a forbidden transition in low density ambient, any broadening of this emission line is the result of disturbed kinematics in the NLR of AGN, which can be extended over kpc-scales (Pogge 1989) as opposed to the dense, sub-pc sized BLR

and

$$x = 0.01\frac{N_e}{\sqrt{T}} \tag{4.7}$$

The left term of eq 4.5 is the ratio of the 3→1 to the 2→1 transition, F(λ6716)/F(λ6731) in [SII]; A_{31} and A_{21} are the Einstein coefficient of same transitions, g_2 and g_3 are the statistical weights of the second and third energetic level respectively; Υ_{21} and Υ_{32} are the collision strengths of 2→1 and 3→2 transitions; T is the temperature and N_e, the electron density of the gas. We derived the last quantity from the emission line ratio of the broadest components of [SII]$\lambda\lambda$6717,6731, obtained from the fit of XID5435, the highest signal-to-noise target. We measured a ratio of 1.02, that corresponds to electron density n_e of 670 cm^{-3}. The quantities we used to derive the density of the outflowing gas are indicated in Table 4.2.

Table 4.2: Quantities useful to determine density of outflowing gas (Pradhan 1976).

Flux ratio	A_{31}	A_{21}	Υ_{21}	Υ_{32}	Temperature (K)
1.02	2.6 10^{-4}	8.8 10^{-4}	2.16	6.16	10^4

Since this electronic density is representative of this specifit source, we decided to adopte a value of n_e=500 cm^{-3}, which is a mean value of the typical electron densities found in the NLR, i.e n_e=100-1000 cm^{-3} (Rodriguez Zaurin et al. 2013) and which is consistent with the value obtained from the stacked spectrum of those sources with broad components.

In order to calculate the mass of outflowing gas, we followed the model presented in Cano-Diaz et al. 2012 and similar to that previously described in section 1.4.4: the wind occurs in a conical region, with opening angle Ω, where the ionized clouds are distribuited uniformely.

The mass of outflowing ionized gas is given by

$$M_{out}^{ion} = \int_V 1.27 m_H n_e f dV \tag{4.8}$$

where m_H is the mass of hydrogen atom and n_e is the volume density of electrons. Considering that the [OIII]λ5007 line luminosity can be expressed as:

$$L([OIII])) = \int_V \epsilon_{[OIII]} f dV \tag{4.9}$$

where V is the volume occupied by the outflowing ionized gas, f is the filling factor (which gives the fraction of the volume occupied by denser clouds) of the [OIII] emitting clouds in the outflow and $\epsilon_{[OIII]}$ the emissivity of [OIII]λ5007. Assuming that the most of oxygen in the outflow is in O^{+2} form, the emissivity can be expressed as:

$$\epsilon_{[OIII]} = 5 \cdot 10^{-3} h\nu_{[OIII]} 10^{[O/H]} erg\ s^{-1}\ cm^{-3} \tag{4.10}$$

where $10^{[O/H]}$ is the oxygen abundance in solar units.

Combining 4.8, 4.9 and 4.10 it is possible to derive the following expression for mass of ionized outflow:

$$M_{out}^{ion} = 5.33 \cdot 10^7 \frac{CL_{44}([OIII])}{\langle n_{e3} \rangle\, 10^{[O/H]}}\ M_{\odot} \tag{4.11}$$

where L_{44}([OIII]) is the [OIII] luminosity in units of 10^{44} erg s^{-1}, $\langle n_{e3} \rangle$ is the average electron density in units of 10^3 cm^{-3} and C is the condensation factor that is assumed to be equal to 1, assuming that all ionizing gas clouds have the same density.

We computed L[OIII] from the flux of the broad components only, not corrected for extinction, since we have not corrected the fluxes of Hα and Hβ for the stellar absorption. We found an average mass of ionized outflow of 10^5 M$_{\odot}$, which is only a fraction of the total gas content.

The mass outflow rate of the gas is given by

$$\dot{M}_{out}^{ion} = \langle \rho \rangle\, v \Omega R^2 \tag{4.12}$$

where $\langle \rho \rangle = M_{out}^{ion}/V$ is the average mass density over the whole volume occupied by the outflow, $V = \frac{4}{3}\pi R^3 \frac{\Omega}{4\pi}$ Combining eq 4.11 in 4.12 the ionized outflow rate is obtained:

$$\dot{M}_{out}^{ion} = 164 \frac{CL_{44}([OIII]) v_3}{\langle n_{e3} \rangle\, 10^{[O/H]} R_{Kpc}} M_{\odot} yr^{-1} \tag{4.13}$$

where v_3 is the outflow velocity in units of 10^3 km s^{-1}, that in our case corresponds to the velocities derived by means of non-parametric definitions. We associated the 2nd percentiles or 98th percentiles of the flux contained in the emission line profiles, with the maximum projected velocities of the outflows, according to the velocity shift of the broad kinematic component with respect to the narrow one, positive or negative.

R$_{\text{Kpc}}$ is the radius of outflowing region in units of Kpc. We do not have spatial information thus we used a typical value of 5 Kpc, assuming that the outflow is galaxy-wide extended. Assuming a solar metallicity, we found an average value of 2 10^{-1} M$_{\odot}$ yr^{-1}.

This is a lower limit of the total outflow rate, since the ionized gas is probably accompaneid by a neutral/molecular outflow. (Rupke& Veilleux 2013) The total outflow rate can be up to an order of magnitude higher, as observed in the QSO Mrk231 in the local Universe (Feruglio et al 2010)

4.5.2 Kinetic power associated to the ionized outflowing gas

After finding the mass of the ionized gas involved we derived its kinetic power, as follows:

$$P_K^{ion} = 5.17 \cdot 10^{43} \frac{C L_{44}([OIII]) v_3^3}{\langle n_{e3} \rangle \, 10^{[O/H]} R_{Kpc}} erg \ s^{-1} \tag{4.14}$$

where L$_{44}$([OIII]),v_3, $\langle n_{e3} \rangle$, R_{Kpc} were described above. The results are indicated in Table 4.3. Since we obtained the kinetic power of outflowing ionized gas, we should consider these value as a lower limit of the total outflow kinetic power, which can be one order of magnitude higher.

It is possible to estimate a total outflow kinetic power by assuming an energy-conserving bubble inflated by energy injected at a constant rate and expanding into a uniform medium with ambient density n_0 (cm^{-3}), firstly proposed by Heckman et al (1990) and put forward again by Harrison et al 2014. In this case the kinetic power can be given by:

$$\dot{E}_K^{out} = 3 \cdot 10^{44} R_{Kpc}^2 v_3^3 n_{0.5} erg \ s^{-1} \tag{4.15}$$

where R_{Kpc} has the same meaning as in eq 4.13, $n_{0.5}$ is n_0 in units of 0.5 cm^{-3}. Heckman et al. 1990 estimated this quantity by means of shock models, relating the density measured in the post-shock [SII] zone to the preshock density. Considering that our flux ratio of $R_{[SII]} = \frac{F_{\lambda 6716}}{F_{\lambda 6731}}$ is consistent to that found by Nesvadba et al. 2008, we used $n_{0.5} = 1$ as in Nesvadba et al. 2008. Following Harrison et al 2014 for v_3 we used the value of W_{80}, the velocity width of the line that contains 80 % of the emission line flux.

Since this model assumes a spherical outflow (covering factor=1) the values obtained can be considered as an upper limit of kinetic energy rate. The fiducial values we used are the means in log space of these two quantities we derived above. These values suffer from large uncertainties thus they are representative values of the order of magnitude of the expected total outflow power associated with the broad components measured in our sample. The values obtained using these two models and the mean values are listed in Table 4.3.

Table 4.3: Outflow kinetic power of the ionized gas derived from Eq. 4.14, Eq. 4.15 and the mean of the two values

XID	$log P_K^{ion}$	$log \dot{E}_K^{out}$	$log \dot{E}$
2021	38.65	44.38	41.51
2218	40.26	45.88	43.07
2195	40.30	45.05	42.68
293	41.38	45.74	43.57
2681	39.48	44.58	42.03
5002	40.76	45.05	42.9

To understand if the central AGN is able to sustain the outflows or not, we compared the mean value of the outflow kinetic power, defined above, with the bolometric AGN luminosity as derived in Section 2.6 . The inferred $\dot{E}$ are in the range of 0.3-30% of the AGN bolometric luminosity. This result is consistent with AGN-driven models (King et al. 2012). The comparison is represented in fig 4.4.

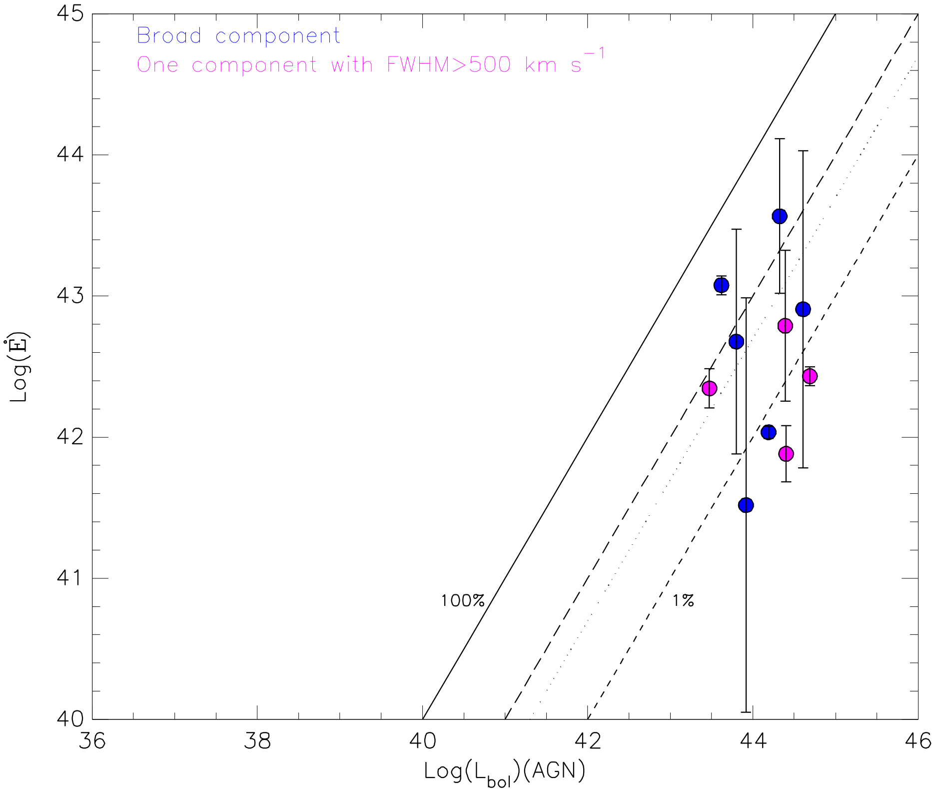

Figure 4.4: The mean value of kinetic power associated to outflows versus bolometric AGN luminosity. The blue circles represent the sources with [OIII]λ5007 broad component. Sources with only one significative component of [OIII]λ5007 emission-line profile with FWHM>500 Km/s (magenta circle) were plotted. The solid, the long-dashed, dotted and short- dashed lines represent the 100 %, 10 %, 5% and 1% ratios, respectively.

We also checked if the inferred kinetic power can be sustained by star formation processes. Stellar winds and Supernovae (SNe) can drive starburst winds by means of their mechanical energy and momentum. The energy returned from starbursts was estimated by many models (Leitherer & Heckman 1995, Leitherer et al. 1999), in particular to determine the observable properties of the starbursting population, a combination of stellar evolution models, empirical spectral libraries and atmospheric models are used. The mechanical luminosities is calculated using different starburst histories and various metallicities, varying the shape and mass limits of the stellar initial mass function (IMF). Considering a solar-metallicity and a Salpeter IMF, the mechanical luminosity released by winds and SNe are constant beyond ∼40 Myr and dipends on SFR as follows (Veilleux et al. 2005):

$$\dot{E}(SF) \sim 7 \cdot 10^{41}(SFR/M_{\odot}yr^{-1}) \tag{4.16}$$

The kinetic energy associated to stellar winds has been computed from the SFR of our targets, derived from SED fitting and listed in Table 2.5. The comparison between the mean value of kinetic power associated to the outflow and the predicted kinetic output from SF is shown in figure 4.5. As we can see, five out of ten lie above the 100% line, thus for these sources the kinetic outflow expected from stellar wind and SN may be not enough to drive the observed outflows.

Furthermore in starburst galaxies without an AGN at the center, velocities larger than 500-600 km s^{-1} are not expected (e.g. Murray et al. 2005; Ceverino & Klypin 2009; Lagos et al. 2013) and feedback models are unable to reproduce high velocities observed in the winds. In our cases three sources have v>900 km s^{-1}, suggesting that an AGN origin for the outflows is favoured.

The energetic comparison is based on lower and upper limits, in order to keep into account the total content of outflows and not just the ionized one, instead keeping into account the outflows velocity argument, the AGN rather than the on-going star-formation may be the major driver for the presence of the observed broad components for three sources (XID293, XID2218, XID2195).

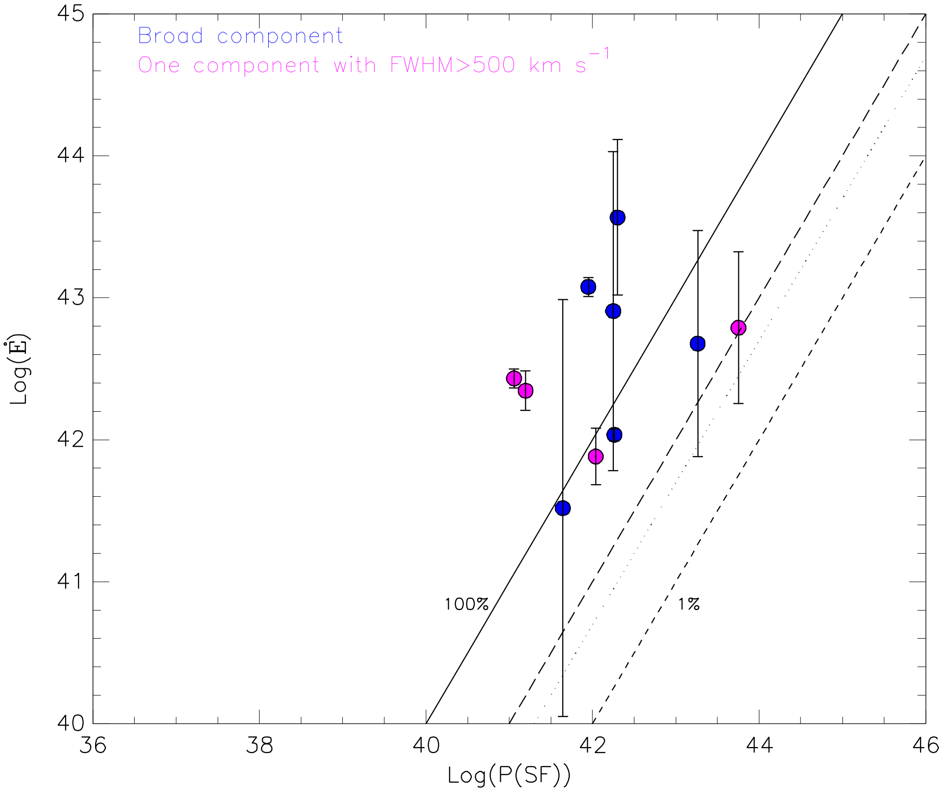

Figure 4.5: The mean value of kinetic power associated to outflows versus the predicted kinetic output from SF. The blue circles represent the sources with [OIII]λ5007 broad component. Sources with only one significative component of [OIII]λ5007 emission-line profile with FWHM>500 km/s (magenta circle) were plotted. The solid, the long-dashed, dotted and short- dashed lines represent the 100 %, 10 %, 5% and 1% ratios, respectively.

Chapter 5

Summary and perspectives

The most successful models of galaxy evolution invoke interactions between accreting SMBHs and their host galaxies in order to reproduce the most fundamental properties of today's galaxy population (Di Matteo et al. 2005, Vogelsberger 2014). These models assume that part of the energy released by the AGN drives gas and dust from the central regions of a galaxy, affecting the final mass of the host galaxy. In fact the winds originated in such events can sweep out the gas in galaxy, quench star formation and terminate its own activity, when no fuel is then more available. Observational evidences are needed to prove what models suggest. Large-scale outflows in luminous QSO at both low and high redshift have been detected with several methods (e.g. mm and FIR spectroscopy) using the kinematics of the [OIII]λ5007 emission line, which is a good tracer of the kinematics of the ionised gas in the NLR, since as a forbidden transition this emission line can not be produced in the high-density sub-parsec scales of the BLR.

In this thesis work we presented the analysis of 25 obscured X-ray selected AGN in the COSMOS field with z<0.8 and with bolometric luminosities of $L_{bol} = 10^{42-45} erg\ s^{-1}$, for which [OIII]$\lambda$5007 emission line is visible in SDSS spectra. The resolution of SDSS spectra allowed us to obtain interesting results about the characterization of outflows in our targets.

We modelled the spectra of all the sample using two kinds of models for fitting Hβ, [OIII]λ,λ4959,5007, Hα,[NII]$\lambda\lambda$6548,6581 and [SII]$\lambda\lambda$6716,6731. Choosing between the two models for each target we were able to construct the BPT diagram for 12 sources, in order to investigate the location of sources in the diagram (see figure 4.1). 8 sources lie in the NL AGN region and 4 in the composite AGN/SF one. For two sources we were able to build the BPT for the narrow and broad component separately, where for one of these the narrow component lies in the composite region and the broad in the NL AGN region. We can not derive physical constraints for the poor statistics and since we do not have spatial information but, as Rodriguez-Zaurin et al. (2013) emphasize, a different behaviour may exist between the two components, suggesting a different dominant mechanism of ionization.

The spectral analysis made by means of IRAF task SPECFIT returned the FWHM of the emission lines included in the models. We compared the FWHM of the broadest components of [OIII]λ5007 line with the total observed [OIII]λ5007 luminosity, which is often considered to be an indicator of the average AGN power. We compared our results with those found in literature on Type 2 QSOs and Seyferts (figure 4.2). We found that our results are consistent with those derived in other samples despite our lower luminosities.

A direct link between the outflows and the central engine is obtained comparing the broad FWHM with the intrinsic bolometric AGN luminosity (figure 4.3), but no clear trend is found. Our results can be seen as an extension at low luminosity of the most update results at large luminosities, thanks to accurate estimates of bolometric luminosities listed in Table 2.5 and derived with SED fitting, as mentioned in section 2.7.

In order to characterize the velocities and the widths of the [OIII] emission line profile we used non parametric definitions, following Harrison et al (2014). In particular we used the 2nd or 98th percentiles, according to the shift of the broad component respect to the narrow one, as the maximum proiected velocity of the gas. We proceeded to characterize the kinematics of the outflow, finding the mass of the ionized gas involved and its kinetic power. We determined a lower and upper limit of the kinetic power, in a similar way used by Cano-Diaz et al. (2012) for the former, and associated to the ionized gas, and Heckman et al (1990) for the latter, that estimated the total outflow kinetic power, assuming a model based on an expanding bubble in a uniform medium.

In order to understand if the central engine is the physical mechanism that is driving outflows, we compared the mean value of the upper and lower limits with the bolometric AGN luminosity. The inferred $\dot{E}$ are in the range of 0.3-30% of the AGN bolometric luminosity (Figure 4.4). This result is consistent with AGN-driven models (King et al. 2012). We also compared the mean value of kinetic power associated to the ouflow with the predicted kinetic output from SF, following Veilleux et al. 2005, finding that five sources lie above the 100% line (i.e. one to one correlation) suggesting that SN may be not enough to drive the observed outflows (Figure 4.5).

We therefore conclude that central nucleus is the most likely origin of the observed emission in outflowing winds.

But it is necessary to improve the adopted method to assess the effect of AGN feedback. This can be achieved with follow-up observations, spatially resolved spectroscopy, with the analysis of a larger number of sources, in order to improve the statistical significance of results or by menas of IR spectroscopy, in order to analyzed sources at high redshift since[OIII] emission line is shifted to NIR band.

An example of what is found using integral field spectroscopy is that of Davies et al. (2014). They analyzed a know starburst-AGN composite galaxy NGC7130. Using diagnostic diagrams they found a smooth distribution, i.e. a mixing sequence, of points from the star-forming to the AGN region. This traces variations in AGN fraction from HII regions outside of the AGN NLR to the AGN in the centre of the galaxy (Kewley et al.2013). As it is shown in the fig. 5.1 the mixing sequence is separated into spaxels classified as HII regions (black), composite (red) and AGN-dominated (blue and green).

The spaxels colored blue occupy the nuclear region of the galaxy, consistent with emission due to pure AGN as well as photoionisation by a galactic wind. The spaxels colored green form a ring around the nuclear region of the galaxy, consistent with emission dominated by AGN photoionisation with some contribution from star formation. The red spaxels form the same ring but star-formation and AGN activity are both energetically significant. The black spaxels are in the region beyond the AGN ENLR.

This example suggests how spatially resolved spectra can improve the results, providing additional information. Furthermore this can be extended to higher redshift thanks to MUSE and KMOS/SINFONI.

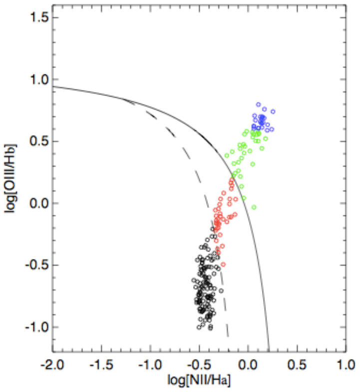

Figure 5.1: Diagnostic diagrams showing the variation in ionisation state of the gas in NGC 7130. The solid lines in the diagrams trace the theoretical upper bound to pure star-formation (Kewley et al. 2001), the dashed line indicates the empirical upper bound to pure star-formation (Kauffmann et al. 2003). The smooth distribution of points from the pure star-forming region to the AGN region on the diagnostics is indicative of starburst-AGN mixing.

In order to estimate the true energetics associated to the outflows, slit resolved spectroscopy may be critical in that sense, furthermore a crucial role may have in mapping the spatial distribution of the SFR, as traced by the narrow component of Hα. For example Cano-Diaz et al (2012) investigated the suppression of star formation in luminous quasar 2QZJ002830.4-281706 at z=2.4. What they found is one of the first direct observational evidence of star formation suppression by quasar feedback at high z. They revealed a powerful outflow by the velocity field traced by the [OIII]λ5007 line, estimated an outflow rate of ionized gas of 200 $M_\odot$ yr^{-1}, which is a lower limit of the total gas outflow rate, since the ionized component is accompaneid by a neutral/molecular outflow. The map of the narrow component of Hα suggests that the SF is not distribuited uniformly, it is mostly found in the regions not directly invested by the outflow and heavily suppressed in the region where the strongest outflow is detected (Figure 5.2).

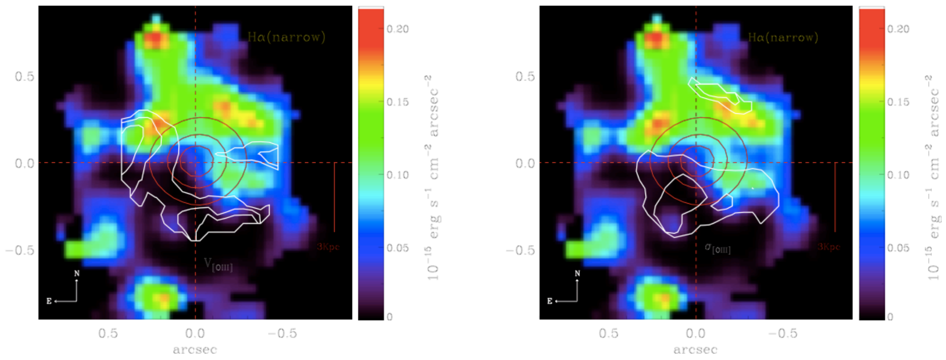

Figure 5.2: Map of the narrow component of Hα. *(left)* The white contours identify the strongest gas outflow traced by the highly blueshifted [OIII] line *(right)* The white contours identify the highest velocity dispersion region, which is likely the region where the strong outflow interacts with the host galaxy disk.

Appendices

Appendix A

Atlas of XMM-SDSS spectra

Table A.1: Objects classification

1	BL AGN (broad line AGN)
2	NL AGN (narrow line AGN)
3	Galaxies

`http://dr10.sdss3.org/spectrumDetail?mjd=52235&fiber=338&plateid=501`

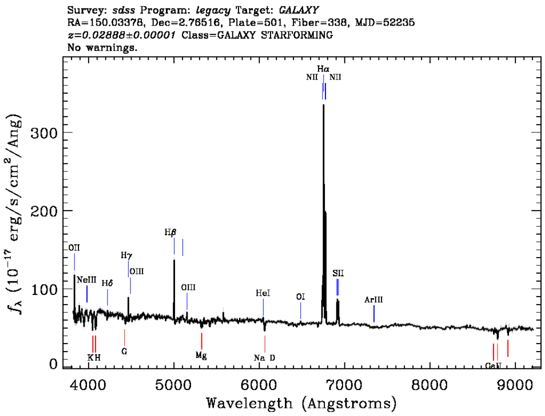

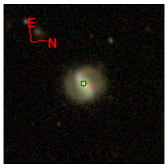

A.1

Xid	$zfinal$	$class$	$LogL_x$
5352	0.029	3	39.99

`http://dr10.sdss3.org/spectrumDetail?mjd=52235&fiber=318&plateid=501`

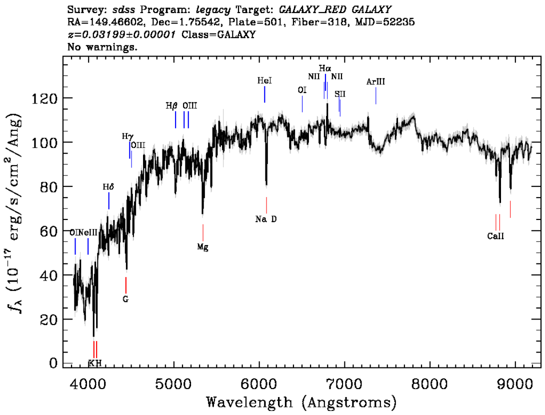

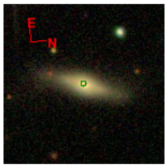

A.1

Xid	$zfinal$	$class$	$LogL_x$
60443	0.032	3	39.93

`http://dr10.sdss3.org/spectrumDetail?mjd=51994&fiber=577&plateid=500`[H]

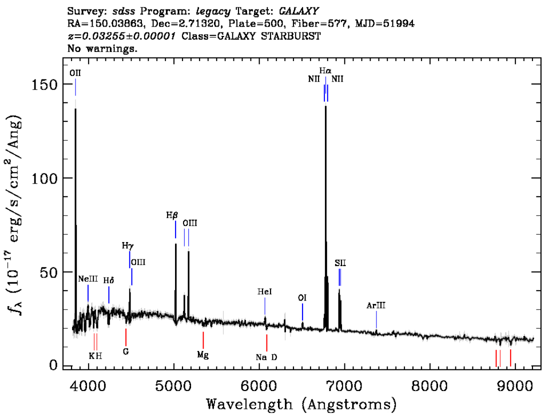

A.1

Xid	$zfinal$	$class$	$LogL_x$
54132	0.033	3	39.62

`http://dr10.sdss3.org/spectrumDetail?mjd=51994&fiber=597&plateid=500`

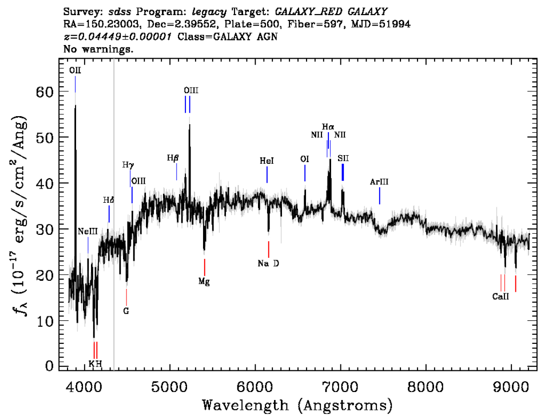

A.1

Xid	$zfinal$	$class$	$LogL_x$
140	0.045	2	40.83

`http://dr10.sdss3.org/spectrumDetail?mjd=52289&fiber=218&plateid=572`

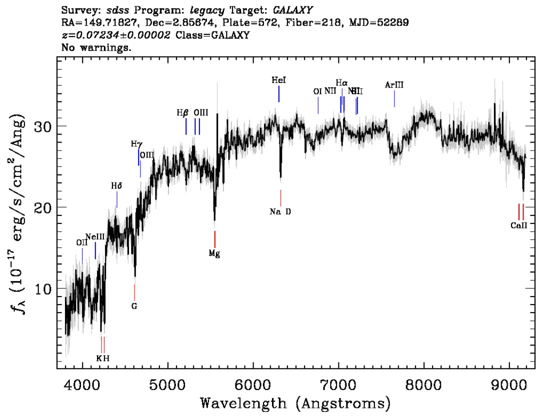

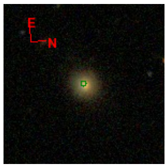

A.1

Xid	$zfinal$	$class$	$LogL_x$
5164	0.072	3	41.19

`http://dr10.sdss3.org/spectrumDetail?mjd=51994&fiber=538&plateid=500`

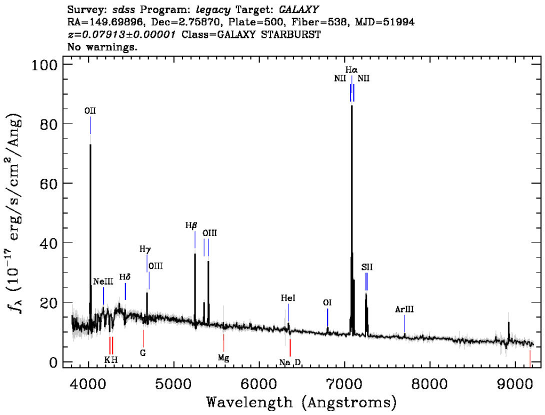

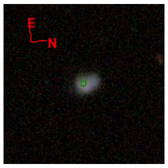

A.1

Xid	$zfinal$	$class$	$LogL_x$
5089	0.079	3	40.42

`http://dr10.sdss3.org/spectrumDetail?mjd=51994&fiber=536&plateid=500`

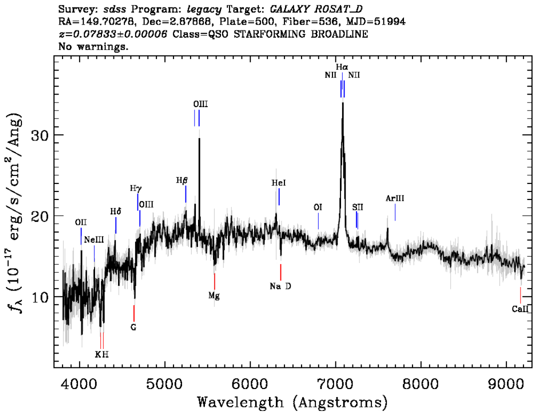

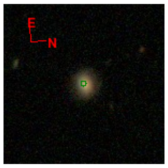

A.1

Xid	$zfinal$	$class$	$LogL_x$
5435	0.079	2	41.42

`http://dr10.sdss3.org/spectrumDetail?mjd=52235&fiber=345&plateid=501`

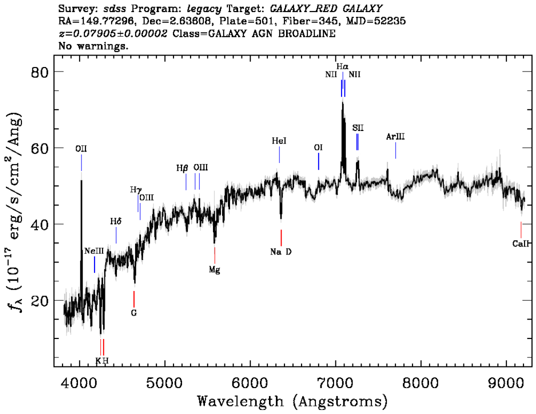

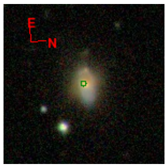

A.1

Xid	$zfinal$	$class$	$LogL_x$
5284	0.079	2	40.88

`http://dr10.sdss3.org/spectrumDetail?mjd=52235&fiber=280&plateid=501`

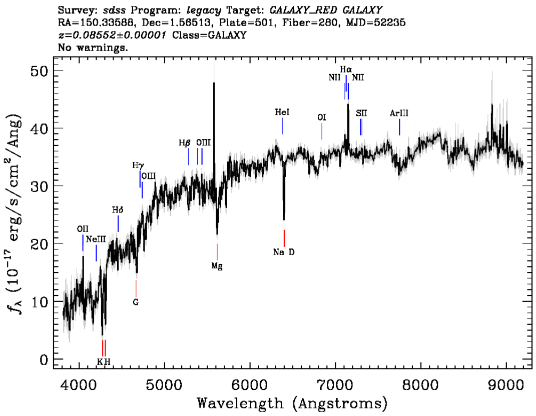

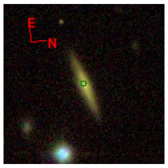

A.1

Xid	$zfinal$	$class$	$LogL_x$
53730	0.086	3	41.21

`http://dr10.sdss3.org/spectrumDetail?mjd=51994&fiber=520&plateid=500`

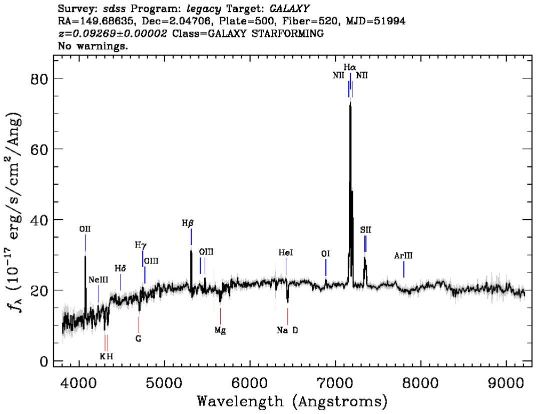

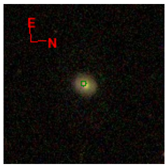

A.1

Xid	$zfinal$	$class$	$LogL_x$
5570	0.093	3	41.25

`http://dr10.sdss3.org/spectrumDetail?mjd=52235&fiber=226&plateid=501`

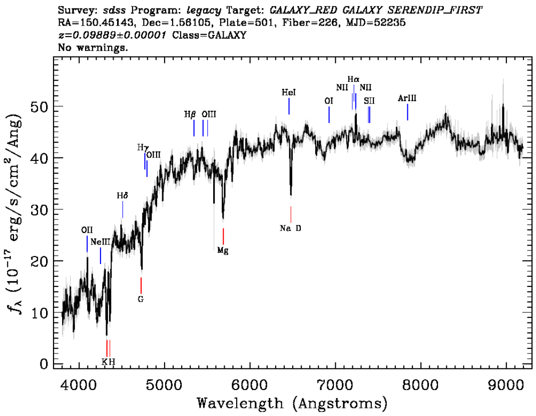

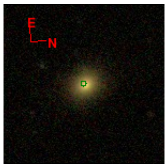

A.1

Xid	$zfinal$	$class$	$LogL_x$
53738	0.099	3	40.79

`http://dr10.sdss3.org/spectrumDetail?mjd=51994&fiber=170&plateid=500`

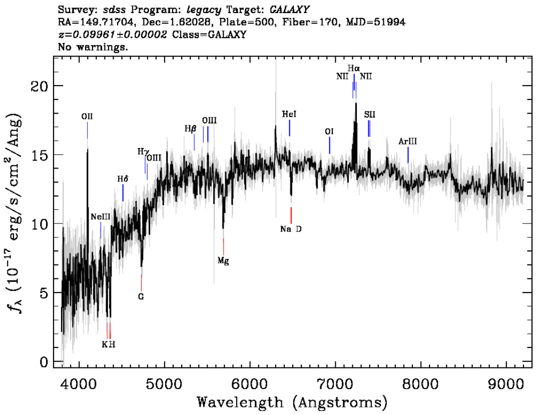

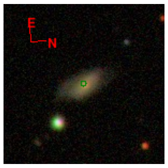

A.1

Xid	$zfinal$	$class$	$LogL_x$
60425	0.1	3	41.44

`http://dr10.sdss3.org/spectrumDetail?mjd=51994&fiber=604&plateid=500`

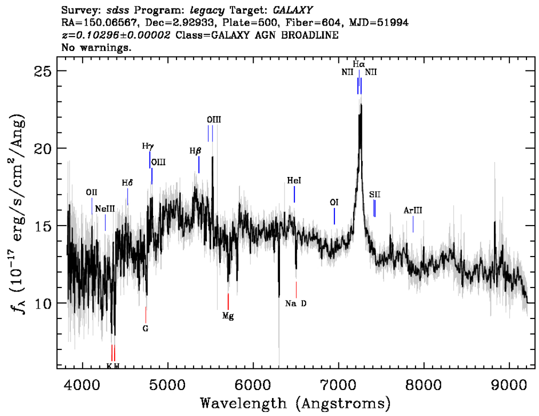

A.1

Xid	$zfinal$	$class$	$LogL_x$
5617	0.103	1	42.08

`http://dr10.sdss3.org/spectrumDetail?mjd=52235&fiber=372&plateid=501`

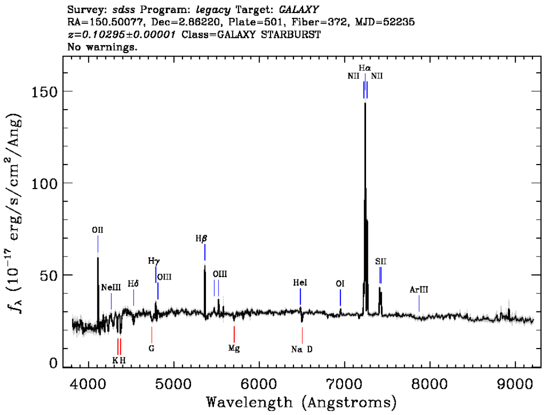

A.1

Xid	$zfinal$	$class$	$LogL_x$
60095	0.103	3	41.72

http://dr10.sdss3.org/spectrumDetail?mjd=51994&fiber=68&plateid=500

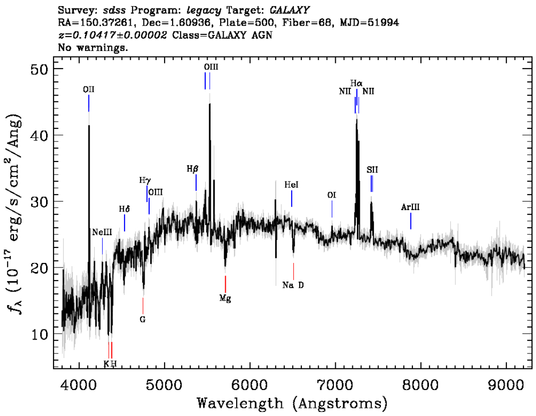

A.1

Xid	$zfinal$	$class$	$LogL_x$
2021	0.104	2	42,91

http://dr10.sdss3.org/spectrumDetail?mjd=52235&fiber=383&plateid=501

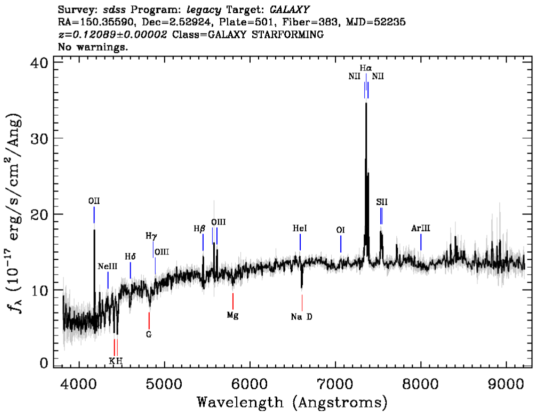

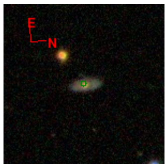

A.1

Xid	$zfinal$	$class$	$LogL_x$
60104	0.121	3	41.86

http://dr10.sdss3.org/spectrumDetail?mjd=52235&fiber=381&plateid=501

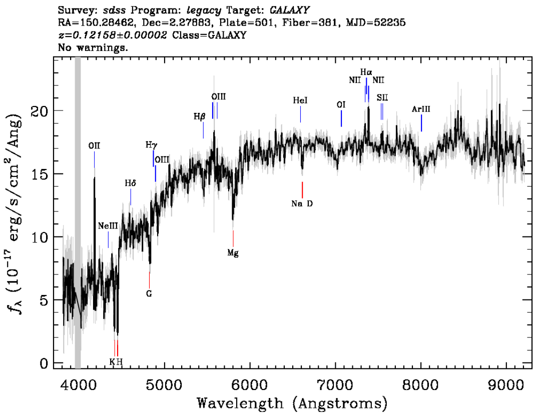

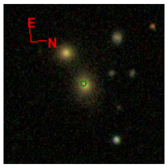

A.1

Xid	$zfinal$	$class$	$LogL_x$
60011	0.122	3	41.79

http://dr10.sdss3.org/spectrumDetail?mjd=52235&fiber=467&plateid=501

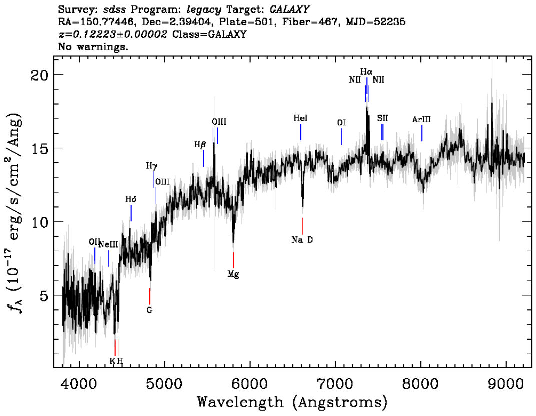

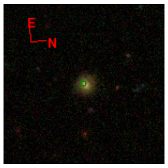

A.1

Xid	$zfinal$	$class$	$LogL_x$
60085	0.122	3	41.35

`http://dr10.sdss3.org/spectrumDetail?mjd=52235&fiber=439&plateid=501`

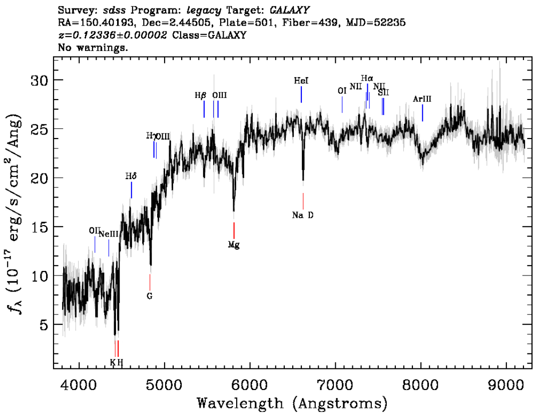

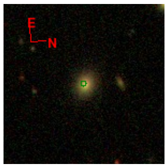

A.1

Xid	*zfinal*	*class*	*LogL$_x$*
550	0.123	3	41.84

`http://dr10.sdss3.org/spectrumDetail?mjd=51994&fiber=587&plateid=500`

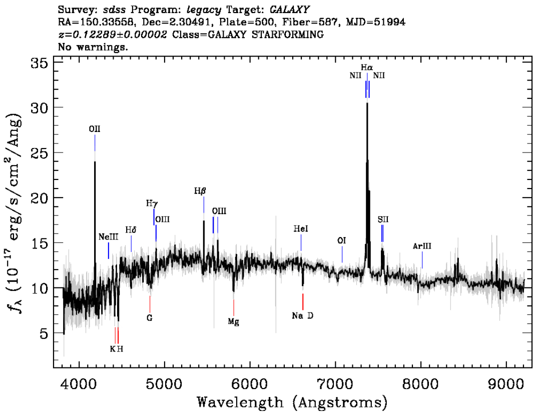

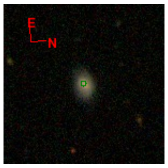

A.1

Xid	*zfinal*	*class*	*LogL$_x$*
1533	0123	3	41.08

`http://dr10.sdss3.org/spectrumDetail?mjd=52235&fiber=325&plateid=501`

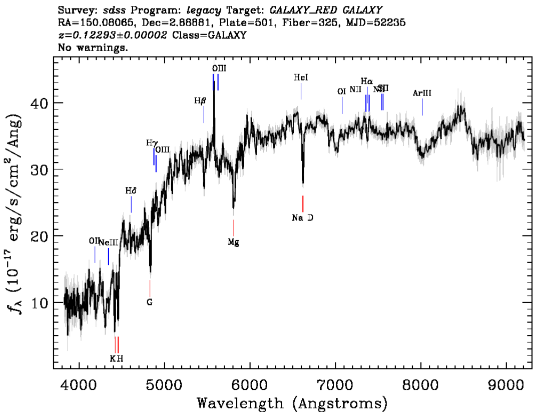

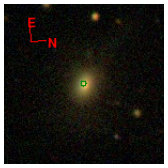

A.1

Xid	*zfinal*	*class*	*LogL$_x$*
5614	0.123	3	41.46

`http://dr10.sdss3.org/spectrumDetail?mjd=52235&fiber=342&plateid=501`

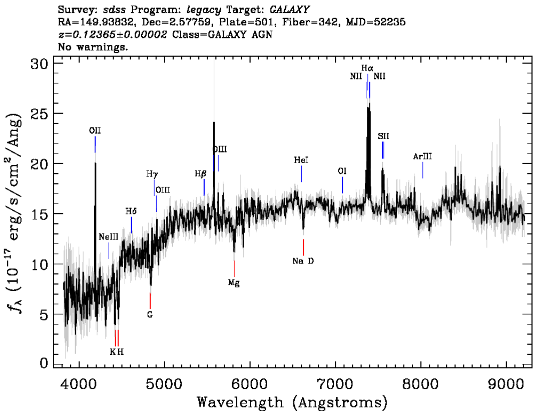

A.1

Xid	*zfinal*	*class*	*LogL$_x$*
54517	0.124	2	41.6

http://dr10.sdss3.org/spectrumDetail?mjd=51994&fiber=625&plateid=500

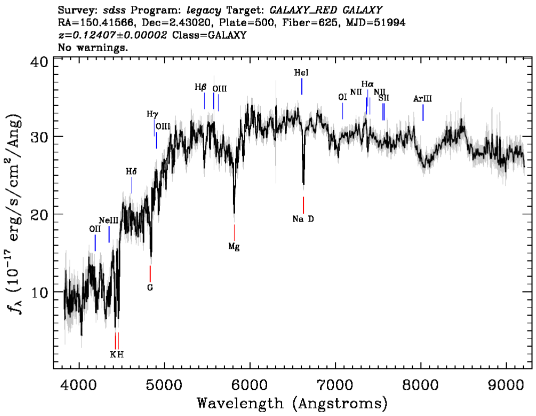

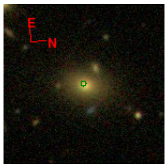

A.1

Xid	$zfinal$	$class$	$LogL_x$
73	0.124	2	42.09

http://dr10.sdss3.org/spectrumDetail?mjd=52235&fiber=231&plateid=501

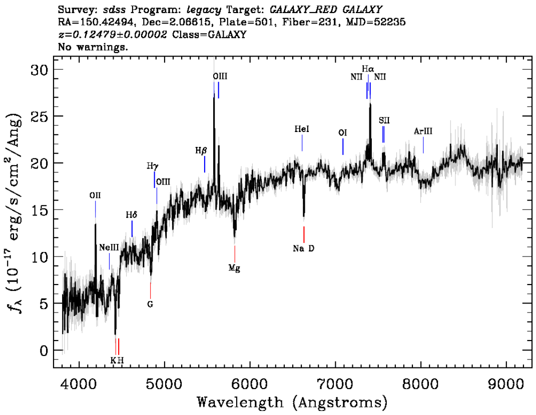

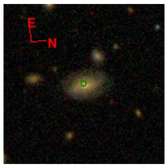

A.1

Xid	$zfinal$	$class$	$LogL_x$
2608	0.125	2	42.37

http://dr10.sdss3.org/spectrumDetail?mjd=52235&fiber=341&plateid=501

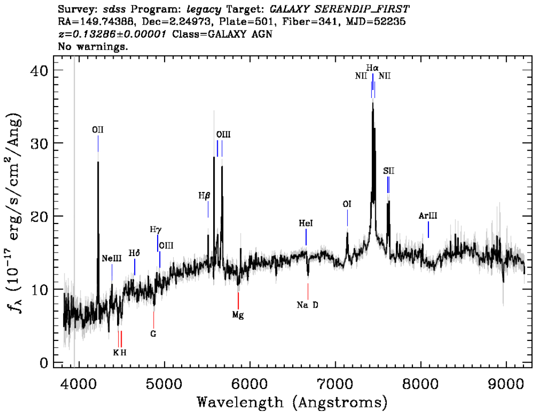

A.1

Xid	$zfinal$	$class$	$LogL_x$
4	0.132	1	42.56

http://dr10.sdss3.org/spectrumDetail?mjd=52235&fiber=335&plateid=501

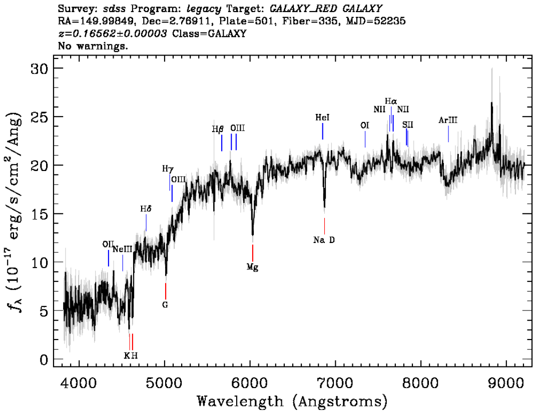

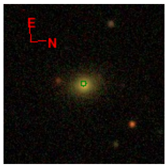

A.1

Xid	$zfinal$	$class$	$LogL_x$
5595	0.166	3	41.73

`http://dr10.sdss3.org/spectrumDetail?mjd=55630&fiber=193&plateid=4737`

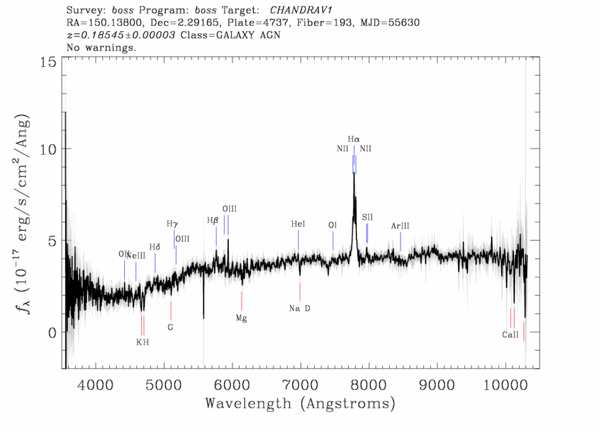

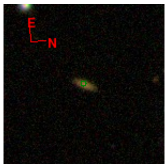

A.1

Xid	$zfinal$	$class$	$LogL_x$
157	0.1854	2	42.86

`http://dr10.sdss3.org/spectrumDetail?mjd=55630&fiber=191&plateid=4737`

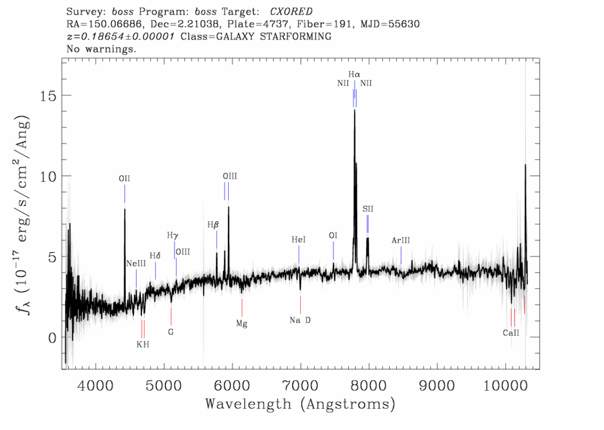

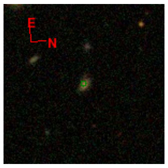

A.1

Xid	$zfinal$	$class$	$LogL_x$
255	0.1865	3	42.03

`http://dr10.sdss3.org/spectrumDetail?mjd=55630&fiber=927&plateid=4737`

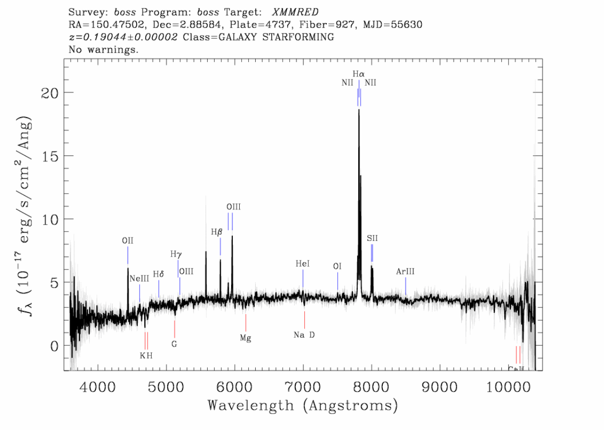

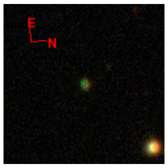

A.1

Xid	$zfinal$	$class$	$LogL_x$
5328	0.1904	3	42.04

`http://dr10.sdss3.org/spectrumDetail?mjd=55630&fiber=90&plateid=4737`

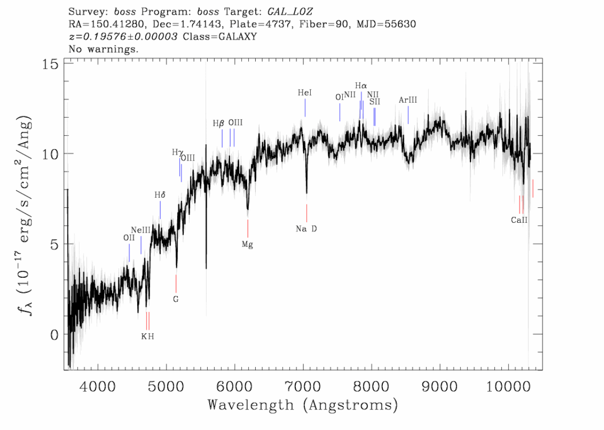

A.1

Xid	$zfinal$	$class$	$LogL_x$
53742	0.1958	3	41.66

`http://dr10.sdss3.org/spectrumDetail?mjd=52235&fiber=412&plateid=501`

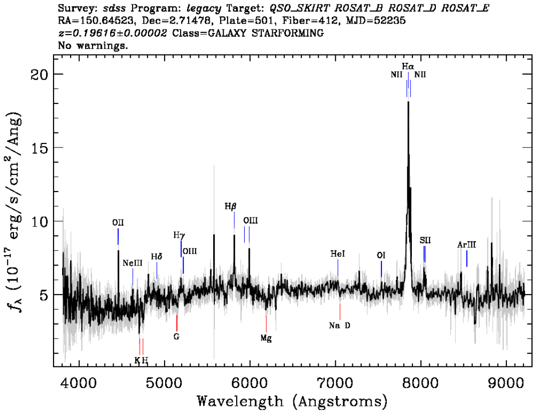

A.1

Xid	$zfinal$	$class$	$LogL_x$
5121	0.196	1	42.42

`http://dr10.sdss3.org/spectrumDetail?mjd=55630&fiber=70&plateid=4737`

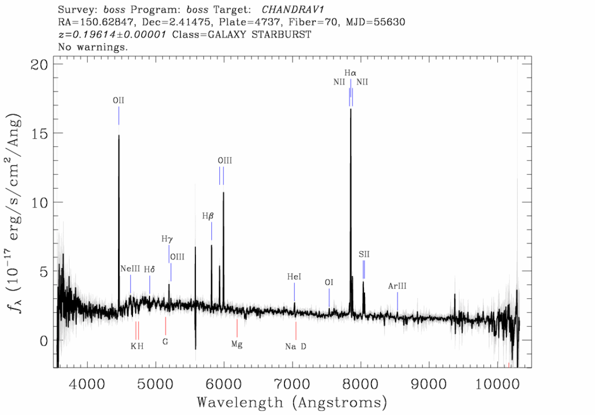

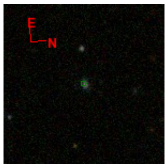

A.1

Xid	$zfinal$	$class$	$LogL_x$
5028	0.1961	3	41.67

`http://dr10.sdss3.org/spectrumDetail?mjd=55630&fiber=967&plateid=4737`

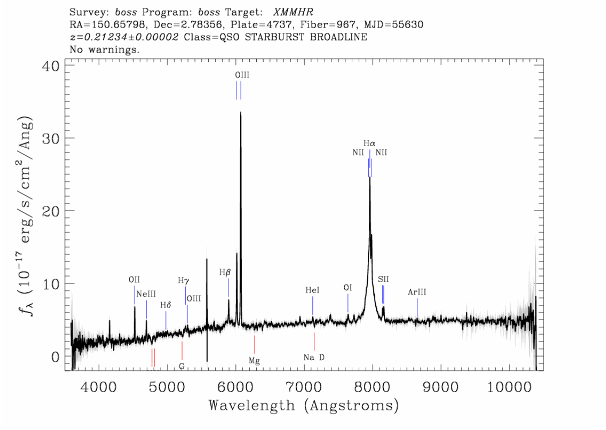

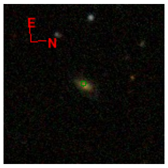

A.1

Xid	$zfinal$	$class$	$LogL_x$
5114	0.2123	1	43.11

`http://dr10.sdss3.org/spectrumDetail?mjd=52235&fiber=414&plateid=501`

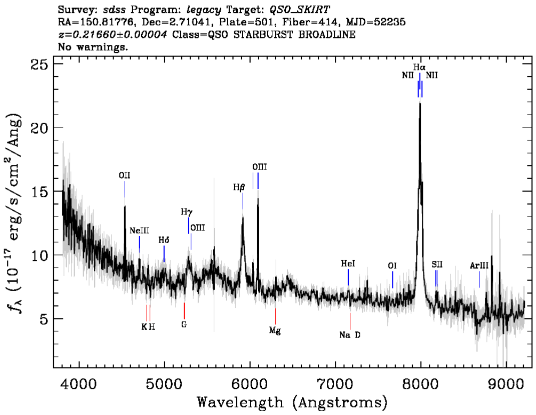

A.1

Xid	$zfinal$	$class$	$LogL_x$
5248	0.217	1	42.41

`http://dr10.sdss3.org/spectrumDetail?mjd=51994&fiber=21&plateid=500`

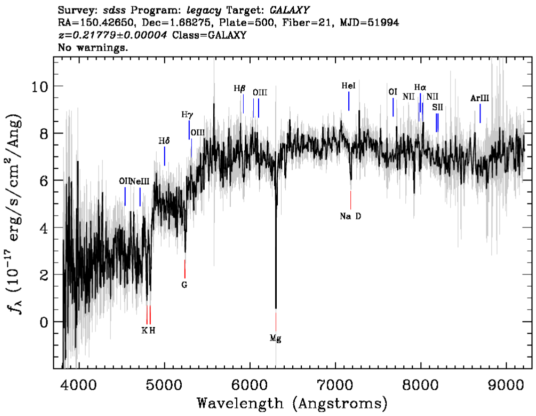
Survey: *sdss* Program: *legacy* Target: *GALAXY*
RA=150.42650, Dec=1.68275, Plate=500, Fiber=21, MJD=51994
z=0.21779±0.00004 Class=GALAXY
No warnings.

A.1

Xid	*zfinal*	*class*	$LogL_x$
2576	0.218	3	42.31

`http://dr10.sdss3.org/spectrumDetail?mjd=55630&fiber=804&plateid=4737`

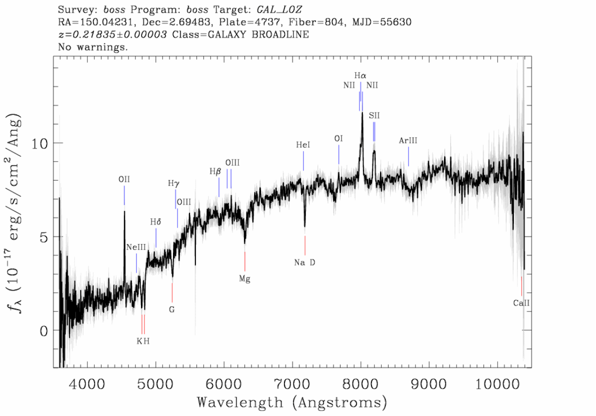
Survey: *boss* Program: *boss* Target: *CAL_LOZ*
RA=150.04231, Dec=2.69483, Plate=4737, Fiber=804, MJD=55630
z=0.21835±0.00003 Class=GALAXY BROADLINE
No warnings.

A.1

Xid	*zfinal*	*class*	$LogL_x$
5075	0.2184	2	41.94

`http://dr10.sdss3.org/spectrumDetail?mjd=55630&fiber=136&plateid=4737`

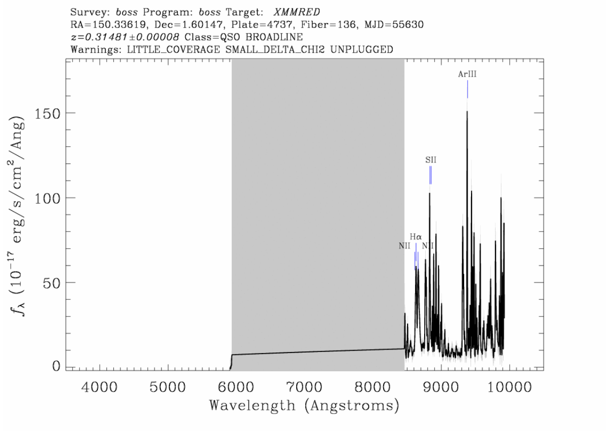

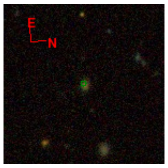

A.1

Xid	$zfinal$	$class$	$LogL_x$
2186	0.234	30	41.85

`http://dr10.sdss3.org/spectrumDetail?mjd=55630&fiber=95&plateid=4737`

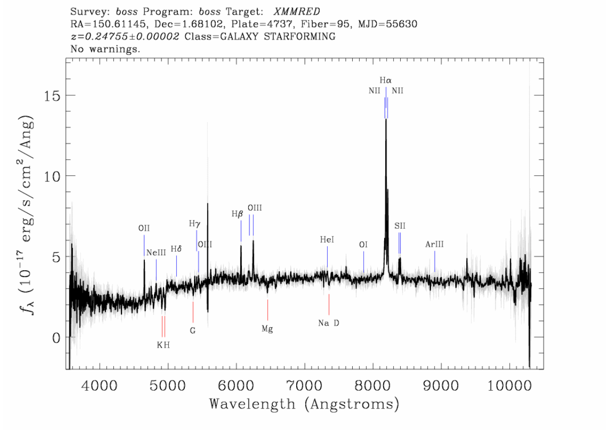

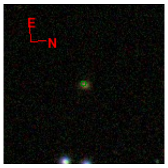

A.1

Xid	$zfinal$	$class$	$LogL_x$
2218	0.2475	2	42.63

`http://dr10.sdss3.org/spectrumDetail?mjd=51994&fiber=578&plateid=500`

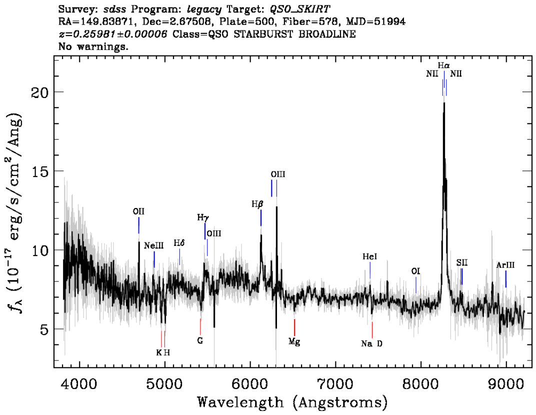

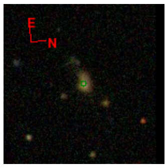

A.1

Xid	$zfinal$	$class$	$LogL_x$
5112	0.26	2	43.21

`http://dr10.sdss3.org/spectrumDetail?mjd=55630&fiber=253&plateid=4737`

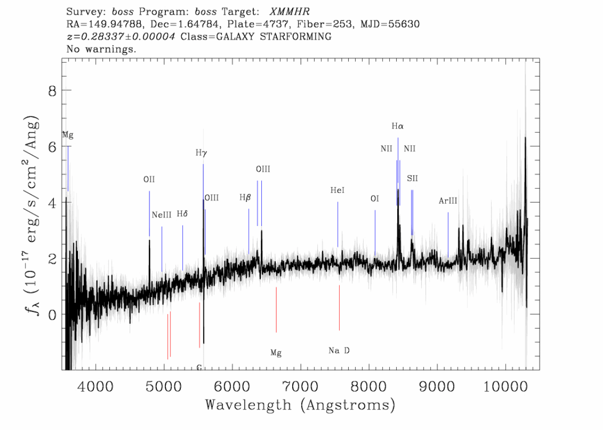

A.1

Xid	$zfinal$	$class$	$LogL_x$
5443	0.2834	2	43.32

`http://dr10.sdss3.org/spectrumDetail?mjd=55630&fiber=700&plateid=4737`

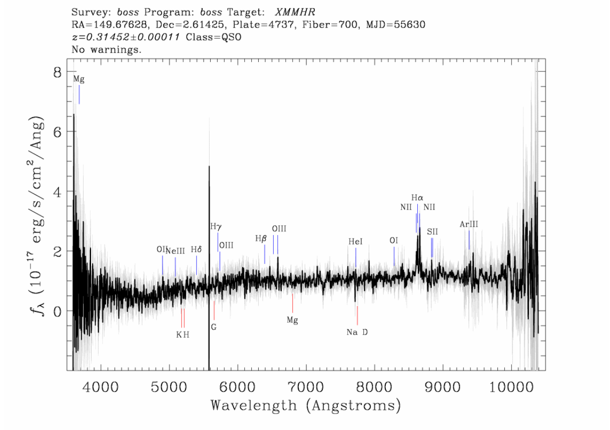

A.1

Xid	$zfinal$	$class$	$LogL_x$
5537	0.3145	2	42.43

`http://dr10.sdss3.org/spectrumDetail?mjd=55630&fiber=885&plateid=4737`

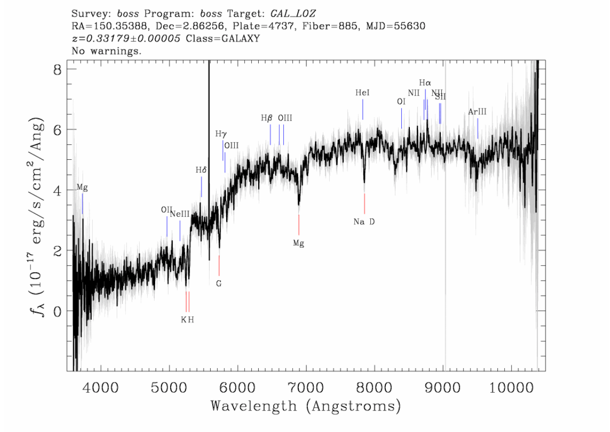

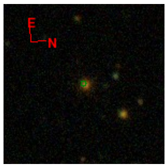

A.1

Xid	$zfinal$	$class$	$LogL_x$
10112	0.3318	3	42.85

`http://dr10.sdss3.org/spectrumDetail?mjd=55630&fiber=275&plateid=4737`

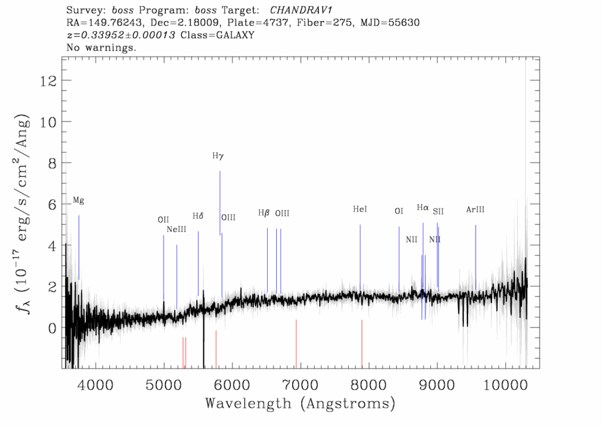

A.1

Xid	$zfinal$	$class$	$LogL_x$
5612	0.3395	3	41.94

`http://dr10.sdss3.org/spectrumDetail?mjd=55630&fiber=304&plateid=4737`

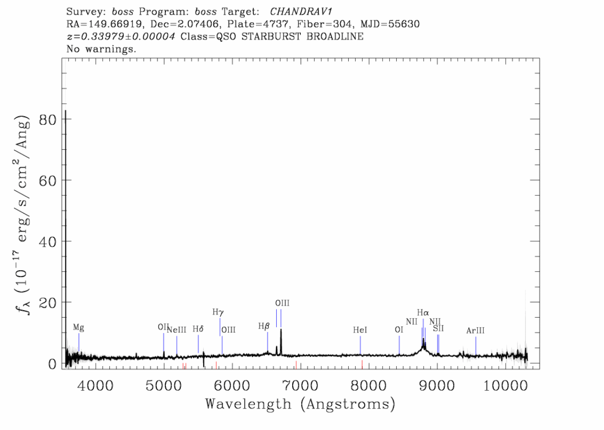

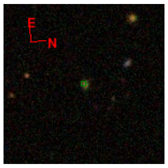

A.1

Xid	$zfinal$	$class$	$LogL_x$
417	0.3398	1	43.29

`http://dr10.sdss3.org/spectrumDetail?mjd=52235&fiber=360&plateid=501`

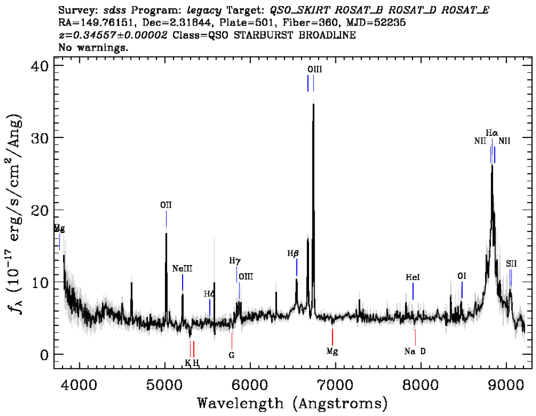

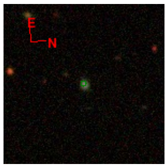

A.1

Xid	$zfinal$	$class$	$LogL_x$
3	0.345	1	44.23

`http://dr10.sdss3.org/spectrumDetail?mjd=51994&fiber=488&plateid=500`

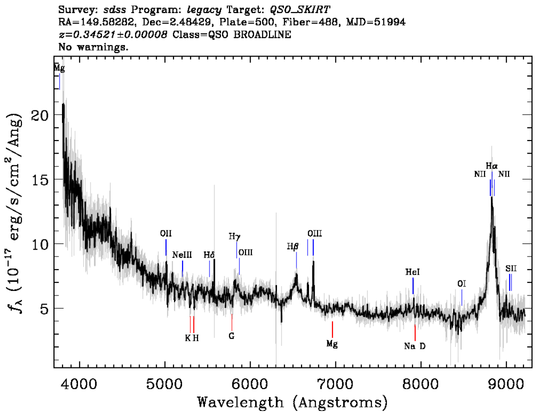

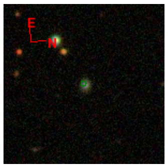

A.1

Xid	$zfinal$	$class$	$LogL_x$
2016	0.345	1	43.43

`http://dr10.sdss3.org/spectrumDetail?mjd=51994&fiber=527&plateid=500`

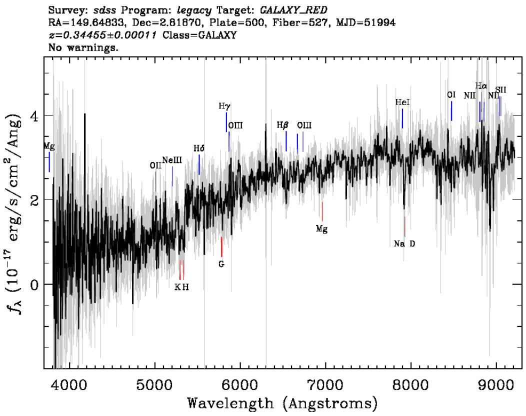

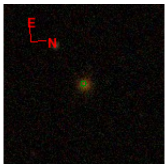

A.1

Xid	$zfinal$	$class$	$LogL_x$
5181	0.345	3	41.23

`http://dr10.sdss3.org/spectrumDetail?mjd=55630&fiber=940&plateid=4737`

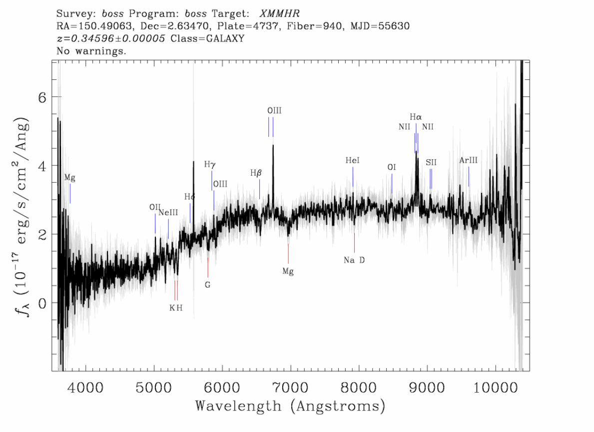

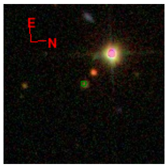

A.1

Xid	$zfinal$	$class$	$LogL_x$
191	0.346	2	42.82

`http://dr10.sdss3.org/spectrumDetail?mjd=51994&fiber=111&plateid=500`

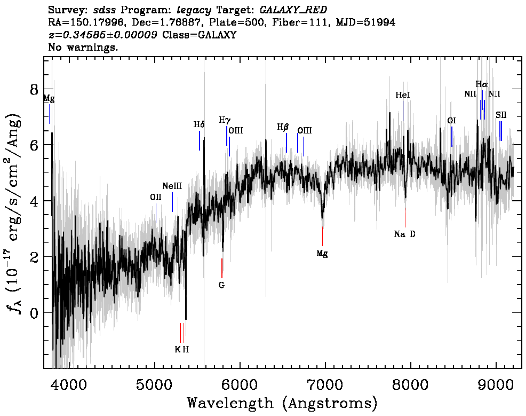

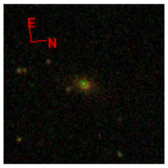

A.1

Xid	$zfinal$	$class$	$LogL_x$
70095	0.346	2	42.34

`http://dr10.sdss3.org/spectrumDetail?mjd=55630&fiber=198&plateid=4737`

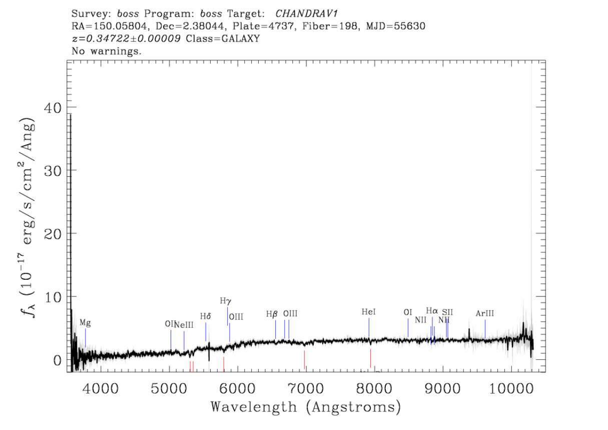

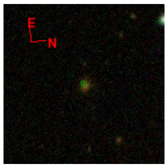

A.1

Xid	$zfinal$	$class$	$LogL_x$
241	0.3472	2	42.39

`http://dr10.sdss3.org/spectrumDetail?mjd=55630&fiber=235&plateid=4737`

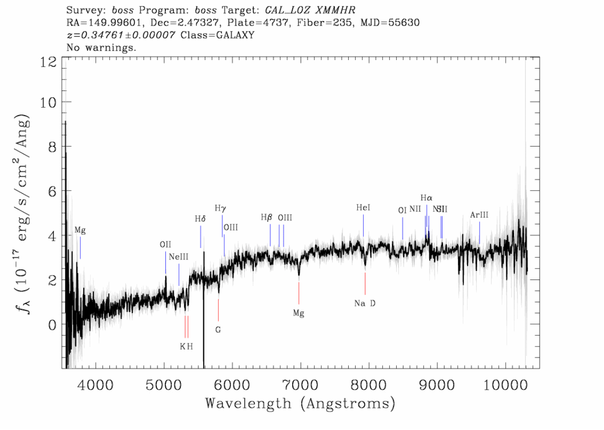

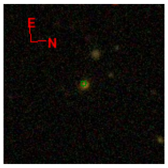

A.1

Xid	$zfinal$	$class$	$LogL_x$
10569	0.3476	3	42.44

`http://dr10.sdss3.org/spectrumDetail?mjd=55630&fiber=898&plateid=4737`

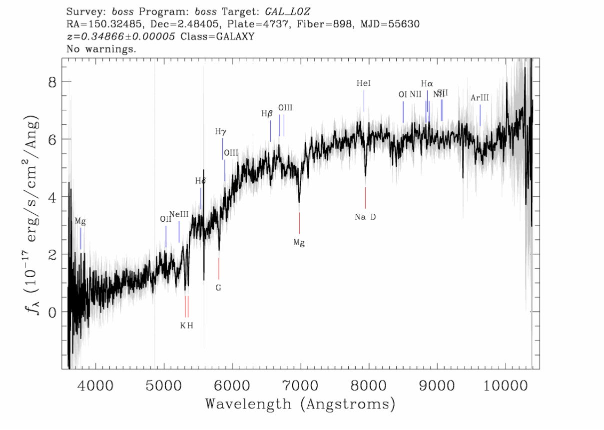

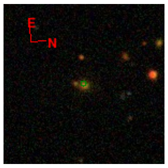

A.1

Xid	$zfinal$	$class$	$LogL_x$
311	0.3487	3	41.88

`http://dr10.sdss3.org/spectrumDetail?mjd=51994&fiber=596&plateid=500`

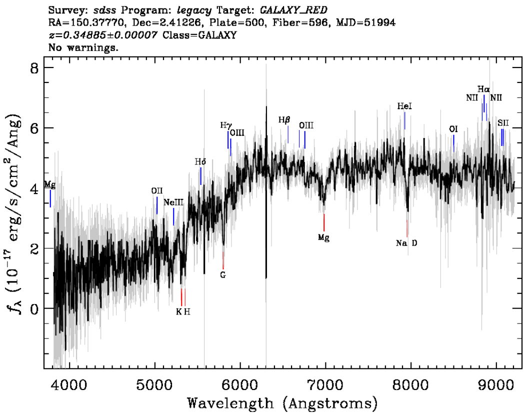

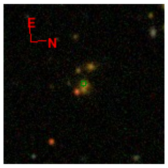

A.1

Xid	*zfinal*	*class*	*LogL$_x$*
546	0.348	3	42.63

`http://dr10.sdss3.org/spectrumDetail?mjd=51994&fiber=607&plateid=500`

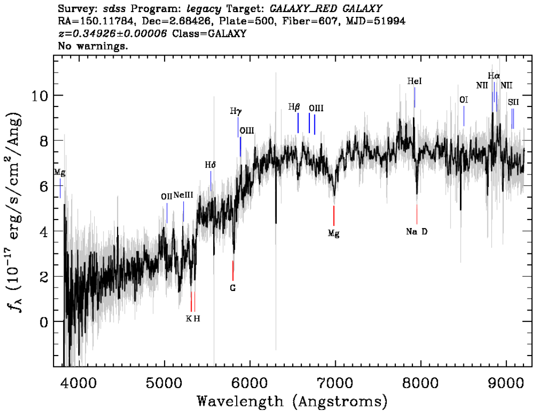

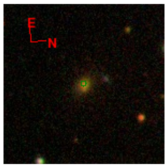

A.1

Xid	*zfinal*	*class*	*LogL$_x$*
5118	0.349	2	41.92

`http://dr10.sdss3.org/spectrumDetail?mjd=51994&fiber=584&plateid=500`

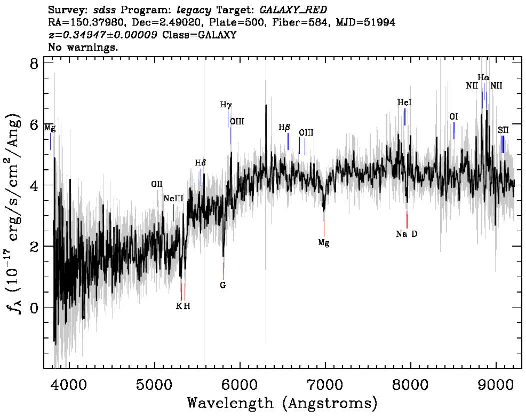

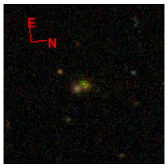

A.1

Xid	$zfinal$	$class$	$LogL_x$
54	0.35	2	42.49

`http://dr10.sdss3.org/spectrumDetail?mjd=55630&fiber=129&plateid=4737`

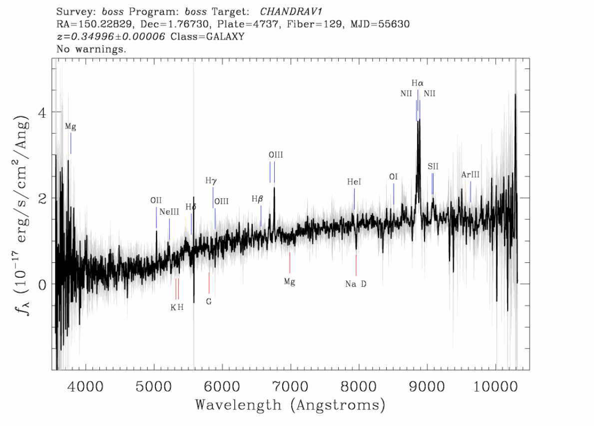

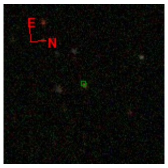

A.1

Xid	$zfinal$	$class$	$LogL_x$
385	0.35	2	43.0

`http://dr10.sdss3.org/spectrumDetail?mjd=55630&fiber=270&plateid=4737`

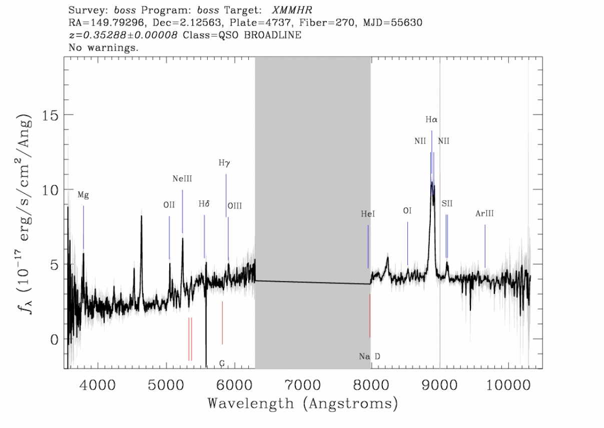

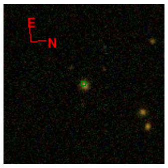

A.1

Xid	$zfinal$	$class$	$LogL_x$
392	0.3529	2	42.07

`http://dr10.sdss3.org/spectrumDetail?mjd=55630&fiber=263&plateid=4737`

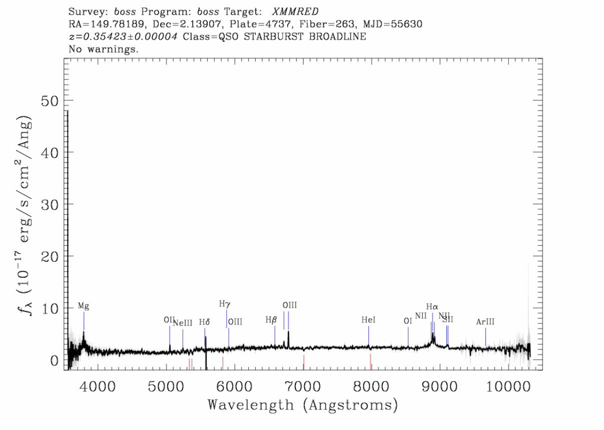

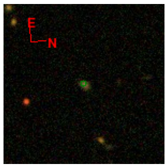

A.1

Xid	$zfinal$	$class$	$LogL_x$
63	0.3542	1	42.94

`http://dr10.sdss3.org/spectrumDetail?mjd=55630&fiber=317&plateid=4737`

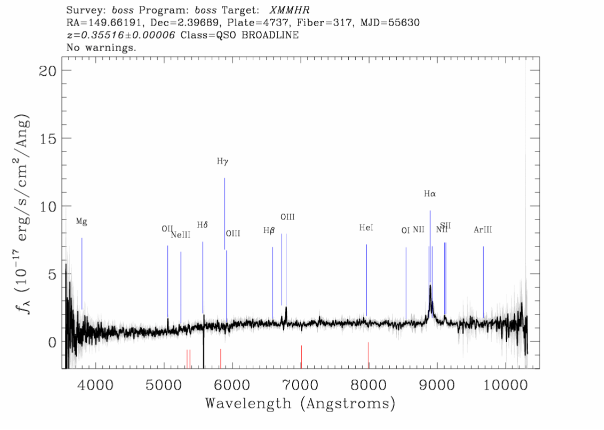

A.1

Xid	$zfinal$	$class$	$LogL_x$
1429	0.3552	1	43.44

`http://dr10.sdss3.org/spectrumDetail?mjd=52235&fiber=386&plateid=501`

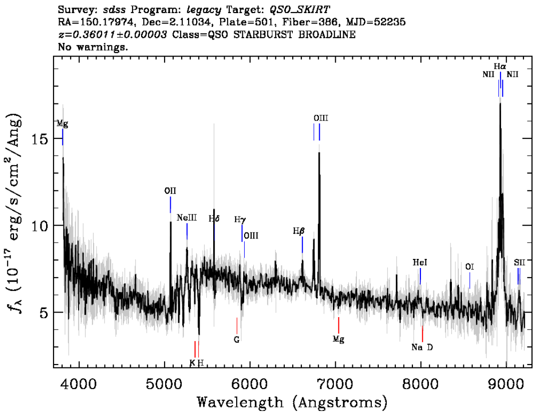

A.1

Xid	$zfinal$	$class$	$LogL_x$
6	0.36	1	43.45

`http://dr10.sdss3.org/spectrumDetail?mjd=51994&fiber=79&plateid=500`

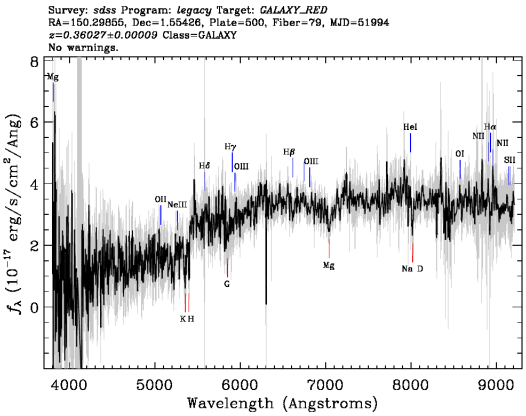

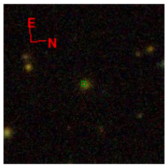

A.1

Xid	$zfinal$	$class$	$LogL_x$
53703	0.36	3	42.54

`http://dr10.sdss3.org/spectrumDetail?mjd=55630&fiber=189&plateid=4737`

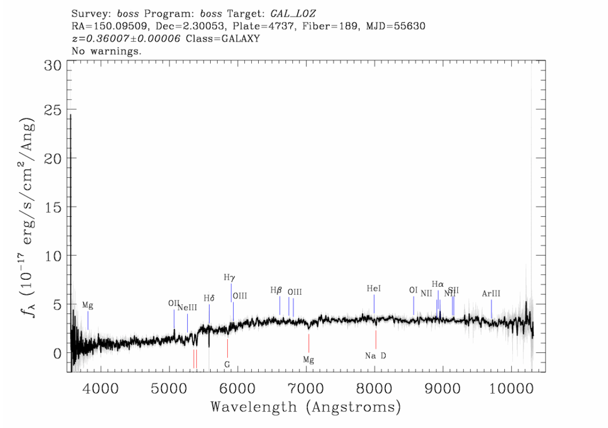

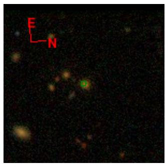

A.1

Xid	$zfinal$	$class$	$LogL_x$
10439	0.3601	3	42.02

`http://dr10.sdss3.org/spectrumDetail?mjd=52235&fiber=261&plateid=501`

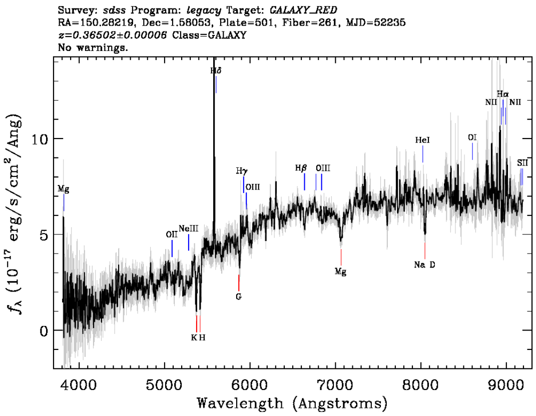

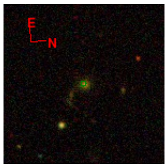

A.1

Xid	$zfinal$	$class$	$LogL_x$
60149	0.365	3	42.44

`http://dr10.sdss3.org/spectrumDetail?mjd=55630&fiber=68&plateid=4737`

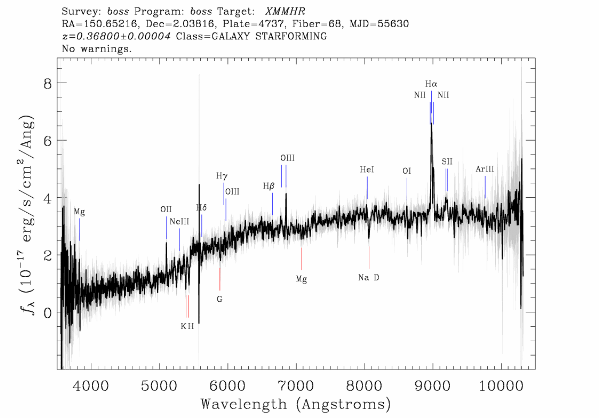

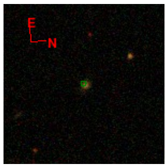

A.1

Xid	$zfinal$	$class$	$LogL_x$
2570	0.368	2	43.35

`http://dr10.sdss3.org/spectrumDetail?mjd=51994&fiber=142&plateid=500`

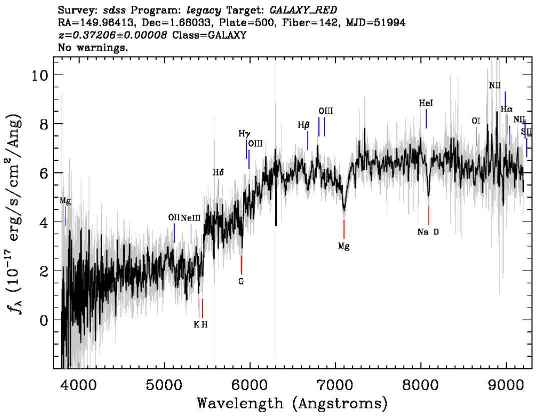

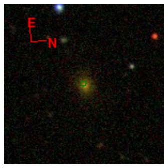

A.1

Xid	$zfinal$	$class$	$LogL_x$
30744	0.372	2	43.01

`http://dr10.sdss3.org/spectrumDetail?mjd=52235&fiber=277&plateid=501`

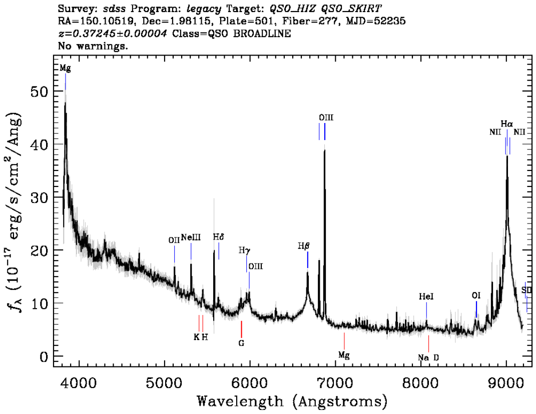

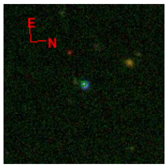

A.1

Xid	$zfinal$	$class$	$LogL_x$
1	0.373	1	43.7

`http://dr10.sdss3.org/spectrumDetail?mjd=55630&fiber=155&plateid=4737`

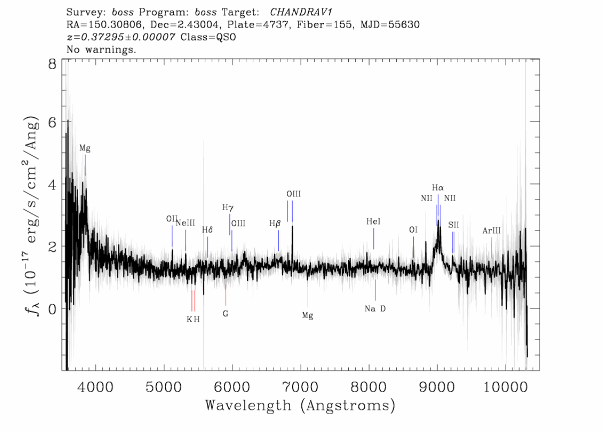

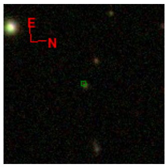

A.1

Xid	$zfinal$	$class$	$LogL_x$
27	0.373	1	43.72

`http://dr10.sdss3.org/spectrumDetail?mjd=52235&fiber=389&plateid=501`

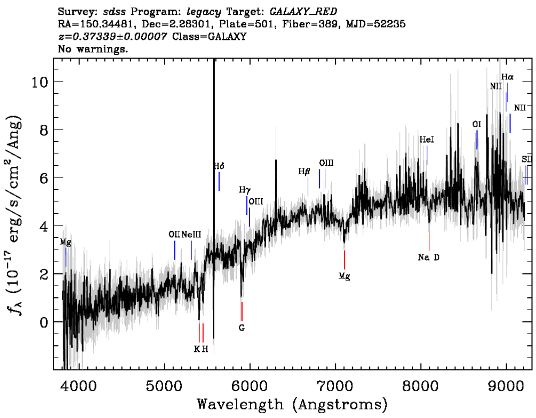

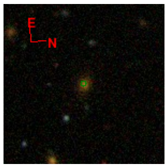

A.1

Xid	$zfinal$	$class$	$LogL_x$
2946	0.373	3	41.81

`http://dr10.sdss3.org/spectrumDetail?mjd=55630&fiber=272&plateid=4737`

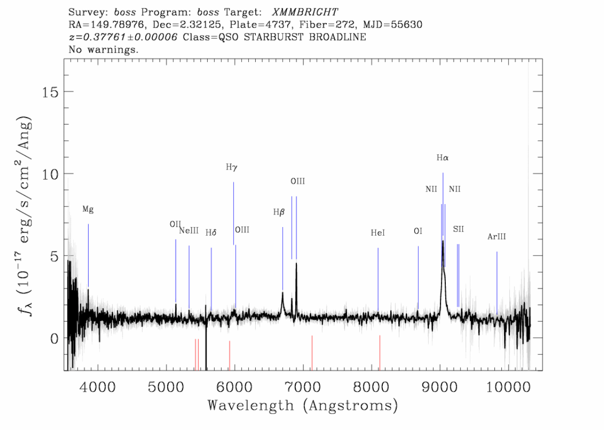

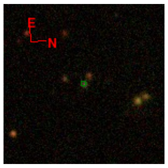

A.1

Xid	$zfinal$	$class$	$LogL_x$
23	0.3776	1	43.59

`http://dr10.sdss3.org/spectrumDetail?mjd=55630&fiber=696&plateid=4737`

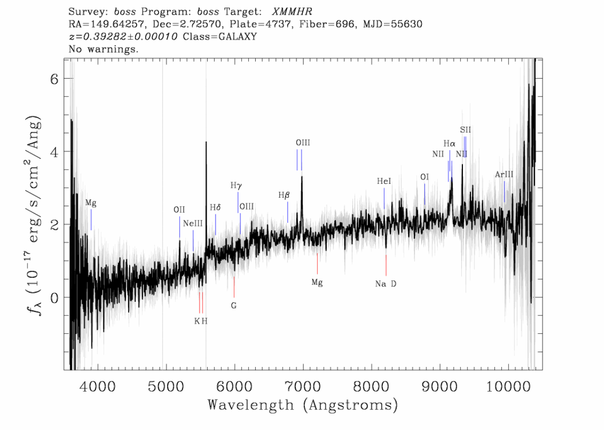

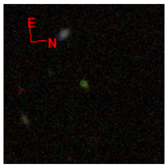

A.1

Xid	$zfinal$	$class$	$LogL_x$
5318	0.3928	2	42.49

`http://dr10.sdss3.org/spectrumDetail?mjd=55630&fiber=93&plateid=4737`

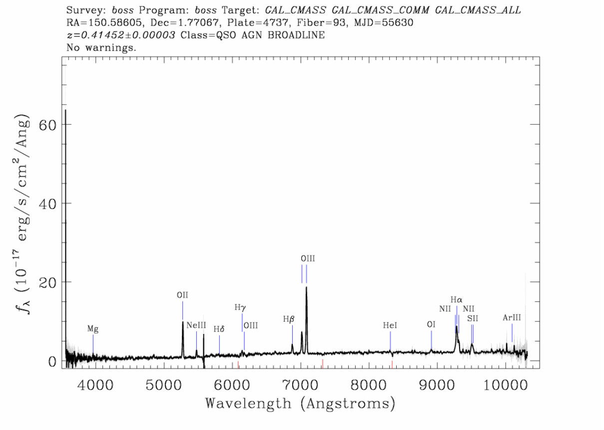

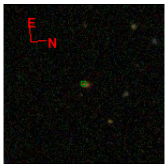

A.1

Xid	$zfinal$	$class$	$LogL_x$
5312	0.4145	1	44.3

`http://dr10.sdss3.org/spectrumDetail?mjd=55630&fiber=114&plateid=4737`

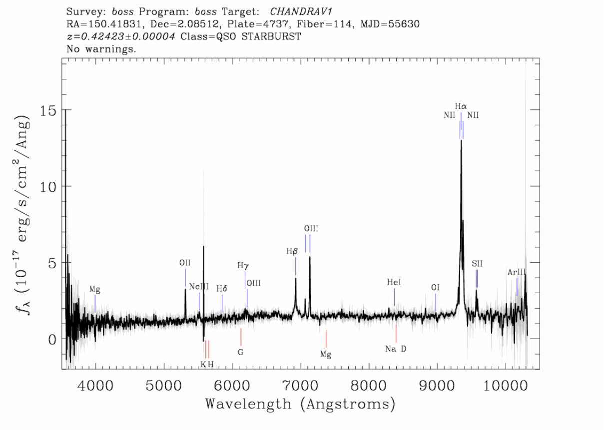

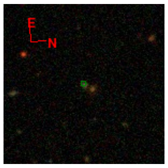

A.1

Xid	$zfinal$	$class$	$LogL_x$
2195	0.4242	2	42.8

`http://dr10.sdss3.org/spectrumDetail?mjd=55630&fiber=145&plateid=4737`

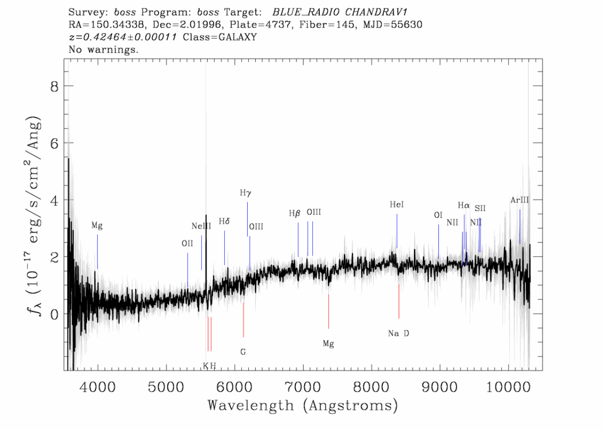

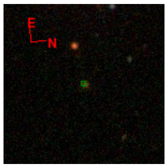

A.1

Xid	$zfinal$	$class$	$LogL_x$
10757	0.4246	3	42.24

`http://dr10.sdss3.org/spectrumDetail?mjd=55630&fiber=808&plateid=4737`

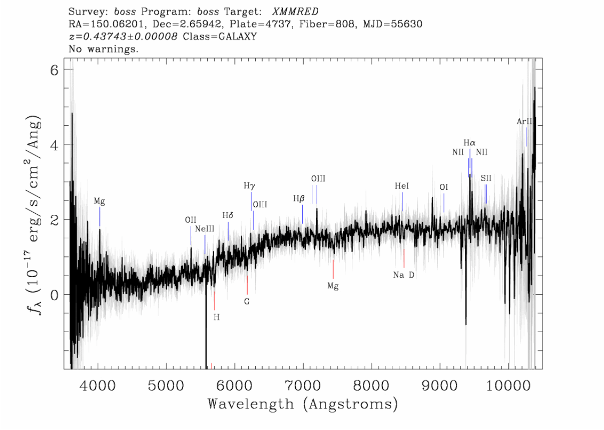

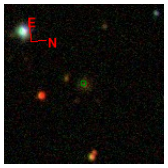

A.1

Xid	$zfinal$	$class$	$LogL_x$
297	0.4374	3	43.07

`http://dr10.sdss3.org/spectrumDetail?mjd=55630&fiber=264&plateid=4737`

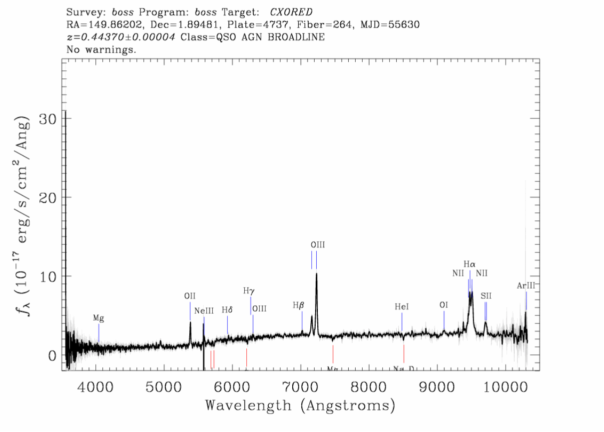

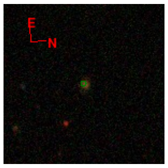

A.1

Xid	$zfinal$	$class$	$LogL_x$
293	0.4437	2	43.28

`http://dr10.sdss3.org/spectrumDetail?mjd=55650&fiber=509&plateid=4738`

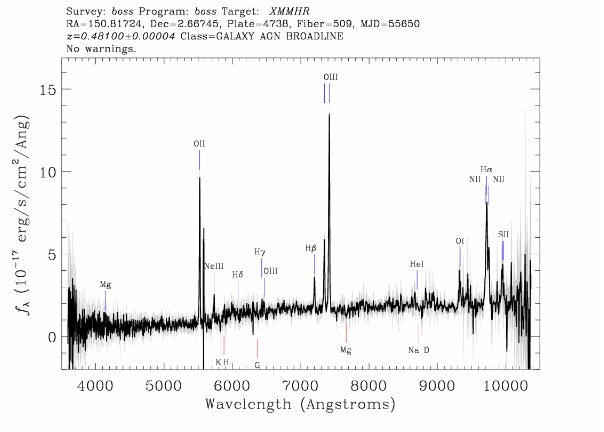

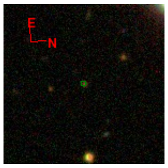

A.1

Xid	$zfinal$	$class$	$LogL_x$
5002	0.481	2	43.53

`http://dr10.sdss3.org/spectrumDetail?mjd=55630&fiber=686&plateid=4737`

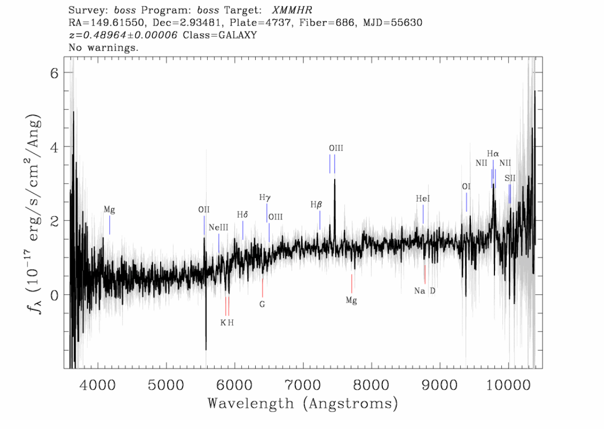

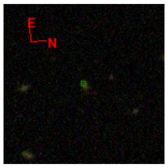

A.1

Xid	$zfinal$	$class$	$LogL_x$
5626	0.4896	2	43.47

`http://dr10.sdss3.org/spectrumDetail?mjd=55630&fiber=206&plateid=4737`

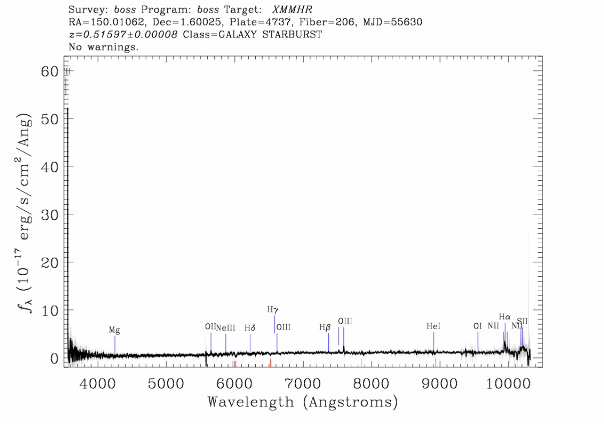

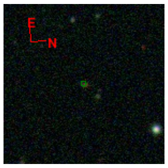

A.1

Xid	$zfinal$	$class$	$LogL_x$
2681	0.5159	2	43.16

`http://dr10.sdss3.org/spectrumDetail?mjd=52235&fiber=475&plateid=501`

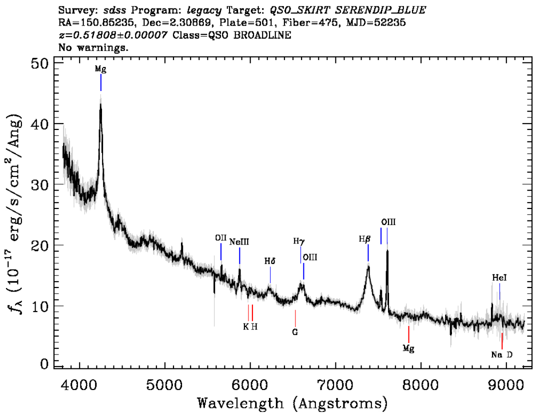
Survey: *sdss* Program: *legacy* Target: *QSO_SKIRT SERENDIP_BLUE*
RA=150.85235, Dec=2.30869, Plate=501, Fiber=475, MJD=52235
z=0.51808±0.00007 Class=QSO BROADLINE
No warnings.

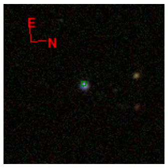

A.1

Xid	*zfinal*	*class*	$LogL_x$
5150	0.518	1	44.31

`http://dr10.sdss3.org/spectrumDetail?mjd=55630&fiber=142&plateid=4737`

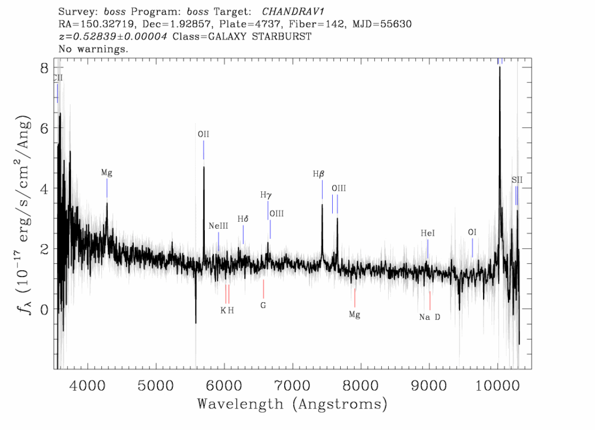
Survey: *boss* Program: *boss* Target: *CHANDRAV1*
RA=150.32719, Dec=1.92857, Plate=4737, Fiber=142, MJD=55630
z=0.52839±0.00004 Class=GALAXY STARBURST
No warnings.

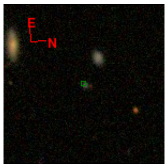

A.1

Xid	*zfinal*	*class*	$LogL_x$
164	0.5284	1	43.0

`http://dr10.sdss3.org/spectrumDetail?mjd=55630&fiber=38&plateid=4737`

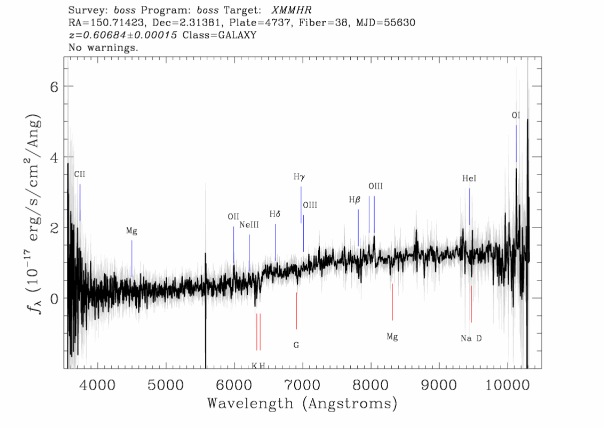

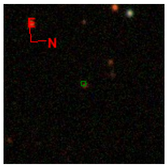

A.1

Xid	$zfinal$	$class$	$LogL_x$
5484	0.6068	2	43.6

`http://dr10.sdss3.org/spectrumDetail?mjd=55630&fiber=179&plateid=4737`

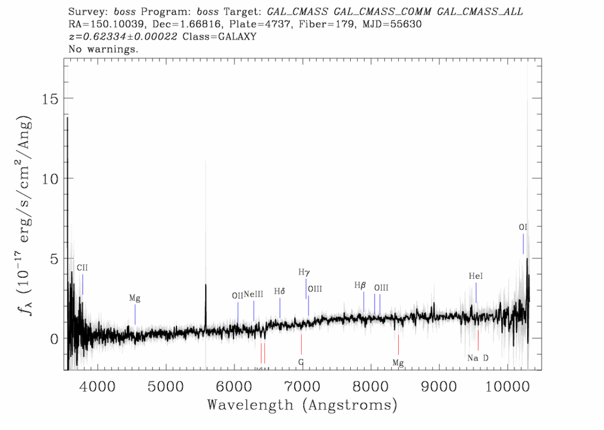

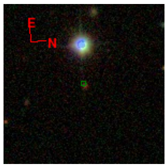

A.1

Xid	$zfinal$	$class$	$LogL_x$
2686	0.6233	2	42.47

`http://dr10.sdss3.org/spectrumDetail?mjd=52235&fiber=430&plateid=501`

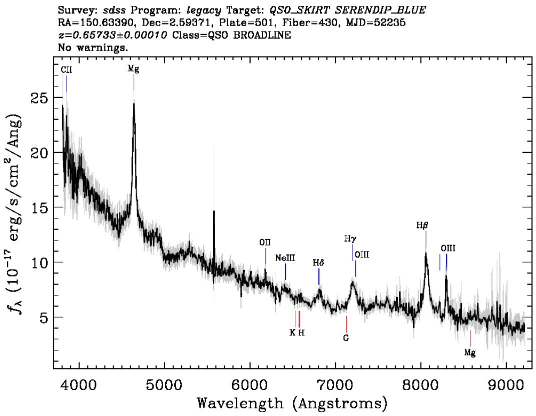

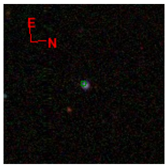

A.1

Xid	$zfinal$	$class$	$LogL_x$
5133	0.658	1	44.03

`http://dr10.sdss3.org/spectrumDetail?mjd=55630&fiber=231&plateid=4737`

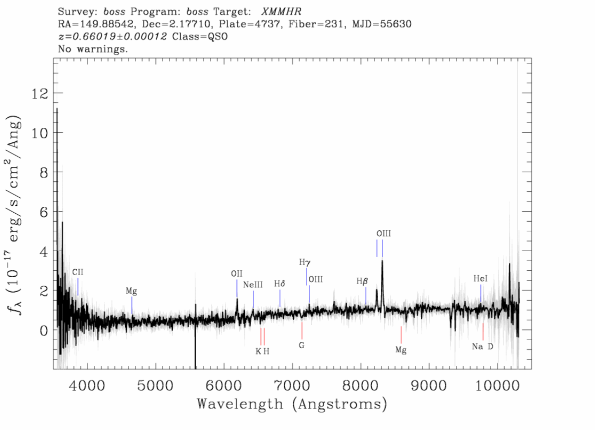

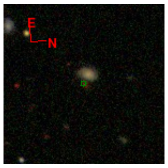

A.1

Xid	$zfinal$	$class$	$LogL_x$
217	0.6602	2	43.34

`http://dr10.sdss3.org/spectrumDetail?mjd=55630&fiber=111&plateid=4737`

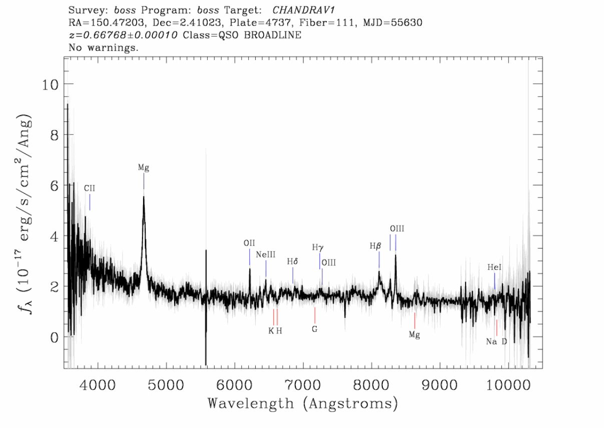

A.1

Xid	$zfinal$	$class$	$LogL_x$
16	0.6677	1	43.66

`http://dr10.sdss3.org/spectrumDetail?mjd=55630&fiber=92&plateid=4737`

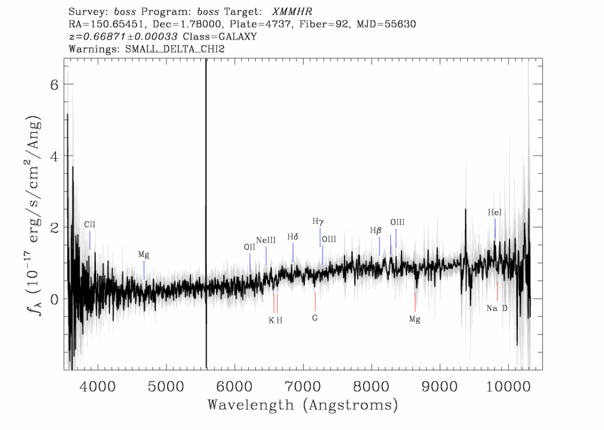

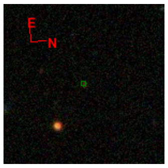

A.1

Xid	$zfinal$	$class$	$LogL_x$
2043	0.6687	2	43.48

`http://dr10.sdss3.org/spectrumDetail?mjd=55630&fiber=112&plateid=4737`

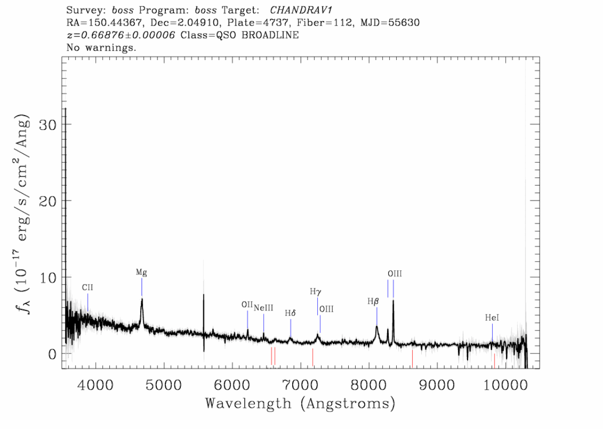

A.1

Xid	$zfinal$	$class$	$LogL_x$
2051	0.6688	1	43.89

`http://dr10.sdss3.org/spectrumDetail?mjd=55630&fiber=222&plateid=4737`

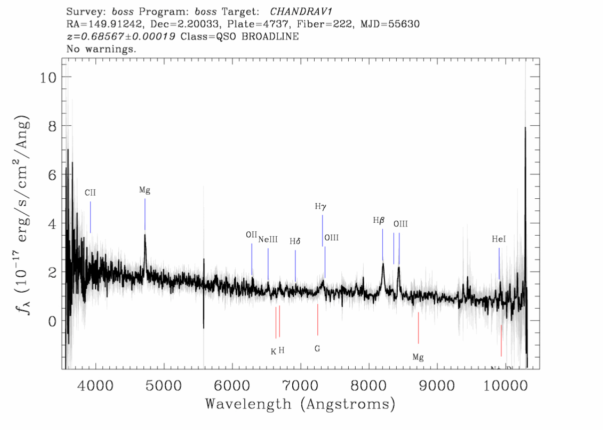

A.1

Xid	$zfinal$	$class$	$LogL_x$
10	0.6857	1	43.81

`http://dr10.sdss3.org/spectrumDetail?mjd=55630&fiber=200&plateid=4737`

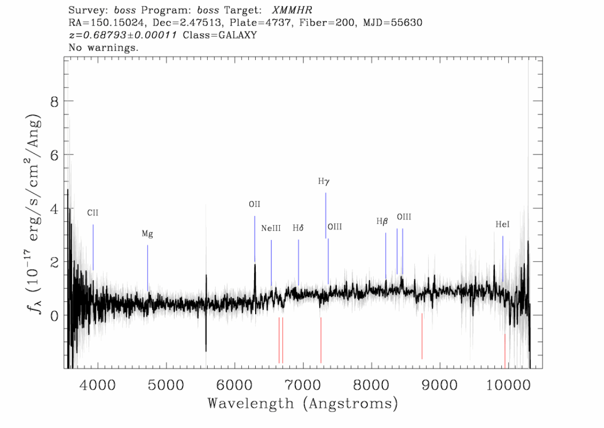

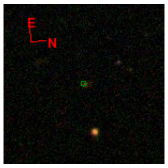

A.1

Xid	$zfinal$	$class$	$LogL_x$
70	0.6879	2	44.0

`http://dr10.sdss3.org/spectrumDetail?mjd=52235&fiber=346&plateid=501`

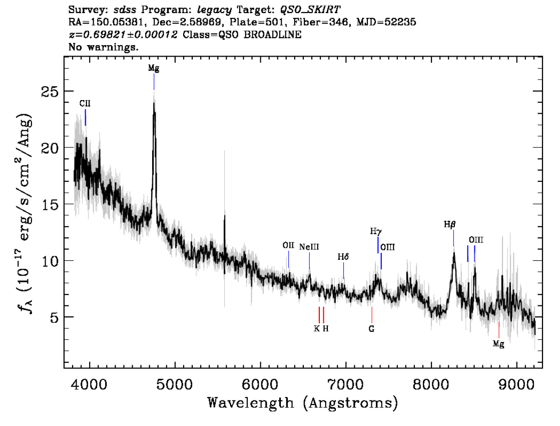

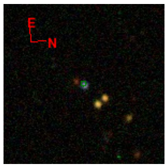

A.1

Xid	$zfinal$	$class$	$LogL_x$
8	0.699	1	44.33

`http://dr10.sdss3.org/spectrumDetail?mjd=55630&fiber=199&plateid=4737`

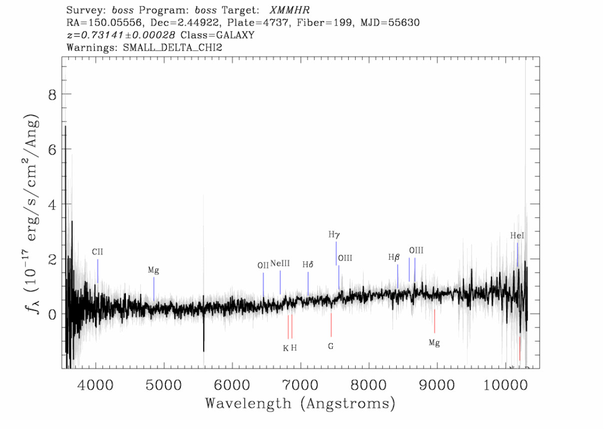

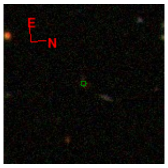

A.1

Xid	$zfinal$	$class$	$LogL_x$
143	0.7314	2	43.6

`http://dr10.sdss3.org/spectrumDetail?mjd=55630&fiber=308&plateid=4737`

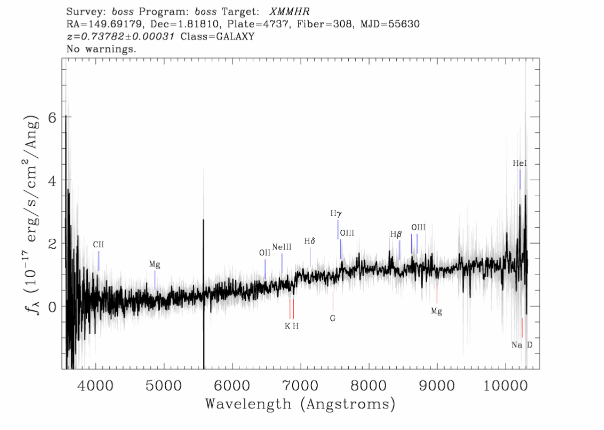

A.1

Xid	$zfinal$	$class$	$LogL_x$
5094	0.7378	2	43.05

`http://dr10.sdss3.org/spectrumDetail?mjd=52235&fiber=327&plateid=501`

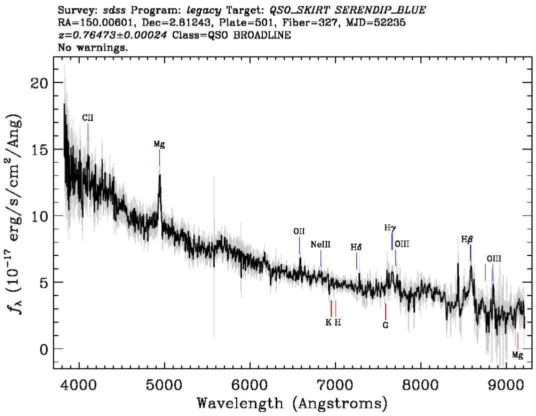

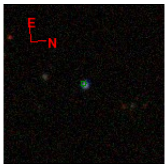

A.1

Xid	$zfinal$	$class$	$LogL_x$
5081	0.766	1	44.29

`http://dr10.sdss3.org/spectrumDetail?mjd=55630&fiber=814&plateid=4737`

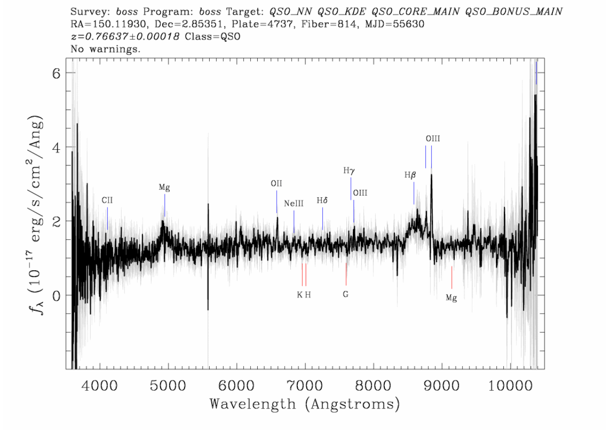

A.1

Xid	$zfinal$	$class$	$LogL_x$
5188	0.7664	1	44.41

`http://dr10.sdss3.org/spectrumDetail?mjd=55630&fiber=74&plateid=4737`

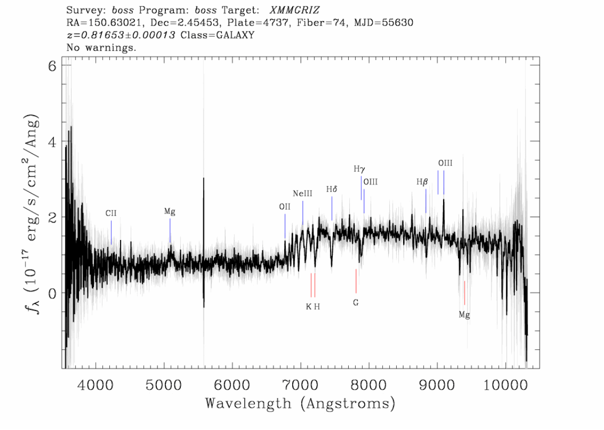

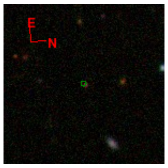

A.1

Xid	$zfinal$	$class$	$LogL_x$
5196	0.8165	2	43.23

`http://dr10.sdss3.org/spectrumDetail?mjd=55630&fiber=362&plateid=4737`

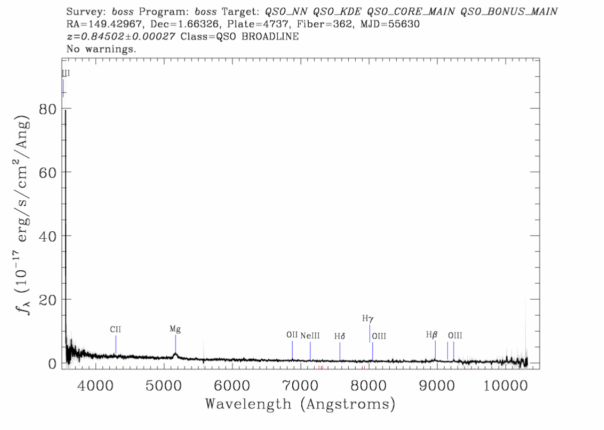

A.1

Xid	$zfinal$	$class$	$LogL_x$
54191	0.845	1	45.22

`http://dr10.sdss3.org/spectrumDetail?mjd=55630&fiber=648&plateid=4737`

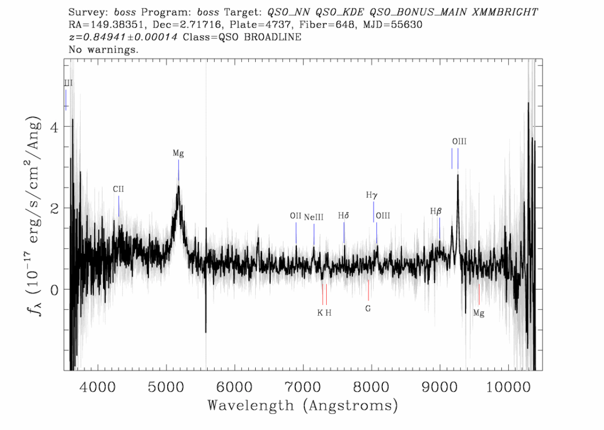
Survey: *boss* Program: *boss* Target: *QSO_NN QSO_KDE QSO_BONUS_MAIN XMMBRIGHT*
RA=149.38351, Dec=2.71716, Plate=4737, Fiber=648, MJD=55630
z=0.84941±0.00014 Class=QSO BROADLINE
No warnings.

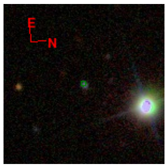

A.1

Xid	$zfinal$	$class$	$LogL_x$
5585	0.8494	1	45.02

`http://dr10.sdss3.org/spectrumDetail?mjd=55630&fiber=973&plateid=4737`

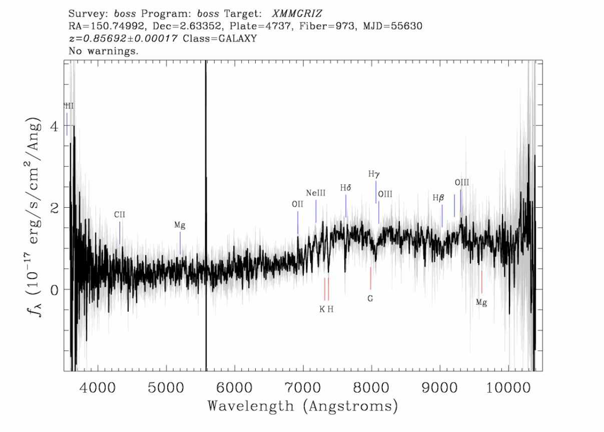
Survey: *boss* Program: *boss* Target: *XMMGRIZ*
RA=150.74992, Dec=2.63352, Plate=4737, Fiber=973, MJD=55630
z=0.85692±0.00017 Class=GALAXY
No warnings.

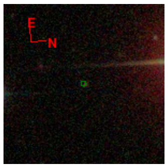

A.1

Xid	$zfinal$	$class$	$LogL_x$
5604	0.8569	2	43.19

`http://dr10.sdss3.org/spectrumDetail?mjd=55630&fiber=118&plateid=4737`

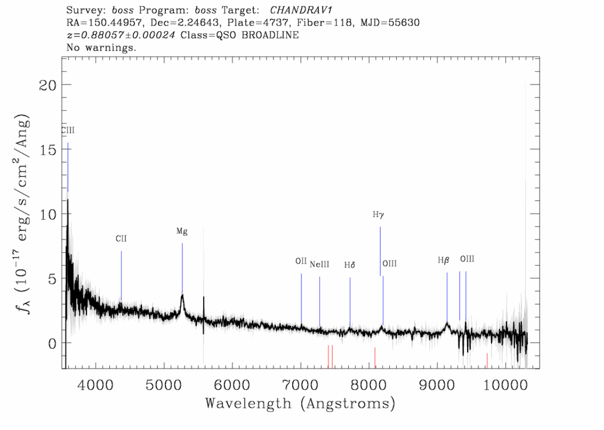

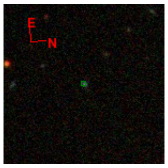

A.1

Xid	$zfinal$	$class$	$LogL_x$
74	0.8806	1	43.93

`http://dr10.sdss3.org/spectrumDetail?mjd=55630&fiber=154&plateid=4737`

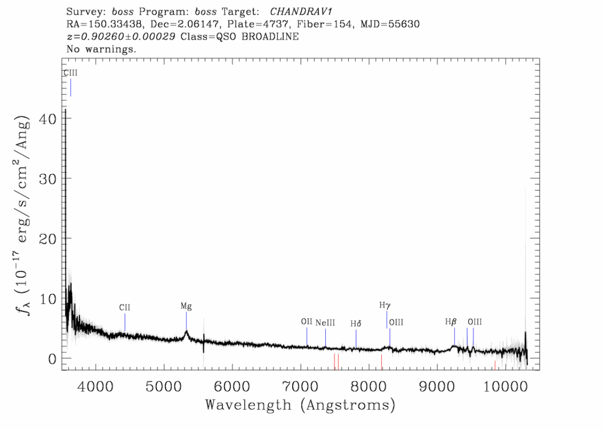

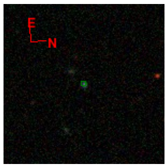

A.1

Xid	$zfinal$	$class$	$LogL_x$
5415	0.9026	1	43.61

`http://dr10.sdss3.org/spectrumDetail?mjd=55630&fiber=104&plateid=4737`

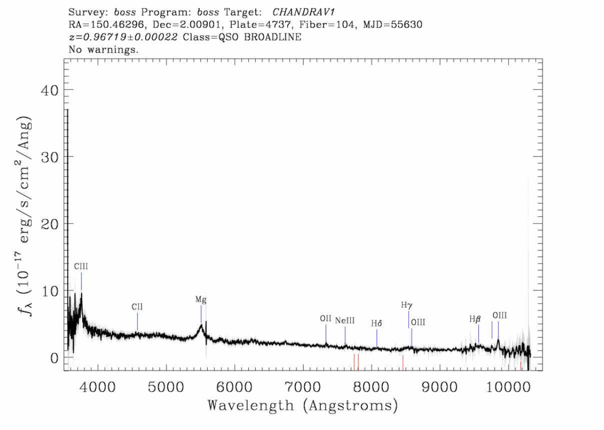

A.1

Xid	$zfinal$	$class$	$LogL_x$
2058	0.9672	1	44.22

`http://dr10.sdss3.org/spectrumDetail?mjd=51994&fiber=626&plateid=500`

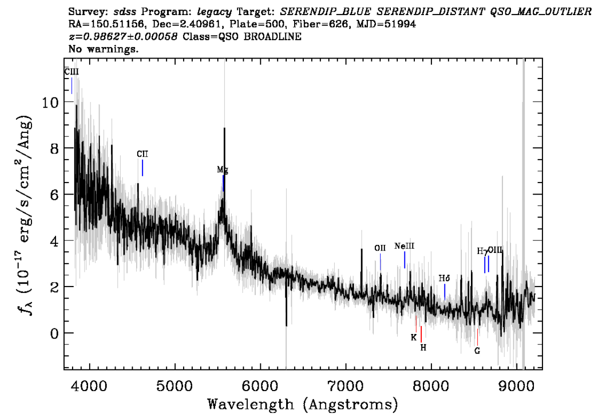

A.1

Xid	$zfinal$	$class$	$LogL_x$
42	0.988	1	44.17

`http://dr10.sdss3.org/spectrumDetail?mjd=51994&fiber=506&plateid=500`

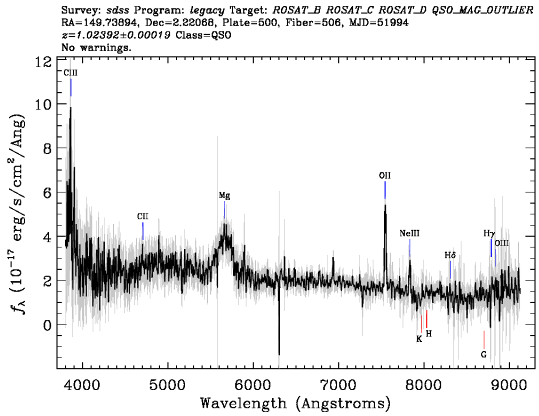
Survey: *sdss* Program: *legacy* Target: *ROSAT_B ROSAT_C ROSAT_D QSO_MAG_OUTLIER*
RA=149.73894, Dec=2.22068, Plate=500, Fiber=506, MJD=51994
z=1.02392±0.00019 Class=QSO
No warnings.

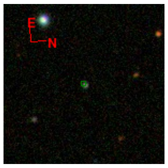

A.1

Xid	$zfinal$	$class$	$LogL_x$
2	1.024	1	45.21

`http://dr10.sdss3.org/spectrumDetail?mjd=52235&fiber=321&plateid=501`

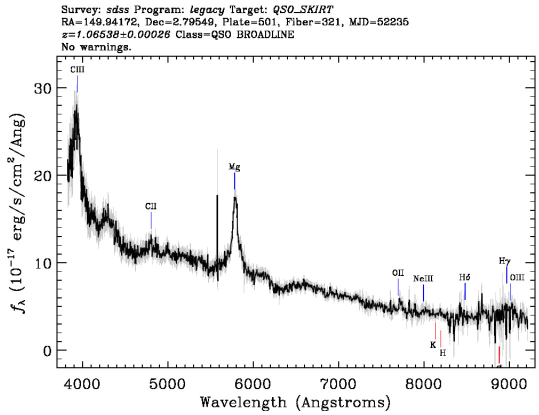
Survey: *sdss* Program: *legacy* Target: *QSO_SKIRT*
RA=149.94172, Dec=2.79549, Plate=501, Fiber=321, MJD=52235
z=1.06538±0.00026 Class=QSO BROADLINE
No warnings.

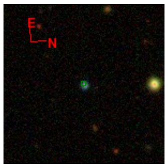

A.1

Xid	$zfinal$	$class$	$LogL_x$
5620	1.067	1	44.54

http://dr10.sdss3.org/spectrumDetail?mjd=52235&fiber=182&plateid=501

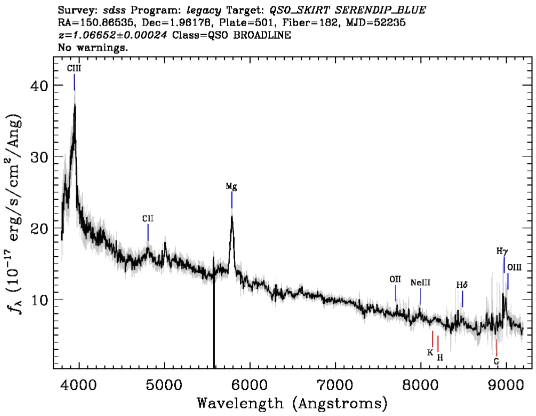

A.1

Xid	$zfinal$	$class$	$LogL_x$
53537	1.067	1	44.74

http://dr10.sdss3.org/spectrumDetail?mjd=51994&fiber=445&plateid=500

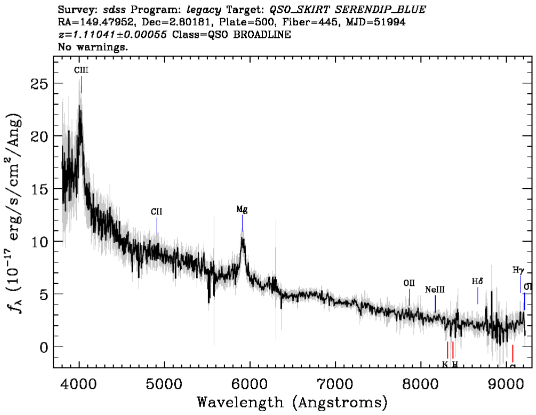

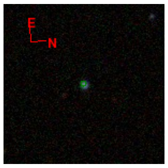

A.1

Xid	$zfinal$	$class$	$LogL_x$
5257	1.111	1	44.37

http://dr10.sdss3.org/spectrumDetail?mjd=55630&fiber=240&plateid=4737

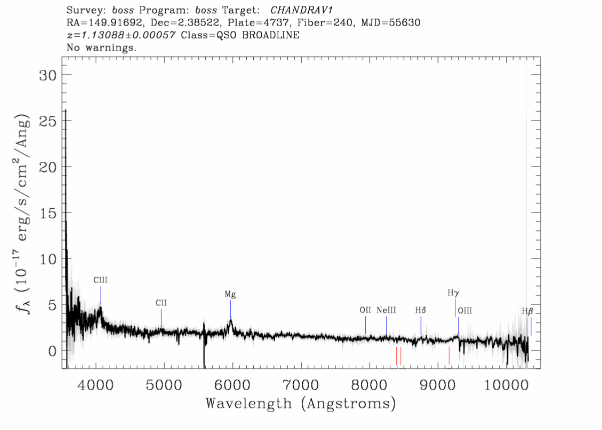

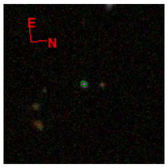

A.1

Xid	$zfinal$	$class$	$LogL_x$
37	1.131	1	44.13

http://dr10.sdss3.org/spectrumDetail?mjd=55630&fiber=22&plateid=4737

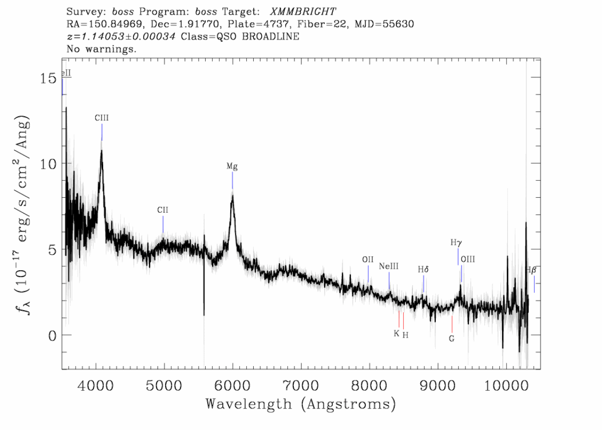

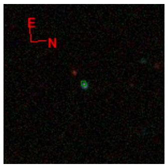

A.1

Xid	$zfinal$	$class$	$LogL_x$
53577	1.14	1	-942.1

`http://dr10.sdss3.org/spectrumDetail?mjd=55630&fiber=149&plateid=4737`

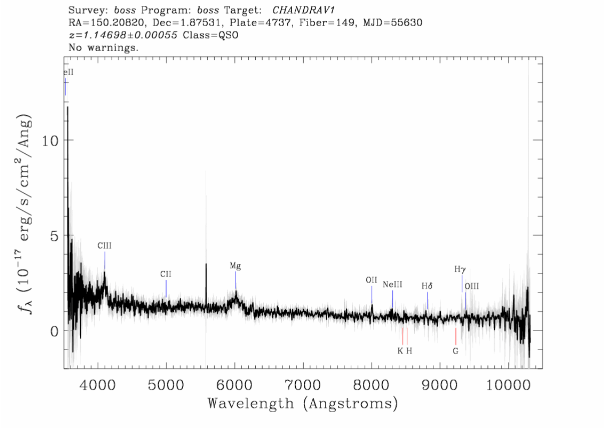
Survey: *boss* Program: *boss* Target: *CHANDRAV1*
RA=150.20820, Dec=1.87531, Plate=4737, Fiber=149, MJD=55630
z=1.14698±0.00055 Class=QSO
No warnings.

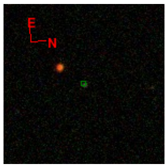

A.1

Xid	$zfinal$	$class$	$LogL_x$
359	1.147	1	43.9

`http://dr10.sdss3.org/spectrumDetail?mjd=52235&fiber=359&plateid=501`

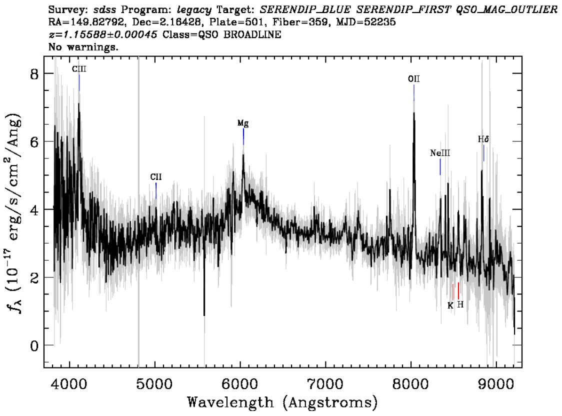
Survey: *sdss* Program: *legacy* Target: *SERENDIP_BLUE SERENDIP_FIRST QSO_MAG_OUTLIER*
RA=149.82792, Dec=2.16428, Plate=501, Fiber=359, MJD=52235
z=1.15588±0.00045 Class=QSO BROADLINE
No warnings.

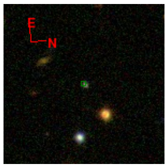

A.1

Xid	$zfinal$	$class$	$LogL_x$
5	1.157	1	45.06

`http://dr10.sdss3.org/spectrumDetail?mjd=51994&fiber=622&plateid=500`

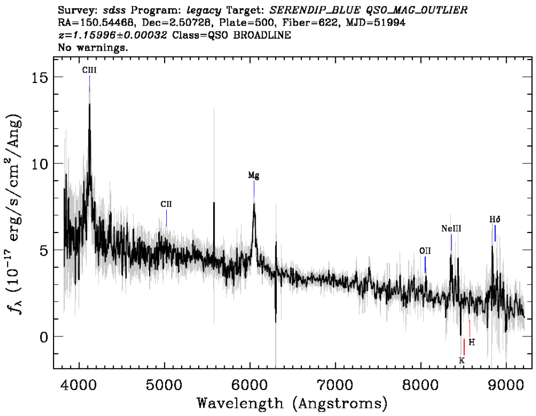

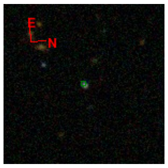

A.1

Xid	$zfinal$	$class$	$LogL_x$
115	1.161	1	44.55

`http://dr10.sdss3.org/spectrumDetail?mjd=51994&fiber=110&plateid=500`

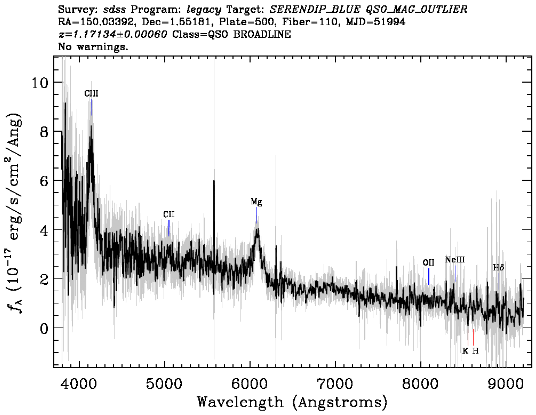

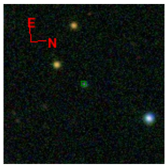

A.1

Xid	$zfinal$	$class$	$LogL_x$
2342	1.171	1	44.83

`http://dr10.sdss3.org/spectrumDetail?mjd=55630&fiber=314&plateid=4737`

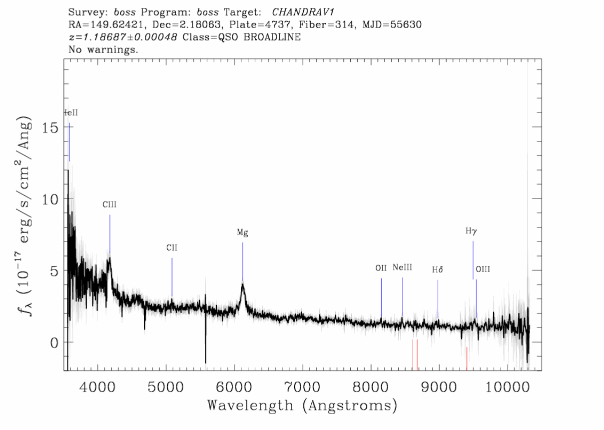

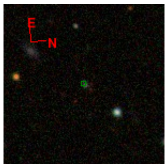

A.1

Xid	$zfinal$	$class$	$LogL_x$
188	1.187	1	44.08

`http://dr10.sdss3.org/spectrumDetail?mjd=55630&fiber=158&plateid=4737`

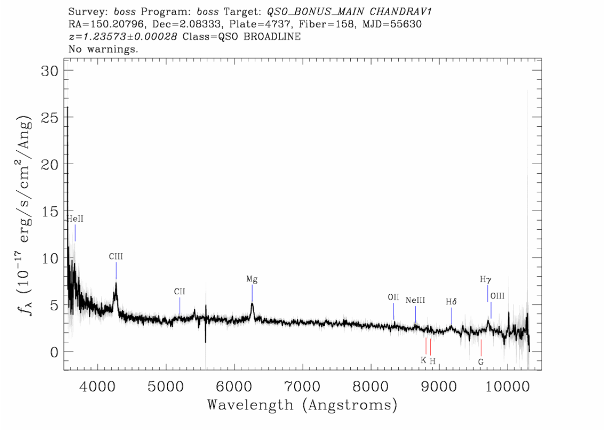

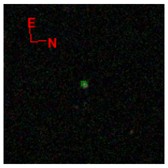

A.1

Xid	$zfinal$	$class$	$LogL_x$
12	1.236	1	44.5

`http://dr10.sdss3.org/spectrumDetail?mjd=54821&fiber=162&plateid=3154`

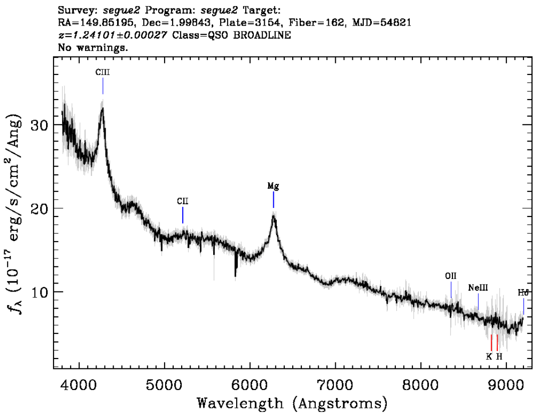

A.1

Xid	$zfinal$	$class$	$LogL_x$
17	1.236	1	44.54

`http://dr10.sdss3.org/spectrumDetail?mjd=55630&fiber=820&plateid=4737`

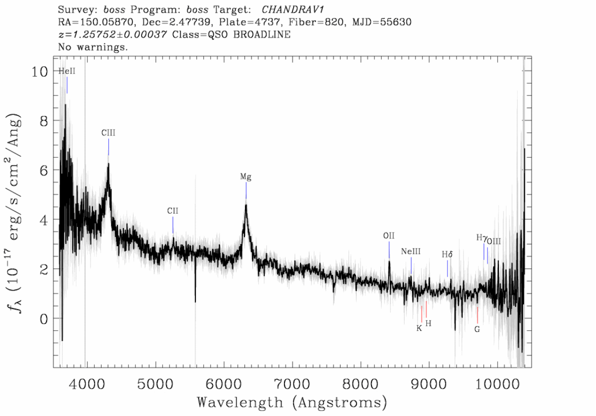

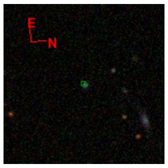

A.1

Xid	$zfinal$	$class$	$LogL_x$
178	1.258	1	43.75

`http://dr10.sdss3.org/spectrumDetail?mjd=51994&fiber=623&plateid=500`

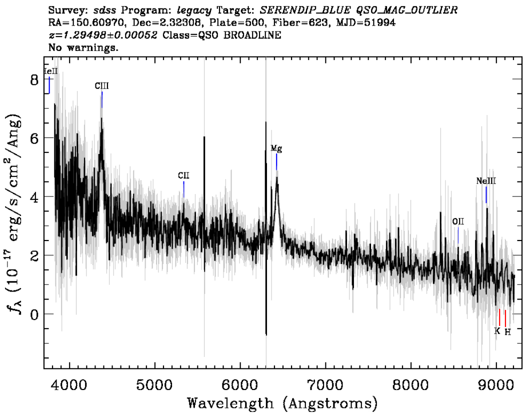

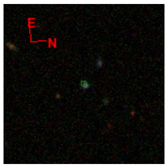

A.1

Xid	$zfinal$	$class$	$LogL_x$
5503	1.294	1	44.45

`http://dr10.sdss3.org/spectrumDetail?mjd=55630&fiber=48&plateid=4737`

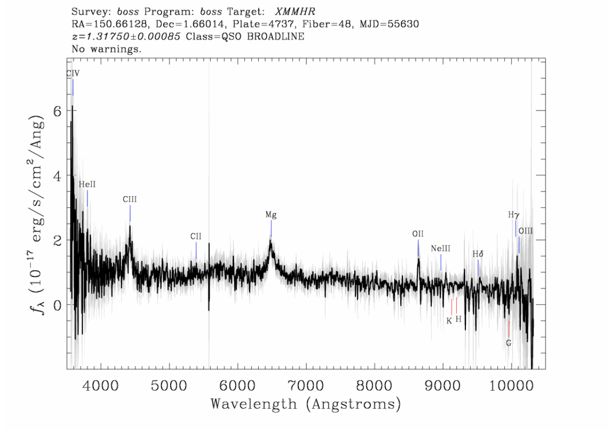

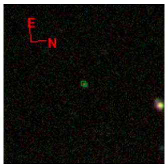

A.1

Xid	$zfinal$	$class$	$LogL_x$
2080	1.317	1	43.97

`http://dr10.sdss3.org/spectrumDetail?mjd=52235&fiber=339&plateid=501`

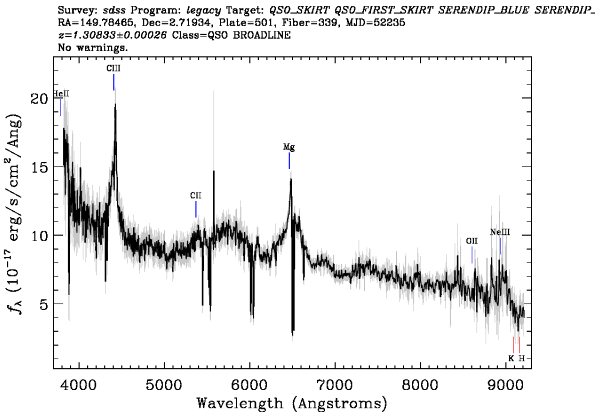

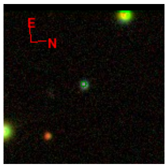

A.1

Xid	$zfinal$	$class$	$LogL_x$
5230	1.317	1	45.53

`http://dr10.sdss3.org/spectrumDetail?mjd=52235&fiber=397&plateid=501`

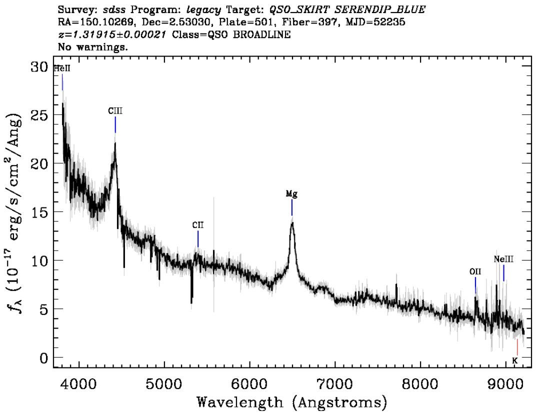

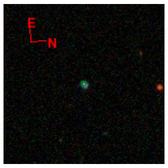

A.1

Xid	$zfinal$	$class$	$LogL_x$
24	1.318	1	44.45

`http://dr10.sdss3.org/spectrumDetail?mjd=51994&fiber=179&plateid=500`

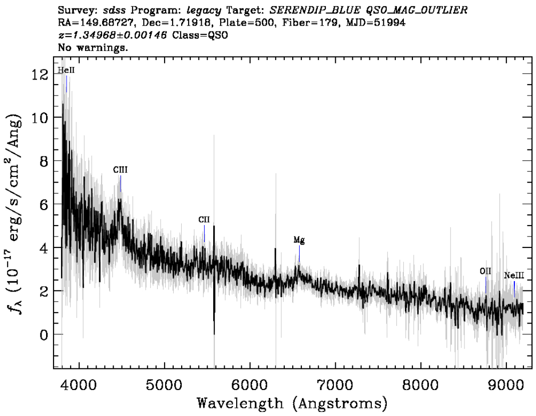

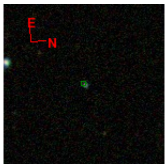

A.1

Xid	$zfinal$	$class$	$LogL_x$
5627	1.337	1	44.04

`http://dr10.sdss3.org/spectrumDetail?mjd=51994&fiber=493&plateid=500`

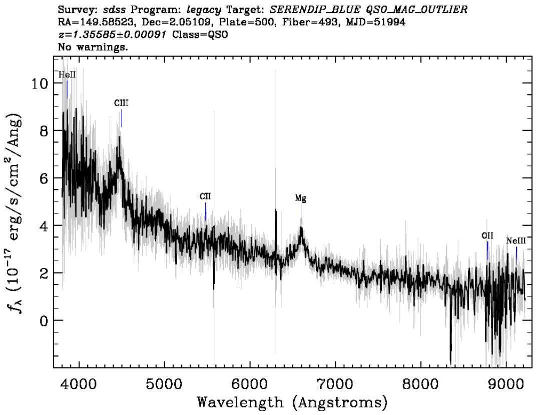

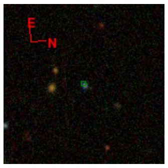

A.1

Xid	$zfinal$	$class$	$LogL_x$
54204	1.356	1	44.22

http://dr10.sdss3.org/spectrumDetail?mjd=51994&fiber=444&plateid=500

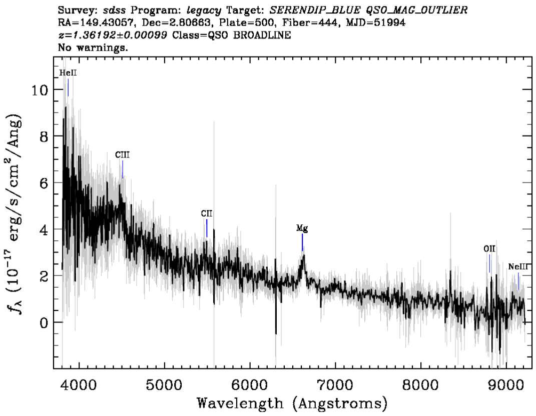

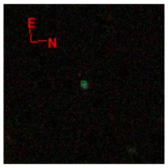

A.1

Xid	$zfinal$	$class$	$LogL_x$
5607	1.359	1	44.06

http://dr10.sdss3.org/spectrumDetail?mjd=51994&fiber=75&plateid=500

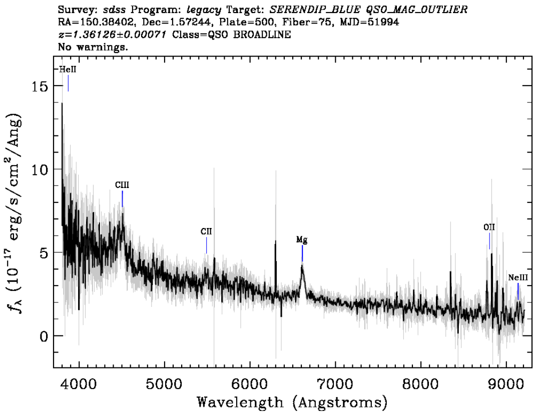

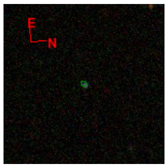

A.1

Xid	$zfinal$	$class$	$LogL_x$
2335	1.36	1	44.14

`http://dr10.sdss3.org/spectrumDetail?mjd=51994&fiber=590&plateid=500`

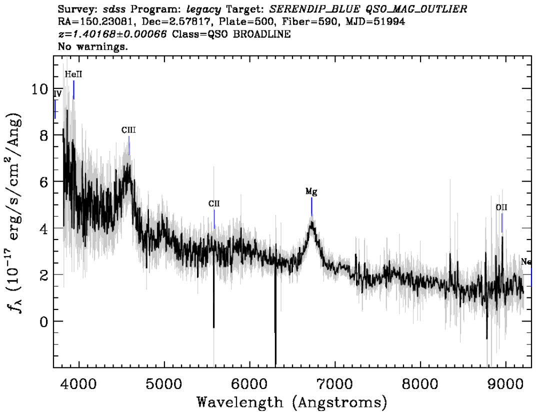

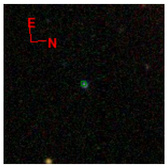

A.1

Xid	$zfinal$	$class$	$LogL_x$
21	1.403	1	44.78

`http://dr10.sdss3.org/spectrumDetail?mjd=51994&fiber=448&plateid=500`

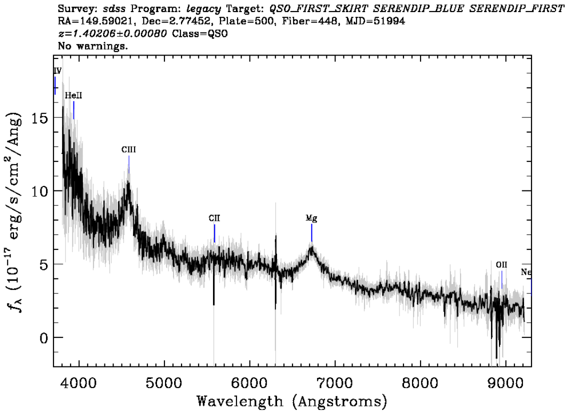

A.1

Xid	$zfinal$	$class$	$LogL_x$
5275	1.403	1	44.83

`http://dr10.sdss3.org/spectrumDetail?mjd=51994&fiber=532&plateid=500`

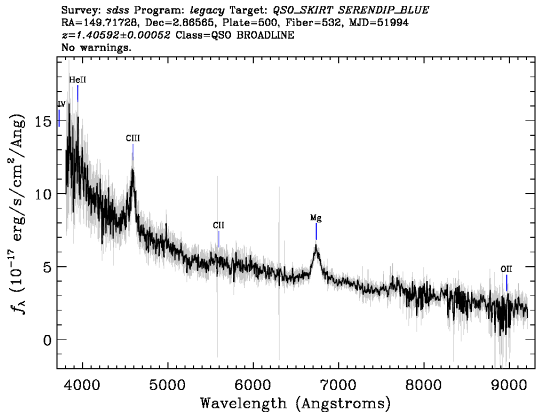

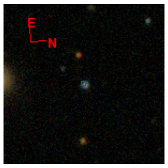

A.1

Xid	$zfinal$	$class$	$LogL_x$
5163	1.407	1	44.83

`http://dr10.sdss3.org/spectrumDetail?mjd=55630&fiber=929&plateid=4737`

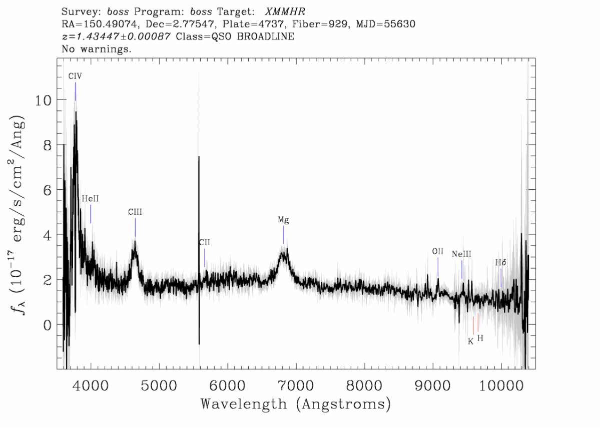

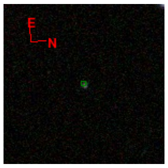

A.1

Xid	$zfinal$	$class$	$LogL_x$
57	1.434	1	44.77

`http://dr10.sdss3.org/spectrumDetail?mjd=55630&fiber=234&plateid=4737`

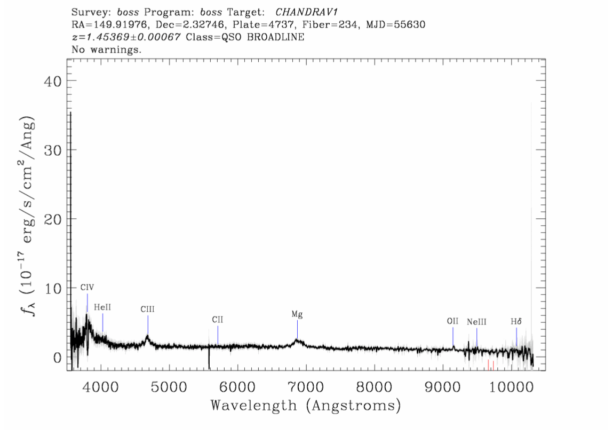

A.1

Xid	$zfinal$	$class$	$LogL_x$
9	1.454	1	44.78

`http://dr10.sdss3.org/spectrumDetail?mjd=51994&fiber=33&plateid=500`

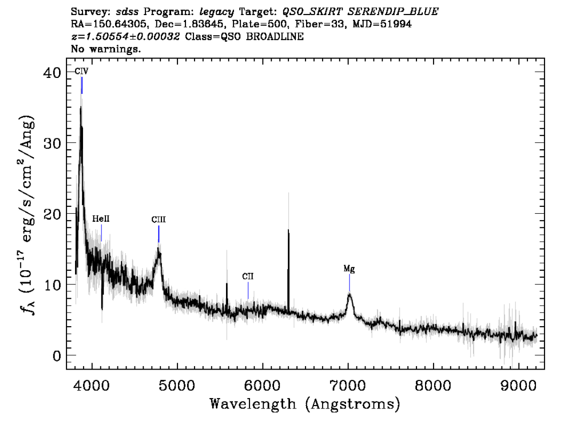

A.1

Xid	$zfinal$	$class$	$LogL_x$
2020	1.506	1	44.66

`http://dr10.sdss3.org/spectrumDetail?mjd=51994&fiber=627&plateid=500`

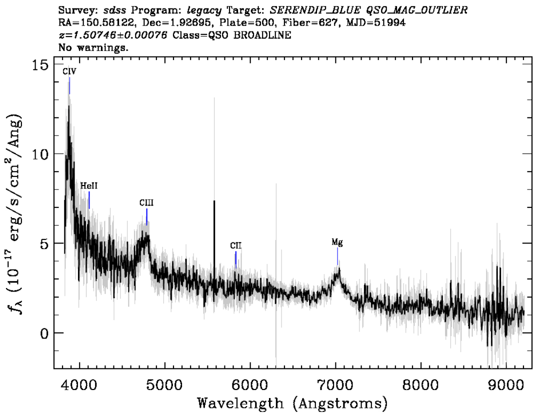

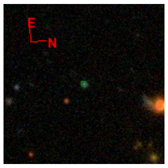

A.1

Xid	$zfinal$	$class$	$LogL_x$
2105	1.509	1	44.32

`http://dr10.sdss3.org/spectrumDetail?mjd=51994&fiber=178&plateid=500`

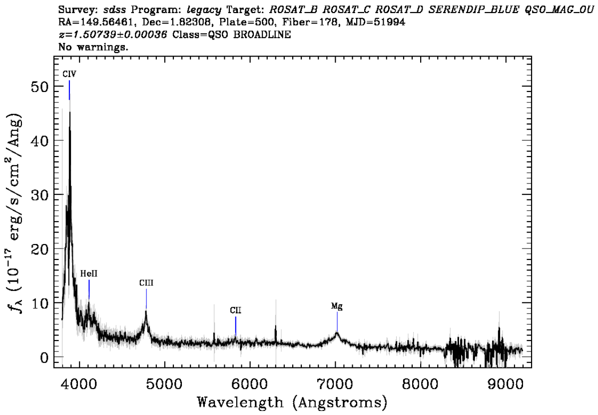

A.1

Xid	$zfinal$	$class$	$LogL_x$
5323	1.509	1	45.04

`http://dr10.sdss3.org/spectrumDetail?mjd=51994&fiber=631&plateid=500`

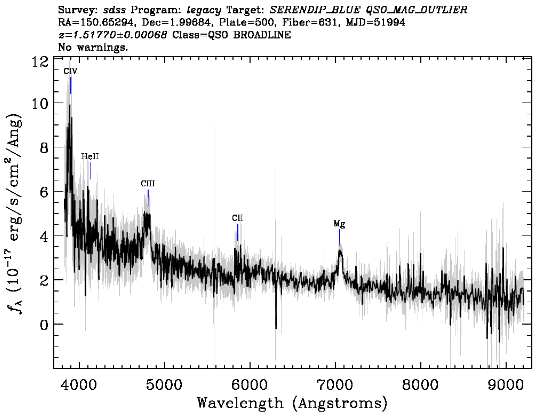

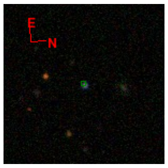

A.1

Xid	$zfinal$	$class$	$LogL_x$
2202	1.516	1	43.82

`http://dr10.sdss3.org/spectrumDetail?mjd=51994&fiber=480&plateid=500`

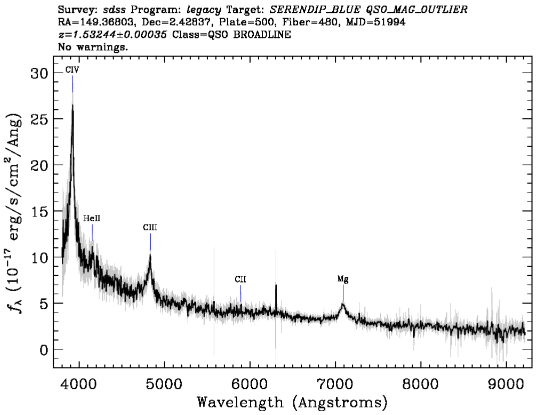

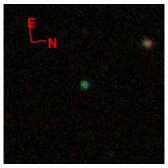

A.1

Xid	$zfinal$	$class$	$LogL_x$
2522	1.536	1	45.02

`http://dr10.sdss3.org/spectrumDetail?mjd=51994&fiber=505&plateid=500`

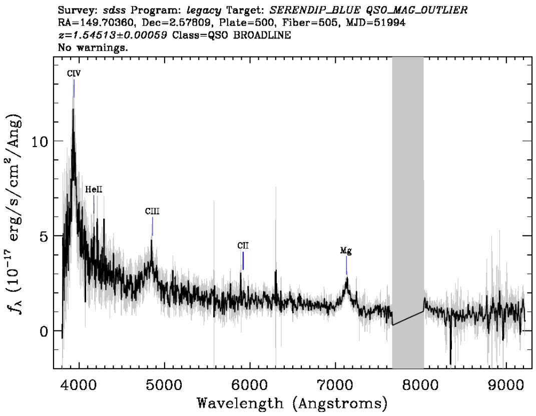

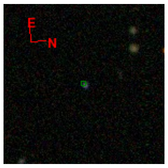

A.1

Xid	$zfinal$	$class$	$LogL_x$
2138	1.551	1	44.89

`http://dr10.sdss3.org/spectrumDetail?mjd=51994&fiber=524&plateid=500`

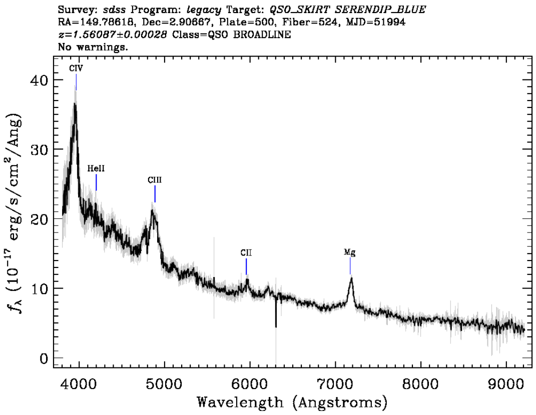

A.1

Xid	$zfinal$	$class$	$LogL_x$
53831	1.556	1	45.0

`http://dr10.sdss3.org/spectrumDetail?mjd=51994&fiber=72&plateid=500`

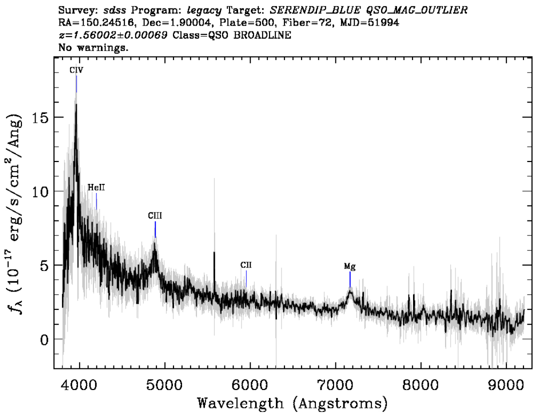

A.1

Xid	$zfinal$	$class$	$LogL_x$
38	1.559	1	44.51

`http://dr10.sdss3.org/spectrumDetail?mjd=51994&fiber=456&plateid=500`

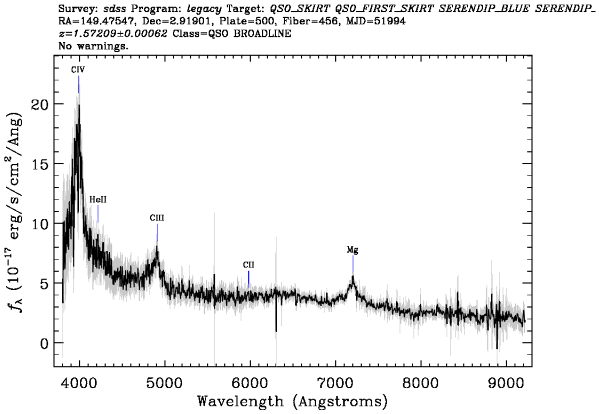

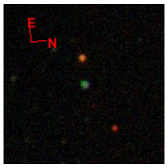

A.1

Xid	$zfinal$	$class$	$LogL_x$
5413	1.569	1	44.68

http://dr10.sdss3.org/spectrumDetail?mjd=51994&fiber=78&plateid=500

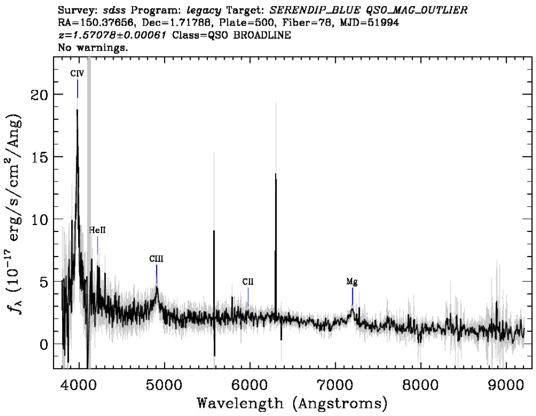

A.1

Xid	$zfinal$	$class$	$LogL_x$
2299	1.571	1	44.19

http://dr10.sdss3.org/spectrumDetail?mjd=51994&fiber=446&plateid=500

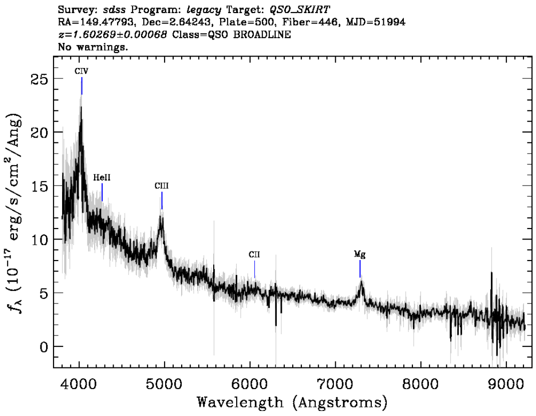

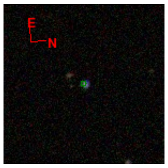

A.1

Xid	$zfinal$	$class$	$LogL_x$
2396	1.6	1	43.44

`http://dr10.sdss3.org/spectrumDetail?mjd=51994&fiber=153&plateid=500`

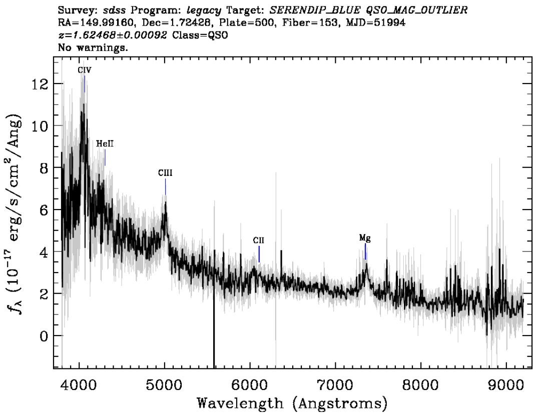

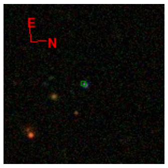

A.1

Xid	$zfinal$	$class$	$LogL_x$
2333	1.618	1	44.82

`http://dr10.sdss3.org/spectrumDetail?mjd=51994&fiber=118&plateid=500`

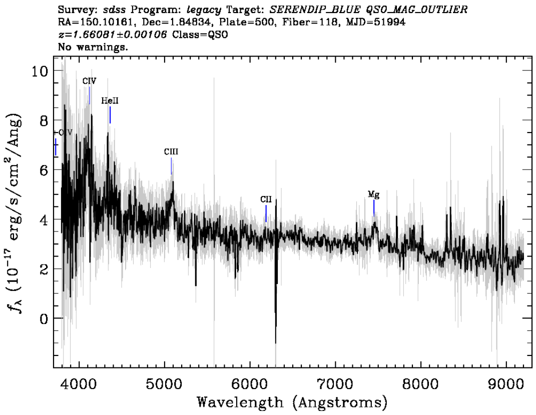

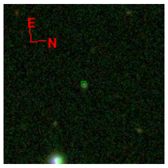

A.1

Xid	$zfinal$	$class$	$LogL_x$
87	1.664	1	44.27

`http://dr10.sdss3.org/spectrumDetail?mjd=52235&fiber=313&plateid=501`

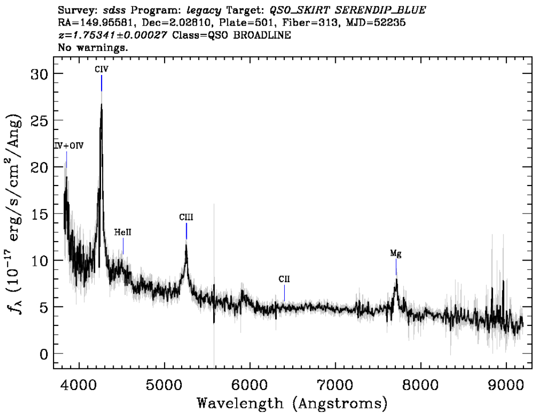

A.1

Xid	$zfinal$	$class$	$LogL_x$
30	1.753	1	44.45

`http://dr10.sdss3.org/spectrumDetail?mjd=55630&fiber=776&plateid=4737`

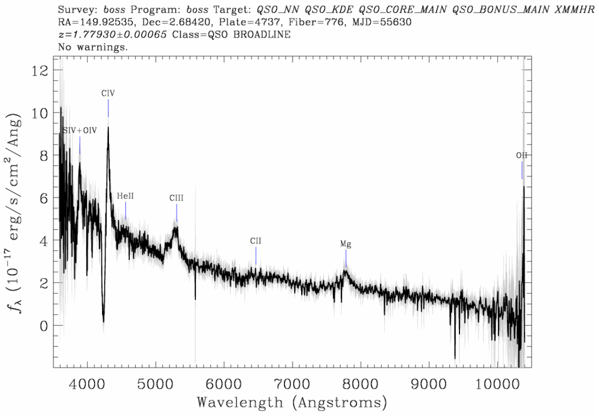

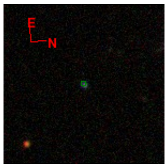

A.1

Xid	$zfinal$	$class$	$LogL_x$
53781	1.779	1	43.77

`http://dr10.sdss3.org/spectrumDetail?mjd=55630&fiber=238&plateid=4737`

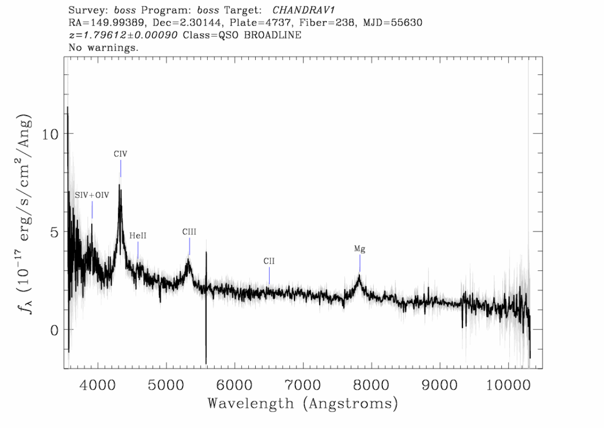

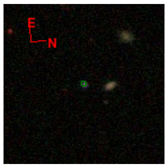

A.1

Xid	$zfinal$	$class$	$LogL_x$
34	1.796	1	44.41

`http://dr10.sdss3.org/spectrumDetail?mjd=51994&fiber=588&plateid=500`

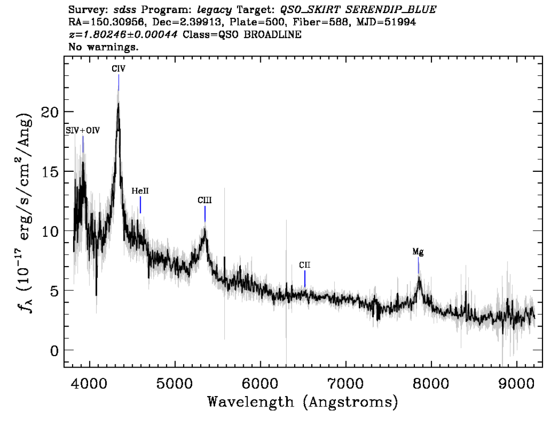

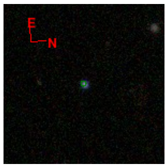

A.1

Xid	$zfinal$	$class$	$LogL_x$
33	1.799	1	44.53

`http://dr10.sdss3.org/spectrumDetail?mjd=52235&fiber=199&plateid=501`

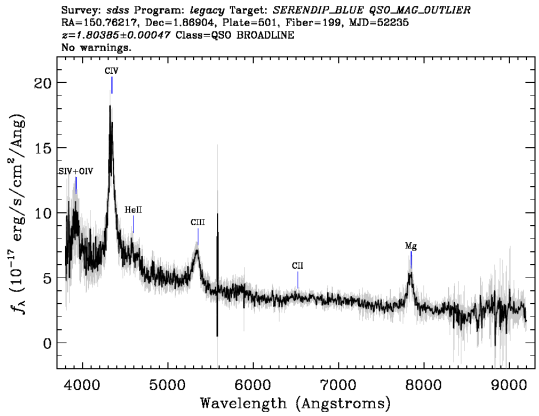

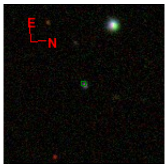

A.1

Xid	*zfinal*	*class*	$LogL_x$
2046	1.8	1	44.69

`http://dr10.sdss3.org/spectrumDetail?mjd=55630&fiber=194&plateid=4737`

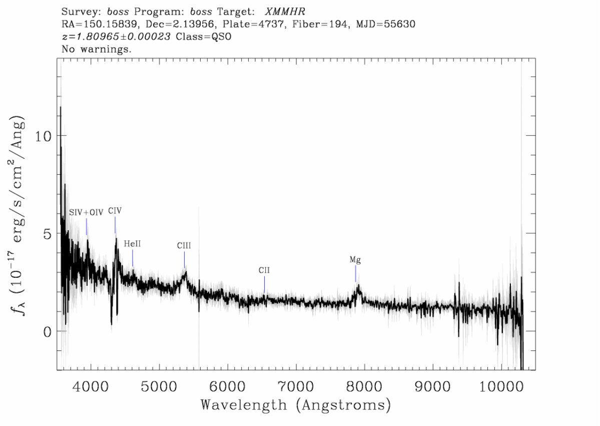

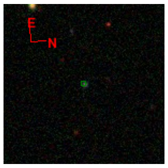

A.1

Xid	*zfinal*	*class*	$LogL_x$
160	1.81	1	44.29

`http://dr10.sdss3.org/spectrumDetail?mjd=51994&fiber=581&plateid=500`

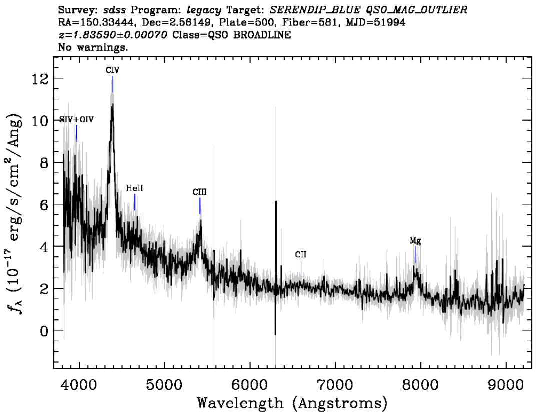

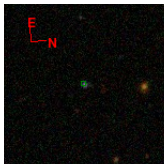

A.1

Xid	$zfinal$	$class$	$LogL_x$
111	1.834	1	44.47

`http://dr10.sdss3.org/spectrumDetail?mjd=51994&fiber=539&plateid=500`

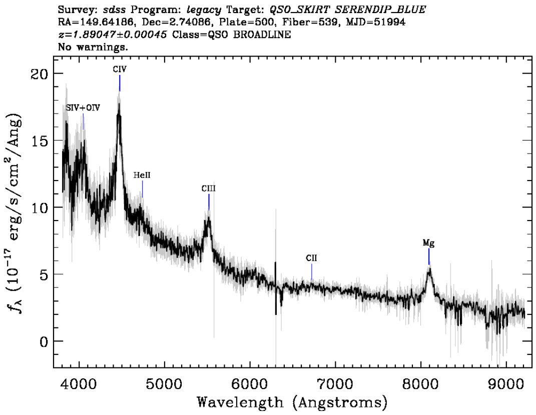

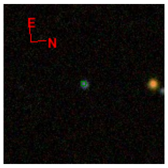

A.1

Xid	$zfinal$	$class$	$LogL_x$
5082	1.888	1	44.77

`http://dr10.sdss3.org/spectrumDetail?mjd=51994&fiber=175&plateid=500`

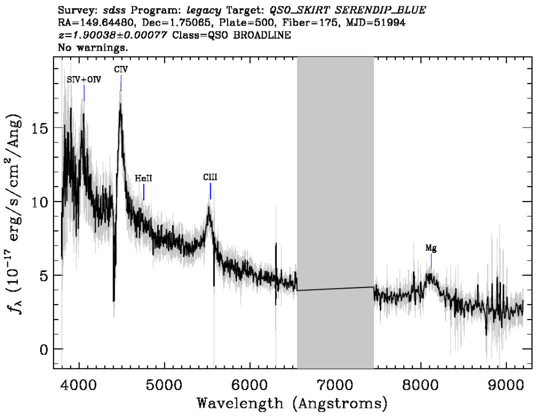

A.1

Xid	$zfinal$	$class$	$LogL_x$
5078	1.899	1	44.49

`http://dr10.sdss3.org/spectrumDetail?mjd=55630&fiber=188&plateid=4737`

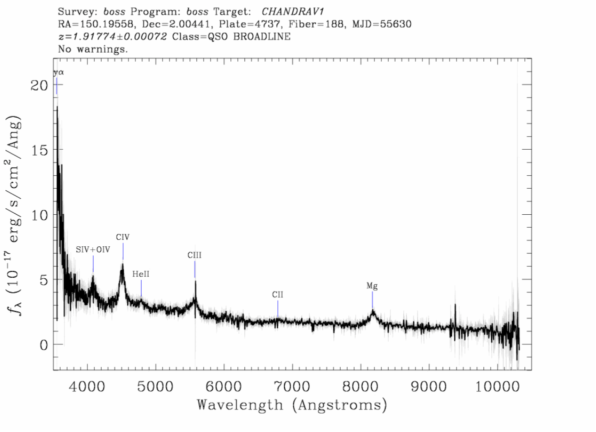

A.1

Xid	$zfinal$	$class$	$LogL_x$
59	1.918	1	44.46

`http://dr10.sdss3.org/spectrumDetail?mjd=52235&fiber=472&plateid=501`

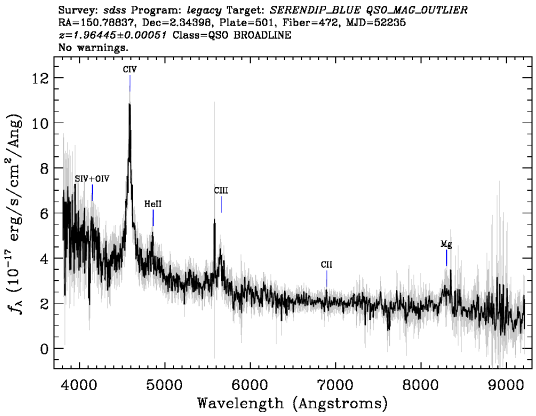

A.1

Xid	$zfinal$	$class$	$LogL_x$
5600	1.967	1	45.02

`http://dr10.sdss3.org/spectrumDetail?mjd=55630&fiber=334&plateid=4737`

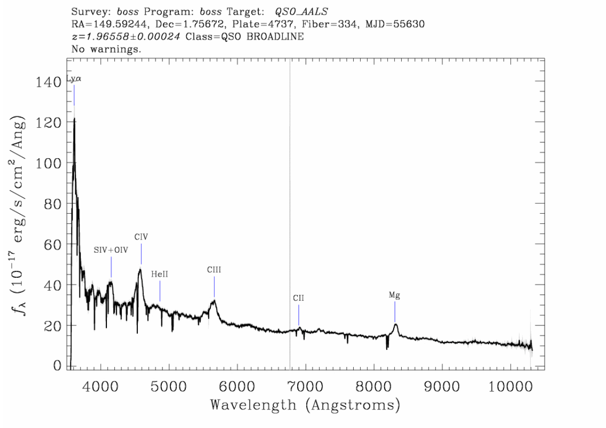

A.1

Xid	$zfinal$	$class$	$LogL_x$
10889	1.966	1	44.74

http://dr10.sdss3.org/spectrumDetail?mjd=51994&fiber=571&plateid=500

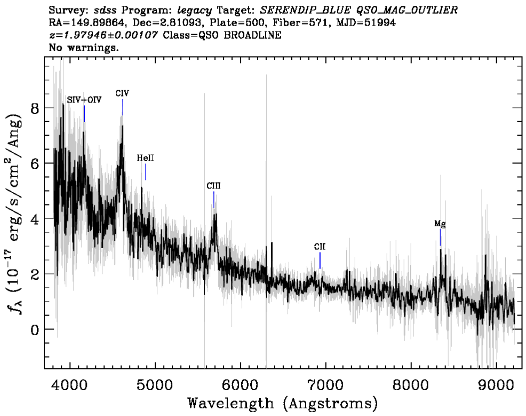

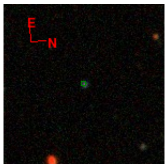

A.1

Xid	$zfinal$	$class$	$LogL_x$
10158	1.98	1	44.19

http://dr10.sdss3.org/spectrumDetail?mjd=52235&fiber=462&plateid=501

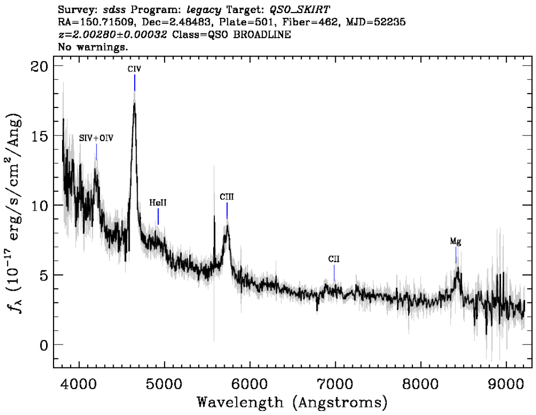

A.1

Xid	$zfinal$	$class$	$LogL_x$
5615	2.005	1	44.65

`http://dr10.sdss3.org/spectrumDetail?mjd=52235&fiber=224&plateid=501`

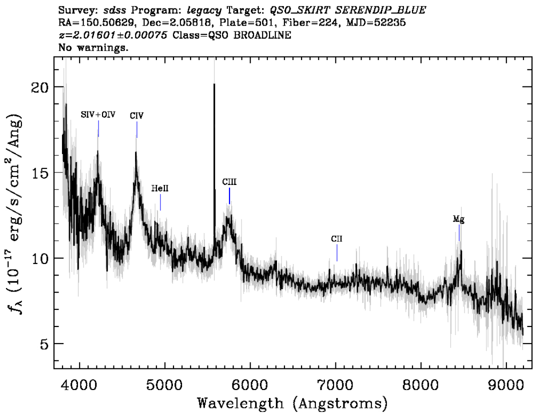

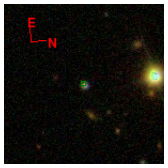

A.1

Xid	$zfinal$	$class$	$LogL_x$
2613	2.008	1	44.27

`http://dr10.sdss3.org/spectrumDetail?mjd=51994&fiber=164&plateid=500`

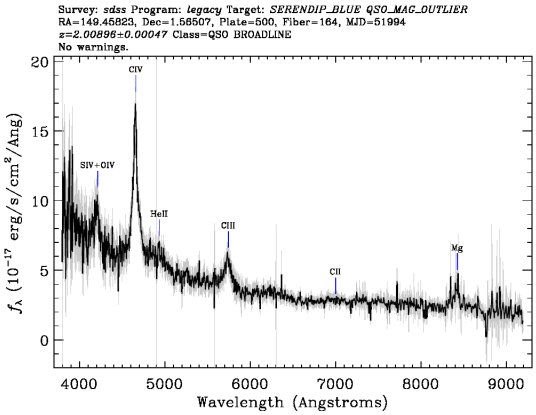

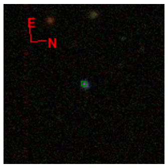

A.1

Xid	$zfinal$	$class$	$LogL_x$
54355	2.011	1	44.53

`http://dr10.sdss3.org/spectrumDetail?mjd=55630&fiber=176&plateid=4737`

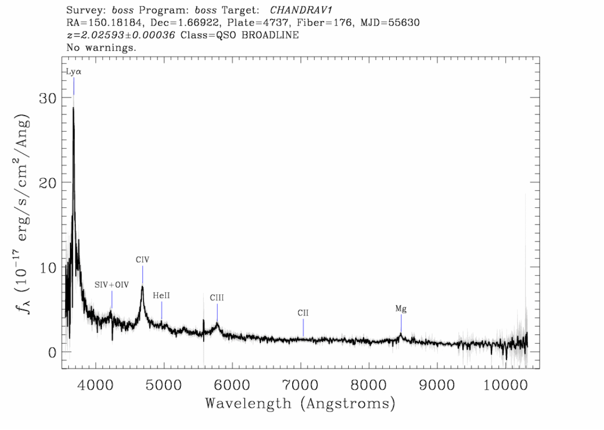

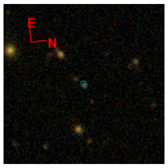

A.1

Xid	$zfinal$	$class$	$LogL_x$
2147	2.026	1	44.54

`http://dr10.sdss3.org/spectrumDetail?mjd=55630&fiber=78&plateid=4737`

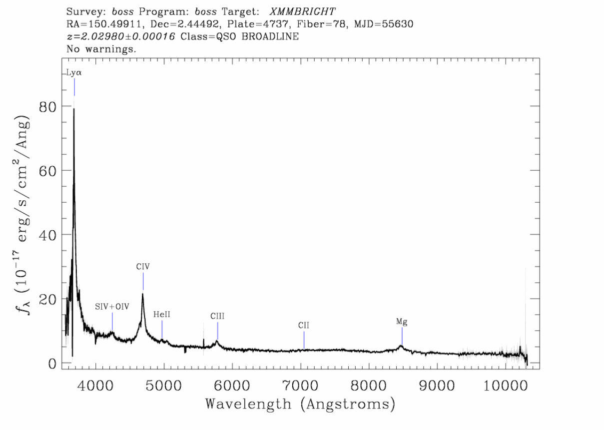

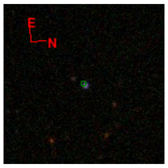

A.1

Xid	$zfinal$	$class$	$LogL_x$
15	2.03	1	45.24

`http://dr10.sdss3.org/spectrumDetail?mjd=52235&fiber=316&plateid=501`

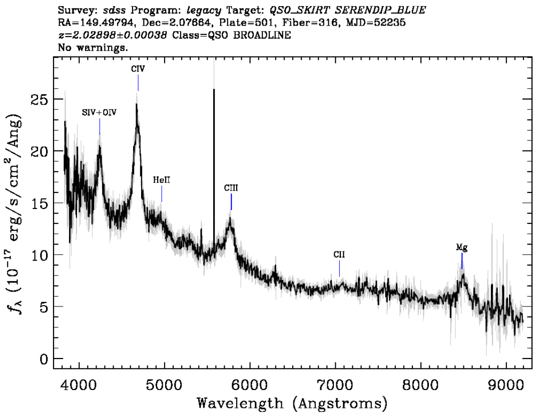

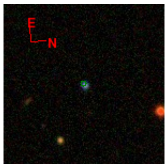

A.1

Xid	$zfinal$	$class$	$LogL_x$
5317	2.03	1	44.41

`http://dr10.sdss3.org/spectrumDetail?mjd=51994&fiber=630&plateid=500`

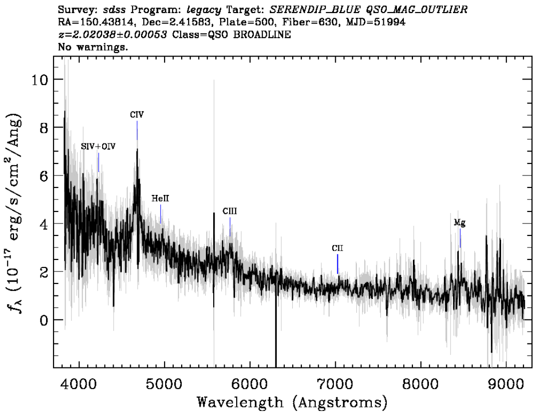

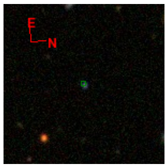

A.1

Xid	$zfinal$	$class$	$LogL_x$
375	2.032	1	44.31

http:
//dr10.sdss3.org/spectrumDetail?mjd=51994&fiber=80&plateid=500

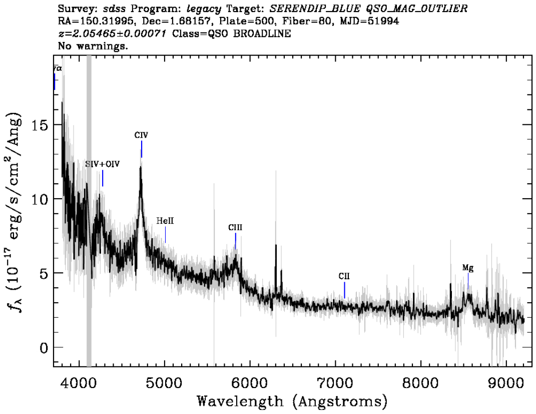

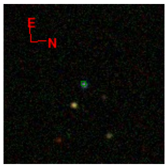

A.1

Xid	$zfinal$	$class$	$LogL_x$
2209	2.055	1	44.79

http://dr10.sdss3.org/spectrumDetail?mjd=51994&fiber=
174&plateid=500

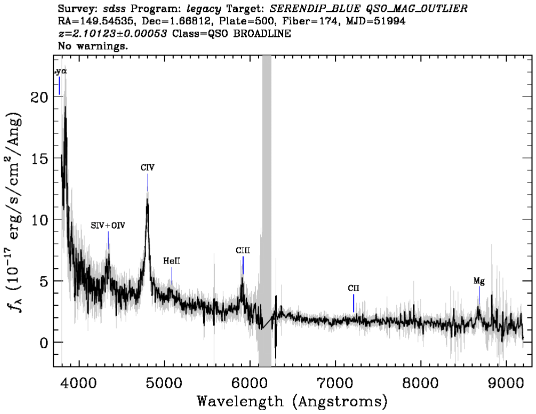

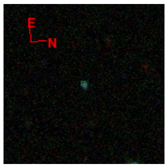

A.1

Xid	$zfinal$	$class$	$LogL_x$
54202	2.102	1	45.17

`http://dr10.sdss3.org/spectrumDetail?mjd=52235&fiber=367&plateid=501`

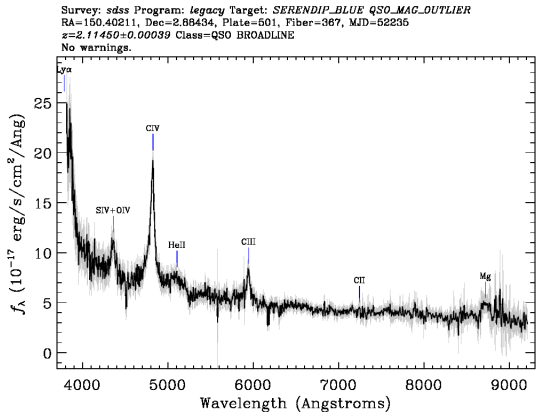
Survey: *sdss* Program: *legacy* Target: *SERENDIP_BLUE QSO_MAG_OUTLIER*
RA=150.40211, Dec=2.88434, Plate=501, Fiber=367, MJD=52235
z=2.11450±0.00039 Class=QSO BROADLINE
No warnings.

A.1

Xid	$zfinal$	$class$	$LogL_x$
96	2.117	1	44.98

`http://dr10.sdss3.org/spectrumDetail?mjd=55630&fiber=974&plateid=4737`

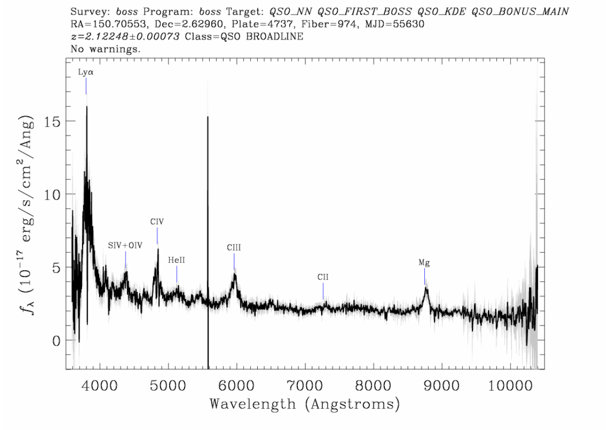
Survey: *boss* Program: *boss* Target: *QSO_NN QSO_FIRST_BOSS QSO_KDE QSO_BONUS_MAIN*
RA=150.70553, Dec=2.62960, Plate=4737, Fiber=974, MJD=55630
z=2.12248±0.00073 Class=QSO BROADLINE
No warnings.

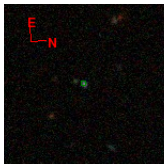

A.1

Xid	$zfinal$	$class$	$LogL_x$
5517	2.122	1	44.64

`http://dr10.sdss3.org/spectrumDetail?mjd=55630&fiber=736&plateid=4737`

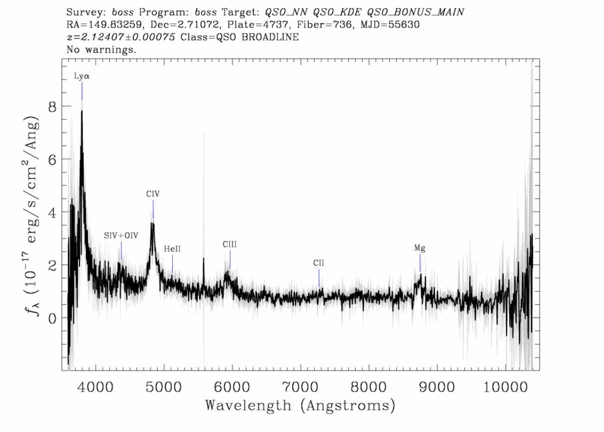

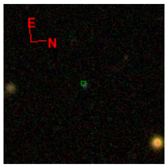

A.1

Xid	$zfinal$	$class$	$LogL_x$
5138	2.124	1	44.27

`http://dr10.sdss3.org/spectrumDetail?mjd=55630&fiber=187&plateid=4737`

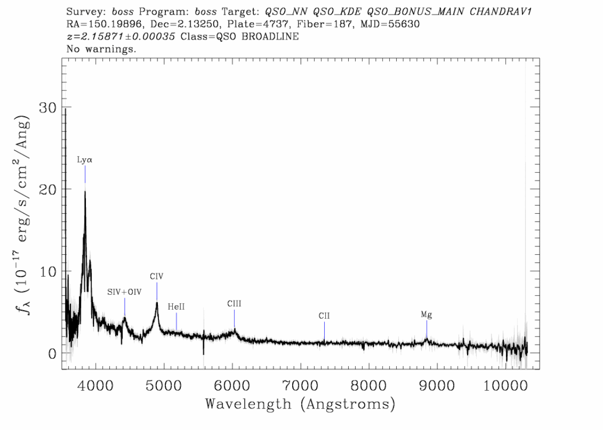

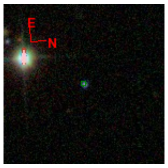

A.1

Xid	$zfinal$	$class$	$LogL_x$
128	2.159	1	44.55

`http://dr10.sdss3.org/spectrumDetail?mjd=55630&fiber=103&plateid=4737`

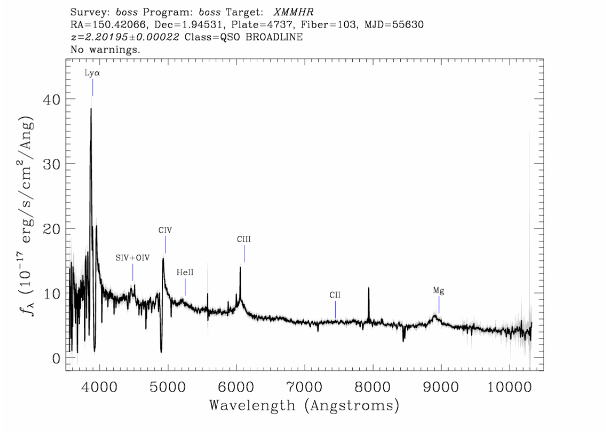

A.1

Xid	$zfinal$	$class$	$LogL_x$
2812	2.176	1	44.39

`http://dr10.sdss3.org/spectrumDetail?mjd=55630&fiber=761&plateid=4737`

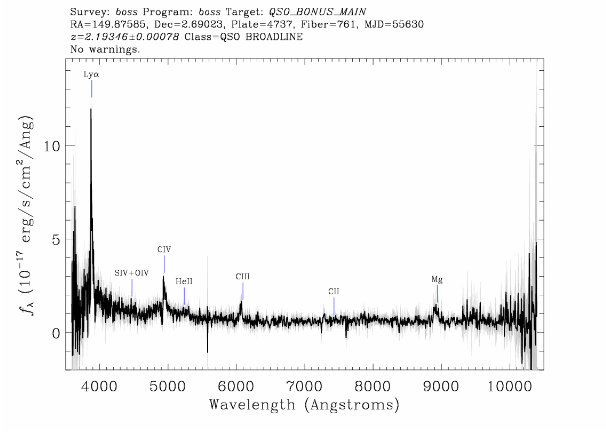

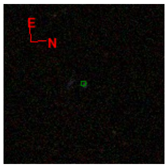

A.1

Xid	$zfinal$	$class$	$LogL_x$
5330	2.193	1	44.24

http://dr10.sdss3.org/spectrumDetail?mjd=55630&fiber=220&plateid=4737

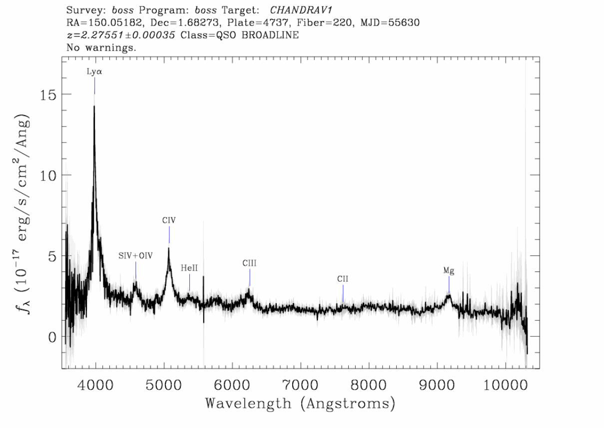

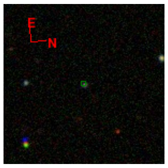

A.1

Xid	$zfinal$	$class$	$LogL_x$
2265	2.276	1	44.36

http://dr10.sdss3.org/spectrumDetail?mjd=55630&fiber=190&plateid=4737

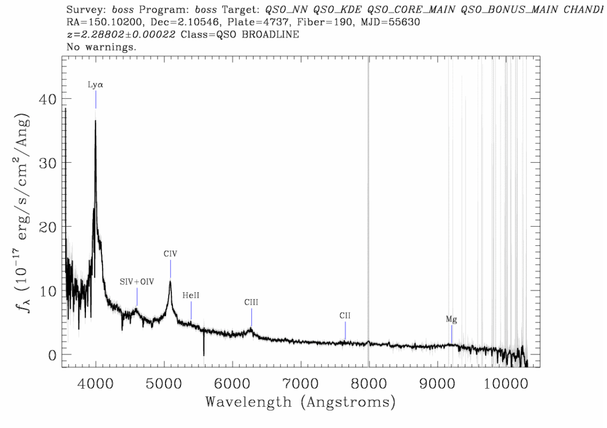

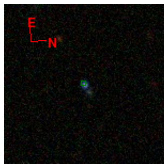

A.1

Xid	$zfinal$	$class$	$LogL_x$
25	2.288	1	44.81

`http://dr10.sdss3.org/spectrumDetail?mjd=55630&fiber=649&plateid=4737`

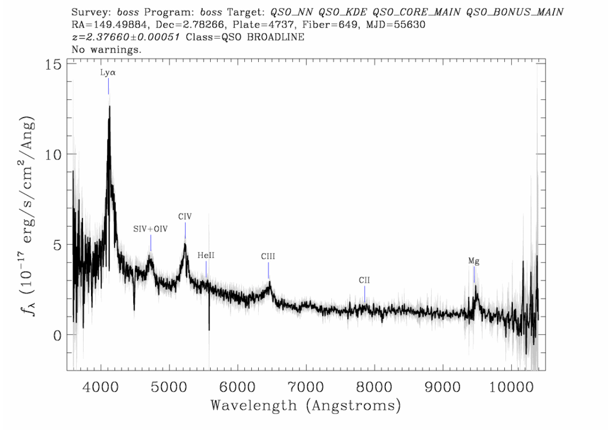

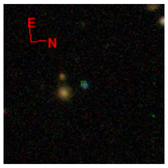

A.1

Xid	$zfinal$	$class$	$LogL_x$
5492	2.376	1	45.26

`http://dr10.sdss3.org/spectrumDetail?mjd=55630&fiber=844&plateid=4737`

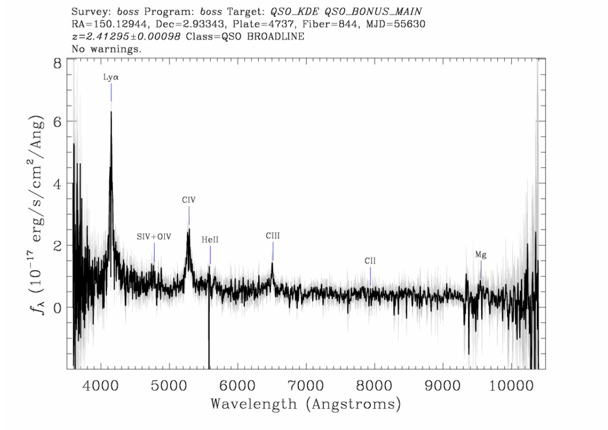

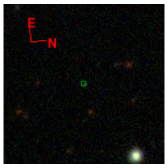

A.1

Xid	$zfinal$	$class$	$LogL_x$
53379	2.413	1	-941.3

`http://dr10.sdss3.org/spectrumDetail?mjd=55630&fiber=262&plateid=4737`

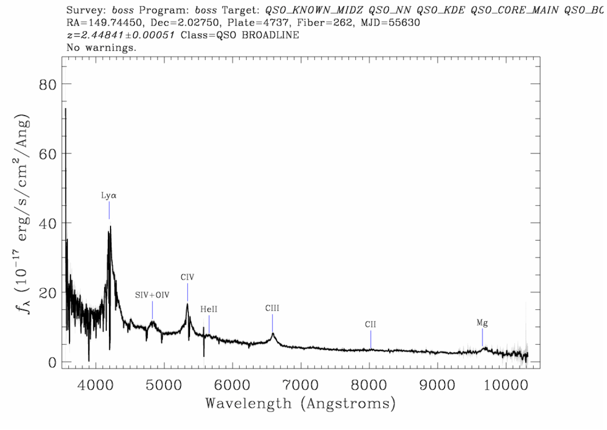

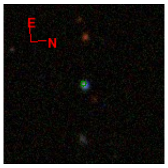

A.1

Xid	$zfinal$	$class$	$LogL_x$
199	2.454	1	45.18

`http://dr10.sdss3.org/spectrumDetail?mjd=55630&fiber=60&plateid=4737`

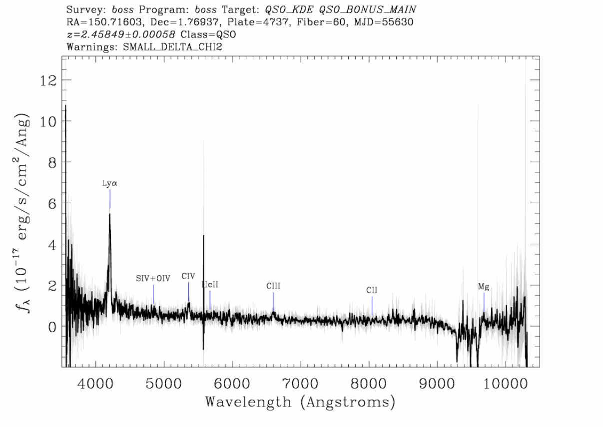

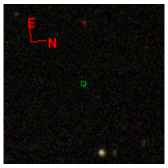

A.1

Xid	$zfinal$	$class$	$LogL_x$
60247	2.458	1	43.83

`http://dr10.sdss3.org/spectrumDetail?mjd=55630&fiber=147&plateid=4737`

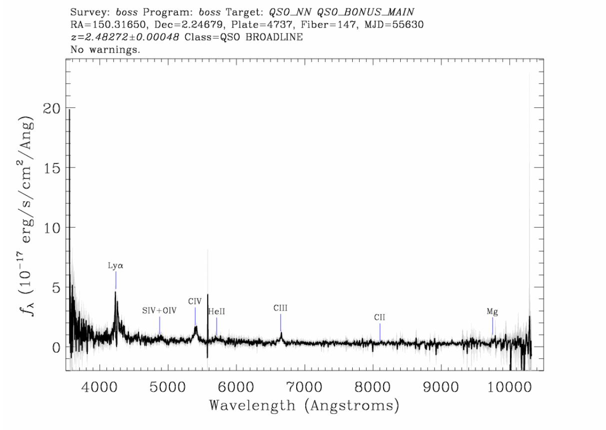

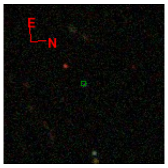

A.1

Xid	$zfinal$	$class$	$LogL_x$
498	2.483	1	44.34

`http://dr10.sdss3.org/spectrumDetail?mjd=51994&fiber=556&plateid=500`

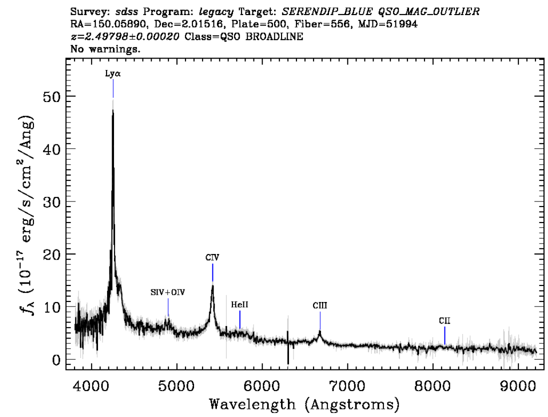

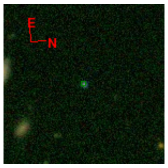

A.1

Xid	$zfinal$	$class$	$LogL_x$
51	2.497	1	44.57

`http://dr10.sdss3.org/spectrumDetail?mjd=52235&fiber=229&plateid=501`

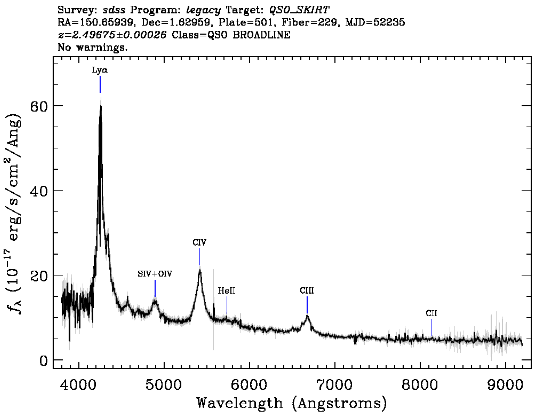

Survey: *sdss* Program: *legacy* Target: *QSO_SKIRT*
RA=150.65939, Dec=1.62959, Plate=501, Fiber=229, MJD=52235
z=2.49675±0.00026 Class=QSO BROADLINE
No warnings.

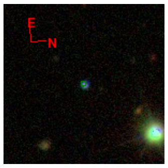

A.1

Xid	*zfinal*	*class*	$LogL_x$
2093	2.506	1	44.81

`http://dr10.sdss3.org/spectrumDetail?mjd=55630&fiber=150&plateid=4737`

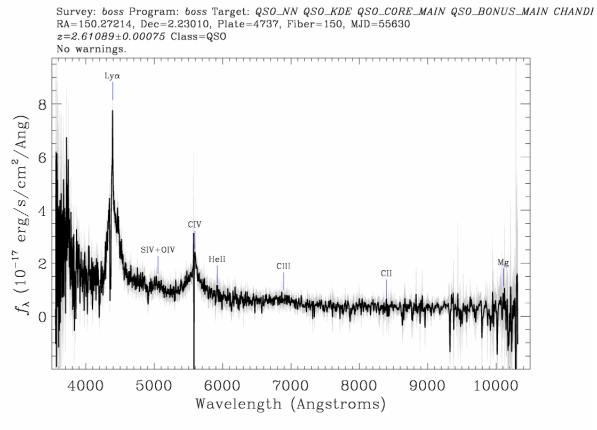

Survey: *boss* Program: *boss* Target: *QSO_NN QSO_KDE QSO_CORE_MAIN QSO_BONUS_MAIN CHANDI*
RA=150.27214, Dec=2.23010, Plate=4737, Fiber=150, MJD=55630
z=2.61089±0.00075 Class=QSO
No warnings.

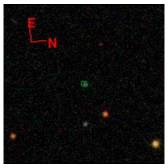

A.1

Xid	*zfinal*	*class*	$LogL_x$
133	2.611	1	44.76

`http://dr10.sdss3.org/spectrumDetail?mjd=51994&fiber=69&plateid=500`

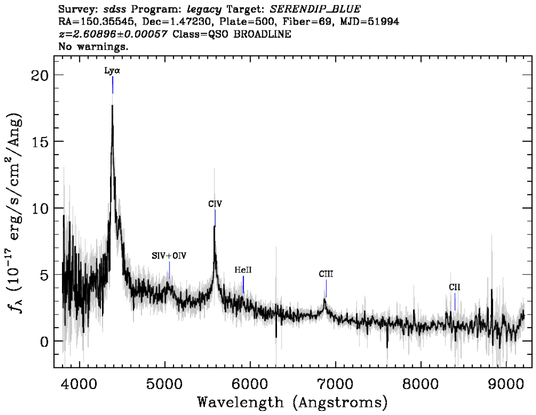

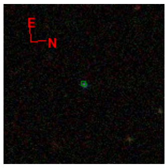

A.1

Xid	$zfinal$	$class$	$LogL_x$
53686	2.614	1	45.01

`http://dr10.sdss3.org/spectrumDetail?mjd=55630&fiber=970&plateid=4737`

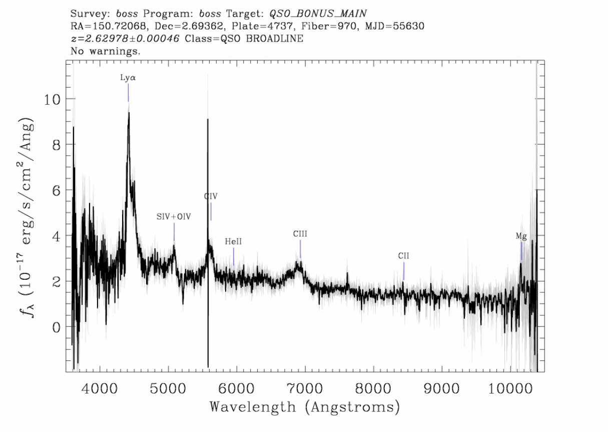

A.1

Xid	$zfinal$	$class$	$LogL_x$
53357	2.63	1	43.97

`http://dr10.sdss3.org/spectrumDetail?mjd=55630&fiber=896&plateid=4737`

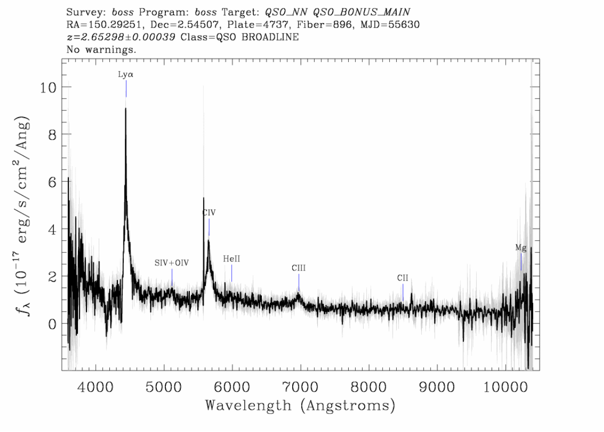

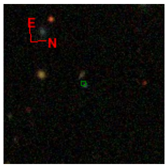

A.1

Xid	$zfinal$	$class$	$LogL_x$
93	2.653	1	44.57

`http://dr10.sdss3.org/spectrumDetail?mjd=55630&fiber=278&plateid=4737`

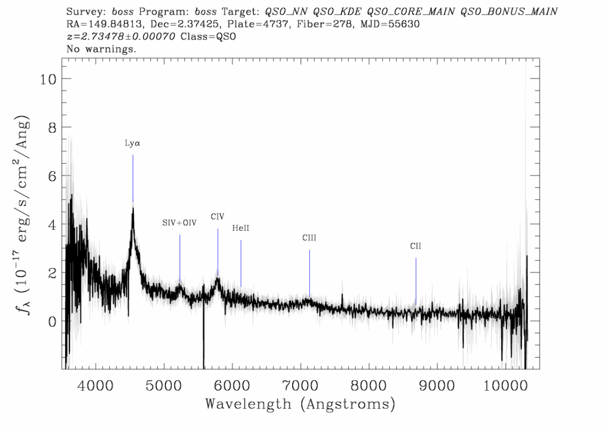

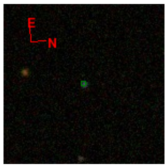

A.1

Xid	$zfinal$	$class$	$LogL_x$
512	2.735	1	44.05

`http://dr10.sdss3.org/spectrumDetail?mjd=55630&fiber=233&plateid=4737`

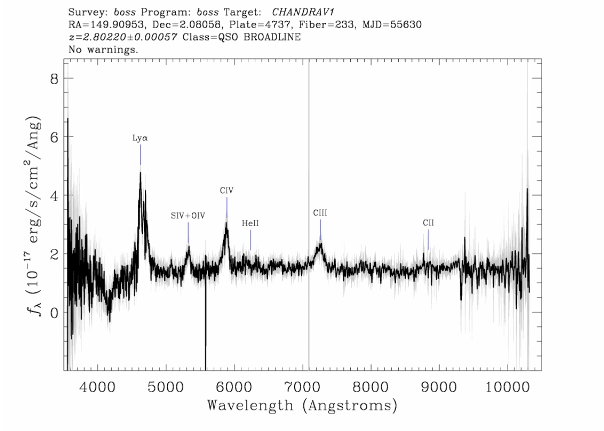

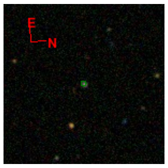

A.1

Xid	$zfinal$	$class$	$LogL_x$
146	2.802	1	44.95

`http://dr10.sdss3.org/spectrumDetail?mjd=55630&fiber=346&plateid=4737`

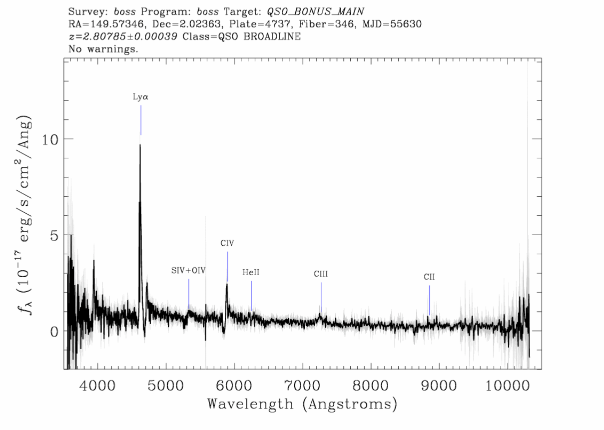

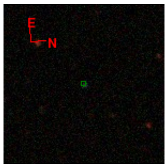

A.1

Xid	$zfinal$	$class$	$LogL_x$
60466	2.808	1	44.12

`http://dr10.sdss3.org/spectrumDetail?mjd=55630&fiber=72&plateid=4737`

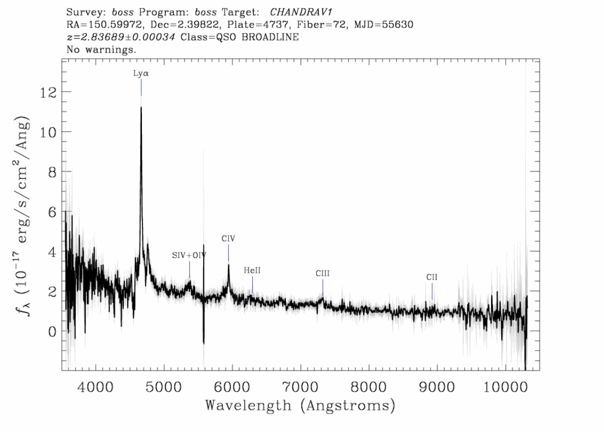

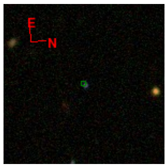

A.1

Xid	$zfinal$	$class$	$LogL_x$
5483	2.837	1	44.68

`http://dr10.sdss3.org/spectrumDetail?mjd=55630&fiber=302&plateid=4737`

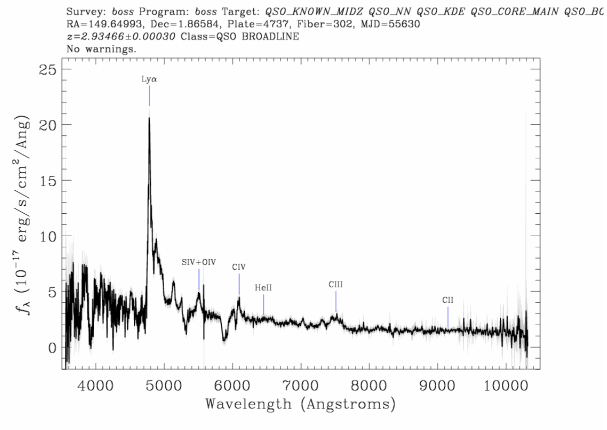

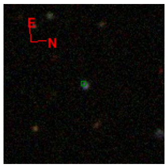

A.1

Xid	$zfinal$	$class$	$LogL_x$
5023	2.934	1	44.08

`http://dr10.sdss3.org/spectrumDetail?mjd=55630&fiber=811&plateid=4737`

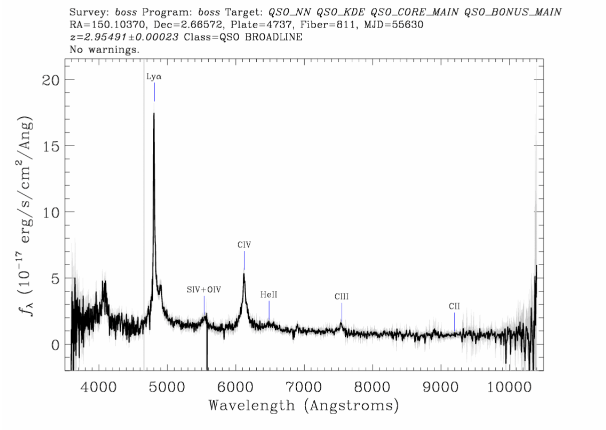

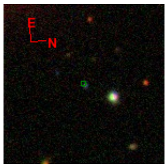

A.1

Xid	$zfinal$	$class$	$LogL_x$
168	2.955	1	44.83

`http://dr10.sdss3.org/spectrumDetail?mjd=55630&fiber=356&plateid=4737`

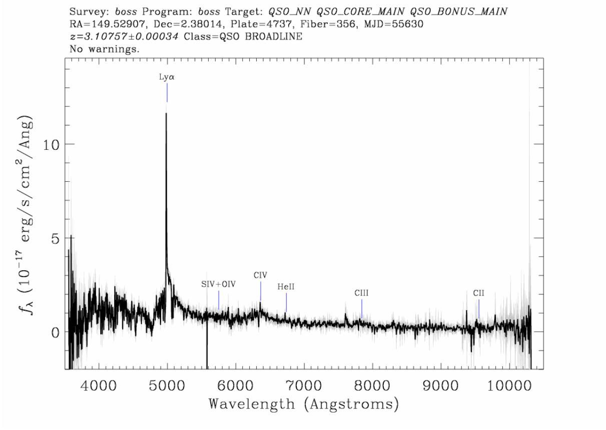

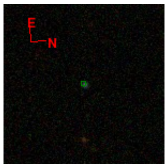

A.1

Xid	$zfinal$	$class$	$LogL_x$
2421	3.108	1	44.86

`http://dr10.sdss3.org/spectrumDetail?mjd=55630&fiber=160&plateid=4737`

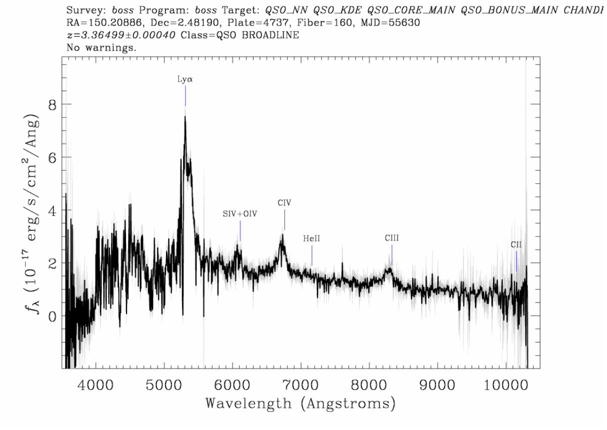

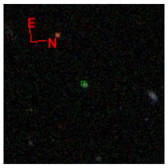

A.1

Xid	$zfinal$	$class$	$LogL_x$
180	3.365	1	44.39

`http://dr10.sdss3.org/spectrumDetail?mjd=55630&fiber=28&plateid=4737`

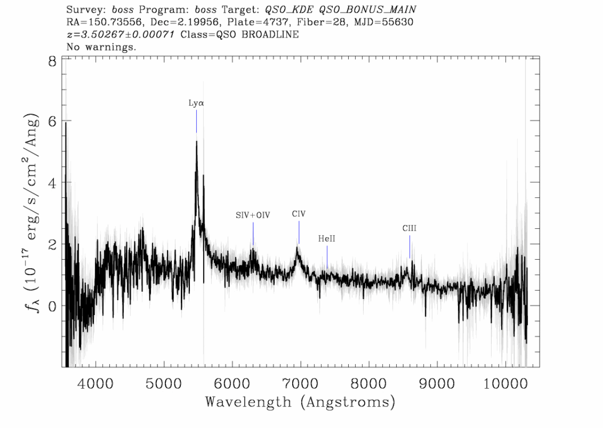

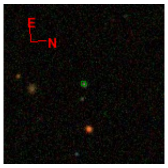

A.1

Xid	$zfinal$	$class$	$LogL_x$
5116	3.503	1	44.88

`http://dr10.sdss3.org/spectrumDetail?mjd=55630&fiber=156&plateid=4737`

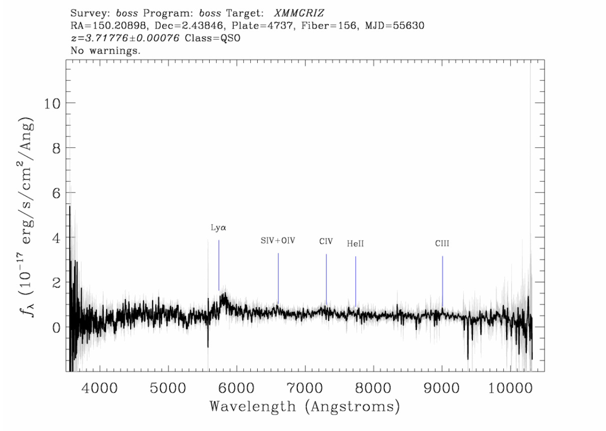

A.1

Xid	$zfinal$	$class$	$LogL_x$
300	3.718	1	44.78

Bibliography

[1] Alexander *et al.* 2010ASPC, 427, 74A

[2] Alexander, D. M.; Hickox, R. C. 2012NewAR, 56, 93A

[3] Allen S. W. *et al.* 2006 MNRAS, 372, 21A

[4] Antonucci, R. 1993 ARA&A, 31, 473A

[5] Balbus, Steven A.; Hawley, John F. 1992ApJ , 400, 610B

[6] Baldwin *et al.* 1981 PASP ,93, 5B

[7] Barnes & Hernquist 1992ARA&A, 30, 705B

[8] Barnes & Hernquist 1996ApJ, 47, 115B

[9] Benson A.J. *et al.* 2003ApJ, 599, 38B

[10] Binney, J., Tabor, G. Astron. Soc. 276, 663-678 (1995)

[11] Bongiorno, A. *et al.*, 2012, MNRAS, 427, 3103B

[12] & Combes 2002A&A, 392, 83B

[13] Bower R.G. *et al.* 2006 MNRAS, 370, 645B

[14] Brandt & Hasinger 2005ARA&A,43, 827B

[15] Brinchmann, J. *et al.* 2004 MNRAS, 351, 1151B

[16] Brusa, M., *et al.*, 2010, ApJ, 716:348369

[17] Brusa M. *et al.*, 2014 arXiv 1409, 1615B

[18] Cano-Diaz *et al.* 2012A&A, 537L, 8C

[19] Capak, P., *et al.*, 2007, ApJS, 172, 99

[20] Cappelluti, N., *et al.*, 2007, ApJS, 172, 341

[21] Cappelluti, N., *et al.*, 2009, A&A, 497, 635

[22] Cardelli, Clayton, and Mathis 1989 ApJ 345, 245

[23] Cattaneo, A., Teyssier, R. 2007 376, 1547-1556

[24] Ceverino D., Klypin A., 2009, ApJ, 695, 292

[25] Chen, X. Y. *et al.*, 2009, A&A Volume 495, Number 2

[26] Cicone *et. al.* 2014 A&A,562A, 21C

[27] Cicone *et. al.* 2012 A&A, 543A, 99C

[28] Cimatti *et. al.* 2013 ApJ, 779L, 13C

[29] Ciotti *et al.* 2010 ApJ, 717, 708C

[30] Ciotti, L., Ostriker, J.P. ApJ, 665, 1038-1056 (2007)

[31] Crenshaw D. M., Schmitt H. R., Kraemer S. B., Mushotzky R. F.,Dunn J. P., 2010, ApJ, 708, 419

[32] Croton *et al.* 2006 MNRAS 365,11

[33] Di Matteo, T. *et al.*, 2005 Nature 433, 604D

[34] Dunn *et al.*, 2010ApJ, 709, 611D

[35] Elvis, M., *et al.*, 2009, ApJS, 184, 158

[36] Elvis, M *et al.* 1994 ApJS, 95,1E

[37] Englmaier & Shlosman 2004, ApJ, 617, L115

[38] Fabian, A.C. 1999 MNRAS, 308L, 39F

[39] Fabian*et al.* 2006 MNRAS, 373L,16F

[40] Fabian *et al.* 2009 MNRAS, 394L, 89F

[41] Fabian, A. C.; Vasudevan, R. V.; Gandhi, P.,2008 MNRAS, 385L, 43F

[42] Fabian, A. C. 2012 ARA&A,50, 455F

[43] Fabian A.C. 2010 IAUS,267, 341F

[44] Fabian A. C. 1994. ARAA 32: 277318

[45] Ferrarese, L. & Merritt, D., 2000 ApJ 539L 9F

[46] Feruglio *et al.* 2010 A&A, 518L, 155F

[47] Fischer *et al.* 2010 A&A, 518, L41

[48] Forster-Schreiber *et al.* 2014 ApJ ,787, 38F

[49] Garcia-Burillo *et al.* 2005 A&A ,441,1011G

[50] Gaskell, C.M.; Ferland, G.J. 1984 PASP , 96, 393G

[51] Gerbhardt, K. *et al.*, 2000 ApJ 539, L13

[52] Gofford J. *et al.*, 2011, MNRAS, 414, 3307

[53] Granato, G.L. *et al.* 2004 ApJ , 600, 580G

[54] Greene, J. E., Zakamska, N. L., Liu, X., Barth, A. J., & Ho, L. C. 2009, ApJ, 702, 441

[55] Greene J. E., Zakamska N. L., Ho L. C., Barth A. J., 2011, ApJ, 732, 9

[56] Gultekin,K. *et al.* 2009 Apj 698,198-221

[57] Gunn & Gott 1972 ApJ 176, 1G

[58] Halpern,J.P.; Steiner, J.E. 1983ApJ , 269L, 37H

[59] Haring, R. *et al.* 2004 ApJ, 604L, 89H

[60] Harrison *et. al* 2012 MNRAS, 426, 1073H

[61] Harrison *et. al* 2014 MNRAS, 441, 3306H

[62] Heckman, T. *et al.*, 2014 arXiv 1403, 4620H

[63] Heckman, T. *et al.* 1984 ApJ, 281, 525H

[64] Heckman,T. *et al.* 2004 ApJ 613,109

[65] Heckman T. M., Miley G. K., van Breugel W. J. M., Butcher H. R.,1981, ApJ, 247, 403

[66] Heckman T. M., Armus L., Miley G. K., 1990, ApJS, 74, 833

[67] Ho, L. C. 2008 ARA&A, 46, 475

[68] Holt, J.; Tadhunter, C. N.; Morganti, R.; Emonts, B. H. C. 2011 MNRAS, 410, 1527H

[69] Holt J., Tadhunter C. N., Morganti R., 2003, MNRAS, 342, 227

[70] Hopkins & Beacom, 2006 ApJ, 651, 142H

[71] Hopkins *et al.* 2007 ApJ, 662, 110H

[72] Hopkins *et al.* 2008 ApJS, 175, 356H

[73] Hopkins 2012 MNRAS.420L, 8H

[74] Ishibashi *et al.* 2012 MNRAS, 427, 2998I

[75] Ishibashi *et al.* 2013 MNRAS, 431, 2350I

[76] Johansson *et al.* 2009 ApJ, 707L, 184J

[77] Karim, A. *et al.* 2011 ApJ, 730, 61K

[78] Kauffmann, G. *et al.* 2003a MNRAS, 346,1055K

[79] Kauffmann, G. *et al.* 2003b MNRAS, 341, 54K

[80] Kewley, L. *et al.*, 2006 MNRAS, 372, 961K

[81] Kewley, L *et al.* 2001 ApJ, 556, 121K

[82] King, A. 2003 ApJ, 596L, 27K

[83] King, A. 2005 ApJ, 635, L121

[84] King A. R., 2010, MNRAS, 402, 1516

[85] King A.*et al.* 2012ApJ, 745L, 34Z

[86] Kormendy, J. *et al.* 1995 ARA&A 33 581K

[87] Kormendy, J. & Gebhardt, K. 2001 AIPC, 586, 363K

[88] Kormendy, J., D.B. Fisher, M.E. Cornell, R. Bender, ApJS 182, 216 (2009)

[89] Kriss, G. 1994 ASPC ,61,437K

[90] Ilbert, O., *et al.*, 2009, ApJ, 690, 1236

[91] Lagos C. d. P., Lacey C. G., Baugh C. M., 2013, MNRAS, 436, 1787

[92] Larson, R.B. 1974 MNRAS,169, 229L

[93] Le Floch, E., *et al.*, 2009, ApJ, 703, 222

[94] Leitherer C *et al.* 1999. ApJS 123:3

[95] Leitherer, Claus; Heckman, Timothy M. 1995 ApJs, 96, 9L

[96] Lilly, S. J., *et al.*, 2009, ApJS, 184, 218

[97] Liu G., Zakamska N. L., Greene J. E., Nesvadba N. P. H., Liu X., 2013, MNRAS, 436, 2576

[98] Lynden-Bell 1969 Nature 223 690L

[99] Lusso, E., *et al.*,2012, MNRAS, 425, 623L

[100] Mac Low M.-M., McCray R., Norman M. L., 1989, ApJ, 337, 141

[101] Madau P. *et al.* 1998 ApJ, 498, 106M

[102] Magorrian, J. *et al.* 1998, AJ 115, 2285M

[103] Marconi, A., *et al.*,2004 MNRAS, 351,169M

[104] McCracken, H., *et al.*, 2010, ApJ, 708, 202

[105] Mellema, G., Kurk, J.D., Rottgering, H.J.A. 2002 A&A 395, L13 L16

[106] Menci, N. *et al.* 2008ApJ, 685, 863M

[107] Merloni, A. & Heinz, S. 2008 MNRAS, 388, 1011M

[108] Merritt, D. & Ferrarese, L. 2001 MNRAS, 320L, 30M

[109] Mullaney *et al.* 2013 MNRAS, 433, 622M

[110] Murray N., Quataert E., Thompson T. A., 2005, ApJ, 618,569

[111] Nayakshin S., Zubovas K., 2012, MNRAS, 427, 372

[112] Nesvadba *et al.* 2008A&A , 491, 407N

[113] Nesvadba *et al.* 2010A&A , 521A, 65N

[114] Ott J., Walter F., Brinks E., 2005, MNRAS, 358, 1453

[115] Osterbrock *et al.* 1989 Astrophysics of gaseous nebulae and active galactic nuclei

[116] Osterbrock *et al.* 2006 Astrophysics of gaseous nebulae and active galactic nuclei, 2nd. ed. by D.E. Osterbrock and G.J. Ferland. Sausalito, CA: University Science Books

[117] Panessa,F.; Bassani, L. 2002A&A, 394, 435P

[118] Phinney, E. S. Theory of Accretion Disks, Proceedings of a NATO Advanced Research Workshop, held in Garching, March 6-10, 1989, Dordrecht: Kluwer, 1989, edited by Friedrich Meyer. NATO Advanced Science Institutes (ASI) Series C, Volume 290, p.457

[119] Pogge R.W., 1989 ApJ ,345,730

[120] Pope, E. C. D. 2011MNRAS, 414, 3344P

[121] Pradhan 1976MNRAS ,177, 31P

[122] Prescott, M. K. M., Impey, C. M., Cool, R. J., & Scoville, N. Z. 2006, ApJ, 644,100

[123] Press & Schechter 1974, ApJ, 187, 425P

[124] Proga, D., Stone, J. M., & Kallman, T. R. 2000, ApJ, 543, 686

[125] Raimundo, S. *et al.*, 2010 MNRAS, 408, 1714R

[126] Rafferty*et al.* 2006 ApJ, 652, 216R

[127] Ranalli P., Comastri A., Seti G., 2003, A&A, 399, 39

[128] Rodriguez-Zaurin *et al.* 2013 MNRAS, 432, 138R

[129] Rupke *et al.* 2011ApJ, 729L, 27R

[130] Rupke & Veilleux 2011ApJ, 729L, 27R

[131] Rupke & Veilleux 2013ApJ, 768 , 75R

[132] Salpeter, E. E. 1964 ApJ, 140, 796S

[133] Salvato, M., *et al.*, 2009, ApJ, 690, 1250

[134] Scoville, N., *et al.* 2007, ApJ, 172:1-8

[135] Schawinski *et al.* 2009 ApJ, 690, 1672S

[136] Shakura, N. I. & Sunyaev, R. A. 1973 IAUS, 55, 155S

[137] Shuder J. M., & Osterbrock, D. E. 1981, ApJ, 250, 55

[138] Silk & Rees, 1998 A&A , 331L,1S

[139] Silk 2013 ApJ , 772, 112S

[140] Springel *et al.* 2005 Nature, 435, 629S

[141] Springel V. *et al.* 2005 MNRAS, 361, 776S

[142] Stern, D. *et al.* 2012 MNRAS 426: 2703-2718

[143] Tadhunter, C. *et. al.* 2014 Nature, 511, 440T

[144] Tombesi F., Cappi M , *et al.* 2010, A&A, 521, A57

[145] Tremonti *et. al.* 2007ApJ, 663L, 77T

[146] Trump, J. R., *et al.*, 2007, ApJS, 172, 383

[147] Trump, J. R., *et al.*, 2009, ApJ, 696, 1195

[148] Urry, C. M. & Padovani, P. 1995 PASP, 107, 803U

[149] Urrutia T., Lacy M., Spoon H., Glikman E., Petric A., Schulz B., 2012, ApJ, 757, 125

[150] Veilleux, S. & Osterbrock, D. 1987 NASCP2466,737V

[151] Veilleux S., Cecil G., Bland-Hawthorn J., 2005, ARAA, 43,769

[152] Vogelsberger *et al.* 2014 Nature, 509, 177V

[153] Wagner, A.Y., Bicknell, G.V., Umemura, M. ApJ 2012 757, 136 160

[154] Wampler *et al.* 1975ApJ,198L, 49W

[155] Whitaker *et al.* 2013 ApJ,770L, 39W

[156] White & Rees 1978, MNRAS.183, 341W

[157] White & Frenk 1991ApJ ,379 , 52W

[158] Whittle *et al.* 1985MNRAS.213, 1W

[159] Wilson & Heckman 1985 Astrophysics of Active Galaxies and Quasi stellar objects pp 39-109

[160] Zakamska, Nadia L.; Greene, Jenny E. 2014MNRAS, 442, 784Z

[161] Zhang, J. S., Henkel, C., Guo, Q. et al. 2010, ApJ., 708, 1528.

[162] Zinn *et al.* 2013 ApJ , 774 , 66Z

[163] Zubovas K., King A., 2012, ApJL, 745, L34